Title
Fatigue Bond Characteristics and Modeling of Near Surface Mounted FRP Reinforcements in Concrete

Author
Wang, Xun

Publication Date
2021

Peer reviewed|Thesis/dissertation

Fatigue Bond Characteristics and Modeling of Near Surface Mounted FRP Reinforcements in Concrete

By

XUN WANG
DISSERTATION

Submitted in partial satisfaction of the requirements for the degree of

DOCTOR OF PHILOSOPHY

in

Civil and Environmental Engineering

in the

OFFICE OF GRADUATE STUDIES

of the

UNIVERSITY OF CALIFORNIA

DAVIS

Approved:

Lijuan “Dawn” Cheng, Chair

John E. Bolander

Rob Y. H. Chai

Committee in Charge

2021

TABLE OF CONTENTS

LIST OF SYMBOLS

a = smaller edge length of the rectangular NSM strip (mm); or constant of curve fitting;

α_r = concrete edge distance (mm);

A = experimental parameters obtained by regression analysis;

A_f = cross-sectional area of NSM reinforcement (mm^2);

A_c = cross-sectional area of concrete joint specimen (mm^2);

b, d_f = larger edge length of the rectangular NSM strip (mm);

b_c = width of FRP plate (mm);

b_p = width of concrete block (mm);

B = experimental parameters obtained by regression analysis;

c = constant of curve fitting;

c_1, c_2 = constants determined from concrete tensile tests;

C_1, C_2, D_1, D_2, D_3, D_4, E_1, E_2 = coefficients from regression analysis;

C_1^i, C_2^i and C_3^i = introduced constants of the i^{th} element;

d_a = maximum aggregate size (mm);

d_b = rod diameter (mm);

d_c = depth of the adhesive cover (mm); or concrete damage variable in compression;

d_g = depth of concrete groove (mm);

d_t = concrete damage variable in tension;

dx = constant interval between two consecutive strain gages (mm);

$d\varepsilon_i$, $d\varepsilon_f(x)$ = difference in strain readings of two consecutive strain gauges;

B = experimental parameter obtained by regression analysis;

D = damage variable of cohesive element;

E_0 = initial concrete elastic modulus (MPa);

E_a = Young's modulus of epoxy adhesive (MPa);

E_c = Young's modulus of concrete (MPa);

E_f = Young's modulus of NSM FRP reinforcement (MPa);

E_{nn}, E_{ss}, E_{tt} = elastic tensile or shear stiffness of cohesive element (MPa);

E_{ns}, E_{nt}, E_{st} = coupling stiffness term of cohesive element (MPa);

E_p = Young's modulus of FRP plate (MPa);

E_s = concrete secant modulus at σ_0 (MPa);

f_c = concrete compressive strength (MPa);

f_f = tensile strength of FRP reinforcement (MPa);

f_t = concrete tensile strength (MPa);

f_t^a = tensile strength of adhesive (MPa);

F = applied cyclic load (N); or evolution of the CDP yield function;

F_f = post-failure friction force (kN);

f = average post-failure friction (MPa);

G = non-associated potential plastic flow;

G_1, G_2, G_2' = local stress coefficient at interfaces;

G_a = adhesive shear modulus (GPa);

G_f = interfacial fracture energy per unit area (N/mm);

G_F = fracture energy absorbed per unit crack area in widening the crack from zero to w_c ($N \cdot m/m^2$);

h_c = height of free concrete edge (mm); or crack band width (mm);

i = location index of local bond stress; or index of the finite element;

k = the ratio of groove size (width or depth) to FRP reinforcement dimension;

K_c = ratio of the second stress invariant on the tensile meridian, $q_{(TM)}$, to that on the compressive meridian, $q_{(CM)}$;

K_{nn} = stiffness in the normal direction of cohesive element (MPa/mm);

K_{nn}^a = stiffness of epoxy adhesive in the normal direction (MPa/mm);

K_{nn}^{f} = stiffness of CFRP strip in the normal direction (MPa/mm);

K_{ss}, K_{tt} = stiffness in the first and second shear direction of cohesive element (MPa/mm), respectively;

l_e = edge length of a concrete element (mm);

L, L_b = bond length (mm);

L_d = debonding length that is close to the loaded end (mm);

L_d^1 = debonding length at the 1st fatigue cycle (mm);

L_d^k = debonding length at the k^{th} fatigue cycle (mm);

L_{eff} = effective bond length over which the bonded joints provides at least 97% of the maximum theoretical bond strength (mm);

L_f = bond failure limit (mm);

L_p = perimeter of the failure plane or the NSM reinforcement (mm);

L_R = fatigue load range (kN);

LR_{max} = maximum fatigue load ratio (%);

L_s = bond length within the softening stage (mm);

L_s^1 = softening length at the 1st fatigue cycle (mm);

L_s^k = softening length at the k^{th} fatigue cycle (mm);

L_{sm} = softening length corresponding to the maximum pull-out force of the bonded joints (mm);

L_{sm}^u = softening length corresponding to the maximum theoretical bond strength (mm);

L_{su} = ultimate softening length (mm);

n = empirical parameter; or modular ratio between concrete and adhesive;

n_1, n_2, n_3 = notation to indicate the number of elements in different bond regions;

N = number of fatigue cycles;

N_f = number of fatigue cycles to failure or fatigue life;

$\bar{p}$ = hydrostatic pressure stress (MPa);

P, P_f = pull-out force of the joint specimen (kN);

P_{f_exp} = pull-out force of specimens on average obtained from the DPT (kN);

P_{f_model} = pull-out force predicted by the analytical model (kN);

P_{max} = magnitude of upper limit of the applied fatigue load range (kN);

$P_{max}{}^{u}$ = theoretical load-carrying capacity of the bonded joints (kN);

P_{min} = magnitude of lower limit of the applied fatigue load range (kN);

$\bar{q}$ = Mises equivalent effective stress (MPa);

S = cyclic mean bond stress range (S_{max} - S_{min}) (MPa); or predicted stress by the linear elastic traction-separation relationship for the current strain without damage (MPa);

S_{min} = smallest cyclic bond stress (MPa);

S_{max} = largest cyclic bond stress (MPa);

t_a = thickness of epoxy adhesive layer (mm);

t_n = normal traction of cohesive element (MPa);

$t_n{}^0$ = peak value of the nominal stress in the normal direction to the interface (MPa);

t_s, t_t = shear traction, along the local 1- and 2-direction of cohesive element (MPa), respectively;

$t_s{}^0$, $t_t{}^0$ = peak value of the nominal stress in the first and second shear direction (MPa), respectively;

t_d, t_w = vertical and horizontal distance of the failure plane that develops into the substrate concrete from the groove (mm), respectively;

t_f = half width of CFRP strip (mm);

t_p = thickness of FRP plate (mm);

T_{force} = force tolerance (N);

T_{slip} = slip tolerance (mm);

u_c = axial displacement of concrete block (mm);

u_f = axial displacement of FRP reinforcement (mm);

v = lateral deformation of concrete (mm);

v_g = lateral deformation of concrete at which the normal stress in adhesive reaches its tensile capacity (mm);

w = concrete crack opening displacement (mm);

w_c = critical concrete crack opening displacement (mm);

w_g = width of concrete groove (mm);

x_0 = free end of the bond line (mm);

x_6 = coordinate of the strain gage at the free end (mm);

x = distance from the free end (mm);

x_{i-1}, x_i = start and end coordinate of the i^{th} element (mm);

x_{n1} = boundary between elastic and softening bond region at the 1st fatigue cycle (mm);

x_{n2} = boundary between elastic and softening bond region at the 1st fatigue cycle (mm);

x_{n3} = loaded end of the bond line at the 1st fatigue cycle (mm);

x_k, x_{k-1} = coordinates of immediate neighboring strain gauges measured from the loaded end (mm);

X = distance measured from the free end (mm);

β_e = reduction coefficient due to edge distance;

β_L = reduction factor due to bond length;

γ = groove height-to-width ratio;

δ, δ_i = relative slip between NSM FRP reinforcement and concrete (mm);

δ_1 = relative slip corresponding to the local bond strength (mm);

δ_f = relative slip at debonding (mm);

δ_{fe} = relative slip at the free end (mm);

δ_n^0 = relative displacement between the top and bottom of the cohesive layer corresponding to t_n^0 (mm);

δ_s^0, δ_t^0 = relative displacement corresponding to t_s^0 and t_t^0 (mm), respectively;

ΔS = difference between the predicted stress and actual softening stress (MPa);

ε = eccentricity;

ε_0 = concrete compressive strain corresponding to σ_0;

ε_{0c}^{el} = elastic compressive strain corresponding to the undamaged concrete

ε_{0t}^{el} = elastic tensile strain corresponding to the undamaged concrete;

ε_6 = strain at the free end;

ε_c = concrete compressive strain;

ε_c^{in} = concrete inelastic strain in compression;

ε_c^{pl} = concrete plastic strain in compression;

ε_n = normal strain of cohesive element;

ε_{k-1}, ε_k = strain readings from immediate neighboring strain gauges;

ε_s, ε_t = shear strain of cohesive element;

ε_t^{ck} = concrete cracking strain;

ε_c^{el} = elastic compressive strain corresponding to the damaged concrete;

ε_t^{el} = elastic tensile strain corresponding to the damaged concrete;

ε_t^{pl} = concrete plastic strain in tension;

ε_u = ultimate concrete strain at crushing failure;

ΔLR = fatigue load range ratio (%);

ΔP = amplitude of fatigue load (kN);

$\Delta\sigma$ = stress amplitude (MPa);

λ, λ_1^i, λ_2^i = introduced symbols to simplify the expression;

μ = coefficient of friction at the FRP/adhesive interface; or viscosity parameter of the CDP model in ABAQUS

σ_0 = maximum concrete compressive stress (MPa);

σ_{b0} = initial biaxial compressive yield stress (MPa);

σ_c = concrete compressive stress (MPa);

$\bar{\sigma}_c\left(\varepsilon_c^{pl}\right)$ = effective compressive cohesion stress (MPa);

σ_{c0} = initial concrete yield stress in compression (MPa);

σ_f = axial stress of NSM FRP reinforcement (MPa);

$\bar{\sigma}_{max}$ = maximum principal effective stress (MPa);

σ_t = concrete tensile stress (MPa);

$\bar{\sigma}_t\left(\varepsilon_t^{pl}\right)$ = effective tensile cohesion stress (MPa);

σ_{t0} = uniaxial concrete tensile stress at failure (MPa);

σ_u = ultimate concrete stress at crushing failure (MPa);

τ = local bond stress (MPa);

τ_1 = local bond stress near the loaded end (MPa);

τ_{1max} = fatigue bond strength of τ_1 (MPa);

$\tau_{1max,static}$ = static bond strength of τ_1 (MPa);

τ_a = shear strength of adhesive (MPa);

τ_{avg} = average bond stress (MPa);

τ_f = local bond strength (MPa);

$\tau_{f,static}$ = static local bond strength (MPa);

$\tau_f^i(N)$ = local bond strength for the i^{th} finite element at the N^{th} fatigue cycle (MPa);

τ_i = average local bond stress between two consecutive strain gauges at the FRP and adhesive interface (MPa);

$\tau_i(\delta)$ = local bond stress-slip relationship for the i^{th} finite element (MPa);

τ_r = residual local bond strength (MPa);

$\tau_{r,static}$ = static residual bond strength (MPa);

$\tau_r^i(N)$ = residual local bond strength for the i^{th} finite element at the N^{th} fatigue cycle (MPa);

φ = dilation angle of the concrete measured in the meridian plane at high confining (hydrostatic) pressure (°);

φ_p = aspect ratio of the failure plane; and

$\langle \cdot \rangle$ = Macaulay bracket which yields the number inside the bracket only if it is positive otherwise yields zero.

LIST OF FIGURES

LIST OF TABLES

ACKNOWLEDGEMENTS

I would like to acknowledge all the people who have helped me during my pursuit of the doctoral degree at the University of California, Davis. Without their encouragement and support my doctoral study would be hard to imagine and impossible to complete.

First, I would like to express my sincerest appreciation to my research advisor, Dr. Lijuan "Dawn" Cheng, for her invaluable guidance, infinite patience and tremendous support throughout my doctoral program. It is a great honor and pleasure to be her student and work with her in the past unforgettable five years. I am truly grateful to Dr. Rob Y. H. Chai and Dr. John E. Bolander for taking time to review this dissertation and providing valuable suggestions and comments. I also would like to appreciate the faculty members in Civil and Environmental Engineering at UC Davis: Dr. Sashi Kunnath, Dr. Mark M. Rashid, Dr. N. Sukumar, Dr. Amit Kanvinde, Dr. Brian H. Maroney, Dr. Yannis Dafalias, Dr. Bassam Younis, as well as Dr. Valeria La Saponara from Mechanical and Aerospace Engineering. Their outstanding lectures, research advice and teaching experience are beneficial to my work and study.

I would like to express my special appreciation to my MS degree advisor, Dr. Zhao Liu at the Southeast University for his valuable advice and continuous support of my doctoral study.

I want to sincerely thank all my colleagues and friends at UC Davis: Jinjie Dai, Chao Fan, Youyou Zhang, Bitan Ding, Zhaoying Zhang, Xi Chen, Chaoyu Qiu, Dongxuan Yang, Zhelun Zhang, Qiwei Zhang, Han Yang, Hexiang Wang, Xiangpeng Li, Junyu Xiao, Yu Fen, Li Shan, Yaming Pan, Brendan Grayson-Wallace, Ardalan Hosseini, Emmanuel Vazquez, Yordan Nikolov, Ivy Rivas. It was happy and memorable to study and work with them.

I would like to thank the laboratory technicians of CEE department: Mr. Bill Sluis, Mr. Daret Kehlet and Mr. Victor Jones, for their kind help and technical support. Without their valuable time and knowledge in handcraft and machining work, it was not possible to complete my lab experiment.

My big gratitude to my best friend Yun Xu for his support and concern in my daily life, and his continuous encouragement to me to pursue for the doctoral degree.

Finally, I would like to express my deepest gratitude to my parents for their understanding, support and encouragement through my long years of education. This dissertation is dedicated to my parents for their unconditional love and care for me.

Fatigue Bond Characteristics and Modeling of Near Surface Mounted FRP Reinforcements in Concrete

ABSTRACT

Reinforced concrete (RC) has been extensively used for construction of building and bridge infrastructures for over a century, yet the corrosion of steel reinforcement may significantly limit the long-term performance of these structures. Instead of demolition and reconstruction, retrofitting and strengthening of the existing structures to extend their service life and upgrade their load-carrying capacity to accommodate the modern demand is often more cost efficient and practical. In this realm, fiber-reinforced polymer (FRP) composite materials have shown more potential than steel plates because they are corrosion-free, higher in strength and stiffness to weight ratios, lightweight and more durable. In the recent years, using the near-surface mounted (NSM) FRP composites to strengthen the deficient structures has attracted broad research attention, as a promising alternative to the externally bonded (EB) FRP method. However, research on the characteristics of bond between NSM FRP and concrete under fatigue loading is still lacking, and a comprehensive study focusing on the bond level is necessary prior to the practical implementation in the field.

This research aims to significantly advance our understandings of the bond development and failure mechanism of NSM carbon FRP (CFRP) reinforcements in concrete under fatigue loading, as well as the influence on the local bond characteristics induced by the key parameters. A total of 84 NSM CFRP-to-concrete joint specimens, with a dimension of 350 × 300 × 150 mm, were constructed and tested under a single shear direct pull-out configuration, including 24 specimens under static loading and 60 specimens under fatigue loading. Investigated variables in the experiment include: different cross-sectional shape (rod vs. strip), surface treatment of NSM reinforcement (roughened, sand-coated, sand-coated and spirally wound), adhesive type (one three-component epoxy and three two-component epoxies), concrete strength (two concrete batches) and fatigue load range (10-50%, 10-60%, and 10-70% of the corresponding static load-carrying capacity P_f). The local bond degradation was observed for all the specimens under fatigue

loading. In general, the bond regions closer to the loaded end of the specimen were firstly developed to resist the applied fatigue load. With the gradual local bond degradation within these regions, more bond regions were further developed along the bond line toward the free end during the fatigue cycles. This phenomenon was accompanied by a peak local bond stress migration from the loaded end to the free end of the specimen. The specimen failed when the residual load-carrying capacity was unbale to balance the applied fatigue load.

The test results also indicated that the fatigue cycles changed the failure mechanism of CFRP rod specimens from concrete and epoxy breakage under static loading to interfacial debonding between FRP and adhesive by different extents, but the CFRP strip specimens had the same interfacial debonding failure mode in both loading cases. In addition, under the same 10-60%P_f fatigue load range, specimens using CFRP strip with sand-coated and spirally wound surface and three-component epoxy had a better resistance to fatigue degradation and longer fatigue life. Furthermore, a higher fatigue load range (i.e., 10-70%P_f) significantly shorten the fatigue life of specimens, but the concrete strength did not noticeably affect the fatigue bond behavior.

An analytical model adopting the finite element method (FEM) was proposed based on a trilinear local bond stress-slip law (representing the distinctive linear elastic, softening and debonding stages), and it provided good agreement with the experimental data under both static and fatigue loading cases. The model well captured the migration of the peak local bond stress toward the free end of the NSM FRP-to-concrete bonded joints during fatigue cycles, and it visualized the bond development and failure procedure because of the local bond degradation. Additionally, the parametric study based on the analytical model confirmed the importance of the local bond strength, as well as the positive effect induced by a higher residual bond strength ratio and a higher Young's modulus of FRP reinforcements on the fatigue life of specimen.

To supplement the experimental study, a three-dimensional (3D) finite element (FE) modeling using the concrete damaged plasticity (CDP) model in ABAQUS was adopted to simulate both NSM CFRP rod and strip joint specimens under the static direct pull-out force. The concrete breakage failure of CFRP rod

specimen and interfacial debonding failure of CFRP strip specimen were successfully reproduced in the analysis. The parametric study from the numerical simulation showed that a higher dilation angle and concrete strength could increase the load-carrying capacity of the specimen, but the influence caused by groove dimension was negligible.

To sum up, this research conducts a thorough investigation on the fatigue bond characteristics of NSM FRP-to-concrete joint specimens both experimentally and analytically. Model predictions in terms of pull-out force, distribution of FRP strain and local bond stress, and relative slip between FRP reinforcement and concrete are verified by the experimental study. The proposed strategy of FE modeling also provides an efficient alternative to the static direct pull-out test to study the bond performance of NSM CFRP reinforcements in concrete.

CHAPTER ONE

1 INTRODUCTION

1.1 Motivation and research background

The near-surface mounted (NSM) technique of using fiber reinforced polymer (FRP) composites, has been considered as a promising approach to increase the load-carrying capacity of existing reinforced concrete (RC) structures which are substandard according to the current specifications. It has demonstrated many superior features over the existing externally bonded (EB) technique such as: (1) faster installation due to reduced work of surface preparation; (2) less prone to debonding failure thus more efficient use of FRP materials; (3) better endurance to environmental corrosion and less visual impact (De Lorenzis and Teng 2007; Coelho et al. 2015).

To ensure the bond quality which is critical to the full utilization of FRP materials, a great number of experimental studies have been carried out focusing on the bond behavior and failure mechanism of NSM FRP-adhesive-concrete bonded joints which primarily focuses on the bond length or groove dimensions (Seracino et al. 2007a; Oehlers et al. 2008; Novidis and Pantazopoulou 2008; Galati and De Lorenzis 2009; Soliman et al. 2011; Sharaky et al. 2013), concrete strength (Seracino et al. 2007b; Al-Mahmoud et al. 2011; Douadi et al. 2019), multiple parameters such as FRP material (glass, carbon, basalt), FRP cross-sectional shape (round, strip, rectangular), FRP surface treatment (smooth, roughened, grooved, ribbed, spirally wound, sand-coated, sand-coated and spirally wound) and type of adhesive (De Lorenzis et al. 2004; Barros and Costa 2010; Bilotta et al. 2011; Palmieri et al. 2012; Ceroni et al. 2012; Lee et al. 2013; Khshain et al. 2015; Torres et al. 2016).

However, most of these studies only aimed at the static or short-term performance of NSM FRP strengthened concrete structures. Other aspects related to their durability and long-term performance have not been comprehensively investigated. The fatigue performance of transportation infrastructures, e.g., bridges, has a significant influence on their service life since the moving vehicle loads applied to bridges could cause a frequent stress variation in the strengthened structures using NSM FRP reinforcements. The

cyclic loading creates microcracks at the interface between FRP and epoxy adhesive, and this damage could accumulate progressively and finally lead to failure (Yun et al. 2008; Carloni and Subramaniam 2013; Fernandes et al. 2015). Although a considerable number of studies on the bond using either direct pull-out test (DPT) or beam pull-out test (BPT) have been reported in the literature, investigation of the aforementioned parameters and construction details to better understand their behavior under fatigue loading is rather limited. Sena Cruz et al (2006) carried out a series of BPT to assess the bond behavior of NSM CFRP strip-to-concrete bonded joints with different bond lengths (60, 90 or 120 mm) under both monotonic and cyclic loading. Specimens being applied by 10 unloading/reloading cycles with a fixed-load level (60, 75 or 90%) had negligible influence on their ultimate pull-out force. However, a significant post-peak load decrease of the bond stiffness was observed. Yun et al. (2008) developed a double shear DPT configuration to compare the fatigue bond behavior of four different FRP bonding systems, including EB, NSM, fiber anchored (FA) and hybrid bonded (HB) techniques. It was concluded that the NSM system had the smallest bond stiffness, fastest bond development under fatigue loading but could produce a higher ductility in the structural members. Based on test results on bond and slab specimens under fatigue loading, Fernandes et al. (2015) reported progressive degradation of the bond stiffness that was observed from the DPT specimens during the fatigue cycles. Chen and Cheng (2016) conducted a series of DPT for both CFRP rod and strip specimens under fatigue loading. The test results revealed significant degradation in the local bond strength although the average bond strength only displayed a small decrease. Al-Saadi and Al-Mahaidi (2016) tested DPT specimens for fatigue life using smooth and roughened NSM CFRP strips. A longer fatigue life was obtained in specimens using roughened CFRP strip and the fatigue load range showed a drastic influence on the fatigue life of the DPT specimens. However, none of these studies systematically investigated the local bond characteristics and degradation under fatigue in the aspect of various key parameters, e.g., details of FRP, epoxy and concrete, as per those have been comprehensively studied in the static DPT.

Studies on the fatigue bond behavior of NSM FRP-adhesive-concrete joints is the key to comprehend the response and failure mechanism of structural members under fatigue loading. Although

analytical models to predict full-range local bond behavior has been proposed in the past (Yuan et al. 2004), the only available model to predict the fatigue bond behavior of NSM FRP bonded joints was constructed by Chen and Cheng (2016) and it was based on the bilinear local bond-stress slip relationship and theory of cohesive zone. However, this bilinear relationship ignores the residual bond stress that exists after the local deboning occurs according to many experimental observations (Soliman et al. 2010; Lee et al. 2013; Al-Saadi et al. 2018). Excluding the contribution of such a post-debonding residual bond stress, the local bond stress-slip or load-slip relationship of the NSM FRP-to-concrete joints declines immediately after the local debonding occurs, resulting in an underestimation of the bond capacity.

1.2 Scope and methodology

In view of the current gap in knowledge regarding the bond behavior of NSM FRP in concrete under fatigue loading, this research aims at systematically assessing the influence on the fatigue bond performance induced by different parameters, including the cross-sectional shape of NSM CFRP reinforcement, surface treatment of CFRP reinforcement, type of epoxy adhesive, fatigue load range and concrete strength. A total number of 84 CFRP-to-concrete joint specimens were casted in the lab and tested through the single shear direct pull-out configuration to measure their local bond characteristics under both static and fatigue loading case.

In the meantime, analytical models are proposed to predict both the static and fatigue bond behavior of the NSM CFRP-to-concrete bonded joints. The static portion of the model was revised from an existing model developed by Yuan et al. (2004) but improved by using a more realistic three-stage local bond stress-slip relationship measured and validated by the experiment. The fatigue portion of the model, on the other hand, adopted the finite element method (FEM) to simulate the progression of damaged bond regions and predict the development of local bond behavior under fatigue loading. The local bond degradation laws under fatigue cycles for both CFRP rod and strip specimens were derived from the experimental study to form the basis of the analytical model.

In addition, due to the intrinsic complexity of bond issue for NSM FRP in concrete because of the combined use of three different materials (i.e., FRP, adhesive and concrete) and two interfaces (i.e., interface between FRP and adhesive, interface between adhesive and concrete), the local bond behavior of the NSM CFRP-to-concrete joints is hard to accurately predict and the stress variation within substrate concrete is even more difficult to collect. As a result, three-dimensional finite element models using the software package ABAQUS were built in this research adopting the concrete damaged plasticity (CDP) model, as a supplement to the experimental study, to further explore the failure mechanism of the concrete specimens under the static direct pull-out force for both NSM CFRP strip and rod cases. Parameters such as the dilation angle of concrete, concrete strength, groove width and different interfacial stress-slip models were focused to explore their influence on the overall bond behavior of the NSM CFRP reinforcement in concrete.

1.3 Dissertation organization

This dissertation contains seven chapters and has been organized in the following sequence:

Chapter 1 presents the motivation and background of this research, as well as its scope and methodology.

Chapter 2 introduces the basic concepts of both EB and NSM FRP system and presents the state-of-art reviews on their bond behaviors under fatigue loading. Current research issues and possible future directions are summarized.

Chapter 3 introduces the analytical models proposed in the literatures to predict the stage-by-stage bond behavior of NSM FRP-to-concrete joints. Semi-empirical prediction equations corresponding to different failure modes are proposed as well and calibrated by the NSM FRP DPT database in the literatures.

Chapter 4 elaborates the experimental study on the NSM FRP bond characteristics under fatigue loading. Test observations and results of the 84 specimens are discussed in detail. The influence on the fatigue bond behaviors induced by cross-sectional shape of CFRP reinforcement, surface treatment of

CFRP reinforcement, type of epoxy adhesive, fatigue load range and concrete strength are presented. The local bond degradation laws are derived as well.

Chapter 5 proposed an analytical model based on the concept of FEM to predict the bond behavior of NSM CFRP in concrete under fatigue cycles. The trilinear local bond stress-slip relationship is adopted representing a typical three-stage bond development observed in the experimental study. A comparison between the analytical model and the test results obtained in Chapter 4 is presented. Parametric studies on the local bond strength, residual bond strength ratio and Young's modulus of FRP reinforcement are conducted as well to investigate their influence on the fatigue bond behavior of NSM FRP in concrete.

Chapter 6 presents a three-dimensional FE modeling procedure of the NSM FRP-to-concrete bonded joints. Theoretical background and modeling strategies are introduced in the chapter. The failure mechanism of both CFRP rod and strip case under the static direct pull-out force observed in the experiment are successfully reproduced in the numerical simulation. The effect of dilation angle, concrete strength, and groove width on the overall bond performance has been studied.

Chapter 7 draws the main conclusions of this research and provides an overview on the potential research directions in the future.

1.4 Research significance

This research conducts a comprehensive experimental study on the bond characteristics of NSM CFRP in concrete under fatigue loading. The effect of cross-sectional shape of FRP reinforcement, surface treatment of FRP reinforcement, type of epoxy adhesive, fatigue load range and concrete strength are well investigated. Test results on the local bond behaviors of NSM CFRP in concrete during fatigue cycles are documented and illustrated, which help understand the local bond degradation and failure mechanism of NSM FRP applied to concrete structures under fatigue loading. Both semi-empirical equations and analytical models are proposed to predict the load-carrying capacity and failure modes of the NSM FRP in concrete, as well as the local bond behavior (i.e., distributions of local bond stress, FRP strain and relative slip, etc.) under both static and fatigue loading cases. The methodology established in this study can also be applied to future research on the flexural or shear strengthening cases of structural members by using

NSM FRP. Various parameters affecting the bond performance of NSM CFRP in concrete under fatigue loading are studied and discussed, and the conclusions can facilitate the field application of NSM FRP in the long run. The three-dimensional finite element simulation of NSM FRP-to-concrete bonded joints provides a good alternative to the experimental study to estimate the overall bond performance under the static direct pull-out force, and it visualizes the development of damage in the substrate concrete. The modeling strategy can be further utilized in the numerical analysis of NSM FRP strengthened concrete structures under more complicated loading scenarios.

CHAPTER TWO

2 LITERATURE REVIEW

2.1 Overview

This chapter starts with the basic concept of FRP-based techniques implemented in retrofitting concrete structures, namely, externally bonded (EB) and near-surface mounted (NSM) technique. Relevant issues of the NSM FRP technique are further discussed. This state-of-the-art review primarily focuses on the bond performance of NSM and EB FRP reinforcement in concrete under fatigue loading. The review provides essential background information to the subsequent chapters and highlights the significance and unique contribution of this research.

2.2 FRP systems

Research on implementation of FRP composites in strengthening and retrofitting of existing structures began as early as mid-1980s (Hollaway 2011). Due to their high strength, low self-weight and good resistance to corrosion, FRPs have been considered as a promising alternative to traditional strengthening techniques, such as steel plate bonding, section enlargement and external post-tensioning. A FRP system is typically composed of fibers and resin used to create the composite laminate, where the resin is used to bond the FRP to concrete substrate and applicable coatings are used to protect the constituent materials (ACI 2008).

The Externally Bonded (EB) technique is a common method for its easy handling and transportation, less false work needed during installation, etc. In this method applied to beam strengthening, FRP plates or laminates are attached to the tensile surfaces and/or the side surfaces of the beam by virtue of adhesives in conjunction with extra FRP jacketing for anchorage at beam ends to enhance the bond (Fig. 2.1). Comprehensive research has been conducted on the EB systems (Khalifa et al. 1998; Bonacci and Maalej 2001; El-Hacha et al. 2001; Kang et al. 2012; Oudah and El-Hacha 2013) where increased flexural capacity, shear capacity and fatigue life were observed. However, several drawbacks still exist in the EB FRP method, such as the delamination

issue under uneven bonding surface, irresistible feature to fire, risk of vandalism and performance degradation when exposed to severe environment (Hollaway 2011).

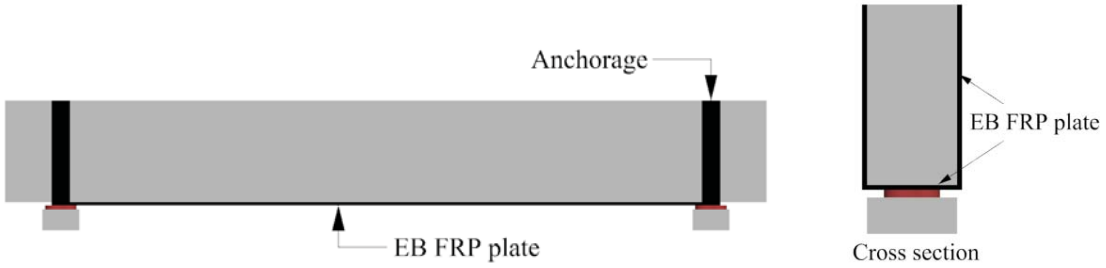

Fig. 2.1 Typical EB FRP strengthening system for concrete beams

As an alternative to the EB FRP, the near-surface mounted (NSM) technique was proposed in the early 2000s (Pellegrino and Sena-Cruz 2016), which revealed many unique advantages over the traditional EB method. In this method, the NSM reinforcement is embedded in the precut grooves or slots in the concrete cover of the structural members, followed by filling the grooves or slots with resins or mortars up to the concrete surface (Fig. 2.2). A better bond performance between the reinforcement and the concrete is achieved (Lee and Cheng 2011) and the durability issues are alleviated as well.

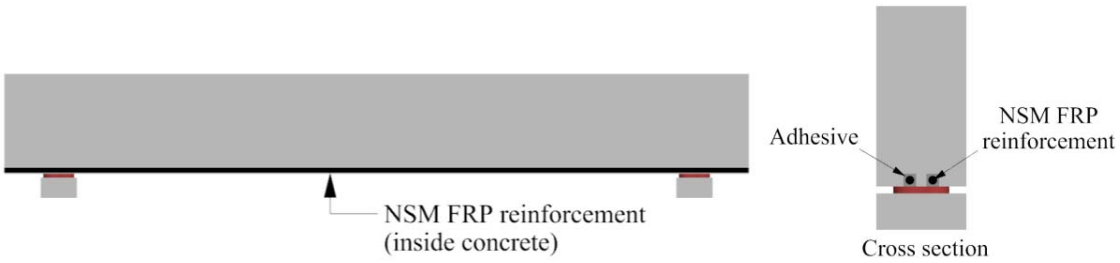

Fig. 2.2 Typical NSM FRP strengthening system for concrete beams

2.3 Research background of NSM FRP

Substantial research has been conducted in the recent decades to investigate the behavior of RC members strengthened with NSM FRP, including flexural and shear strengthening of RC beams, seismic retrofitting, prestressing techniques, bond behavior and durability performance subjected to environmental exposures, etc. Some representative studies are summarized below.

The experimental study conducted by El-Hacha and Rizkalla (2004) indicated a significant increase in load-carrying capacity, flexural stiffness and ductility of RC T-beams strengthened with NSM FRP reinforcements. A full composite action between the CFRP strips and concrete was achieved for beams strengthened with NSM method, and these beams were failed by CFRP rupture. However, for beams strengthened with EB method, they failed at a much lower load level because of the debonding failure mode of CFRP strips. Likewise, Lee and Cheng (2010) tested 11 full-scale RC slab overhang specimens strengthened in negative bending moment regions with various types of NSM FRP reinforcements. The test results verified the efficiency of NSM technique in increasing the flexural capacity of RC slabs. And specimens strengthened with NSM FRP reinforcements with pretreated surface (e.g., textured, sand-coated, and ribbed) and square cross-section shape displayed better performance in the experiment.

In terms of shear strengthening of using NSM FRP reinforcement, Dias and Barros (2010) conducted a series of RC T-beams shear strengthened with either NSM CFRP laminates or U-shaped EB CFRP sheets. They concluded that the NSM method was more effective than the EB method in increasing the beam shear resistance as well as the deformation capacity at failure. Besides, beams strengthened with NSM CFRP laminates at an inclination angle of 45º behaved the best among all the specimens. Al-Mahmoud et al. (2015) confirmed the effectiveness of using NSM CFRP rods to strengthen the rectangular RC beams in shear, with either epoxy resin or mortar as the filling material of the groove. They also verified the model proposed by De Lorenzis and Nanni (2001) to estimate the shear contribution by FRP reinforcements. Moreover, based on the Simplified Modified Compression Field Theory (SMCFT), Baghi and Barros (2017) proposed a new model to predict the beam shear strength strengthened with NSM FRP and this model agreed well with the database collected from the open literatures.

On the other hand, to examine the seismic response of RC structures strengthened with NSM FRP reinforcements, experimental efforts have also been made focusing on different structural components. For example, Kaya et al. (2017) tested seven full-scale exterior beam-column joint

specimens strengthened with NSM and ETS (embedded through section) CFRP ropes under cyclic lateral loading but only found small improvement in strength and energy dissipation capacity, though NSM method performed better than ETS method. Fahmy and Wu (2016) used NSM basalt FRP (BFRP) bars to enhance the seismic performance of existing RC columns with deficient lap-splice zones. Test results indicated a substantial increase in both energy dissipation and ultimate strength of columns under cyclic lateral loading, and the strengthening efficiency was higher using BFRP bars with spirally roughened surface than the smooth ones. In addition, pseudo-static cyclic loading test on the reinforced masonry (RM) walls strengthened with NSM FRP reinforcements was conducted by Al-Jaberi et al. (2018). A remarkable increase in both the flexural capacity and dissipated energy of the strengthened RM walls was observed compared to the controlled group.

Last but not the least, the study on the RC members strengthened with NSM reinforcements under severe environment is important to assess the long-term performance of structures. Hence, Omran and EL-Hacha (2014) investigated the combined effect of sustained load and freeze-thaw cycles on the RC beams strengthened with prestressed NSM CFRP strips. Although test observations indicated the reduced flexural cracks of specimens strengthened with NSM CFRP strips, they were more prone to debonding under the combined freeze-thaw exposure and sustained load. Al-Mahmoud et al. (2014) also tested concrete beam specimens strengthened with either EB CFRP laminate or NSM CFRP rod, after the exposure of 300 freeze-thaw cycles or the immersion in 3.5% salted tap water for 120 days. Specimens strengthened with EB CFRP laminate had a significant drop in load-carrying capacity in either environmental condition, however, only negligible changes were found for specimens strengthened with NSM CFRP rods.

2.4 Bond performance of NSM FRP under fatigue load

Unlike the short-term behavior, the long-term performance of NSM strengthened structures has not been fully investigated. Since the NSM FRP reinforcements are protected by the concrete cover, corrosion due to ambient environment is not usually considered in this strengthening technique. According to some limited exposure experiments for NSM FRP in concrete (Al-

Mahmoud et al. 2014; Silva et al. 2014; Garzón-Roca et al. 2015), minor changes have been found of specimens strengthened with NSM reinforcements when exposed to severe exposures, such as freeze-thaw cycles, wet-dry cycles and immersion in chlorides.

Although the precut grooves provide larger bonding area between the NSM FRP reinforcement and concrete, reducing the bond degradation under various loading conditions, fatigue issues still exist for the NSM FRP and the strengthened structures. Fatigue loading may compromise the durability of the NSM system and lead to deterioration and/or weakening of the individual components of the composite structure, e.g., steel bar, concrete or FRP reinforcement (Yost et al. 2007). In particular, the interface between concrete and adhesive and the one between FRP and adhesive are at a higher risk of debonding under the fatigue loading. However, the corresponding mechanism of debonding are still not fully understood. Very few studies have been carried out focusing on the bond performance of NSM FRP system under fatigue loading. Reliable fatigue bond prediction models for the NSM FRP reinforcement in concrete are still limited and need to be further investigated (Oudah and El-Hacha 2013). A thorough review of the existing literatures along with the available conclusions regarding bond performance of NSM FRP in concrete under fatigue loading are summarized in the following subsections.

2.4.1 Configuration of direct pull-out test

To directly capture the bond behavior under fatigue loading, experimentally studies using direct pull-out test (DPT) were primarily adopted by researchers. Configurations of DPT can be categorized into four major types (Coelho et al. 2015), as illustrated in Fig. 2.3. These configurations are designed to study the different aspects of the NSM FRP-to-concrete bonded joints for different research purposes and determined by the feasibility in the laboratory. In view of the eccentric location for the NSM FRP implemented in beam flexural strengthening, the single shear with the concrete block being under tension [Fig. 2.3(b)] is the most representative one among these configurations. However, to prevent the out-of-plane overturning or side sway during the

fatigue loading (Chen and Cheng 2015; Yun et al. 2008), the single shear with clamped concrete block [Fig. 2.3(a)] is more widely adopted in practical experiments.

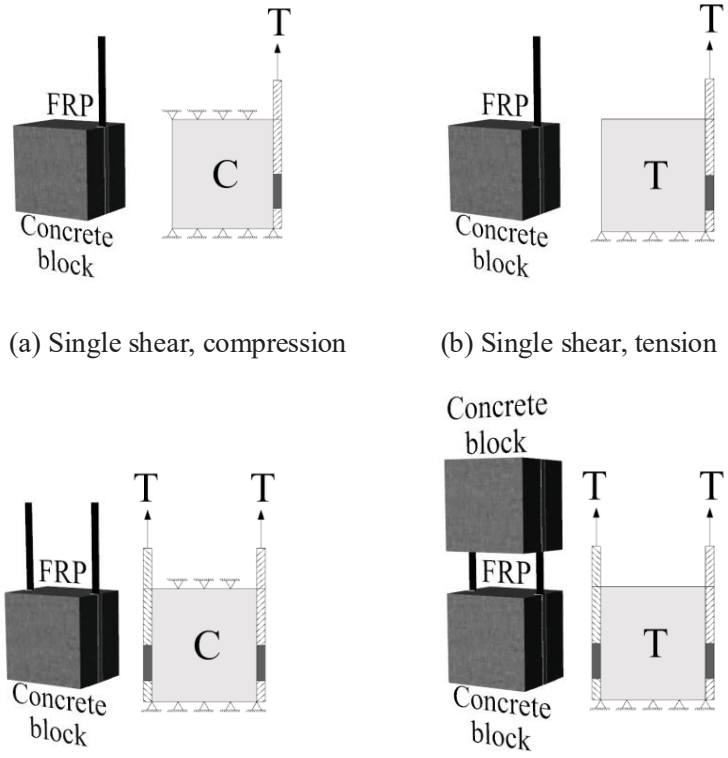

(a) Single shear, compression (b) Single shear, tension

(c) Double shear, compression (d) Double shear, tension

Fig. 2.3 DPT configurations for NSM FRP under fatigue loading

2.4.2 Bond length and groove dimensions

The bond length, L_b, is a major parameter that affects the bond fatigue life of NSM FRP system. It should be longer than the development length, L_d, which is defined as the critical length to develop sufficient bond strength of FRP under designed load to prevent premature failure mode (ACI 2008). It has been found that for DPT, the average bond stress at the interfaces will increase with the increase of L_b up to a threshold (L_d), after which it decreases (Coelho et al. 2015). Although the effective development length depends on many parameters, such as groove dimensions, type of FRP reinforcement, surface treatment of FRP reinforcement, adhesive type, concrete strength, etc., the threshold is usually taken as 100 mm (Coelho et al. 2015).

The effect of groove dimensions on the bond strength has not been fully understood due to both the intrinsic complexity of bond failure mechanism and the influence caused by various parameters mentioned above. Some conclusions were drawn based on experimental observations. For example, Al-Mahmoud et al. (2011) found that the width of the groove showed a positive effect on the ultimate pull-out force when it was less than $2.5d_b$ (where d_b is the rod diameter), after which it caused negative effect. Lee and Cheng (2013) proposed the optimum groove sizes by means of the Classification and Regression Trees for different test configurations. The optimal groove dimensions of $1.5d_b \times 1.5d_b$ or $2.0d_b \times 2.0d_b$ (width × depth) were recommended for most cases.

The bond lengths adopted in representative literatures for NSM FRP in concrete under fatigue loading are summarized in Table 2.1, in conjunction with the corresponding groove dimensions and FRP details. In general, due to the accumulated bond damage under fatigue loading, e.g., micro-cracks propagation at interfaces or relative slip between FRP reinforcement and adhesives, the bond length is more conservative than the static counterpart to prevent any premature failure. Nevertheless, the bond length used in Fernandes et al.'s testing series was only 60 mm, which yet still utilized 82% of the ultimate capacity of the CFRP strip under the monotonic loading (Fernandes et al. 2015).

Table 2.1 Summary of groove and FRP details for NSM FRP bond tests under fatigue loading

Group	FRP type	FRP surface treatment	FRP dimensions (mm)	Bond length (mm)	Young's Modulus (GPa)	Groove dimensions length×depth×width (mm)
Yun et al. (2008)	GFRP rod	-	16	100	64	400×25×25
Chen and Cheng (2015)	CFRP rod	Sand-coated and spirally wound	10	250	147	350×25×15
	CFRP strip	Roughened	4.5×16	250	180	350×25×15
Fernandes et al. (2015)	CFRP strip	Smooth	1.4×10	60	169.5	200×15×5
Al-Saadi et al. (2016, 2017)	CFRP strip	Smooth	1.4×10	180	212	180×15×5
		Roughened	1.4×20	180	212	180×30×5

2.4.3 Other parameters

In addition to a major contribution by bond length and groove dimensions, the bond performance under fatigue loading for NSM FRP-to-concrete bonded joints is affected by many other parameters, such as different FRP materials, cross-sectional shape of FRP reinforcement, surface treatment of FRP reinforcement, and adhesive type, concrete strength, etc. However, because a coupling effect among these parameters exists, the independent influence due to any of these factors on the fatigue bond behavior is indeterminate. However, some useful observations from the experiments have been provided by previous studies.

Among different types of surface treatment, the sand-coated and spirally wound rod was found to result in a fatigue life almost three times as long as the roughened strip due to the additional friction and mechanical interlocking on the surface (Chen and Cheng 2015). Moreover, the roughened CFRP strip presented a better fatigue life than the smooth CFRP strip (Al-Saadi and Al-Mahaidi 2016). Specimens using an innovative high-strength, self-compacting, cementitious adhesives (IHSSC-CA) showed a better bond performance with a longer fatigue life than specimens with polymer cement-based adhesive (Al-Saadi et al. 2017). It was also found that the axial stiffness was effective in limiting the size of the damage zone of NSM CFRP bond during the fatigue cycles, but it did not have a significant effect on the fatigue crack propagation (Chen and Cheng 2016). Considerable heat was generated at high fatigue frequency (8 Hz), which substantially decreased the fatigue life of the FRP systems (Adimi et al. 2000).

2.4.4 Local bond stress distribution

In general, the bond development and local bond stress distribution of NSM FRP-to-concrete interface under fatigue loading along the entire bond length is nonlinear, where the local bond stress mainly depends on the relative slip between the FRP reinforcement and concrete. Some representative local bond stress-slip laws are presented to better understand the bond development (Coelho et al. 2015), as illustrated in Fig. 2.4, where τ is the local bond stress, τ_f is the local bond

strength, δ is the relative slip between FRP reinforcement and concrete, δ_1 is the relative slip corresponding to τ_f, and δ_f is the relative slip at debonding. It should also be noted that the ACI model (ACI 2008) simply adopted a constant value (6.9 MPa) for the local bond stress and the SA (Standards Australia, SA 2008) model is based on an assumption represented by a single descending line.

Due to the local bond stress-slip laws, the local bond stress at the loaded end of the NSM FRP-to-concrete bonded joints generally increases during the early cycles of the fatigue loading, assuming the upper fatigue load limit is small. As the number of fatigue cycles increases, the relative slip at the loaded end accumulates to the value of δ_1, followed by a gradual decrease in local bond stress. In the meantime, if the bond length L_b is longer than the development length L_d, indicating a fully development of the local bond stress, the peak stress will migrate toward the free end, as illustrated in Fig. 2.5. This unique development of the stress distribution during the fatigue cycles was observed and reported by different research groups (Bizindavyi 2003; Soliman et al. 2011; Chen and Cheng 2015; Fernandes et al. 2015). Note that the peak value of the local bond stress was reported to decline as the number of fatigue cycles increased (Chen and Cheng 2015), which could be possibly explained by the progressive bond degradation at the interfaces of the FRP-to-concrete bonded joints during the fatigue cycles.

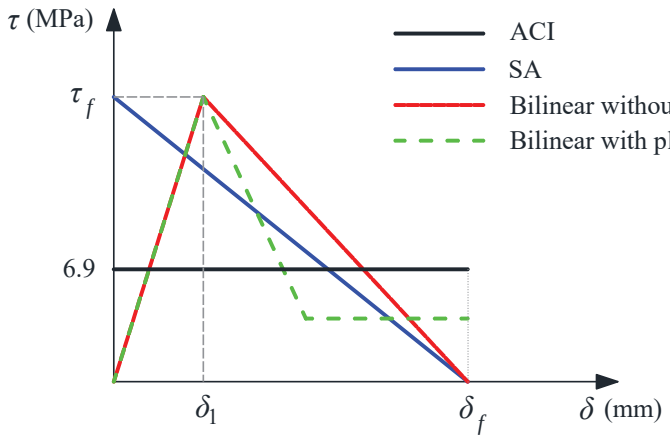

Fig. 2.4 Local bond stress-slip laws for NSM FRP-to-concrete bonded joints (Coelho et al. 2015)

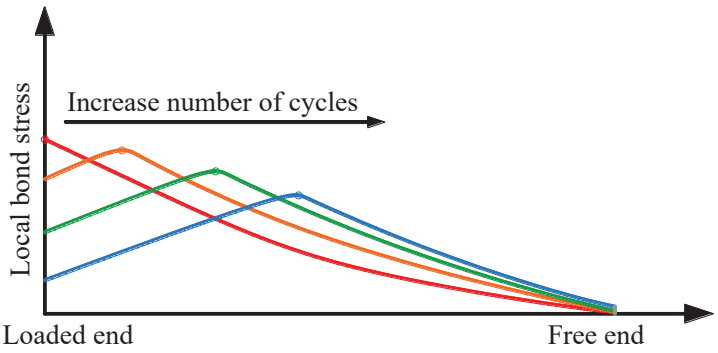

Fig. 2.5 Migration of peak local bond stress under fatigue loading for NSM FRP-to-concrete bonded joints (adapted from Chen and Cheng 2016)

2.4.5 Relative slip vs. the number of fatigue cycles at the loaded end

As aforementioned, the local bond stress depends on the relative slip between the FRP reinforcement and concrete; therefore, the relative slip serves as an effective measure of the local bond degradation under fatigue loading. A typical three-stage curve representing the relative slip vs. the number of fatigue cycles at the loaded end has been proposed in different studies (Fernandes et al. 2015; Al-Saadi and Al-Mahaidi 2016). As conceptually depicted in Fig 2.6, the slip increases drastically within the first several cycles during the first stage, which is followed by a more stable progressive slip growth during the second stage. The slip increases rapidly again during the third stage until the NSM FRP-to-concrete bonded joints reaches its fatigue life.

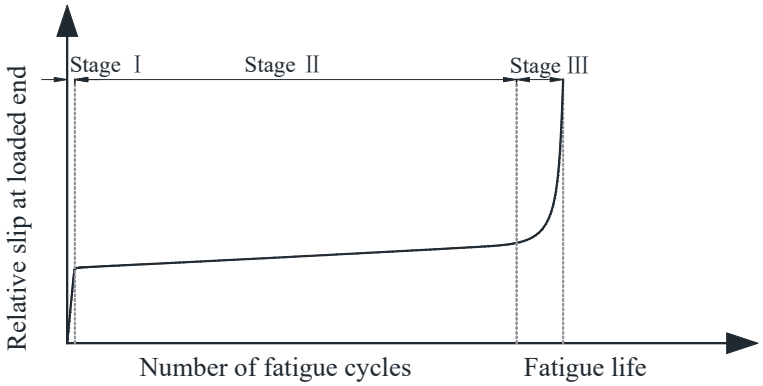

Fig. 2.6 Relative slip vs. number of fatigue cycles at the loaded end for NSM FRP-to-concrete bonded joints (adapted from Fernandes et al. 2015)

2.4.6 Failure modes

The major failure mode reported by relevant publications for NSM FRP fatigue bond tests was the debonding failure at the FRP/adhesive interface (Chen and Cheng 2015; Fernandes et al. 2015; Al-Saadi et al. 2017). Limited by the small database of fatigue bond tests for NSM FRP systems, the rupture failure mode of FRP reinforcement was only observed in one study, where the rupture occurred outside the bonded region near the loaded end because of the good bond achieved between the CFRP strip and the surrounding epoxy adhesive (Al-Saadi and Al-Mahaidi 2016).

Despite the different mechanisms leading to the bond degradation, the types of failure mode of NSM FRP-to-concrete bonded joints under fatigue loading should be similar to that under monotonic loading. Coelho et al. (2015) summarized four major bond failure modes for NSM FRP systems: (1) failure at the FRP/adhesive interface; (2) failure at the adhesive/concrete interface; (3) cohesive failure in adhesive; and (4) cohesive failure in concrete (Fig. 2.7). Notice that when the bond is strong enough to prevent these failures by measures of using sufficient long bond length, solid surface treatment of FRP reinforcement (to reach good mechanical interlocking), appropriate groove dimensions and high-performance adhesives, etc., the rupture of FRP is possible. Nevertheless, the specific failure mode of NSM FRP reinforcement in concrete is still unpredictable due to the lack of satisfactory analytical models to estimate the bond strength corresponding to different type of failure mode.

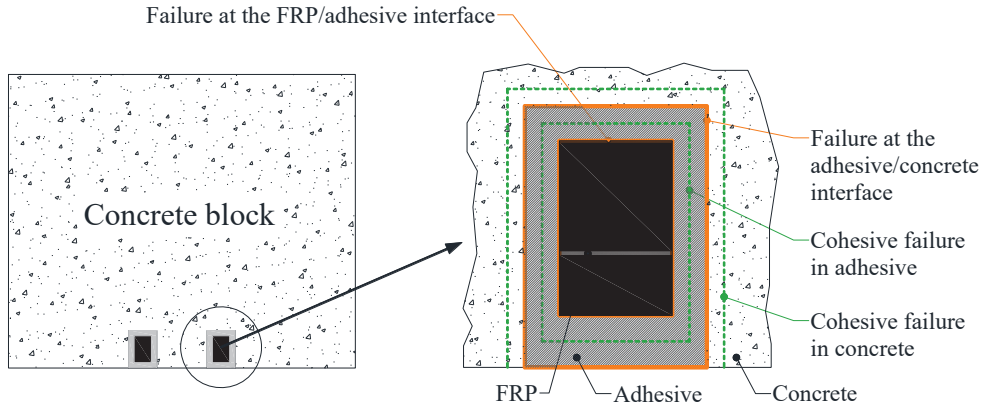

Fig. 2.7 Typical bond failure modes of NSM FRP-to-concrete bonded joints (Coelho et al. 2015)

2.4.7 Post-fatigue performance

For specimens survived the designated number of fatigue cycles (upper limit), their post-fatigue performance can be obtained by applying the monotonic load till failure. Yun et al. (2008) found that for NSM FRP strengthened specimens under high-level loading, the post-fatigue test revealed a reduction in the bond stiffness compared to the control group, yet the ultimate strength was even higher because of a longer curing time of epoxy. The post-fatigue monotonic test conducted by Fernandes et al. (2015) also showed a similar observation that the initial bond stiffness of the NSM FRP strengthened specimens dropped significantly under fatigue loading but their ultimate pull-out force was only slightly smaller (i.e., 6%) than that of the control group. Likewise, the post-fatigue test results from Al-Saadi and Al-Mahaidi (2016) indicated a negligible effect on the bond performance of NSM FRP strengthened specimen under fatigue loading when the fatigue load range was low.

2.5 Bond performance of EB FRP under fatigue load

To better understand the NSM FRP-to-concrete bonded joints under fatigue loading, bond tests of EB FRP in concrete under fatigue loading are reviewed in this section regardless of the difference in failure mechanism and testing configuration. Although the NSM FRP system involves more parameters such as groove dimensions, cross-sectional shape and surface treatment of FRP reinforcement, which inevitably complicates the bond failure mechanism under applied load, the EB FRP and NSM FRP systems still share many similarities in both experimental observations and theoretical advancement.

2.5.1 EB FRP bond tests

Similar to the NSM FRP DPT, several different setup configurations have been adopted to investigate the bond performance of EB FRP-to-concrete bonded joints. Fig. 2.8 illustrates the four representative types, where T and C represent the tensile and compressive force, respectively, and L is the bond length of FRP plate attached to the concrete block. It can be seen from the illustration

that the concrete is under tension for both case (a) and (c), but under compression for both case (b) and (d). In view of the same reason previously described for the NSM FRP technique, the single shear pull-out test should be the most representative configuration. Nevertheless, due to the advantage of symmetry, the double shear pull-out test has been mostly adopted, followed by the second most popular setup, which is the single shear pull-out test due to its simplicity (Chen et al. 2001).

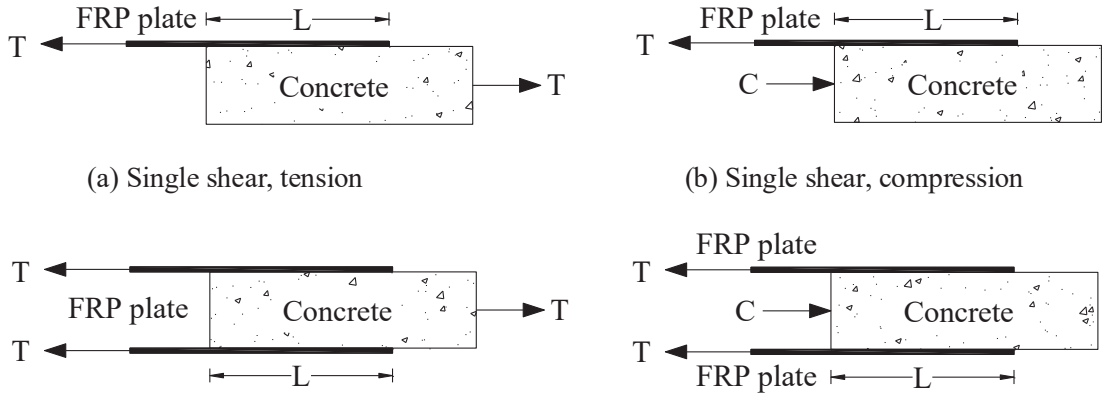

Fig. 2.8 Typical configuration of DPT for EB FRP under fatigue loading (Chen et al. 2001)

2.5.2 Bond length

Following the same concept as in the NSM FRP system, the bond length also plays a pivotal role in the bond performance of EB FRP-to-concrete bonded joints. This bond length should be longer than the development length or effective bond length, L_d, a threshold beyond which any further extension in the bond length is unbale to increase the bond strength, to guarantee a fully development of the joint and improve the ductility of the failure process (Chen and Teng 2001; Yuan et al. 2004). In addition, the available analytical models of predicting the bond strength are typically based on the assumption that the bond length should be long enough or even infinite to achieve the full-range bond behavior (Wu et al. 2012).

As a result, the bond length should be selected conservatively in the test to obtain a complete debonding process and verify the reliability of proposed models. Karbhari et al. (2006) summarized

and compared different bond strength models based on fracture mechanics for EB FRP system and indicated that the FRP plate stiffness E_pt_p has a positive effect (where E_p and t_p are the Young's modulus and thickness of FRP plate, respectively). The compressive strength of concrete f_c, on the other hand, has a negative effect on the development length for all collected models. Karbhari et al. (2006) also calculated various development lengths by using these models with a concrete strength range of 20-60 MPa while maintaining other material properties constant (width of FRP plate b_c = 305 mm, width of concrete block b_p = 300 mm, ratio between adhesive shear modulus and thickness G_a/t_a = 1.73 GPa/mm, and E_pt_p = 77.4 GPa-mm). The minimum value thus obtained was larger than 80 mm. A similar development length of 100 mm was also reported by Iwashita et al. (2007). Table 2.2 summarizes the bond length adopted by available EB FRP-to-concrete DPT tests under fatigue loading in the literatures, in conjunction with the details of the FRP material used. It should be noted that all the bond lengths used were long enough to prevent the premature failure during the fatigue cycles.

Table 2.2 Bond length for EB FRP fatigue bond tests

Group	FRP type	Dimensions of FRP plate width×thickness (mm)	Modulus of elasticity (GPa)	Bond length (mm)
Bizindavyi et al. (2003)	GFRP	25.4×1	29.2	220, 300
	CFRP	25.4×0.33	75.7	300
		50.8×0.33		160
		50.8×0.66		300
Iwashita et al. (2007)	PBO[a]	50×0.128	235	200
Carloni et al. (2012)	CFRP	25×0.167	230	152
Zheng et al. (2014)	CFRP	50×0.23	220-232	100, 150, 250
		40, 60×0.23	-	250
		50×0.46	-	250

[a] PBO = poly-*p*-phenylenebenzobisoxazole.

2.5.3 Other parameters

Except for loading factors such as fatigue load amplitude, the effect on the bond fatigue life is not fully understood due to material properties and specimen geometries related to FRP laminate,

adhesive and concrete block. Bizindavyi et al. (2003) reported that a longer bond length and a wider FRP laminate width contributed to a lower FRP stress level which led to a longer fatigue life.

On the other hand, debonding mechanisms of FRP-to-concrete bonded joints under static loading have been investigated extensively and different fracture mechanics-based models have been proposed to estimate the bond strength. Some of these findings are beneficial for the design of specimen configurations for EB FRP bonded joints under fatigue loading. Chen and Teng (2001) pointed out that the width ratio of the FRP plate to concrete block, b_p/b_c, has a significant effect on the ultimate bond strength, where a smaller b_p/b_c resulted in a higher ultimate bond strength. Yuan et al. (2004) observed a slight increase in the applied load even after the initiation of debonding, which could be explained by the aggregate interlocking and friction in the debonding zone. Based on fracture mechanics, Dai et al. (2005) suggested that the interfacial load-carrying capacity should be determined by the interfacial fracture energy G_f, which depended on the properties of concrete, adhesives and FRP stiffness. Using adhesives with lower shear stiffness could substantially improve G_f and the ductility of the joint but decrease the maximum bond. Wu and Jiang (2014) also drew similar conclusions that the maximum bond strength and the development length was mainly controlled by three factors, namely, FRP stiffness, concrete strength, and width factor. Yao et at (2005) conducted an experimental study focusing on the effect of height of free concrete edge h_c and loading offset. Their results indicated that a smaller h_c led to a lower bond strength, and the loading offset had a significant effect on the bond strength for short bond length but insignificant for long bond length.

2.5.4 Crack propagation and strain distribution

A three-stage crack propagation was identified during the bond fatigue experiment for EB FRP by Bizindavyi et al. (2003), as illustrated in Fig. 2.9. Stage I occurred over the region I near the loaded end of the specimen during the initial 10-15% of the fatigue life, after which the crack suddenly developed into the concrete substrate. For stage II, the crack continued to propagate along

the adhesive/concrete interface gradually in region II, which took place during approximately 50-75% of the fatigue life. Stage III highlighted the ultimate failure of the joint, where the crack propagated rapidly into a certain depth of the concrete substrate. Stage III occupied the last 10-15% of the entire fatigue life.

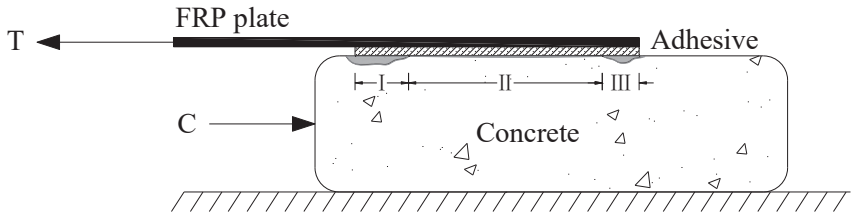

Fig. 2.9 Three-stage crack propagation of EB FRP-concrete joints under fatigue cycles (Bizindavyi et al. 2003)

In addition, a similar three-stage strain distribution along the EB FRP laminate during the fatigue cycles was obtained by Bizindavyi et al. (2003), Iwashita et al. (2007) and Zheng et al. (2014), which corresponds well to the three-stage crack propagation described above. As shown in Fig. 2.10, during stage I, the local bond stress only exists in a limited region next to the loaded end, which is also referred to as the stress-transferring zone (STZ). It should be noted that the slope of the FRP strain is proportional to the local bond stress. Then the STZ propagates gradually toward the free end during stage II, similar to the "migration" phenomenon observed in the peak local bond stress as illustrated in Fig. 2.5. Finally, when the residual bond strength becomes unable to balance the applied load, the debonding failure occurs during stage III.

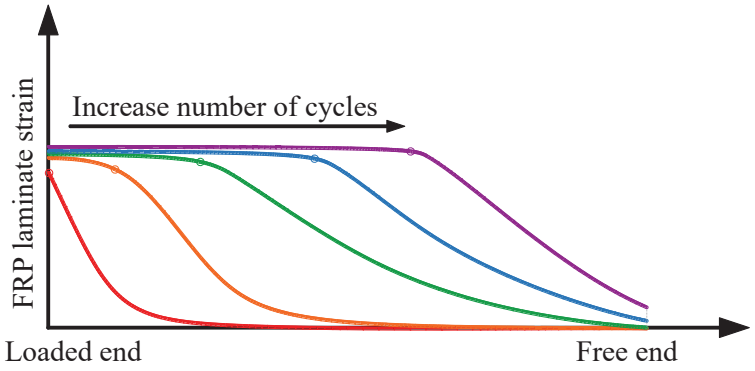

Fig. 2.10 Schematic strain distribution of EB FRP laminate under fatigue loading

2.5.5 Relative slip vs. the number of fatigue cycles at the loaded end

Zheng et al. (2014) reported test results of relative slip development during the fatigue cycles at the loaded end for EB FRP-to-concrete bonded joints and a qualitative three-stage relative slip vs. the number of fatigue cycles curve was recorded in the similar way to that of the NSM FRP system (Fig. 2.6). The relative slip at the loaded end for the EB FRP system also has a rapid increase of slip during the initial stage, a stable increase during the second stage and a drastic unstable increase of slip leading to failure during the ultimate stage.

2.5.6 Failure modes

The failure modes of EB FRP in concrete under fatigue loading are not easy to predict due to uncertainties caused by many factors including material properties, type of test configuration, loading scheme and construction quality of specimens, etc. As illustrated in Fig. 2.11, the observed failure modes in practical fatigue tests can be summarized in a sequence of their occurrence rates from high to low (Bizindavyi et al. 2003; Iwashita et al. 2007; Carloni et al. 2012; Zheng et al. 2014): (1) failure at the adhesive/concrete interface; (2) failure on the concrete substrate (debonding into cement mortar or aggregate); (3) failure in the adhesives; (4) FRP delamination between plies; and (5) FRP rupture. It should be noted that the failure mode (4) only occurs in specimens reinforced by two or more plies of FRP and the failure mode (5) only occurs when the maximum applied cyclic stress level approaches the static strength of the FRP laminate (Bizindavyi et al. 2003). However, the failure at the FRP/adhesive interface has not been reported yet in the literatures, which could be due to the small database on the EB FRP fatigue bond tests.

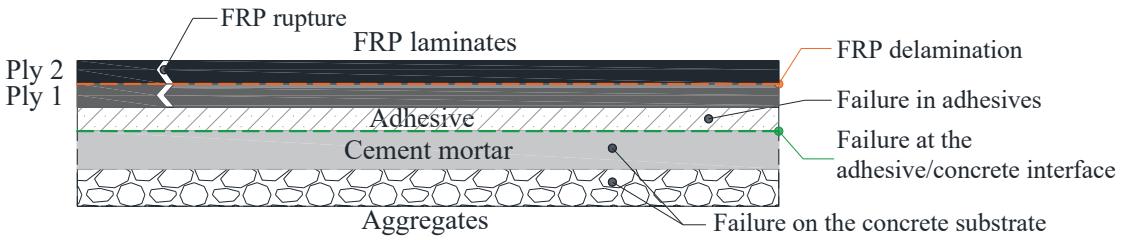

Fig. 2.11 Typical failure modes of EB FRP in concrete under fatigue loading

2.5.7 Post-fatigue performance

For specimens that survive the expected number of cycles and do not fail under fatigue loading, the DPT is typically applied to estimate their post-fatigue bond strength. The post-fatigue behavior of these specimens is compared with the control group, which is loaded monotonically up to failure (static). The post-fatigue test conducted by Carloni et al. (2012) revealed a significant decrease in the stiffness of EB FRP strengthened specimens after the fatigue cycles. When the residual bond length was still longer than the development length regardless of some debonding of the EB FRP in concrete after fatigue cycles, the load-carrying capacity remained unchanged as compared to the static case. The strain distribution along the FRP laminate at the same load level was not significantly influenced either by the fatigue cycles. Although the post-fatigue test was not conducted in some of the studies, a trend of stiffness decrease in the EB FRP laminate in concrete was also observed as the increase of the fatigue cycles (Bizindavyi et al. 2003; Zheng et al. 2014), which was in agreement with the post-fatigue test results of NSM FRP reinforcement in concrete.

2.6 Fatigue life models

It is a common practice to use stress (S) vs. number of fatigue cycles to failure (N) relationship in a logarithmic scale, also known as the S-N curve, to describe the dependency of fatigue life on the stress level of material. This S-N curve is usually applied to both concrete and steel reinforcement to estimate the fatigue life of material under cyclic loading (ACI 215R-92). However, for NSM FRP-to-concrete bonded joints, the governing factor to determine its fatigue life is complicated. The FRP stress, bond stress at interfaces, shear stress of adhesive, and concrete stress can all affect the fatigue life of the joint, and they are closely related to the different failure modes described above. In addition, the lack of DPT for NSM FRP-to-concrete bonded joints under fatigue loading leads to the insufficient understanding of the debonding mechanism of NSM FRP reinforcement with respect to the number of fatigue cycles. Most of the existing models are based

on regression analysis, which is similar to the EB FRP case. Therefore, the fatigue bond behavior has not been well understood and the analytical models capable of predicting the fatigue life of NSM FRP-to-concrete bonded joints are extremely limited. Nevertheless, the existing fatigue life models available in the open literature for both NSM and EB FRP in concrete are reviewed in the following subsections.

2.6.1 Models for NSM FRP-to-concrete bonded joints

(a) Chen and Cheng (2015) model

Chen and Cheng (2015) realized the importance of local bond strength at the interface between NSM FRP reinforcement and adhesive in the fatigue bond behavior of the joint. They conducted a series of DPTs of the boned joints and measured the degraded local bond strength at a target number of fatigue cycles. The degradation laws of the local bond strength with respect to the number of fatigue cycles were derived in relation to the static bond strength as below. However, these two equations are unable to predict the fatigue life of the bonded joints directly.

$$\frac{\tau_{1\max}}{\tau_{1\max,\text{static}}} = -0.1965\log_{10} N + 1 \qquad \text{for circular NSM rod} \qquad (2.1)$$

$$\frac{\tau_{1\max}}{\tau_{1\max,\text{static}}} = -0.1985\log_{10} N + 1 \qquad \text{for rectangular NSM strip} \qquad (2.2)$$

where N = number of fatigue cycles; τ_1 = local bond stress near the loaded end (MPa); $\tau_{1\max}$ = fatigue bond strength of τ_1 (MPa); $\tau_{1\max,\text{static}}$ = static bond strength of τ_1 (MPa). τ_1 can be calculated by:

$$\tau = \frac{d_b}{4} E_f \frac{d\varepsilon_f(x)}{dx} \qquad \text{for circular NSM rod} \qquad (2.3)$$

$$\tau = \frac{ab}{2(\mathrm{a}+\mathrm{b})} E_f \frac{d\varepsilon_f(x)}{dx} \qquad \text{for rectangular NSM strip} \qquad (2.4)$$

where d_b = diameter of the circular NSM rod (mm); E_f = Young's modulus of FRP reinforcement (MPa); $d\varepsilon_f(x)$ = difference in strain reading between the two consecutive strain gauges on the NSM

FRP reinforcement; dx = distance between the two consecutive strain gauges on the NSM FRP reinforcement (mm); and a, b = smaller and larger edge length of the rectangular NSM strip (mm), respectively.

(b) Al-Saadi et al. (2016, 2017) model

Al-Saadi et al. (2016, 2017) tested a series of NSM CFRP-to-concrete bonded joints under fatigue loading. The fatigue load range L_R was determined as a portion to the static pull-out force P_f, with a maximum fatigue load P_{max} varying from 60%P_f to 90%P_f and a fixed 10% fatigue load ratio (P_{min}/P_{max}) where P_{min} is the minimum fatigue load. Fatigue models are calibrated from the test data points of specimens with different CFRP strip dimensions and adhesive types as follows.

$$L_R = 26.465 - 1.7587 \log_{10} N_f \quad \text{for FS10E} \tag{2.5}$$

$$L_R = 34.916 - 1.1539 \log_{10} N_f \quad \text{for FS20E} \tag{2.6}$$

$$L_R = 32.48 - 2.4442 \log_{10} N_f \quad \text{for FR10E} \tag{2.7}$$

$$L_R = 47.634 - 3.0383 \log_{10} N_f \quad \text{for FR20E} \tag{2.8}$$

$$L_R = 5.546 - 0.3854 \log_{10} N_f \quad \text{for FS10C} \tag{2.9}$$

$$L_R = 6.9058 - 0.4168 \log_{10} N_f \quad \text{for FS20C} \tag{2.10}$$

$$L_R = 10.078 - 0.6825 \log_{10} N_f \quad \text{for FR10C} \tag{2.11}$$

$$L_R = 21.678 - 1.4506 \log_{10} N_f \quad \text{for FR20C} \tag{2.12}$$

$$L_R = 88.284 - 11.874 \log_{10} N_f \quad \text{for FR20IC} \tag{2.13}$$

where $L_R = (P_{max} - P_{min})$ = fatigue load range (kN); N_f = number of fatigue cycles to failure. The specimen designation, e.g., FS10E in Eq. 2.5, was referred to the following definitions where F = fatigue test; S = smooth CFRP strip; R = rough CFRP strip; 10, 20 = width of CFRP strips (10 mm and 20 mm), respectively; E = epoxy adhesive; C = polymer cement-based adhesive; and IC = innovative high-strength self-compacting cementitious adhesive (IHSSC-CA).

2.6.2 Models for EB FRP-to-concrete bonded joints

(a) Bizindavyi et al. (2003) model

Bizindavyi et al. conducted an experimental study on the EB FRP-to-concrete bonded joints under cyclic loading. Investigated parameters includes the type of FPR material (i.e., glass and carbon fiber), bond length, width of FRP laminate and cyclic bond stress level. The fatigue life of the tested specimen was interpreted as a typical *S*-*N* format as below.

$$\ln S = a - c \ln N_f \tag{2.14}$$

$$S_{\min or \max} = F_{\min or \max} / (bL) \tag{2.15}$$

where $S = (S_{max} - S_{min})$ = cyclic mean bond stress range (MPa); F = applied cyclic load (N); b = width of FRP laminate (mm); L = bond length of FRP laminate (mm); and a, c = constants obtained by curve fitting from the test data.

(b) Iwashita et al. (2007) model

Iwashita et al. (2007) used the maximum fatigue load ratio, which equals to the applied maximum fatigue load over the static pull-out force P_f, to estimate the fatigue life of the EB FRP-to-concrete bonded joints. The maximum fatigue load ratio tested varied from 20% to 70% with a constant minimum load ratio as 10%, and the fatigue model was given as follows.

$$LR_{\max} = a - c \log_{10} N_f \tag{2.16}$$

where LR_{max} = maximum fatigue load ratio (%); a, c = constants obtained by curve fitting from the test data.

(c) Zheng et al. (2014) model

Likewise, Zheng et al. (2014) tested 20 EB CFRP-to-concrete bonded joint specimens using a double shear configuration under both static and fatigue loading. The studied parameters included bond length, width and thickness of CFRP laminate, and different fatigue load levels. The proposed fatigue models depend on either the amplitude of fatigue load or the CFRP stress amplitude, and they were presented as below.

$$\Delta P = 41.687 - 4.491 \ln N_f \tag{2.17}$$

$$\log_{10} \Delta\sigma = 3.488 - 0.115 \log_{10} N_f \tag{2.18}$$

where ΔP = amplitude of fatigue load (kN); and $\Delta\sigma$ = CFRP stress amplitude (MPa).

2.6.3 Regression analysis

Although the fatigue life models proposed in these literatures agreed well with their corresponding experiment results, they are not applicable to other experiments across the literatures because of different specimen configurations and loading scenarios. General fatigue life models for both NSM and EB FRP in concrete are needed for the design of strengthened concrete structures. Some insights are provided into the bond fatigue behavior in the aforementioned studies, where the fatigue life models can be categorized into three types: (1) a linear relationship between the fatigue load range and the logarithmic fatigue life; (2) a linear relationship between the average bond stress range and the logarithmic fatigue life; and (3) a linear relationship between the maximum fatigue load ratio and the logarithmic fatigue life. However, due to different specimen configurations and material properties used in those studies, neither the fatigue load range nor the average bond stress range is reliable for being used to predict the fatigue life of any strengthened specimens. Therefore, the relationship between the fatigue load range ratio (or the maximum fatigue load ratio) and the logarithmic fatigue life is more reasonable for adoption to perform a regression analysis using the database collected from the literature. Specimens that did not fail within the target fatigue cycles (upper limit), e.g., 200 or 300 million cycles, are not considered herein to ensure that all specimens included in the database had reached their true fatigue life. In this case, 72 DPT specimens for NSM FRP and 16 DTP specimens for EB FRP are included herein and their corresponding trend lines are presented in Figs. 2.12-2.15. The prediction equations of fatigue life for both NSM FRP and EB FRP are thus derived in the following form, respectively:

$$\Delta LR = -2.62 \ln N_f + 90.72 \qquad \text{for NSM FRP} \tag{2.19}$$

$$LR_{\max} = -2.46 \ln N_f + 99.73 \qquad \text{for NSM FRP} \qquad (2.20)$$

$$\Delta LR = -5.59 \ln N_f + 102.61 \qquad \text{for EB FRP} \qquad (2.21)$$

$$LR_{\max} = -5.84 \ln N_f + 116.19 \qquad \text{for EB FRP} \qquad (2.22)$$

where ΔLR = fatigue load range ratio (%); and $LR_{\max}$ = maximum fatigue load ratio (%).

It can be seen that the prediction equations (Eqs. 2.19-2.22) provide a lower accuracy as compared with the corresponding experiment data. As previously mentioned, the bond fatigue performance for both NSM and EB FRP in concrete depends on many factors mentioned. Therefore, a general fatigue life model should not simply depend on the fatigue load ratio or the fatigue load range ratio, but also need to take into account the contribution from the FRP properties, adhesive type, surface treatment of FRP reinforcement, groove size, concrete strength, etc. On the other hand, the inaccuracy and unreliability of the current fatigue life models can also be attributed to the small database of the bond tests for both NSM and EB FRP in concrete under fatigue loading.

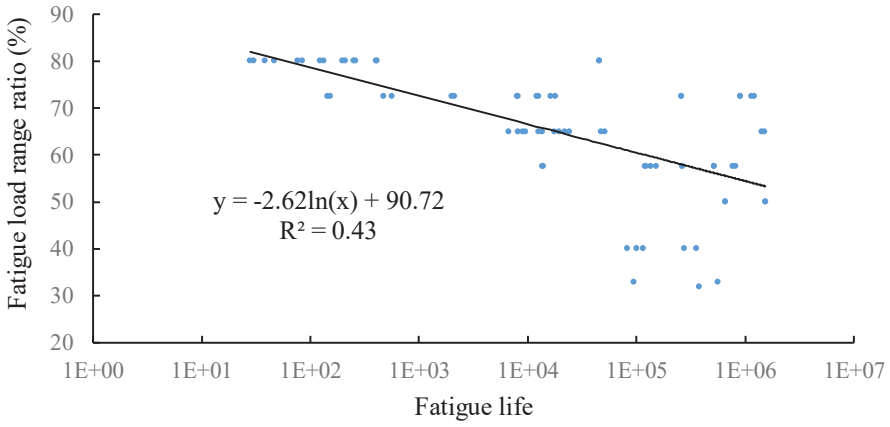

Fig. 2.12 Relationship of fatigue load range ratio vs. fatigue life for NSM FRP in concrete (Eq. 2.19)

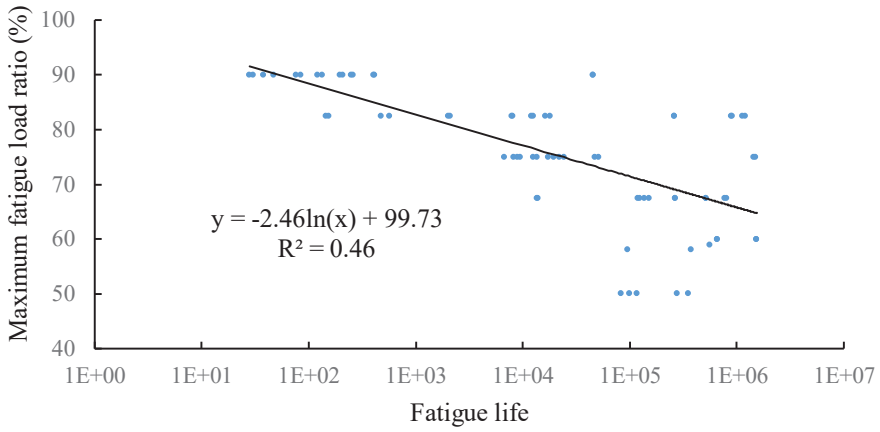

Fig. 2.13 Relationship of maximum fatigue load range ratio vs. fatigue life for NSM FRP in concrete (Eq. 2.20)

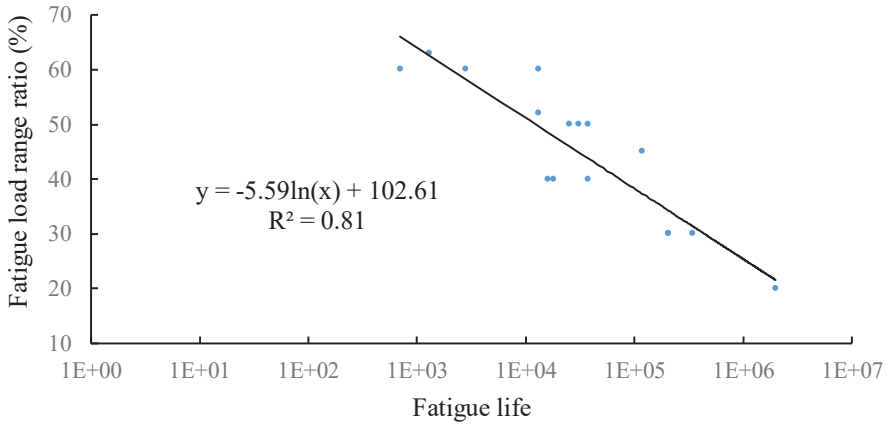

Fig. 2.14 Relationship of fatigue load range ratio vs. fatigue life for EB FRP in concrete (Eq. 2.21)

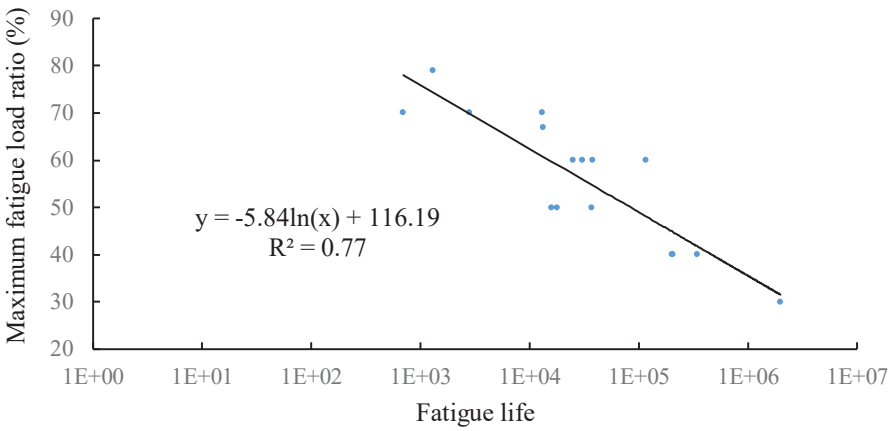

Fig. 2.15 Relationship of maximum fatigue load range ratio vs. fatigue life for EB FRP in concrete (Eq. 2.22)

2.7 Summary and future research

2.7.1 Summary

Two major FRP-based strengthening techniques using EB and NSM FRP systems are reviewed in this chapter. As an alternative to the EB FRP, the NSM FRP emerges with a better durability by embedding the FRP reinforcement into the concrete groove and covered by adhesives. Extensive studies have been conducted on the NSM FRP technique in various aspects including, but not limited to, flexural or shear strengthening for RC beams, seismic retrofitting, prestressing techniques, bond behaviors and durability issues. Although some experiments have been carried out, which demonstrated the good performance of the NSM FRP-to-concrete bonded joints exposed to severe environments, the fatigue-related issues associated with the deterioration of bond performance are not well investigated and hence deserve more comprehensive study.

The existing experiments are collected that are directly associated with the bond performance and interfacial crack propagation under fatigue loading for both NSM and EB FRP in concrete. Observations of the bond behavior during fatigue tests are summarized in terms of the local bond stress or FRP strain distribution along the bond line, the relationship of loaded end slip vs. the

number of fatigue cycles, the failure modes and the post-fatigue performance. Based on the theoretical analysis and the experimental studies reported in literatures, the influence on bond performance of FRP-to-concrete bonded joints induced by either geometric or material variables can be summarized as follows:

- The bond length of both EB and NSM FRP should be longer than the development length L_d to obtain sufficient bond strength and prevent premature debonding failure during DPT. The threshold of development length L_d for both EB and NSM FRP in concrete is around 100 mm;
- An appropriate groove dimension has positive influence on the ultimate pull-out force of NSM FRP-to-concrete bonded joints. The optimal groove dimensions are suggested as $1.5d_b \times 1.5d_b$ or $2.0d_b \times 2.0d_b$ (width × depth). For EB FRP system, a smaller width ratio of FRP plate to concrete block b_p/b_c leads to a higher ultimate bond strength;
- Surface treatment of the FRP reinforcement has a significant effect on the fatigue life of NSM FRP in concrete. The sand-coated and spirally wound rod surface shows a better performance than the roughened strip. The smooth strip shows the weakest bond performance. NSM FRP specimens using innovative high-strength self-compacting cementitious adhesive (IHSSC-CA) show better bond performance with a longer fatigue life than those using polymer cement-based adhesive. The axial stiffness of NSM FRP is effective in limiting the size of the damage zone under fatigue loading but it does not have a significant effect on the fatigue crack propagation. High fatigue frequency (8 Hz) substantially decreases the fatigue life of FRP-to-concrete bonded joints;
- For EB FRP in concrete, the interfacial fracture energy G_f plays a vital role in the bond strength, which is controlled by the properties of concrete and adhesive, as well as the FRP stiffness. The height of free concrete edge h_c of concrete block and the loading offset significantly influence the bond test result;
- A migration phenomenon of the peak local bond stress or FRP strain toward the free end of bond line exists in both EB and NSM FRP in concrete under fatigue loading. A three-stage

crack propagation is reported by researchers, which is in agreement with a three-stage strain distribution along FRP laminate during the fatigue cycles for EB FRP in concrete;

- A typical three-stage loaded end slip vs. the number of cycles response is observed for both EB and NSM FRP-to-concrete bonded joints. In general, it starts with a rapid increase of slip during the initial stage and is followed by a stable increase during the second stage. Then the slip increases rapidly again until the debonding failure occurs during the third stage;
- Different failure modes exist for EB and NSM FRP DPT. Despite some rare cases of FRP rupture due to high fatigue load levels, the major failure modes in DPT are: (1) failure at the FRP/adhesive interface; (2) failure at the adhesive/concrete interface; (3) cohesive failure in adhesive; and (4) cohesive failure in concrete;
- Similar post-fatigue performance is observed for both EB and NSM FRP systems. The FRP bond stiffness decreases significantly after fatigue cycles but the ultimate load-carrying capacity remains unchanged (or only slightly reduces) when the residual bond length is still longer than the development length; and
- The fatigue life models for both EB and NSM FRP systems in the literature can be categorized into three types: (1) a linear relationship between the fatigue load range and the logarithmic fatigue life; (2) a linear relationship between the average bond stress range and the logarithmic fatigue life; and (3) a linear relationship between the maximum fatigue load ratio and the logarithmic fatigue life. However, none of the existing fatigue life models is capable of providing a reliable prediction for the fatigue life of EB or NSM FRP-to-concrete bonded joints with a satisfying accuracy.

2.7.2 Future research

The bond fatigue performances of both EB and NSM FRP in concrete are vital for their service life, and the corresponding theories should be well established to provide a reliable estimation of the bond capacity before practical design and applications. Few experiments have

been carried out focusing on the fatigue behaviors of EB and NSM FRP in concrete on bond level, which is critical for retrofitted structures. Moreover, with such a small database on bond fatigue tests, the accuracy of the proposed empirical model is questionable. In light of this research gap, the following aspects regarding the bond fatigue performance of EB and NSM FRP in concrete deserve further attention:

- The concrete compressive strength and the groove dimensions (for NSM FRP) or width ratio (for EB FRP) have been verified to have significant effect on the maximum local bond strength. Reliable models to quantify this effect is, however, still limited in static case let along the condition under fatigue cycles;
- Although parameters such as the axial stiffness of FRP reinforcement and the shear stiffness of adhesives are reported to have some minor effects on the bond behavior under static loading, their influence under fatigue loading is still unknown;
- The local bond-slip behavior under fatigue loading is important to the derivation of analytical solution of the local bond stress distribution and the prediction of fatigue life for FRP-to-concrete bonded joints. However, the mechanisms of local bond degradation under fatigue cycles are not well established yet. As a result, it is necessary to identify a rational relationship between the local bond strength and the number of fatigue cycles before any analytical study;
- The local bond stress or FRP strain distribution along the bond line is hard to capture during the experiment due to the large scattering, which adds to the difficulty of building a solid local bond-slip relationship. An alternative is to use the finite element method, but obstacles exist to simulate the debonding process at the bond interfaces of FRP-to-concrete bonded joints and few studies have yielded reliable results. Nevertheless, it could be a viable approach; and
- The current analytical models are highly dependent on the failure modes since they are essentially related to the final state of the specimens. Hence, it is preferable to define a standard categorizing these failure modes observed during the direct pull-out test for FRP-to-concrete bonded joints.

CHAPTER THREE

3 ANALYTICAL MODELS TO PREDICT BOND PERFORMANCE AND FAILURE MODES OF NSM FRP-TO-CONCRETE BONDED JOINTS

3.1 Overview

Analytical models to predict the bond strength of both EB and NSM FRP-to-concrete bonded joints under static loading have been comprehensively studied in the recent decade (Yuan et al. 2001; Yuan et al. 2004; Seracino et al. 2007a; Ceroni et al. 2012; Zhang et al. 2014; Biscaia et al. 2016). As an early attempt, Yuan et al. (2001) derived the theoretical solution for the load-carrying capacity of EB FRP in concrete based on different interfacial constitutive laws. Yuan et al. (2004) then presented a closed-form analytical solution to describe the full-range behavior of EB FRP-to-concrete bonded joints by using the bilinear local bond stress-slip relationship. Overall, the predicted load-slip curve at the loaded end agreed well with the experiment results. Years later, when the NSM FRP technique emerged as a promising alternative to EB FRP, researchers applied these theories to the NSM FRP with some modifications. Seracino et al. (2007a) proposed a general expression to estimate the load-carrying capacity for both EB and NSM FRP in concrete by means of an idealized linear descending local bond stress-slip relationship. An important definition of the debonding failure plane for both EB and NSM FRP cases was also provided. This semi-empirical expression was later adopted by the SA (Standards Australia, SA 2008). Zhang et al. (2014) proposed another bond strength model for the NSM CFRP strip-to-concrete bonded joints based on a nonlinear local bond stress-slip law via a 3D meso-scale FE model. The model was compared to the Seracino et al.'s model (2007a) where the accuracy was verified by a test database collected from the literature. Although these models are capable of predicting the bond strength of the NSM FRP reinforcement in concrete and the predictions agree with the test results to certain extent, they

are restricted to scenario where the cohesive failure in concrete dominates. Yet most test observations have revealed the complex failure mechanisms of NSM FRP-to-concrete bonded joints, failure modes such as FRP rupture, adhesive splitting, debonding at the FRP/adhesive or adhesive/concrete interface and concrete splitting could occur predominantly or in a mixed mode. Analytical models capable of differentiating these different types of failure mode of NSM FRP in concrete are still limited. In light of this research gap, this chapter intends to provide a strategy to estimate the bond strength associates with different types of failure mode, as well as to predict the potential failure mode of the bonded joints based on material properties and specimen geometries for NSM FRP reinforcement in concrete.

3.2 Analytical model and governing equations

As mentioned in Chapter 2, the direct pull-out test (DPT) is widely considered by researchers as an effective way to investigate the bond performance of NSM FRP in concrete. In such a case, a typical analytical model based on the compressive DPT configuration is described below to introduce the fundamentals for NSM FRP-to-concrete bonded joints (Yuan et al. 2004; Seracino et al. 2007a).

As shown in Fig. 3.1(a), it is a typical single shear DPT with the concrete block under compression. The dimensions of the FRP reinforcement, groove (adhesive) and concrete block remain constant throughout modeling. The Young's modulus of FRP reinforcement and the concrete block is defined as E_f and E_c, respectively. The cross-sectional area of the FRP reinforcement and the concrete block is defined as A_f and A_c, respectively. The following important assumptions are adopted to derive the governing equations of the model:

(1) Both the FRP reinforcement and concrete are homogenous and linear elastic;

(2) The bending effect of the analytical model is neglected;

(3) The axial stress is uniformly distributed over the cross-section for both FRP reinforcement and the concrete block; and

(4) The bond length is long enough to perform the full-range bond behavior.

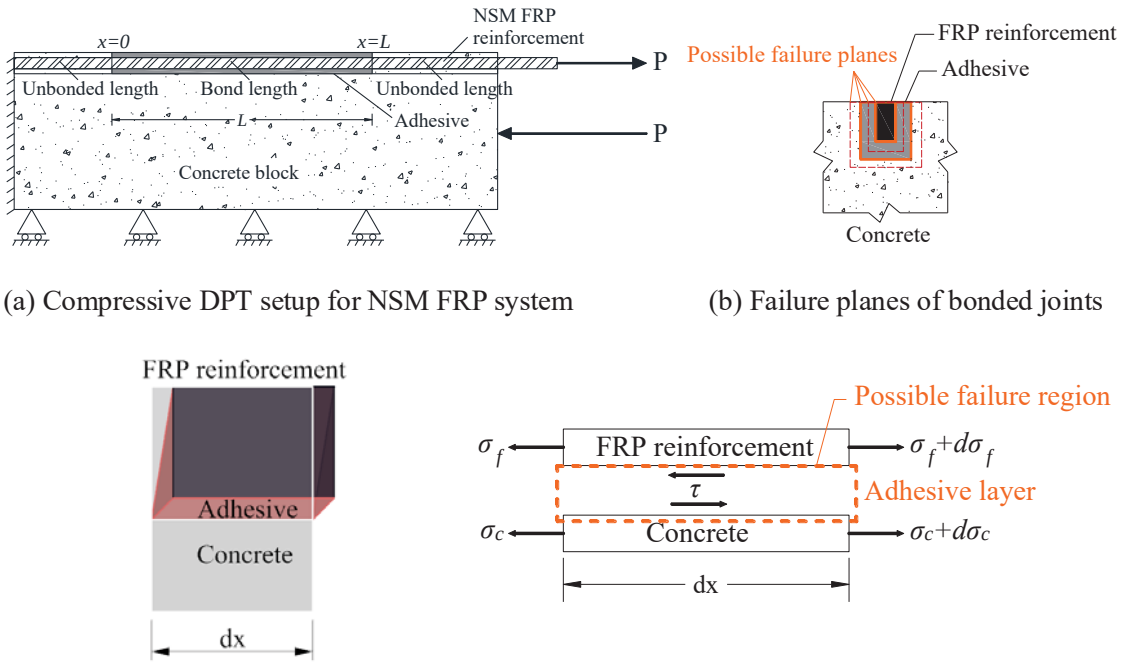

(a) Compressive DPT setup for NSM FRP system (b) Failure planes of bonded joints

(c) Deformation of bonded joints under load (d) Stress transfer from FRP reinforcement to concrete

Fig. 3.1 Analytical model of DPT for NSM FRP system

Therefore, if the FRP reinforcement and concrete block have sufficient capacity to resist the applied load, the most possible failure mode will be the mode II interfacial fracture (shear) failure. But the potential failure planes could be located within the FRP/adhesive interface, the adhesive/concrete interface or the interface between adhesive and concrete substrate. To facilitate this, a key parameter L_p is defined herein as the perimeter of the failure plane (Oehlers et al. 2008; Ali et al. 2008) [Fig. 3.1(b)]. As shown in Fig. 3.1(c), the shear deformation of the adhesive layer, which includes both the actual adhesive and the materials adjacent to the adhesive, helps transfer the applied load from FRP reinforcement to concrete block. Thus, the representative element can be illustrated in Fig. 3.1(d) and the corresponding equilibrium equations can be derived as:

$$\frac{d\sigma_f}{dx} = \frac{\tau L_p}{A_f} \tag{3.1}$$

$$\sigma_f A_f + \sigma_c A_c = 0 \tag{3.2}$$

where τ = local bond stress; σ_f = axial stress of FRP reinforcement; and σ_c = axial stress of concrete block.

The constitutive laws for the adhesive layer, FRP reinforcement and concrete block are given as:

$$\tau = \tau(\delta) \tag{3.3}$$

$$\delta = u_f - u_c \tag{3.4}$$

$$\sigma_f = E_f \frac{du_f}{dx} \tag{3.5}$$

$$\sigma_c = E_c \frac{du_c}{dx} \tag{3.6}$$

where δ = relative slip between FRP reinforcement and concrete block; u_f = axial displacement of FRP reinforcement; and u_c = axial displacement of concrete block.

By substituting Eqs. 3.2-3.6 into Eq. 3.1, the governing equation for this NSM FRP bonded joints under applied load can be derived as:

$$\frac{d^2\delta}{dx^2} - \lambda^2\tau = 0 \tag{3.7}$$

where

$$\lambda^2 = L_p\left(\frac{1}{A_f E_f} + \frac{1}{A_c E_c}\right) \tag{3.8}$$

Since all the material properties are considered as known parameters, the theoretical solution to this secondary differential equation can be easily solved if the local bond stress-slip relationship $\tau(\delta)$ is given.

3.3 Local bond stress-slip relationship

Similar to the constitutive law of concrete or steel, the local bond stress-slip relationship depicts the essential behavior of the bonded joints with respect to the capacity of load transfer from the FRP reinforcement to the surrounding concrete. Two major categories of bond stress-slip

models have been proposed by researchers: (1) linear bond stress-slip relationship; and (2) nonlinear bond stress-slip relationship. Models of the former category are widely accepted for design purposes and some representative ones have already been introduced in Chapter 2 (Fig. 2.4). The mathematical descriptions of these linear models are illustrated as follows:

Linear Model I – This model is basically linear elastic in that the local bond stress τ increases linearly with the increase of the relative slip [Fig. 3.2(a)]. When the interfacial fracture energy G_f of the bonded joints is reached, the stress drops down to zero immediately without any softening behavior.

$$\tau(\delta) = \begin{cases} \dfrac{\tau_f}{\delta_f}\delta & for\ 0 \le \delta \le \delta_f \\ 0 & for\ \delta > \delta_f \end{cases} \tag{3.9}$$

where τ_f = local bond strength; δ_f = maximum slip of the bonded joints; and G_f = interfacial fracture energy which is defined as the area under the local bond stress-slip curve and indicates the energy required for this bonded joints to fail in the shear mode.

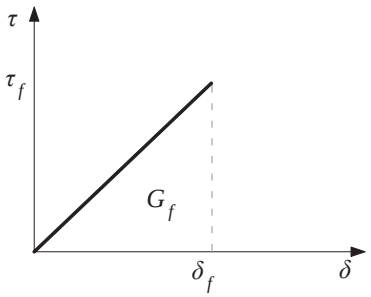

(a) Linear ascending model

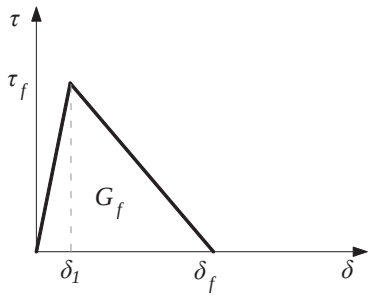

(b) Bilinear model

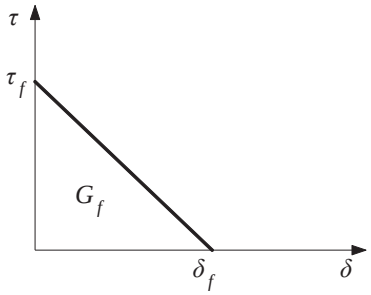

(c) Linear descending model

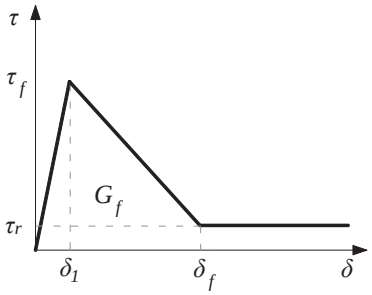

(d) Trilinear model

Fig. 3.2 Linear local bond stress-slip models for NSM bonded joints

Linear Model II – This bilinear model has two stages, the bond stress τ ascends with the increase of the relative slip before the local bond strength τ_f is reached [Fig. 3.2(b)]. The following softening stage indicates the interfacial fracture process with a linear descending trend until the debonding failure occurs. The bilinear model is a rational model representing the local bond characteristics observed in the physical bond tests and has been adopted by many researchers (e.g., Yuan et al. 2004, Diab et al. 2009, Ceroni et al. 2012, Chen and Cheng 2015).

$$\tau(\delta)=\begin{cases}\dfrac{\delta}{\delta_1}\tau_f & for\ 0\le\delta\le\delta_1\\ \dfrac{\delta_f-\delta}{\delta_f-\delta_1}\tau_f & for\ \delta_1<\delta\le\delta_f\\ 0 & for\ \delta>\delta_f\end{cases} \tag{3.10}$$

where δ_f = slip at the loaded end corresponding to the local bond strength τ_f.

Linear Model III – In view of the small value of δ_1 as compared to δ_f observed in the physical bond tests, the ascending stage of the bilinear model could be neglected and thus a more simplified descending model is yielded [Fig. 3.2(c)]. Note that for the same local bond strength τ_f and maximum relative slip δ_f, the area under the local bond stress-slip curve with respect to all these three linear bond stress-slip models (I, II and III) is the same. In other words, the interfacial fracture energy G_f is an inherent property of the bonded joints and independent of the local bond stress-slip model that being considered.

$$\tau(\delta)=\begin{cases}\left(1-\dfrac{\delta}{\delta_f}\right)\tau_f & for\ 0\le\delta\le\delta_f\\ 0 & for\ \delta>\delta_f\end{cases} \tag{3.11}$$

Linear Model IV – This trilinear model was proposed by Chen and Cheng (2017) by taking the small amount of residual bond stress into account, which is contributed by the interlocking and mechanical friction at the failure interface. Despite that slight difference in residual bond strength

after debonding, the entire local bond stress-slip relationship for the trilinear model before the maximum slip is the same as that of the bilinear model.

$$\tau(\delta)=\begin{cases}\dfrac{\delta}{\delta_1}\tau_f & \text{for } 0\le\delta\le\delta_1\\ \dfrac{\delta_f-\delta}{\delta_f-\delta_1}\left(\tau_f-\tau_r\right)+\tau_r & \text{for } \delta_1<\delta\le\delta_f\\ \tau_r & \text{for } \delta>\delta_f\end{cases} \tag{3.12}$$

where τ_r = residual local bond stress after the maximum slip δ_f has been reached.

Nonlinear Model I – Similar to the linear descending model, this exponentially descending bond stress-slip relationship describes a softening stage starting from the local bond strength τ_f and nonlinearly drops down to zero with the increase of relative slip [Fig. 3.3(a)]. The area under the curve should be a constant property the same as other models and equals to the interfacial fracture energy G_f.

$$\tau(\delta)=\tau_f e^{-\left(\frac{\tau_f}{G_f}\delta\right)} \tag{3.13}$$

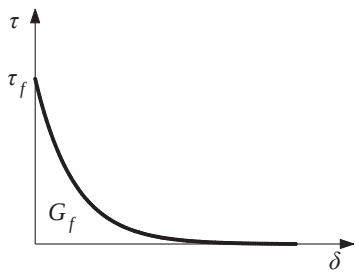

(a) Exponentially descending model

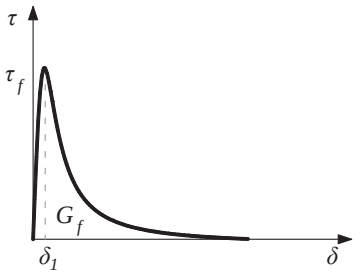

(b) Nakaba et al. (2001)'s model

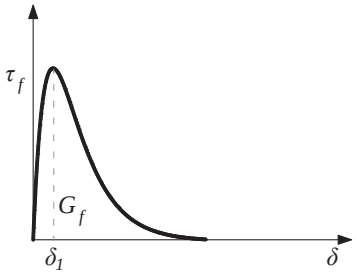

(c) Dai et al. (2005)'s model

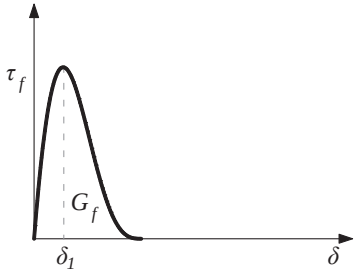

(d) Zhang et al. (2013)'s model

Fig. 3.3 Nonlinear bond stress-slip models for NSM bonded joints

Nonlinear Model II – This model was derived from the curve-fitting of experimental data by Nakaba et al. (2001). It contains both the ascending and softening stages with a nonlinear bond stress-slip relationship [Fig. 3.3(b)].

$$\tau(\delta) = \tau_f \left[\frac{\delta}{\delta_1} \frac{n}{(n-1)+(\delta/\delta_1)^n} \right] \tag{3.14}$$

where n = empirical parameter.

Nonlinear Model III – This exponential model was proposed by Dai et al. (2005) and agreed well with the practical experimental results [Fig. 3.3(c)]. The theoretical solution to estimate the bond behavior and load-carrying capacity of the bonded joints based on this local bond stress-slip model was provided by Biscaia et al. (2016).

$$\tau(\delta) = 2BG_f \left(e^{-B\delta} - e^{-2B\delta} \right) \tag{3.15}$$

where B = experimental parameter obtained by regression analysis.

Nonlinear Model IV – This expression was proposed by Zhang et al. (2013) by means of a 3D meso-scale FE model [Fig. 3.3(d)]. For the ascending branch, the slope magnitude decreases continuously until the bond strength is reached. For the descending branch, the slope magnitude increases firstly but followed by a decreasing trend with the further increase of relative slip.

$$\tau(\delta) = A\left(\frac{2B-\delta}{B} \right)^2 \sin\left(\frac{\pi}{2} \cdot \frac{2B-\delta}{B} \right) \quad with \quad \delta \le 2B \tag{3.16}$$

where A and B = experimental parameters obtained by regression analysis.

3.4 Theoretical bond behavior under static load

Given the governing equations of the assumed bonded joints model and local bond stress-slip relationship, the full-range bond behavior under the applied static load is derived next. In this context, the theoretical solution to the secondary ordinary deferential equation (ODE) represented by Eq. 3.7 depends on the selection of the local bond stress-slip model. There is no doubt that the model should capture the characteristics of the bond stress-slip relationship and be both accurate

and representative when compared to the laboratory test results. The description of the model should also be concise and allow for the availability of mathematical derivation explicitly based on the governing equations. In addition, the expressions to predict the distribution of local bond stress, relative slip between FRP and concrete, and FRP stress along the bond line should be practical for design purpose. Therefore, the bilinear local bond stress-slip relationship, which is the most widely adopted model by researchers, is selected herein to perform the theoretical derivation (Yuan et al. 2004). An important premise of the following derivation process is that the bond length should be long enough to perform the full-range bond behavior of the bonded joints.

3.4.1 Linear elastic stage I

Assume the free end of the bond line is the origin (i.e., $x = 0$) and the loaded end is $x = L$, where L = the bond length of the bonded joints [Fig. 3.1(a)]. When the slip at the loaded end is less than δ_1, the entire bond line is within the linear elastic stage. By substituting the term of Eq. 3.10 for $0 \le \delta \le \delta_1$ into the governing equation Eq. 3.7, the secondary ODE is obtained as follows:

$$\frac{d^2\delta}{dx^2} - \lambda_1^2 \delta = 0 \tag{3.17}$$

where

$$\lambda_1^2 = \frac{\tau_f L_p}{\delta_1}\left(\frac{1}{A_f E_f} + \frac{1}{A_c E_c}\right) \tag{3.18}$$

The boundary conditions of stage I are:

$$\sigma_f(0) = 0 \tag{3.19}$$

$$\sigma_c(0) = 0 \tag{3.20}$$

$$\sigma_f(L) = \frac{P}{A_f} \tag{3.21}$$

By using these boundary conditions, the explicit solutions to the ODE problem (Eq. 3.17) can be obtained. Expressions of the relative slip, the local bond stress and the axial stress of FRP reinforcement are described as follows:

$$\delta_1 = \frac{P\delta_1\lambda_1}{L_p\tau_f}\frac{\cosh(\lambda_1 x)}{\sinh(\lambda_1 L)} \tag{3.22}$$

$$\tau_1 = \frac{P\lambda_1}{L_p}\frac{\cosh(\lambda_1 x)}{\sinh(\lambda_1 L)} \tag{3.23}$$

$$\sigma_{f1} = \frac{P}{A_f}\frac{\sinh(\lambda_1 x)}{\sinh(\lambda_1 L)} \tag{3.24}$$

A representative local bond stress distribution along the bond line is presented in Fig. 3.4(a). The ultimate state of stage I is when the local bond stress at $x = L$ equals to the local bond strength τ_f [Fig. 3.4(b)]. The maximum pull-out force of stage I can also be obtained as:

$$P_{m1} = \frac{L_p\tau_f}{\lambda_1}\tanh(\lambda_1 L) \tag{3.25}$$

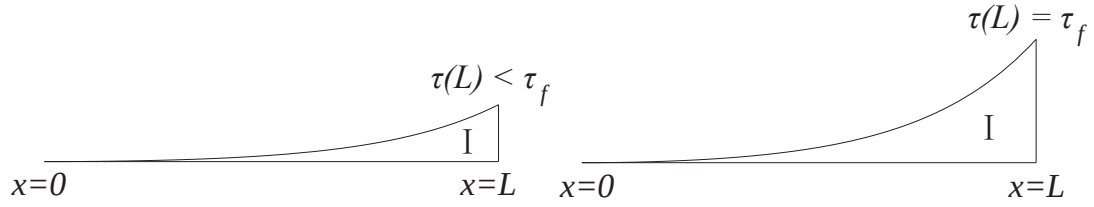

(a) Linear elastic stage I

(b) Ultimate state of stage I

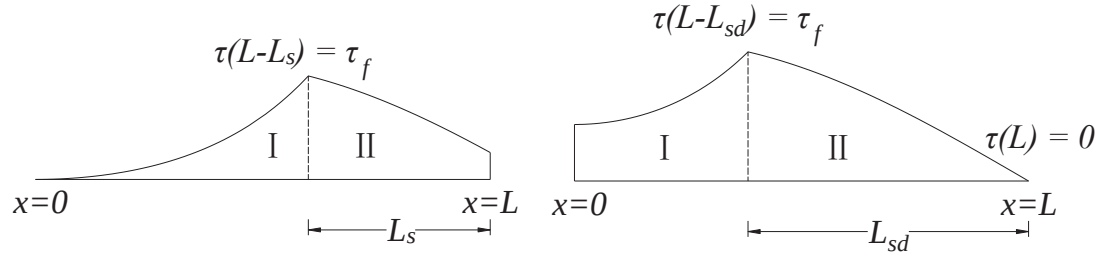

(c) Elastic-softening stage II

(d) Ultimate state of stage II

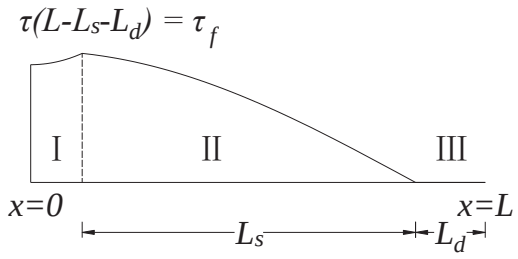

(e) Elastic-softening-debonding stage III

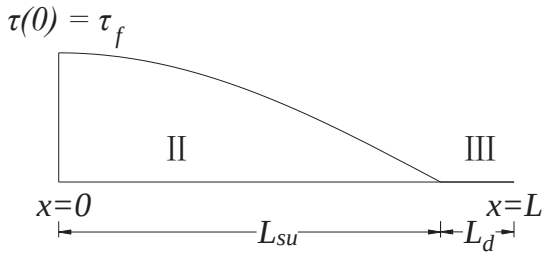

(f) Ultimate state of stage III

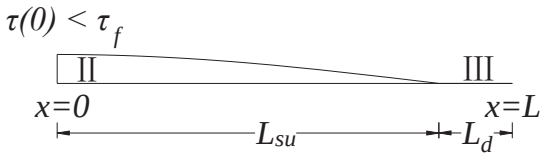

(g) Softening-debonding stage IV

Fig. 3.4 Local bond stress distribution and propagation under static load

3.4.2 Elastic-softening stage II

With the increase of the applied load, the relative slip at $x = L$ reaches δ_1 and initiates the softening stage II starting from the loaded end. As illustrated in Fig. 3.4(c), state I and state II exist concurrently along the bond line. For the region of state I, the governing equation remains the same by Eq. 3.17. For the region of state II, by substituting the term of Eq. 3.10 for $\delta_1 \le \delta \le \delta_f$ into the governing equation Eq. 3.7, the following ODE is obtained:

$$\frac{d^2\delta}{dx^2} - \lambda_2^2\delta = \lambda_2^2\delta_f \tag{3.26}$$

where

$$\lambda_2^2 = \frac{\tau_f L_p}{\delta_f - \delta_1}\left(\frac{1}{A_f E_f} + \frac{1}{A_c E_c}\right) \tag{3.27}$$

The boundary conditions of stage II change to:

$$\sigma_f(0) = 0 \tag{3.28}$$

$$\sigma_c(0) = 0 \tag{3.29}$$

$$\delta\left(L-L_s\right)=\delta_1 \text{ or } \tau\left(L-L_s\right)=\tau_f \tag{3.30}$$

$$\frac{d\delta}{dx} \text{ is continuous at } x=L-L_s \tag{3.31}$$

$$\sigma_f \text{ is continuous at } x=L-L_s \tag{3.32}$$

$$\sigma_f\left(L\right)=\frac{P}{A_f} \tag{3.33}$$

where L_s = softening length. The solutions for the region of state I ($x \in [0, L - L_s]$) are derived as follows:

$$\delta_{\mathrm{I}}=\delta_1\frac{\cosh\left(\lambda_1 x\right)}{\cosh\left[\lambda_1\left(L-L_s\right)\right]} \tag{3.34}$$

$$\tau_{\mathrm{I}}=\tau_f\frac{\cosh\left(\lambda_1 x\right)}{\cosh\left[\lambda_1\left(L-L_s\right)\right]} \tag{3.35}$$

$$\sigma_{f\,\mathrm{I}}=\frac{L_p\tau_f}{A_f\lambda_1}\frac{\sinh\left(\lambda_1 x\right)}{\cosh\left[\lambda_1\left(L-L_s\right)\right]} \tag{3.36}$$

The solutions for the region of state II ($x \in [L - L_s, L]$) are derived as follows:

$$\delta_{\mathrm{II}}=\left(\delta_f-\delta_1\right)\left\{\frac{\lambda_2}{\lambda_1}\tanh\left[\lambda_1\left(L-L_s\right)\right]\sin\left[\lambda_2\left(x-L+L_s\right)\right]-\cos\left[\lambda_2\left(x-L+L_s\right)\right]+\frac{\delta_f}{\delta_f-\delta_1}\right\} \tag{3.37}$$

$$\tau_{\mathrm{II}}=-\tau_f\left\{\frac{\lambda_2}{\lambda_1}\tanh\left[\lambda_1\left(L-L_s\right)\right]\sin\left[\lambda_2\left(x-L+L_s\right)\right]-\cos\left[\lambda_2\left(x-L+L_s\right)\right]\right\} \tag{3.38}$$

$$\sigma_{f\,\mathrm{II}}=\frac{L_p\tau_f}{A_f\lambda_2}\left\{\frac{\lambda_2}{\lambda_1}\tanh\left[\lambda_1\left(L-L_s\right)\right]\cos\left[\lambda_2\left(x-L+L_s\right)\right]+\sin\left[\lambda_2\left(x-L+L_s\right)\right]\right\} \tag{3.39}$$

The pull-out force in terms of the softening length L_s for stage II can be derived by using both Eq. 3.33 and Eq. 3.36 as:

$$P=\frac{L_p\tau_f}{\lambda_2}\left\{\frac{\lambda_2}{\lambda_1}\tanh\left[\lambda_1\left(L-L_s\right)\right]\cos\left(\lambda_2 L_s\right)+\sin\left(\lambda_2 L_s\right)\right\} \tag{3.40}$$

The maximum pull-out force for stage II appears when the first derivative of P with respect to the softening length L_s equals to zero, namely, $\partial P / \partial L_s = 0$ and yields the following expression:

$$\tanh\left[\lambda_1\left(L - L_{sm}\right)\right] = \frac{\lambda_2}{\lambda_1}\tan\left(\lambda_2 L_{sm}\right) \tag{3.41}$$

where L_{sm} = softening length corresponding to the maximum pull-out force of the bonded joints. Then by substituting Eq. 3.41 into Eq. 3.40, the expression for the maximum pull-out for stage II, which is also the bond strength of the bonded joints, is derived as:

$$P_{\max} = P_{m2} = \frac{L_p \tau_f}{\lambda_2}\frac{\delta_f}{\delta_f - \delta_1}\sin\left(\lambda_2 L_{sm}\right) \tag{3.42}$$

For an infinite bond length L, Eq. 3.41 could yield the softening length L_{sm}^u corresponding to the maximum theoretical bond strength for the given bonded joints as:

$$L_{sm}^u = \frac{1}{\lambda_2} a\tan\frac{\lambda_1}{\lambda_2} \tag{3.43}$$

If one defines the effective bond length L_{eff} as the length over which the bonded joints provides at least 97% of the maximum theoretical bond strength, for an ideal joint with an infinite bond length, the effective bond length L_{eff} can be derived in the following format:

$$P_{\max}^{97\%} = 0.97 P_{\max}^u = 0.97\frac{L_p \tau_f}{\lambda_2}\frac{\delta_f}{\delta_f - \delta_1}\sin\left(\lambda_2 L_{sm}^u\right) \rightarrow \sin\left(\lambda_2 L_{sm}^{97\%}\right) = 0.97\sin\left(\lambda_2 L_{sm}^u\right) \tag{3.44}$$

Such that

$$L_{sm}^{97\%} = \frac{1}{\lambda_2} a\sin\left(0.97\sqrt{\frac{\delta_f - \delta_1}{\delta_f}}\right) \tag{3.45}$$

By substituting Eq. 3.45 back into Eq. 3.41 and it yields:

$$L_{eff} = \frac{1}{\lambda_1} a\tanh\left(\frac{\lambda_2}{\lambda_1}\tan\left(\lambda_2 L_{sm}^{97\%}\right)\right) + L_{sm}^{97\%} \tag{3.46}$$

3.4.3 Elastic-softening-debonding stage III

The debonding initiates when the relative slip at $x = L$ increases to the maximum slip δ_f which also implies that the local bond stress at the loaded end decreases to zero [Fig. 3.4(d)]. In such a case, by using Eq. 3.38 with the boundary condition $\tau_{II}(L) = 0$, the softening length L_{sd} with respect to the start of debonding state III can be derived as the following equation:

$$\tanh\left[\lambda_1\left(L - L_{sd}\right)\right] = \frac{\lambda_1}{\lambda_2}\cot\left(\lambda_2 L_{sd}\right) \tag{3.47}$$

During the debonding process, as illustrated in Fig. 3.4(e), three different stress distribution modes coexist along the bond line. For the regions of state I ($x \in [0, L - L_d - L_s]$) and state II ($x \in [L - L_d - L_s, L - L_d]$), the theoretical solutions of the relative slip, local bond stress and axial stress of FRP reinforcement remain the same as those in stage II, except replacing the bond length L by the residual bond length ($L - L_d$) as follows:

$$\delta_{\mathrm{I}} = \delta_1 \frac{\cosh\left(\lambda_1 x\right)}{\cosh\left[\lambda_1\left(L - L_d - L_s\right)\right]} \tag{3.48}$$

$$\tau_{\mathrm{I}} = \tau_f \frac{\cosh\left(\lambda_1 x\right)}{\cosh\left[\lambda_1\left(L - L_d - L_s\right)\right]} \tag{3.49}$$

$$\sigma_{f\mathrm{I}} = \frac{L_p \tau_f}{A_f \lambda_1} \frac{\sinh\left(\lambda_1 x\right)}{\cosh\left[\lambda_1\left(L - L_d - L_s\right)\right]} \tag{3.50}$$

$$\delta_{\mathrm{II}} = \left(\delta_f - \delta_1\right)\left\{\frac{\lambda_2}{\lambda_1}\tanh\left[\lambda_1\left(L - L_d - L_s\right)\right] sin\left[\lambda_2\left(x - L + L_d + L_s\right)\right] - \cos\left[\lambda_2\left(x - L + L_d + L_s\right)\right] + \frac{\delta_f}{\delta_f - \delta_1}\right\} \tag{3.51}$$

$$\tau_{\mathrm{II}} = -\tau_f\left\{\frac{\lambda_2}{\lambda_1}\tanh\left[\lambda_1\left(L - L_d - L_s\right)\right] sin\left[\lambda_2\left(x - L + L_d + L_s\right)\right] - \cos\left[\lambda_2\left(x - L + L_d + L_s\right)\right]\right\} \tag{3.52}$$

$$\sigma_{f\mathrm{II}} = \frac{L_p \tau_f}{A_f \lambda_2}\left\{\frac{\lambda_2}{\lambda_1}\tanh\left[\lambda_1\left(L - L_d - L_s\right)\right] cos\left[\lambda_2\left(x - L + L_d + L_s\right)\right] + sin\left[\lambda_2\left(x - L + L_d + L_s\right)\right]\right\} \tag{3.53}$$

where the debonding length L_d could be derived from the boundary condition $\tau_{II}(L - L_d) = 0$ as follows:

$$L_d = L - L_s - \frac{1}{\lambda_1} a \tanh\left[\frac{\lambda_1}{\lambda_2}\cot\left(\lambda_2 L_s\right)\right] \tag{3.54}$$

Since the debonding region is unable to provide any extra resistance towards the external load, the pull-out force in term of the softening length L_s for stage III can be derived by using the boundary condition $\sigma_{f\text{III}}(L - L_d) = P/A_f$ as follows:

$$P = \frac{L_p \delta_f}{\lambda_2}\left\{\frac{\lambda_2}{\lambda_1}\tanh\left[\lambda_1\left(L - L_d - L_s\right)\cos\left(\lambda_2 L_s\right)\right] + \sin\left(\lambda_2 L_s\right)\right\} \tag{3.55}$$

For the region of state III, by substituting the term of Eq. 3.10 for $\delta > \delta_f$ into the governing equation Eq.7, the third ODE is obtained as follows:

$$\frac{d^2\delta}{dx^2} = 0 \tag{3.56}$$

Likewise, the boundary conditions for state III are:

$$\delta\left(L - L_d\right) = \delta_f \tag{3.57}$$

$$\frac{d\delta}{dx} \text{ is continuous at } x = L - L_d \tag{3.58}$$

Therefore, the solutions for the region of state III ($x \in [L - L_d, L]$) are derived as follows:

$$\delta_{\text{III}} = \frac{\lambda_2\left(\delta_f - \delta_1\right)}{\sin\left(\lambda_2 L_s\right)}x + \delta_f - \frac{\lambda_2\left(\delta_f - \delta_1\right)\left(L - L_d\right)}{\sin\left(\lambda_2 L_s\right)} \tag{3.59}$$

$$\tau_{\text{III}} = 0 \tag{3.60}$$

$$\sigma_{f\text{III}} = \frac{P}{A_f} \tag{3.61}$$

The ultimate state of stage III is when the relative slip at the free end reaches the maximum slip δ_f, and it also indicates the end of the linear elastic state I on the bond line [Fig. 3.4(f)]. In this circumstance, the relationship between the bonded and debonding region can be presented by:

$$L_d = L - L_s \tag{3.62}$$

Substituting Eq. 3.62 into Eq. 3.54, the ultimate softening length L_{su} is obtained as:

$$L_{su} = \frac{\pi}{2\lambda_2} \tag{3.63}$$

3.4.4 Softening-debonding stage IV

During the last the softening-debonding stage IV, the propagation of debonding region stops and the softening length maintains constant as L_{su}. Meanwhile, the local bond stress at the free end continues to decrease until the bonded joints is unable to bear any load. The local bond stress distribution mode for stage IV is the combination of state II and state III. The governing equation for each state is the same as Eq. 3.26 and Eq. 3.56, respectively, but the boundary conditions are different and described as follows:

$$\sigma_f(0) = 0 \tag{3.64}$$

$$\sigma_f(L_{su}) = \frac{P}{A_f} \tag{3.65}$$

$$\sigma_c(0) = 0 \tag{3.66}$$

$$\delta(L_{su}) = \delta_f \tag{3.67}$$

$$\frac{d\delta}{dx} \text{ is continuous at } x = L_{su} \tag{3.68}$$

Accordingly, the theoretical solutions for the region of state II ($x \in [0, L_{su}]$) and state III ($x \in [L_{su}, L]$) are derived as follows:

$$\delta_{\text{II}} = \delta_f - \frac{P\lambda_2(\delta_f - \delta_1)}{L_p\tau_f}\cos(\lambda_2 x) \tag{3.69}$$

$$\tau_{\text{II}} = \frac{P\lambda_2}{L_p}\cos(\lambda_2 x) \tag{3.70}$$

$$\sigma_{f\,\text{II}} = \frac{P}{A_f}\sin(\lambda_2 x) \tag{3.71}$$

$$\delta_{\mathrm{III}} = \frac{P\lambda_2^{\,2}\left(\delta_f - \delta_1\right)}{L_p\tau_f}x + \delta_f - \frac{\pi P\lambda_2\left(\delta_f - \delta_1\right)}{2L_p\tau_f} \tag{3.72}$$

$$\tau_{\mathrm{III}} = 0 \tag{3.73}$$

$$\sigma_{f\mathrm{III}} = \frac{P}{A_f} \tag{3.74}$$

3.4.5 Load-carrying capacity of bonded joints

The aforementioned four stages describe the analytical full range behavior of the NSM FRP-to-concrete bonded joints based on the bilinear local bond stress-slip relationship. Presumably, if the bond length L is larger than the effective bond length L_{eff} (Eq. 3.46), the full range behavior should be expected and hence a typical load-slip relationship at the loaded end is presented as Fig. 3.5. Segment AB, BC, CD and DE represents the linear elastic stage I, elastic-softening stage II, elastic-softening-debonding stage III and softening-debonding stage IV, respectively. It should be noted that when the bond length is longer than the threshold value of L_{eff}, the load-carrying capacity of the bonded joints is almost identical, and the peak load always exists within stage II (BC) before debonding happens. In addition, with a further increase of the bond length, the emergence of the peak load will migrate from the near end of stage II to the ultimate state of stage II, which could be explained by Eq. 3.41 and Eq. 3.47. Because when the bond length L increases to infinite, Eq. 3.41 and Eq. 3.47 are identical and the corresponding values of L_{sm} and L_{sd} are also the same.

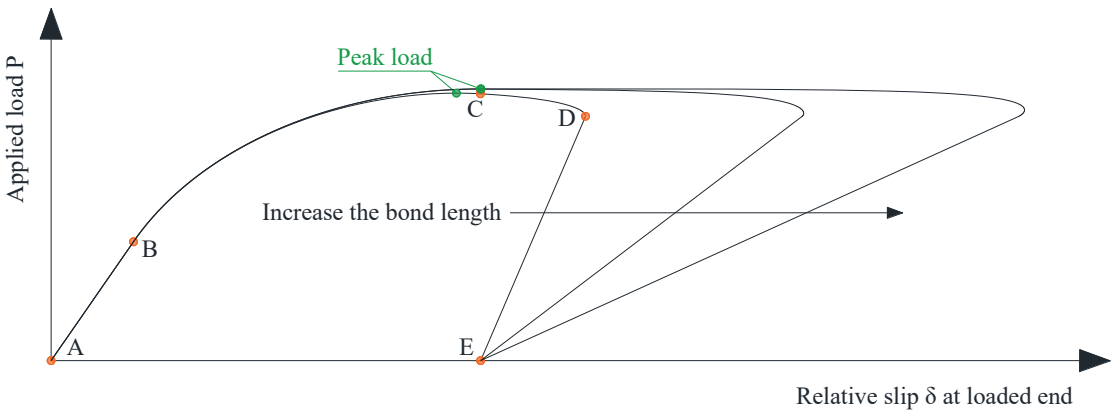

Fig. 3.5 Typical full range load-slip relationship at the loaded for NSM FRP-to-concrete bonded joints with a sufficient bond length

Therefore, one can assume that when the bond length L is larger than the effective bond length L_{eff}, the theoretical load-carrying capacity of the bonded joints is equivalent to $P_{\max}{}^{u}$, which can be derived by substituting Eq. 3.43 into Eq. 3.42 as follows:

$$P_{\max}^{u} = \frac{L_p \tau_f}{\lambda_2}\sqrt{\frac{\delta_f}{\delta_f - \delta_1}} = \sqrt{L_p \tau_f \delta_f \Big/ \left(1/A_f E_f + 1/A_c E_c\right)} \tag{3.75}$$

Eq. 3.42 is applicable to the bonded joints adopting either the local bond stress-slip bilinear model or linear descending model [Figs. 3.2(b) and (c)] with a sufficient bond length. Because the $\tau_f\delta_f$ term in Eq. 3.75 is equal to $2G_f$, which is considered as an inherent property of a bonded joints. If the values of the local bond strength τ_f and the maximum slip δ_f are the same for the bilinear model and the linear descending model, their corresponding theoretical bond strengths are identical. As a result, for a bonded joints with given geometry and material properties, the theoretical prediction of the pull-out force of DPT depends only on L_p, τ_f and δ_f. As aforementioned, the potential failure planes for a bonded joints can be located at the FRP/adhesive interface, the adhesive/concrete interface, or the adhesive and concrete substrate [Fig. 3.1(b)]. Also, the three key parameters L_p, τ_f and δ_f may vary for different failure planes, which will be discussed in detail in the following sections.

3.5 Bond strength for different failure mode

Because of the precut concrete grooves and thicker adhesive layer, failure modes for the bonded joints of the NSM FRP in concrete are distinct from that of the EB FRP. A more efficient utilization of FRP reinforcement for NSM system leads to a possibility of FRP rupture during the DPT, which is rarely observed in the EB bond test. The existing semi-empirical models proposed to estimate the load-carrying capacity of NSM FRP-to-concrete bonded joints in the literature are restricted to the situation of cohesive failure in the concrete adjacent to the epoxy layer (Seracino

et al. 2007a; Zhang et al. 2014). Although this failure mode is most preferable from the design perspective, the lack of design measures to prevent other failure modes makes the experimental result unpredictable. To address this issue, some efforts have been undertaken to estimate the bond strength at different failure planes either analytically or semi-empirically, based on the available DPT data in the open literature for NSM FRP in concrete.

3.5.1 FRP rupture

The occurrence of FRP rupture is supposed to be rare when the specimen configuration for DPT is well designed, but it has been reported by many researchers in laboratory experiments for NSM FRP-to-concrete bonded joints with sufficient bond length (Seracino et al. 2007b; Oehlers et al. 2008; Soliman et al. 2011; Bilotta et al. 2011; Seo et al. 2013; Lee et al. 2013; Khshain et al. 2015; Torres et al. 2016). The expression to estimate the pull-out force at FRP rupture can be simply presented as follows:

$$P_f = f_f A_f \tag{3.76}$$

where f_f = tensile strength of FRP reinforcement.

3.5.2 Cohesive failure in concrete

The cohesive failure in concrete is an ideal failure mode because it maximizes the strengthening effectiveness as failure occurs in the existing structure rather than in the strengthening system (Zhang et al. 2013). For concrete specimens using NSM FRP strip (rectangular shape), which provides a larger perimeter-to-area ratio, the utilization of FRP material is generally higher provided that the bond length is sufficient long. As a result, the cohesive failure in concrete is expected as the predominant failure mode, which has been validated by many experiments (Seracino et al. 2007a; Oehlers et al. 2008; Seo et al. 2013; Khshain et al. 2015).

Seracino et al. (2007a) concluded that for NSM FRP in concrete, a larger aspect ratio of failure plane increased the confinement of the joint, allowing stress transfer across the concrete

crack via aggregate interlocking and friction. In addition, since the failure occurs within the substrate concrete, the concrete compressive strength contributes to the local bond strength τ_f. Thus, semi-empirical models for the two key parameters, τ_f and δ_f, were proposed by regression analysis from test data as follows:

$$\tau_f = \left(0.078\varphi_p + 0.802\right) f_c^{0.6} \tag{3.77}$$

$$\delta_f = \frac{0.976\varphi_p^{0.526}}{\left(0.078\varphi_p + 0.802\right)} \tag{3.78}$$

where φ_p = aspect ratio of the failure plane; and f_c = concrete cylinder compressive strength (MPa).

For FRP strip condition without adhesive cover, the aspect ratio φ_p of the failure plane was defined as (Seracino et al. 2007a):

$$\varphi_p = \frac{d_g + t_d}{w_g + 2t_w} \tag{3.79}$$

where d_g = depth of concrete groove; w_g = width of concrete groove; t_d and t_w = vertical and horizontal distance of the failure plane that develops into the substrate concrete from the groove [Fig. 3.6(a)], respectively; and $t_d = t_w = 1$ mm as recommended by Seracino et al. (2007a).

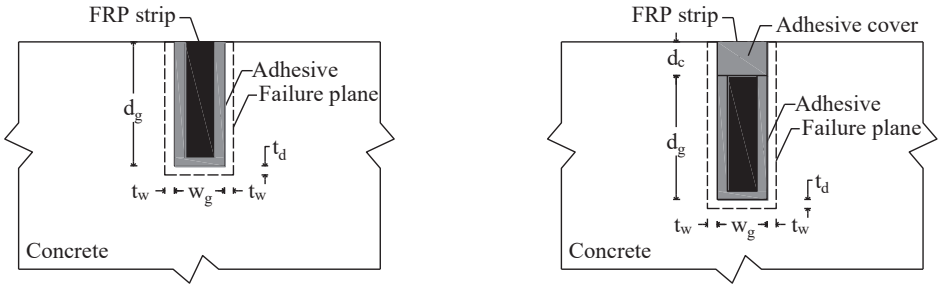

(a) NSM FRP strip without adhesive cover (b) NSM FRP strip with adhesive cover

Fig. 3.6 The failure plane for cohesive failure in concrete substrate

For NSM FRP strip condition with adhesive cover, where the entire NSM strip has been embedded into the groove and accordingly the confinement of FRP reinforcement can be enhanced

by extra adhesive cover [Fig. 3.6(b)]. The revised models of both the local bond strength τ_f and the maximum slip δ_f were proposed by Oehlers et al. (2008) as follows:

$$\tau_f = \left(0.078\varphi_p + 0.802\right) f_c^{0.6} \left(\frac{d_c + d_g}{d_g} \right)^{0.65} \tag{3.80}$$

$$\delta_f = \frac{0.976\varphi_p^{0.526}}{\left(0.078\varphi_p + 0.802\right)} \left(\frac{d_c + d_g}{d_g} \right)^{0.55} \tag{3.81}$$

where d_c = depth of the adhesive cover.

Zhang et al. (2013) proposed the local bond stress-slip model via numerical simulation by using the 3-D meso-scale FE model (Eq. 3.16). It was assumed that both the interfacial fracture energy G_f and the local bond strength τ_f were functions of the concrete strength and groove height-to-width ratio. Thus, exponential equations for G_f and τ_f were derived based on the numerical results and regression analysis as follows:

$$G_f = 0.4\gamma^{0.422} f_c^{0.619} \tag{3.82}$$

$$\tau_f = 1.15\gamma^{0.138} f_c^{0.613} \tag{3.83}$$

where γ = groove height-to-width ratio.

Since for either bilinear local bond stress-slip model or linear descending model, a general equation of $G_f = 0.5\tau_f\delta_f$ is always valid. Thus, δ_f was derived as:

$$\delta_f = 0.7\gamma^{0.284} f_c^{0.006} \tag{3.84}$$

3.5.3 Cohesive failure in adhesive

Except for the common debonding failure in adhesive mentioned above, the splitting crack in epoxy was reported by many researchers (De Lorenzis et al. 2004; Galati and De Lorenzis 2009; Soliman et al. 2011; Lee and Cheng 2013; Sharaky et al. 2013; Torres et al. 2016). However, the effect of splitting in adhesive can be eliminated or minimized by setting an appropriate parameter *k*, which is defined as the ratio of groove size (width or depth) to FRP reinforcement dimension.

De Lorenzis and Teng (2007) summarized that for specimens with $k > 1.5$, the splitting in adhesive could be prevented and this conclusion was validated by Bilotta et al. (2011) in the experiment. Therefore, the splitting failure of epoxy is not considered as a major failure mode herein.

For cohesive failure in adhesive, the local bond strength highly depends on the shear strength of adhesive. But the deformation in the concrete normal to the NSM FRP reinforcement, which is caused by the stress transfer within the development length, also contributes to the local bond strength in adhesive layer. Blaschko (2003) carried out approximately 100 DPTs for NSM FRP strip specimens with different concrete edge distance a_r. For specimens with $a_r > 100$ mm, FRP rupture was found to be the predominant failure mode. For specimens with FRP strip embedded very close to the concrete edge (e.g., $a_r < 20$ mm), the splitting of edge concrete was observed. All the rest of specimens failed inside the adhesive layer. Both the local bond stress-slip relationship at different distance away from the loaded end and the lateral deformation of surrounding concrete were recorded during the test. It was confirmed that the local bond behavior of adhesive were affected by the lateral concrete deformation. Thereafter, a local bond strength model in the adhesive layer associated with the deformation of lateral concrete was proposed as follows:

$$\tau_f = \tau_a \left(1 + \left(0.4 \frac{v}{v_g} \right)^3 \right) e^{-\frac{v}{v_g}} \tag{3.85}$$

where τ_a = shear strength of adhesive; v = lateral deformation of concrete; and v_g = lateral deformation of concrete at which the normal stress in adhesive reaches its tensile capacity.

Based on the test results, two semi-empirical equations intended to predict the pull-out force for the cohesive failure of NSM FRP strip-to-concrete bonded joints was also proposed by Blaschko (2003) as follows:

$$P_f = d_f \tau_a \sqrt[4]{a_r} L_b \left(0.4 - 0.0015 L_b \right) \text{ for } L_b \le 115 \text{ mm} \tag{3.86}$$

$$P_f = d_f \tau_a \sqrt[4]{a_r} \left(26.2 + 0.065 \tanh\left(\frac{a_r}{70} \right) \left(L_b - 115 \right) \right) \text{ for } L_b > 115 \text{ mm} \tag{3.87}$$

where d_f = depth of NSM FRP strip; and $\alpha_r \leq 150$ mm.

Rashid et al. (2008) also conducted an experiment to investigate the concrete edge effect on the bond strength of NSM FRP in concrete. A reduction coefficient β_e was proposed to modify the pull-out force P_f of NSM FRP-to-concrete bonded joints with a sufficient edge distance, assuming no edge effect, i.e.,

$$\beta_e = 0.283\frac{a_r}{d_f} + 0.196 \leq 1 \tag{3.88}$$

In this case, for the common range of FRP strip depth from 10 to 40 mm, the critical edge distance beyond which the edge effect can be neglected is from 28.4 to 113.6 mm.

Galati and De Lorenzis (2009) also reported similar observations that for NSM FRP specimens with edge distance larger than twice the size of concrete groove, there was no reduction in bond strength compared to the control group with sufficient edge distance.

Expect for the experimental studies intended to investigate the edge effect, most DPT specimens collected in this research had a sufficient edge distance and placed the FRP reinforcement in the center line of concrete block. In this circumstance, the edge effect is not considered in this research for simplicity.

3.5.4 Failure at the FRP/adhesive or adhesive/concrete interface

Up to now, there is only one model proposed in the literature to estimate the local bond strength at either the FRP/adhesive or adhesive/concrete interface. Although Hassan and Rizkalla (2004) assumed a constant bond stress along the bond line of NSM FRP in concrete, which was not representative compared to the local bond stress-slip relationship observed in real tests, their research shed light on the bond mechanism at the FRP/adhesive or adhesive/concrete interface. That is, the mechanical interlocking provided by the lugs (surface treatments) of FRP reinforcement is believed to help transfer the stress from FRP reinforcement to the surround materials, e.g., adhesive and concrete. To balance the stress gradient of FRP reinforcement, radial stress emerges

around the FRP reinforcement to provide the friction force needed. Hence, the resultant force is inclined by an angle of friction φ with respect to the radial direction of FRP reinforcement, in which $\tan\varphi$ equals to the coefficient of friction μ at the FRP/adhesive interface (Fig. 3.7).

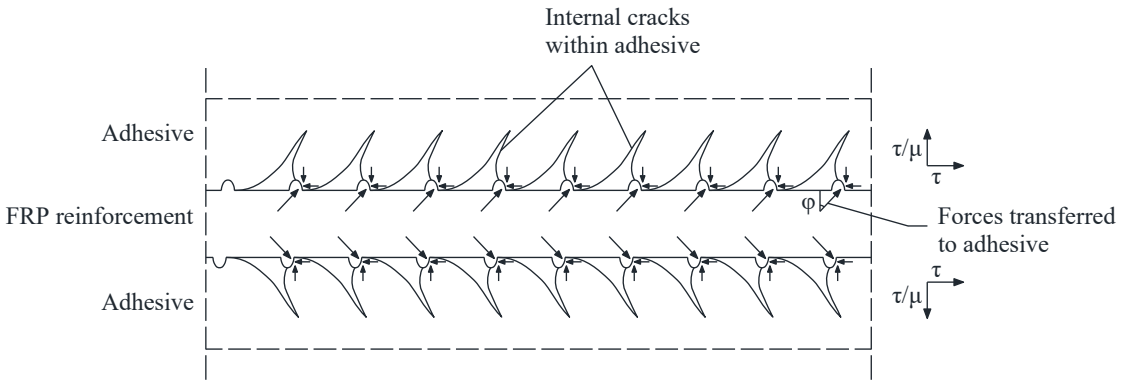

Fig. 3.7 Stress transfer from FRP reinforcement to adhesive at the FRP/adhesive interface (adapted from Hassan and Rizkalla 2004)

The radial stress applied to the surrounding adhesive creates high tensile stress zones at the FRP/adhesive interface as well as the adhesive/concrete interface. Assuming this scenario is a typical plane strain problem, a two-dimensional finite element approach (Hassan and Rizkalla 2004) was adopted to obtain the tensile stress distribution within the FRP-adhesive-concrete region in the transverse direction with respect to the longitudinal FRP reinforcement, as illustrated in Fig. 3.8.

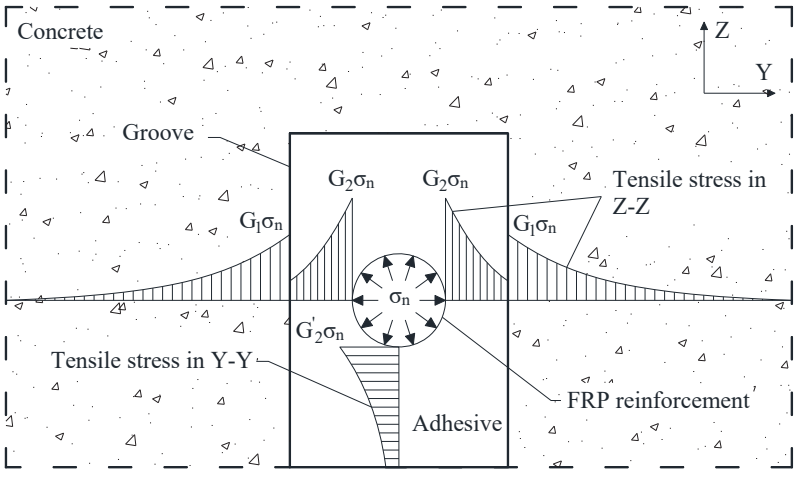

Fig. 3.8 Tensile stress distribution induced by the radial stress of FRP reinforcement (adapted from Hassan and Rizkalla 2004)

By conducting a series of 2D FE model analysis varying the groove dimensions, the material properties of adhesive and concrete, a design chart for the selection of coefficient G_1, G_2 or G_2' was obtained as Fig. 3.9. It should be noted that the elastic modular ratio n between concrete and adhesive was important to the numerical results. Increasing the stiffness of concrete increased the tensile strength at the adhesive/concrete interface. Likewise, increasing the stiffness of adhesive increased the tensile strength at the FRP/adhesive interface. To obtain the most critical situation for both interfaces, an elastic modular ratio n of 40 was used to calculate G_1, and 5 to calculate G_2 or G_2' due to the practical range of n for most cases of concrete and adhesive types (Hassan and Rizkalla 2004).

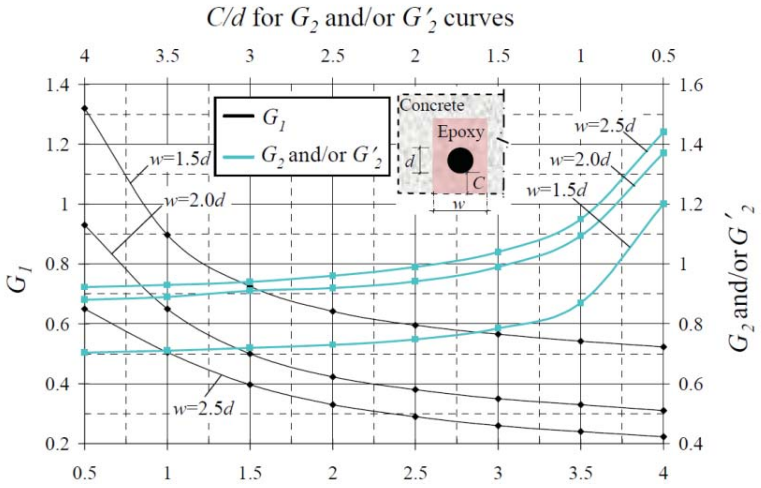

Fig. 3.9 The design char for G_1, G_2 or G_2' with various groove dimensions (Hassan and Rizkalla 2004).

If the tensile stress at the FRP/adhesive or adhesive/concrete interface reached the tensile strength of the material, the maximum allowable radial stress of FRP reinforcement was obtained which finally led to the local bond strength τ_f at the FRP/adhesive or adhesive/concrete interface as follows:

$$\tau_f = \frac{\mu f_t^a}{\mathrm{Max}\left[G_2, G_2'\right]} \quad \text{for the FRP/adhesive interface} \tag{3.89}$$

$$\tau_f = \frac{\mu f_t}{G_1} \qquad \text{for the adhesive/concrete interface} \qquad (3.90)$$

where Max [G_2, G_2'] = larger between G_2 and G_2'; μ = coefficient of friction at the FRP/adhesive interface; f_t^a = tensile strength of adhesive; and f_t = tensile strength of concrete.

However, regardless of the accuracy of the proposed model, the NSM FRP strip case had not been considered for either the FRP/adhesive or adhesive/concrete interface. De Lorenzis and Teng (2007) pointed out that the normal stress produced by FRP strip reinforcement was mostly perpendicular to the depth of strip because the strip width was very small compared to that of rod. Consequently, the vertical tensile stress applied to the surrounding adhesive was negligible, and the failure at both interfaces were less likely to happen. This also contributed to the fact that the dominant failure mode of NSM FRP strip-to-concrete bonded joints was cohesive failure in concrete (Seracino et al. 2007a; Seracino et al. 2007b; Khshain et al. 2015).

3.6 Comparison between the model prediction and DPT database

Models of load-carrying capacity summarized in this research can be assessed by using the DPT database of NSM FRP in concrete collected from the open literature up to date (De Lorenzis et al. 2004; Seracino et al. 2007a; Seracino et al. 2007b; Oehlers et al. 2008; Novidis and Pantazopoulou 2008; Galati and De Lorenzis 2009; Barros and Costa 2010; Al-Mahmoud et al. 2011; Soliman et al. 2011; Bilotta et al. 2011; Palmieri et al. 2012; Seo et al. 2013; Sharaky et al. 2013; Lee et al. 2013; Khshain et al. 2015; Torres et al. 2016). Specimen configurations and test results from 373 specimens are categorized by the different failure modes mentioned above, and the range of key parameters required to estimate the load-carrying capacity of the bonded joints are presented in Table 3.1. Analytical models introduced in the previous sections are further modified based on the DPT database corresponding to different failure modes, respectively, to enhance their accuracy to the best extent.

Table 3.1 Summary of the major parameters included in the DPT database

Number of specimens by FRP material types[a]	C	294	Number of specimens by FRP cross-section types[b]	RO	253
	G	60		ST	62
	B	19		RE	58
Bond length L_b (mm)	30-457.2		Diameter of FRP bar d_b (mm)	6-1 2.7	
Depth of FRP cross-section d_f (mm)	9.8-30.6		Width of FRP cross-section w_f (mm)	1.2-1 01.1	
Depth of groove d_g (mm)	10-50		Width of groove w_g (mm)	3.2-103.1	
Groove height-to-width ratio γ	0.13-6.59		FRP modulus of elasticity E_f (GPa)	16.5-213	
Area of FRP cross-section A_f (mm^2)	12.22-1243.28		Concrete modulus of elasticity E_c (MPa)	18527-43400	
Area of concrete block cross-section A_c (mm^2)	5625-300000		Tensile strength of FRP f_f (MPa)	746-3697	
Compressive strength of concrete f_c (MPa)	22-65.7		Tensile strength of concrete f_t (MPa)	2.2-5.4	
Tensile strength of adhesive f_t^a (MPa)	6.2-61.4		Shear strength of adhesive τ_a (MPa)	12-43	

[a]C = Carbon; G = Glass; B = Basalt; [b]RO = Round; ST = Strip (depth to width ratio larger than 5); RE = Rectangular (depth to width ratio smaller than 5).

3.6.1 FRP rupture

For the failure mode of FRP rupture, because of the discrepancies in the FRP tensile strength between the manufacturer's data and the laboratory test results, Eq. 3.76 was further modified and calibrated from the DPT database for specimens failed by FRP rupture, as follows:

$$P_f = C_1 f_f A_f + C_2 \quad \text{(N)} \tag{3.91}$$

where C_1 = 0.88 and C_2 = 1551 (N) are coefficients obtained from regression analysis. The comparison between the predicted ultimate pull-out force by Eq. 3.91 and the experiment results of DPT specimens failed by FRP rupture is shown in Fig. 3.10. It can be seen that the model agrees well with most test data, and the observed large deviations at a few data points might be caused by the scatter of FRP tensile strength.

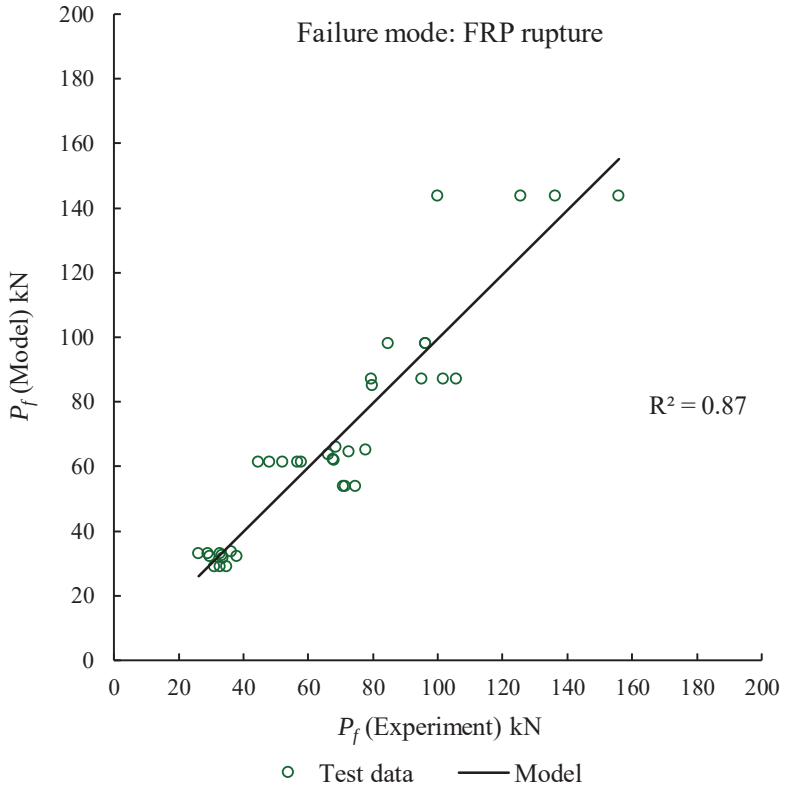

Fig. 3.10 Comparison between the model and test results for the failure mode of FRP rupture

3.6.2 Failure at the FRP/adhesive interface

Regarding the failure at the FRP/adhesive interface, the model proposed by Hassan and Rizkalla (2004) (Eq. 3.89) is adopted and further modified by considering the modular ratio n between the concrete and adhesive. A regression analysis is conducted to calibrate the coefficients needed for the modified model based on the DPT database, and the equations are obtained as follows:

$$\tau_f = \frac{\mu f_t^a}{Max\left[G_2, G_2'\right]\left(D_1 n + D_2\right)} \tag{3.92}$$

$$P_f = D_3 \tau_f L_p L_b + D_4 \quad \text{(N)} \tag{3.93}$$

where $D_1 = 0.131$, $D_2 = 0.0635$, $D_3 = 0.674$ and $D_4 = 8448$ (N) are coefficients derived from the regression analysis; L_p = perimeter of the FRP rod; μ is related to the FRP surface treatment and measured as 0.33 for smooth surface (Hassan and Rizkalla 2004), 0.39 for roughened surface, 0.52 for spirally wounded or ribbed surface, 0.63 for sand-coated surface, 0.74 for sand-coated and spirally wounded surface and infinite for grooved surface (GFRP) by an independent friction test in the laboratory (Zhang 2018). The comparison between the predicted ultimate pull-out force by Eq. 3.93 and the experiment results of DPT specimens failed at the FRP/adhesive interface is shown in Fig. 3.11. It seems that the model predictions reach a good agreement with the test data. However, due to the scatter of the FRP surface roughness, as well as the two-dimensional FE approximation used to determine G_2 and G_2', larger differences can still be observed at a higher load level.

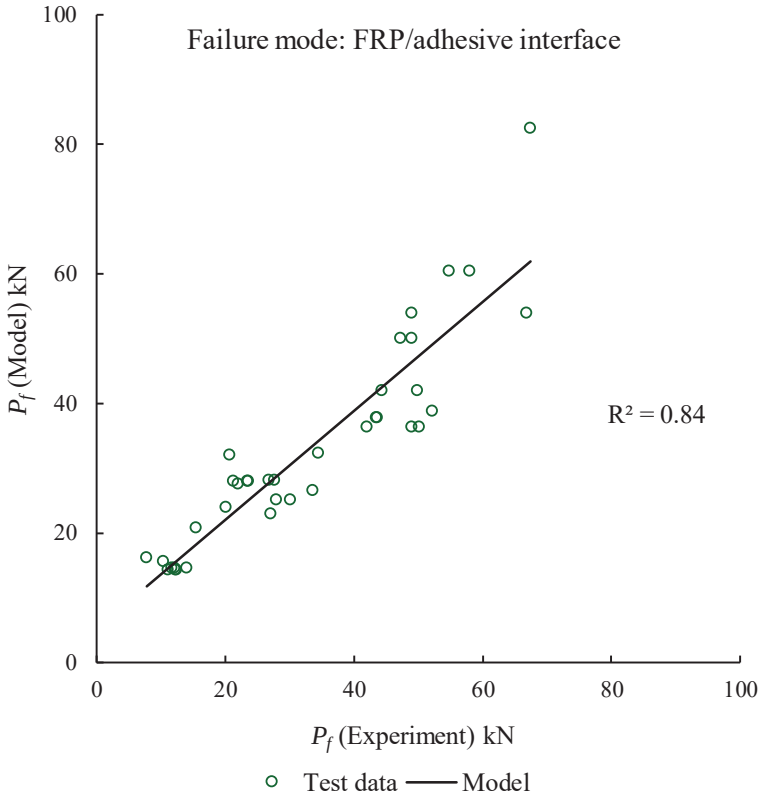

Fig. 3.11 Comparison between the model and test results for failure at the FRP/adhesive interface

3.6.3 Cohesive failure in adhesive or failure at the adhesive/concrete interface

Due to the lack of key parameters reported in the literature for the failure mode at the adhesive/concrete interface, very few specimens can be used to validate the model proposed by Hassan and Rizkalla (2004) (Eq. 3.90). Therefore, this model was not adopted by the current research. Alternatively, because of the similarity between the cohesive failure in adhesive and the failure at the adhesive/concrete interface, a semi-empirical equation to predict the pull-out force by correlating to the adhesive shear strength is proposed based on the regression analysis for both failure modes as follows:

$$P_f = E_1 \tau_a L_p L_b + E_2 \quad \text{(N)} \tag{3.94}$$

where $E_1 = 0.095$ and $E_2 = 17250$ (N) are calibrated coefficients; L_p = perimeter of the centerline between the groove and FRP reinforcement for cohesive failure in concrete; and perimeter of the

concrete groove for failure at the adhesive/concrete interface. The comparison between the predicted pull-out force by Eq. 3.94 and the experiment results of DPT specimens failed by either failure mode is presented in Fig. 3.12. This model successfully captures the trend of the test data, and it also confirms the strong correlation between the shear strength of adhesive and the pull-out force for those test specimens failed in the adhesive layer. However, the shear strength of adhesive usually refers to the manufacturer's product specification and it can fluctuate in the filed application by different extents. It contributes the larger deviation between the model and the test data as shown in the plot.

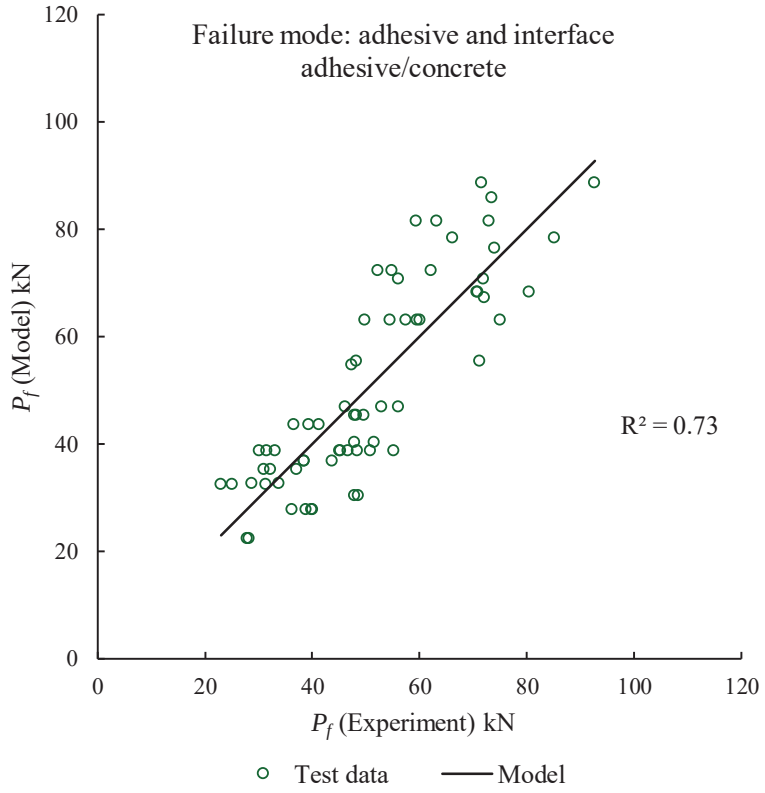

Fig. 3.12 Comparison between the model and test results for cohesive failure in adhesive or failure at the adhesive/concrete interface

3.6.4 Cohesive failure in concrete

Lastly, the local bond strength and the maximum slip model proposed by Oehlers et al. (2008) (Eq. 3.80 and Eq. 3.81) and the model proposed by Zhang et al. (2013) (Eq. 3.83 and Eq. 3.84) in conjunction with Eq. 3.75 are evaluated using the experiment results of DPT specimens failed in concrete. To take into account of the effect due to bond length L_b, a reduction factor β_L is proposed as follows:

$$\beta_L = \frac{L_b}{L_{eff}} \leq 1 \tag{3.95}$$

where L_{eff} = effective bond length described in Eq. 3.46.

In addition, the model proposed by Zhang et al. (2013) (Eq. 3.83 and Eq. 3.84) is slightly modified to consider the contribution from the adhesive cover, similar to the modification made by Oehlers et al. (2008) to the model by Seracino et al. (2007a). Thus, the updated model by Zhang et al.'s (2013) can be expressed as:

$$\tau_f = 1.15\gamma^{0.138} f_c^{0.613} \left(\frac{d_c + d_g}{d_g} \right)^{0.65} \tag{3.96}$$

$$\delta_f = 0.7\gamma^{0.284} f_c^{0.006} \left(\frac{d_c + d_g}{d_g} \right)^{0.55} \tag{3.97}$$

Accordingly, the model to estimate the load-carrying capacity of NSM FRP specimen failed in concrete is derived as follows:

$$P_f = \beta_L \sqrt{L_p \tau_f \delta_f \Big/ \left(1/A_f E_f + 1/A_c E_c \right)} \tag{3.98}$$

The comparison between the predicted pull-out force using Oehlers et al.'s (2008) model (Eq. 3.80 and Eq. 3.81] or the modified model based on Zhang et al.'s (2013) (Eq. 3.96 and Eq. 3.97) and the experiment results of DPT specimens failed in concrete is displayed in Fig. 3.13 and Fig. 3.14, respectively It is evident that the analytical estimation based on the local bond strength and the maximum slip model proposed by Zhang et al. (2013) reaches a better agreement with the

experimental data. As a result, the modified Zhang et al.'s (2013) model is further selected to predict the load-carrying capacity of NSM FRP specimen expected to fail in concrete.

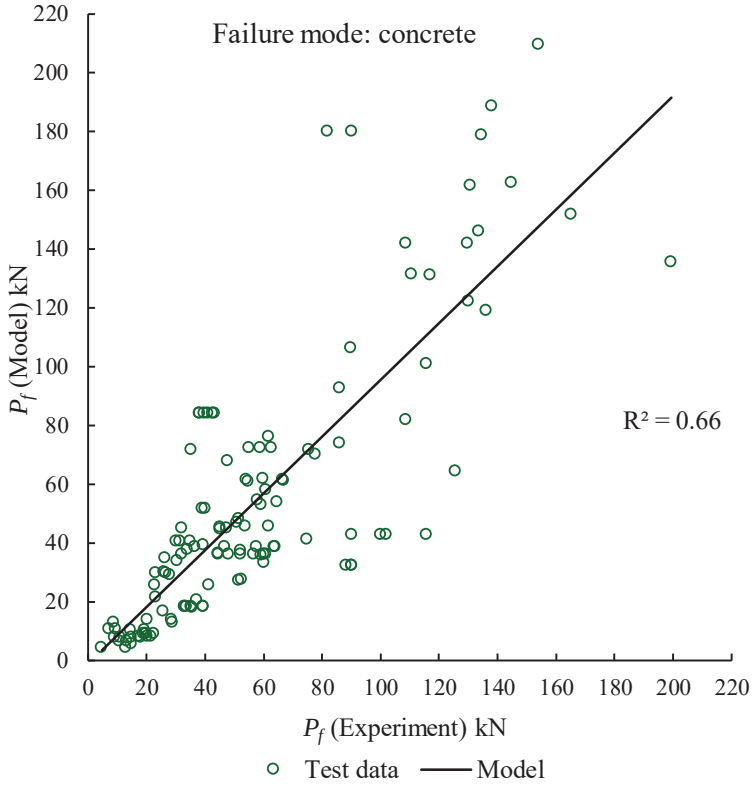

Fig. 3.13 Comparison between the model and test results for cohesive failure in concrete by using Oehlers et al.'s (2008) model

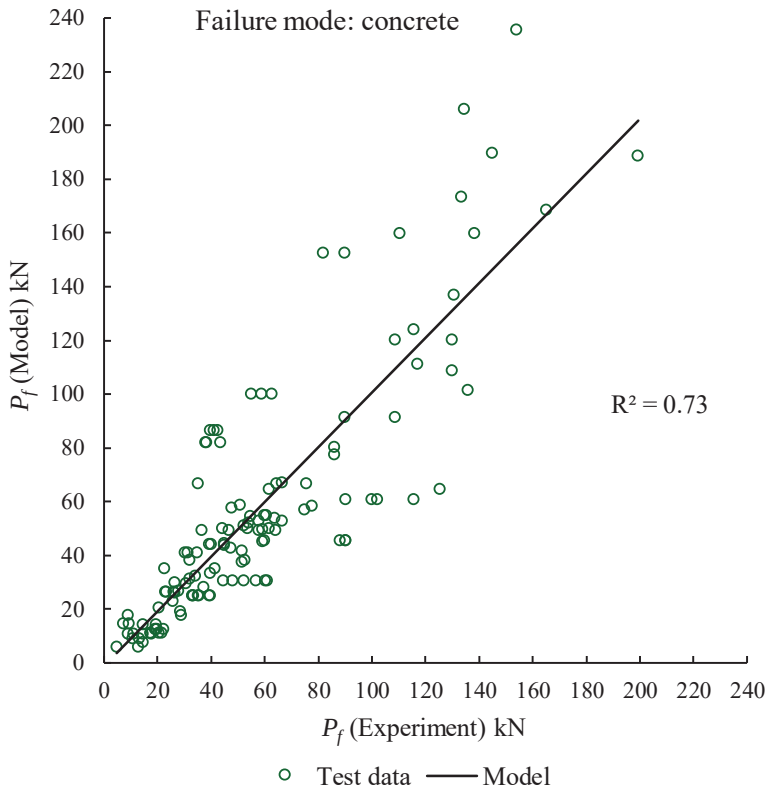

Fig. 3.14 Comparison between the model and test results for cohesive failure in concrete by using Zhang et al.'s (2013) model

3.6.5 Prediction of bond strength and failure mode

Models proposed in the open literature and further modified based on the categorized NSM DPT database corresponding to various failure modes are assessed using the existing experimental data. The predicted pull-out forces are calculated with respect to each of the five different failure modes, using Eq. 3.91 for FRP rupture, Eq. 3.93 for failure at the FRP/adhesive interface, Eq. 3.94 for cohesive failure in adhesive or failure at the adhesive/concrete interface, and Eq. 3.98 for cohesive failure in concrete with the provided geometry and material parameters, respectively. The smallest pull-out force predicted by the five different models becomes the one that governs the load-carrying capacity of the NSM FRP-to-concrete bonded joints, along with the associated failure mode. The comparison between the model prediction and the experimental data of all NSM DPT

specimens in the database is presented in Fig. 3.15. The accuracy of predicted failure mode compared to the observed failure mode in experiment is approximately 60%, as summarized in Table 3.2. It should be noted that only 342 specimens are included in Table 3.2 for the failure mode prediction due to the lack of test information of other specimens.

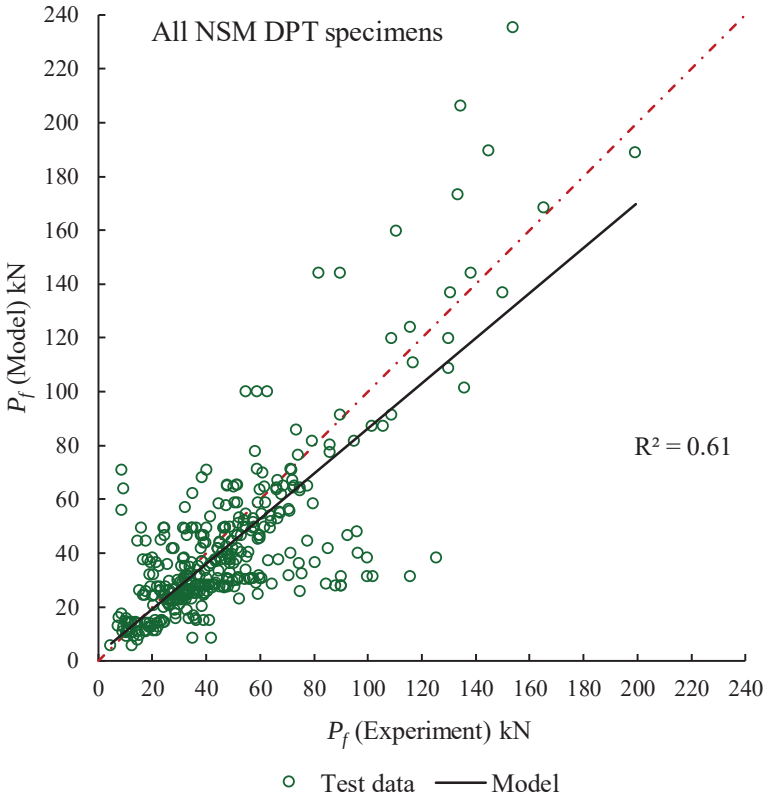

Fig. 3.15 Comparison between the model and test results for all NSM DPT specimens

Table 3.2 Summary of predicted failure modes vs. the experiment results

Failure mode[a]	FRP	F/A	Adhesive	A/C	Concrete
Number of specimens (Model)	14	38	53	26	211
Number of specimens (Experiment)	29	78	59	45	131

[a]FRP = FRP rupture; F/A = failure at the FRP/adhesive interface; Adhesive = cohesive failure in adhesive; A/C = failure at the adhesive/concrete interface; Concrete = cohesive failure in concrete.

It can be seen that the modified models in this study capture the overall trend of the behavior according to the comparison with the test data, however, the reliability is still not satisfactory. In addition, the predicted load-carrying capacity is conservative to some extent because the trend line is below the diagonal dashed line, which represents the equivalent boundary between the model predictions and the experimental data. The accuracy of predicting the failure mode of NSM FRP in concrete under pull-out force is relatively low, which could be partially due to the lack of some key material properties of the test specimens, e.g., shear strength of adhesive, accurate coefficient of friction of FRP reinforcement, as well as the small database regarding different failure modes except for the cohesive failure in concrete.

3.7 Summary

The analytical model to understand the bond behavior of NSM FRP-to-concrete bonded joints is presented in this chapter, along with the governing equations and solutions based on the local bond stress-slip relationship. Representative linear and nonlinear local bond stress-slip models from the literature are summarized herein. Based on the bilinear local bond stress-slip relationship, the theoretical bond behavior of the NSM FRP-to-concrete bonded joints under applied load is predicted using the analytical solutions of the distribution of relative slip, local bond stress and axial stress of FRP reinforcement along the bond line at different development stages. Theoretical equations of the effective bond length, load-carrying capacity of the NSM bonded joints are derived as well, which form the basis to predict the ultimate pull-out forces with respect to different failure modes.

Based on the existing literature, no systematic strategy has been proposed to predict the failure mode of NSM FRP-to-concrete bonded joints under applied load. Semi-empirical models have been developed to estimate the bond capacities with respect to the cohesive failure in adhesive, cohesive failure in concrete, failure at the FRP/adhesive or adhesive/concrete interface. A comprehensive NSM DPT database categorized by different failure modes is collected from the literature to further modify the existing prediction models. All the modified models based on

regression analyses from the categorized DPT database present good agreement with the experiment results to some extent yet not perfect.

These modified models are then used to estimate the load-carrying capacities of the DPT specimens in the database. The minimum ultimate pull-out force among the predicted results using these models is determined as the governing load-carrying capacity and is further compared with the test result. The comparison validates the method proposed by this research as the model captures the overall trend of the behavior on the collected NSM DPT data. However, the deviation between model predictions and the experimental data is still relatively large and the accuracy to predict the failure mode is not satisfactory. Many factors can be counted to result in such condition and some measures should be taken into account to further improve the reliability of the model.

- Although the coefficient of friction μ at the FRP/adhesive interface was experimentally obtained in this study via an independent friction test in the laboratory, the type of FRP surface treatment tested could not represent all the available products on the market. The roughness and quality of the FRP surface treatment could also vary from batch to batch let alone the different production technique adopted by different manufactures. If the manufacturer could provide a quantified roughness of FRP surface treatment, e.g., coefficient of friction μ, the reliability of the model will be improved with no doubt;
- The model for the failure at the FRP/adhesive interface derived from the 2D finite element method is only applicable to FRP rod. Although such a failure mode is less common for FRP strip or rectangular cross-section (likely due to the different normal stress distribution pattern compared to FRP rod), a more rigorous theoretical background is needed to verify this phenomenon;
- The shear strength of adhesive is vital to predict the bond strength of specimen failed in adhesive or at the adhesive/concrete interface. However, for most NSM FRP direct pull-out tests, only the tensile and compressive strengths of the adhesives are available in the open literature. Although some manufacturers provide the shear strength of their adhesive products,

only a minimum value is recommended in their product specification instead of the typical average value, which leads to a larger deviation of the bond strength predicted by the models;

- The local bond strength models for the cohesive failure in concrete are originally developed for NSM FRP strip case and the coefficients used in these models are calibrated from the DPT specimens using FRP strips. Consequently, the prediction of the load-carrying capacity for specimens using FRP rods via these two models could be inappropriate to some extent. To validate the reliability for the FRP rod case, the database of specimens using NSM FRP rods failed by cohesive failure in concrete should be extended;
- The categorization of the failure modes for NSM DPT specimens is important yet has rarely been discussed by researchers. In laboratory experiments, a mixed failure mode is very common, e.g., splitting cracks occurs in adhesive, localized crash of concrete and partial debonding of FRP reinforcement at the loaded end, etc. This phenomenon complicates the decision for a major failure mode. In some cases, a partial failure mode is even less likely to be discovered without cutting the specimen open for post-failure inspection such as the failure at the adhesive/concrete interface. Thus, a better methodology should be employed to detect and differentiate these failure modes;
- The bilinear local bond stress-slip relationship adopted in this study is a conservative model since it neglects the mechanical friction between the two debonding layers when the local debonding occurs at interfaces. Although the trilinear model introduced in section 3.3 considers the post-debonding stage, no experiment so far has accurately measured such a residual bond strength within the debonding region of NSM FRP-to-concrete bonded joints. This requires a well-designed experimental study to validate the reliability of the trilinear model.

CHAPTER FOUR

4 BOND CHARACTERISTICS OF NSM CFRP IN CONCRETE UNDER FATIGUE LOADING

4.1 Overview

This chapter focuses on the fatigue bond performance of various NSM CFRP in concrete using the direct pull-out (DPT) test. A total number of 84 concrete joint specimens from 28 sets, with three identical specimens per set, were tested by a single shear, compressive DPT configuration. The dimension of the concrete block was designed as 350 mm in length, 300 mm in width and 150 mm in depth. Among the 28 specimen sets, 8 sets were static counterparts under the monotonic loading, where they were loaded up to failure to obtain their static load-carrying capacity. The other 20 fatigue specimen sets were tested under a sinusoidal waveform cyclic load range of 10-50%, 10-60% or 10-70% of their corresponding static ultimate pull-out capacity. Investigated in this part of the study was the effect on the bond strength and local bond characteristics due to different cross-sectional shape (rod vs. strip), surface treatment of NSM reinforcement (roughened, sand-coated, sand-coated and spirally wound), adhesive type, concrete strength, and fatigue load range. The behavior of the bond degradation at the interfaces for both the CFRP strip and rod specimens were measured by strain gauges during the fatigue cycles. Empirical models were proposed using the test data accordingly to correlate the local bond strength to the number of fatigue cycles.

4.2 Experimental program

4.2.1 Material properties

Two batches of normal weight concrete were cast with different mix proportion for different targeted concrete strengths, as described in Table 4.1. The mixing proportion of the concrete by weight (cement: fly ash: sand: coarse aggregate: water) is 1: 0.17: 2.57: 3.46: 0.53 for the first batch

of concrete (N) and 1: 0: 1.81: 2.81: 0.5 for the second batch (H), respectively. The first batch was commercial ready-mix concrete ordered in a large quantity while the second batch adopted a smaller size coarse aggregate in conjunction with a lower water-cement ratio targeting a higher compressive strength. The compressive and splitting tensile strength for the first batch of concrete on the day of static DPT was obtained as 46.45 MPa (with a standard deviation of 1.03 MPa) and 2.51 MPa (with a standard deviation of 0.45 MPa) per ASTM C39/C39M (ASTM 2017) and ASTM C496/C496M (ASTM 2017), respectively. This compressive strength was higher than the targeted design level of the order (i.e., 31 MPa at 28-day), as illustrated in Fig. 4.1 with a 7-day interval of concrete strength growth. The strength for the second batch of the concrete was not able to reach a much higher level than that of the first batch due to the use of a lower efficiency mixer on the small quantity needed for the number of specimens in its category. Therefore, the compressive strength was 52.31 MPa (with a standard deviation of 6.1 MPa) and the splitting tensile strength was 2.72 MPa (with a standard deviation of 0.43 MPa), only 12.6% and 8.4% higher than that of the first batch, respectively. Likewise, the average compressive and splitting tensile concrete strength over the 7.5-month fatigue testing period was 45.02 MPa (with a standard deviation of 1.63 MPa) and 2.07 MPa (with a standard deviation of 0.44 MPa) for the first batch of concrete, and 49.11 MPa (with a standard deviation of 6.13 MPa) and 2.64 MPa (with a standard deviation of 0.33 MPa) for the second batch.

Table 4.1 Mix proportions and material properties of concrete

Batch	Mix proportion[a] C: FA: S: CA: W	At 28-day		On the day of test	
		Compressive strength (MPa)	Tensile strength (MPa)	Compressive strength (MPa)	Tensile strength (MPa)
First[b]	1: 0.17: 2.57: 3.46: 0.53	39.1 (2.24)[d]	2.08 (0.50)	46.5 (1.03)	2.51 (0.45)
Second[c]	1: 0: 1.81: 2.81: 0.5	41.8 (2.15)	NA[e]	52.3 (6.1)	2.72 (0.43)

[a]C = cement; FA = fly ash; S = sand; CA = coarse aggregate; W = water;
[b]Coarse aggregates with a maximum dimension of 25 mm were used;
[c]Coarse aggregate with a maximum dimension of 10 mm were used;
[d]Average value of 3 samples (standard deviation); and
[e]Not available due to improper loading rate.

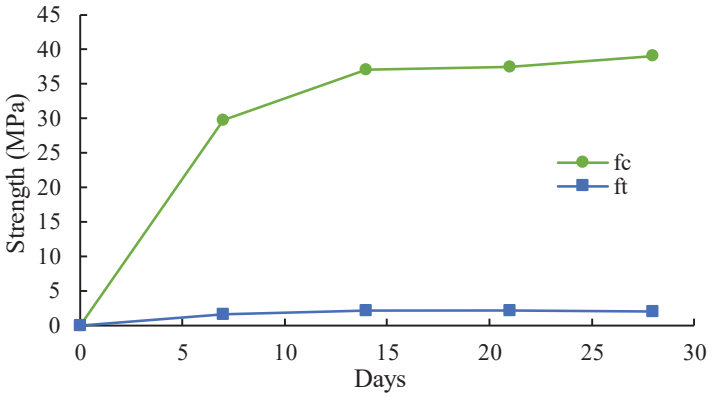

Fig. 4.1 Concrete strength development for the first batch of concrete during the 28 days

As illustrated in Fig. 4.2, four different types of NSM CFRP reinforcement were used: CFRP strip with roughened surface (S-RO), CFRP rod with roughened or textured surface (R-RO), CFRP rod with sand-coated surface (R-SC), and CFRP rod with sand-coated and spirally wound surface (R-SCSW). These selected types represent the commonly used ones for surface treatment and cross-sectional shape in the market for NSM CFRP reinforcements. The tensile strength and elastic modulus of these NSM CFRP reinforcements were obtained experimentally per ASTM D7205/D7205M (ASTM 2016), and the properties are listed in Table 4.2 based on the average of three specimens per set. Generally, rupture of FRP reinforcement should be expected as the failure mode in FRP tensile test, and yet delamination of CFRP was observed simultaneously with the initiation of carbon fiber rupture for tested R-SC specimens and led to a premature failure.

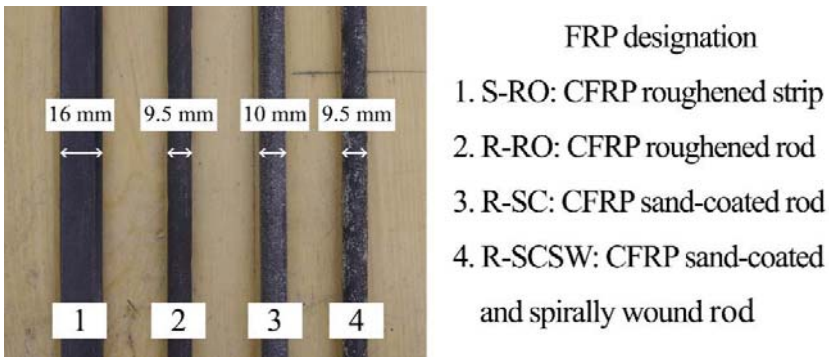

Fig. 4.2 Four types of CFRP reinforcement for DPT

Table 4.2 Material properties of CFRP reinforcement

FRP designation[a]	Dimension[b] (mm)	Cross-sectional area (mm^2)	Perimeter-to-area ratio	Elastic modulus (GPa)	Tensile strength (MPa)	Ultimate tensile strain (%)	Source
S-RO	16×4.5	71.26	0.57	124	2172	1.75	MFR[c]
				168	2532 (61.51[c])	1.51	LAB[d]
R-RO	9.5	71.26	0.42	124	2172	1.75	MFR
				117	1617	1.38	LAB
R-SC	10	78.54	0.40	130	2300	1.77	MFR
				113	1489 (160.02)	1.32	LAB
R-SCSW	9.5	71.26	0.42	124	2172 (83.63)	1.75	MFR
				129	2372	1.84	LAB

[a]The same labeling scheme as aforementioned in Fig. 4.2;
[b]Width and thickness for CFRP strip and diameter for CFRP rod;
[c]Standard deviation except for CFRP reinforcement R-RO since the data is extracted from Lee et al. (2013);
[d]Manufacturer's data; and
[e]Laboratory testing results.

In addition, four types of typical epoxy resin-based adhesives were selected to investigate their influence on the fatigue bond behavior of NSM FRP-to-concrete joints. To minimize the possible premature debonding at adhesive layer, these four epoxy adhesives all have high shear (bond) strength: A1 (Pilgrim-Magmaflow Grout-Pak CF), A2 (Sikadur-32 Hi-Mod), A3 (Simpson-ETI-GV), and A4 (BASF-MasterEmaco ADH 327) with the mechanical properties summarized in Table 3 according to manufacturers' data. It should be noted that A1 is the only three-component epoxy resin with properly graded sand added, i.e., component C (aggregate), while the rest is the typical two-component epoxy resin, i.e., component A (resin) and component B (curing agent). Furthermore, the provided adhesive properties are obtained by following the corresponding instructions, i.e., mix proportions and speed, and tested per different ASTM standards, and sensitive to curing time and environmental temperature. Thus, the deviation of adhesive properties is inevitable in the field application, and the data presented in Table 4.3 is for reference purpose only.

Table 4.3 Material properties of epoxy adhesives

Label	Name	Shear strength (MPa)	Tensile strength (MPa)	Compressive strength (MPa)	Young's modulus (MPa)
A1	Pilgrim-Magmaflow Grout-Pak CF	52.4	14.8	122	12411
A2	Sikadur-32 Hi-Mod	43	48	81.4	1449
A3	Simpson-ETI-GV	27.54	Not available	80	2779
A4	BASF-MasterEmaco ADH 327	34.5	13.8	55.2	2800

4.2.2 Concrete specimen

A total of 84 concrete blocks in 28 sets (3 identical specimens per set) were cast, each with the dimensions of 350 mm in length, 300 mm in width and 150 mm in depth. These dimensions were selected to be the same as the specimen size in several relevant studies in the existing literature for consistency (Seracino et al. 2007a; Lee et al. 2013; Chen and Cheng 2015). The width of 300mm was also considered to be sufficient to prevent concrete edge effect (Blaschko 2003). Plywood formworks were constructed to cast both two batches of concrete in the lab, as presented in Fig. 4.3.

(a) Plywood formworks (b) Normal weight concrete (c) Higher strength concrete

Fig. 4.3 Concrete casting for two batches of concrete blocks

Grooves were first cut on the top surface of the concrete specimens using diamond blade cutting saw and then cleaned thoroughly using pressure washer and compressed air before the embedment of the NSM CFRP reinforcement. The size of the grooves was set as 15 mm in width and 25 mm in depth for CFRP strips, and 20 mm in both width and depth for CFRP rods by following the recommendations of previous studies (Al-Mahmoud et al. 2011; Lee and Cheng 2013), as illustrated in Fig. 4.4(a). The grooves were cut along the entire length of the concrete

blocks but only the middle 250 mm region was filled with adhesive for the bond length. This 250 mm bond length was selected to ensure the full development of the bond strength along the bond length so as to maximize the utilization of CFRP reinforcement (Lee et al. 2013; Chen and Cheng 2015). The remaining 50 mm unbonded region (without adhesive) at each end of the groove was created using rubber putty tapes to prevent the potential edge effect of the concrete block.

The testing parameters in this study included: (1) cross-sectional shape of NSM CFRP reinforcement of round for rod (R) and rectangular for strip (S); (2) CFRP surface treatment of roughened or textured (RO), sand-coated (SC), sand-coated and spirally wound (SCSW); (3) epoxy adhesive type of Pilgrim-Magmaflow Grout-Pak CF (A1), Sikadur-32 Hi-Mod (A2), Simpson-ETI-GV (A3) and BASF-MasterEmaco ADH 327 (A4); (4) fatigue load range of 10-50%, 10-60% and 10-70% of the corresponding static load-carrying capacity; (5) number of fatigue cycles of 10, 100, 1000 and 10,000 or fatigue failure (F); and (6) concrete strength from the first batch (N) and the second batch (H). This exact sequence was then followed in designating the specimens in the test. For example, specimen set R-SCSW-A1-N was tested monotonically to failure, it represents the specimens using sand-coated and spirally wound CFRP rod, adhesive type A1 and normal weight concrete (the first batch). Likewise, specimen set S-RO-A1-1060-1E3-N was tested under fatigue load, it represents the specimens using roughened CFRP strip, adhesive type A1 and normal weight concrete (the first batch), undergoing fatigue load range of 10-60% of the corresponding static capacity (ultimate pull-out force of S-RO-A1-N) up to 1000 cycles. The testing matrix of the 84 specimens is presented in Table 4.4, in which specimen Sets 12-15 and 23-26 aimed to measure the fatigue degradation of local bond strength while other sets focused on the different parameters as described above.

Table 4.4 Testing matrix of NSM FRP DPT specimens under both static and fatigue load

Set	Type	Designation	Surface treatment	Adhesive	Concrete	Fatigue load range (%)	Fatigue cycles
1	Static	R-RO-A1-N	Roughened	A1	1st batch	-	-
2		R-SC-A1-N	Sand-coated	A1	1st batch	-	-
3		R-SCSW-A1-N	Sand-coated and spirally wound	A1	1st batch	-	-
4		S-RO-A1-N	Roughened	A1	1st batch	-	-
5		S-RO-A2-N	Roughened	A2	1st batch	-	-
6		S-RO-A3-N	Roughened	A3	1st batch	-	-
7		S-RO-A4-N	Roughened	A4	1st batch	-	-
8		S-RO-A1-H	Roughened	A1	2nd batch	-	-
9	Fatigue	R-RO-A1-1060-F-N	Roughened	A1	1st batch	10-60	Failure
10		R-SC-A1-1060-F-N	Sand-coated	A1	1st batch	10-60	Failure
11		R-SCSW-A1-1060-F-N	Sand-coated and spirally wound	A1	1st batch	10-60	Failure
12		R-SCSW-A1-1060-1E1-N	Sand-coated and spirally wound	A1	1st batch	10-60	10
13		R-SCSW-A1-1060-1E2-N	Sand-coated and spirally wound	A1	1st batch	10-60	100
14		R-SCSW-A1-1060-1E3-N	Sand-coated and spirally wound	A1	1st batch	10-60	1000
15		R-SCSW-A1-1060-1E4-N	Sand-coated and spirally wound	A1	1st batch	10-60	10,000
16		R-SCSW-A1-1050-F-N	Sand-coated and spirally wound	A1	1st batch	10-50	Failure
17		R-SCSW-A1-1070-F-N	Sand-coated and spirally wound	A1	1st batch	10-70	Failure
18		S-RO-A1-1060-F-N	Roughened	A1	1st batch	10-60	Failure
19		S-RO-A2-1060-F-N	Roughened	A2	1st batch	10-60	Failure
20		S-RO-A3-1060-F-N	Roughened	A3	1st batch	10-60	Failure
21		S-RO-A4-1060-F-N	Roughened	A4	1st batch	10-60	Failure
22		S-RO-A1-1060-F-H	Roughened	A1	2nd batch	10-60	Failure
23		S-RO-A1-1060-1E1-N	Roughened	A1	1st batch	10-60	10
24		S-RO-A1-1060-1E2-N	Roughened	A1	1st batch	10-60	100
25		S-RO-A1-1060-1E3-N	Roughened	A1	1st batch	10-60	1000
26		S-RO-A1-1060-1E4-N	Roughened	A1	1st batch	10-60	10,000
27		S-RO-A1-1050-F-N	Roughened	A1	1st batch	10-50	Failure
28		S-RO-A1-1070-F-N	Roughened	A1	1st batch	10-70	Failure

4.2.3 Test preparation

Five foil strain gauges, with a gauge length of 5 mm, were installed on the surface of each CFRP reinforcement with a constant interval of 50 mm to measure the strain distribution of CFRP within the bonded region during the test [Fig. 4.4(b)]. No strain gauge was installed at the free end due to the commonly adopted zero-strain assumption at the free end (Sharaky et al. 2013; Chen and Cheng 2016). Standard procedures had been followed to install the strain gauges on the CFRP surface per user's manual and a thin layer of wax protection was brushed on top of strain gauge to ensure its proper functioning after the CFRP reinforcement were embedded into the groove. The least wax protection also mitigates the influence of strain gauges on the surface characteristics of CFRP reinforcement.

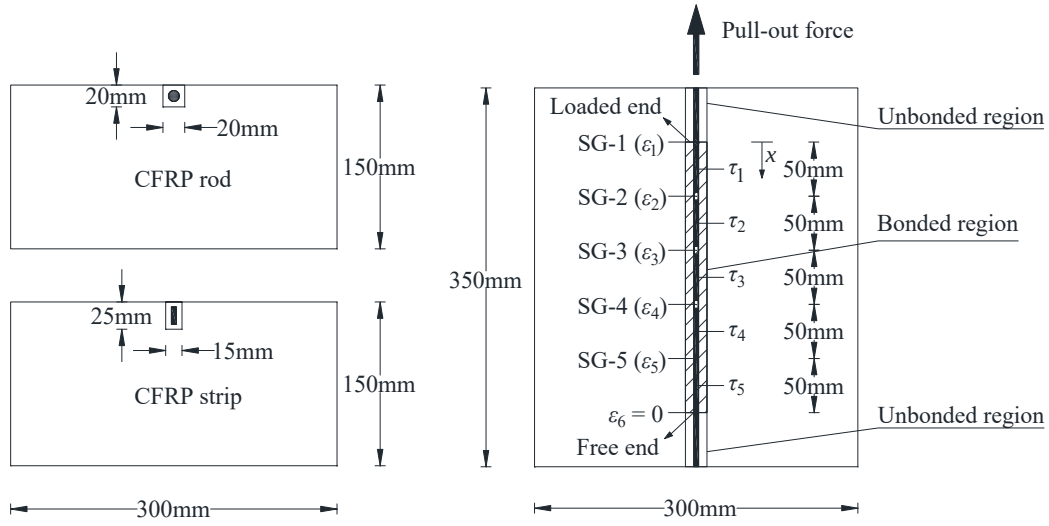

(a) Cross-section and groove dimension (b) Strain gauges distribution

Fig. 4.4 Concrete specimen configuration

To avoid potential slippage in the grip using steel jaw during the DPT, the free end of the NSM reinforcement was inserted into a steel tube, 600 mm long schedule 40 steel tube (sleeve) with an outside diameter of 26.7 mm and wall thickness of 2.87 mm, filled with epoxy adhesives. That free end of NSM rod or strip was further treated by cutting indentations on the surface prior to the installation to prevent the undesired slippage of NSM near the grip during the direct pull-out.

Due to the low surface friction of the NSM strip, a sand-coating layer was also applied onto the surface of the strip at the gripping end in addition to the surface indentation. These additional preparation measures were based on the trial-and-error experience of the sample tests in the laboratory. The concrete groove was carefully washed out with no aggregate debris or dust and further dried out by compressed air to prevent the potential debonding at the interface between adhesive and concrete. Once the filling material of the steel tube was fully cured, the other end of CFRP reinforcement was placed into the groove. Rubber putty tapes were then used to separate the unbonded region of the groove and hold the CFRP reinforcement centered and level for adhesive casting. Different types of epoxy adhesives were mixed by following the product specifications and poured into the grooves of designated concrete blocks with caution. Once the epoxy adhesives were fully cured, specimens were set up under the hydraulic testing machine with the designed configuration to conduct the direct pull-out test.

4.2.4 Test setup

During the DPT, the end of the NSM reinforcement with the steel tube was firmly clamped by the steel jaw, which was connected to the hydraulic head with a built-in load-cell (Fig. 4.5). Two pairs of steel channel plates were fixed on the loading frame, serving as the reaction beam for the concrete specimen hanging below. A thick steel plate and a rubber pad were placed underneath the steel channel plates to evenly distribute the compression load from the reaction beam to the concrete block. As illustrated in Fig. 4.6(a), a pair of push bolts were installed on both the front and back side of the concrete block to balance the moment produced by the eccentric single shear pull-out force on one side, maintaining the specimen vertical throughout the entire test. One linear potentiometer (LP) was mounted at the bottom of concrete block via an aluminum frame to capture the relative displacement between the concrete block and CFRP reinforcement at the free end [Fig. 4.6(b)]. The aluminum frame was fastened to the concrete block moving together with the block to alleviate any potential reading error in the LP for direct measurement. Experimental data

including load, displacement and strain were collected simultaneously using a National Instruments data acquisition system with the LabVIEW software, and the sampling rate was set as 200 Hz for all the data channels.

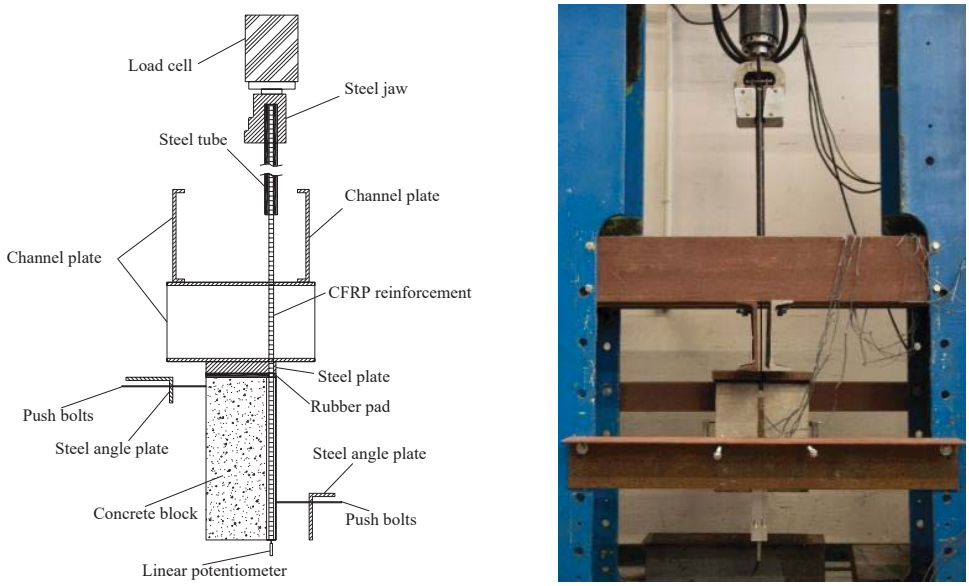

(a) Design illustration (b) Frontal image

Fig. 4.5 Test setup configuration

Among the 28 sets of DPT concrete specimens, the first 8 sets were tested monotonically prior to the fatigue test on the remaining 20 sets (Table 4.4). For the static test, specimens were loaded monotonically until failure under the displacement-control mode using a constant loading rate of 0.02 mm/s to obtain their static capacity, which was used to determine the load range for the subsequent fatigue test. For example, specimen set S-RO-A2-N is the static counterpart of set S-RO-A2-1060-F-N, and set R-RO-A1-N is the static counterpart of set R-RO-A1-1060-F-N. For the fatigue test, a sinusoidal waveform loading profile at a frequency of 2 Hz was used under the load-control mode for safety considerations. This frequency was adopted according to many existing researches on direct pull-out tests using either EB or NSM reinforcement (e.g., Yun et al. 2008; Iwashita et al 2007; Fernandes et al. 2015). To assess the local bond deterioration under fatigue, a load range of 10-60% of the corresponding static capacity was mainly adopted,

representing a typical strain level experienced in bridge structures (Wang and Belarbi 2010; Wahab et al. 2012; Yun et al. 2008; Al-Saadi and Al-Mahaidi 2016). Different load range of 10-50% or 10-70% was also applied to both CFRP rod and strip specimens as well to explore their influence on the local bond behavior. For fatigue specimens, since no significant deterioration was actually observed in many of those specimens up to one million cycles, the upper limit of the fatigue test was set to be one million cycles considering the time constraint and the large number of fatigue specimens in this study. In other words, if a specimen did not experience significant deterioration after one million fatigue cycles, the fatigue loading was terminated followed by a post-fatigue direct pull-out test on the same specimen for the remaining capacity. Likewise, for specimens designed to be loaded up to an expected number of fatigue cycles, i.e., specimen Sets 12-15 and 23-26, the post-fatigue test was conducted at the target number of cycles and the post-fatigue local bond behavior was recorded to derive the degradation law.

(a) Push bolts and aluminum frame (b) LP at the free end

Fig. 4.6 Push bolts and LP setup for the test specimen

4.3 Test observation and results

4.3.1 Test observation

Static

The specimen sets using CFRP rods (Sets 1-3 in Table 4.5) and the sets using roughened CFRP strip (Sets 4-8 in Table 4.5) showed noticeable differences in both the failure mode and the

pull-out force under the monotonic load. The CFRP rod specimens, with roughened (RO), or sand-coated (SC) or sand-coated and spirally wound (SCSW) surface treatment, failed predominately in the concrete substrate followed by the breakage and splitting of the epoxy adhesive (CEB+ES) to different extents (Fig. 4.7). Visible concrete cracks initiated near the adhesive at the loaded end at approximately 50-60% of the ultimate pull-out force. As the load increased, the crack propagated from the surrounding concrete into the epoxy adhesive in the direction perpendicular to the groove. Meanwhile, the concrete crack also propagated longitudinally toward the free end on both sides of the groove, along with the splitting developing on the top surface of the epoxy. The specimen failed abruptly with a loud explosive noise with small pieces of concrete spalling off. Among all the three sets of concrete specimens using CFRP rods, specimen set R-SCSW-A1-N (Set 3) reached the highest average pull-out force of 78.54kN, followed by set R-RO-A1-N (Set 1) with 77.69kN and set R-SC-A1-N (Set 2) with 70.54kN. In addition, the severity of the concrete breakage and epoxy splitting varied from set to set, among which the ones using SCSW rods experienced the most concrete and epoxy cover spalling on top of the CFRP reinforcement [Fig. 4.7(a)] while the ones using RO rods had minor concrete spalling [Fig. 4.7(b)]. In comparison, the specimen set using SC rods experienced the least amount of concrete cracking but more localized to the loaded end, as shown in Fig. 4.7(c). Based on the results, the sand-coated and spirally wound (SCSW) treatment prevailed over the roughened (RO) and sand-coated (SC) treatment as expected. Regardless of these slight differences, these three surface conditions all presented favorable bond efficiency with an average pull-out force close to each other.

Table 4.5 Direct pull-out test results for monotonic loading case

Set	ID	Pull-out force P_f (kN)		Average bond strength τ_{avg} (MPa)		Local bond strength τ_f (MPa)		Failure mode[a]
		Value	Average	Value	Average	Value	Average	
1	R-RO-A1-N-1	81.10	77.69	10.87	10.41	13.76	13.18	CEB+ES
	R-RO-A1-N-2	81.26		10.89		12.40		CEB+ES
	R-RO-A1-N-3	70.72		9.48		13.38		CEB+ES
2	R-SC-A1-N-1	66.27	70.54	8.44	8.98	15.86	16.61	CEB
	R-SC-A1-N-2	70.27		8.95		15.96		CEB
	R-SC-A1-N-3	75.08		9.56		18.01		CEB+ES
3	R-SCSW-A1-N-1	64.81	78.54	8.69	10.53	15.76	17.30	CEB+ES

	R-SCSW-A1-N-2	90.39		12.11		17.43		CEB+ES
	R-SCSW-A1-N-3	80.42		10.78		18.70		CEB+ES
4	S-RO-A1-N-1	51.62	54.39	5.04	5.31	10.31	10.42	F/A
	S-RO-A1-N-2	62.92		6.14		10.88		F/A
	S-RO-A1-N-3	48.62		4.74		10.07		F/A
5	S-RO-A2-N-1	50.40	52.91	4.92	5.16	13.71	11.35	F/A
	S-RO-A2-N-2	34.11		3.33		8.94		F/A
	S-RO-A2-N-3	74.22		7.24		11.41		F/A+CEB
6	S-RO-A3-N-1	46.18	34.10	4.51	3.33	7.36	5.77	F/A
	S-RO-A3-N-2	22.80		2.22		4.27		F/A
	S-RO-A3-N-3	33.32		3.25		5.67		F/A
7	S-RO-A4-N-1	37.53	34.47	3.66	3.36	6.76	6.22	F/A
	S-RO-A4-N-2	31.34		3.06		5.69		F/A
	S-RO-A4-N-3	34.55		3.37		6.22		F/A
8	S-RO-A1-H-1	79.01	62.46	7.71	6.09	12.12	11.11	F/A+CB
	S-RO-A1-H-2	65.91		6.43		12.05		F/A+CEB
	S-RO-A1-H-3	42.46		4.14		9.14		F/A

[a]CB = concrete breakage; CEB = concrete and epoxy breakage; ES = epoxy adhesive splitting; F/A = FRP/adhesive interfacial debonding.

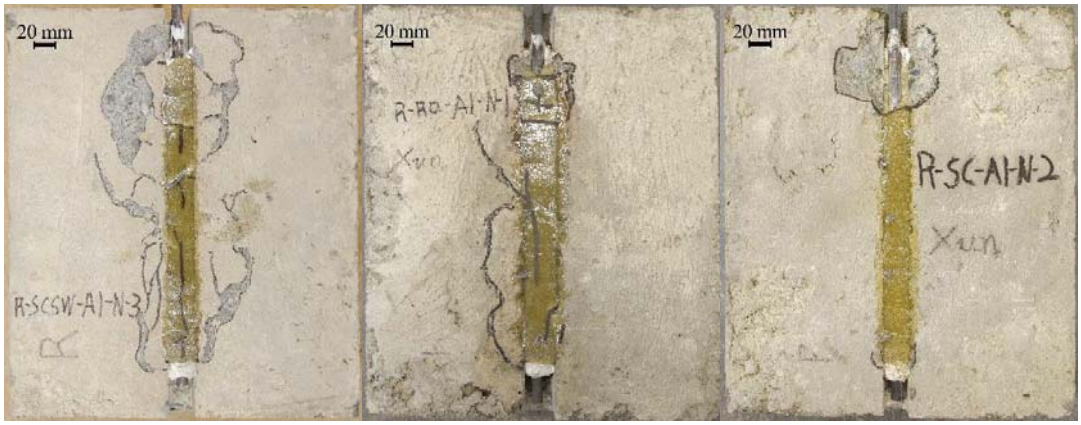

(a) R-SCSW-A1-N-3 (b) R-RO-A1-N-1 (c) R-SC-A1-N-2

Fig. 4.7 Typical failure mode of concrete specimens using CFRP rods under static load (CEB+ES)

The CFRP strip specimens, using different types of epoxy adhesives (A1-A4 for Set 4-7) or higher strength concrete (Set 8), experienced a premature interfacial debonding failure at the FRP and epoxy interface (F/A), as illustrated in Fig. 4.8. In general, no visible crack was observed in concrete and adhesive until the load reached approximately 60-80% of the ultimate pull-out force where sliding noise at the interface was heard. The specimen failed abruptly accompanied by a loud noise and a significant drop in the applied load with a sudden increase in relative slip at the free end. A close inspection after the test revealed a delamination of the FRP surface layer within

the bonded region as shown in Fig. 4.8(a). Minor concrete and epoxy breakage (CEB) or concrete breakage (CB) were also observed at the loaded end for three specimens which reached a higher load level, i.e., S-RO-A2-N-3, S-RO-A1-H-1 and S-RO-A1-H-2, as presented in Figs. 4.8(b) and (c). The average pull-out force of specimen sets using A1 and A2 was much higher than those using A3 and A4, i.e., 54.39 kN (S-RO-A1-N, Set 4), 52.91 kN (S-RO-A2-N, Set 5), 34.10 kN (S-RO-A3-N, Set 6) and 34.47 kN (S-RO-A4-N, Set 7). It can be seen that the pull-out force for these specimen sets had a direct correlation to their corresponding shear strength of the epoxy adhesive used (Table 4.3). The stronger the shear strength of the epoxy adhesive, the higher the theoretical interfacial bond strength with the adoption of other identical parameters in the specimens. On the other hand, although all CFRP strip specimens failed predominately at the interface between FRP and epoxy (F/A), the specimens using higher concrete strength (S-RO-A1-H, Set 8) obtained a 15% higher ultimate pull-out force (62.46 kN) than that of the set with lower concrete strength (S-RO-A1-N, Set 4, 54.39 kN). These differences in both the bond capacity and the failure mode (minor CB for Set 8) implied that the bond efficiency of the NSM FRP-to-concrete joints was enhanced as a result of using concrete with higher compressive strength. Nevertheless, all these strip specimens (Set 5-8) yielded much lower pull-out force than that of the rod specimens (Set 1-3) because of the premature debonding failure, regardless of a higher perimeter-to-area ratio of the CFRP strip than that of the CFRP rod. This premature debonding failure in the strip specimens was also reported in similar DPT studies (e.g., Chen and Cheng 2016) but not in others (e.g., Lee et al. 2013; Khshain et al. 2015). One possible explanation is that the quality of the roughened or textured CFRP strip varied from different production batches, where some poor-quality ones created weakened surface layers on the FRP reinforcement for the full development of the bond strength and the utilization of the FRP. This was also the probable cause for a larger deviation of the pull-out force in the same specimens in the set using the CFRP strip than other sets using the CFRP rod.

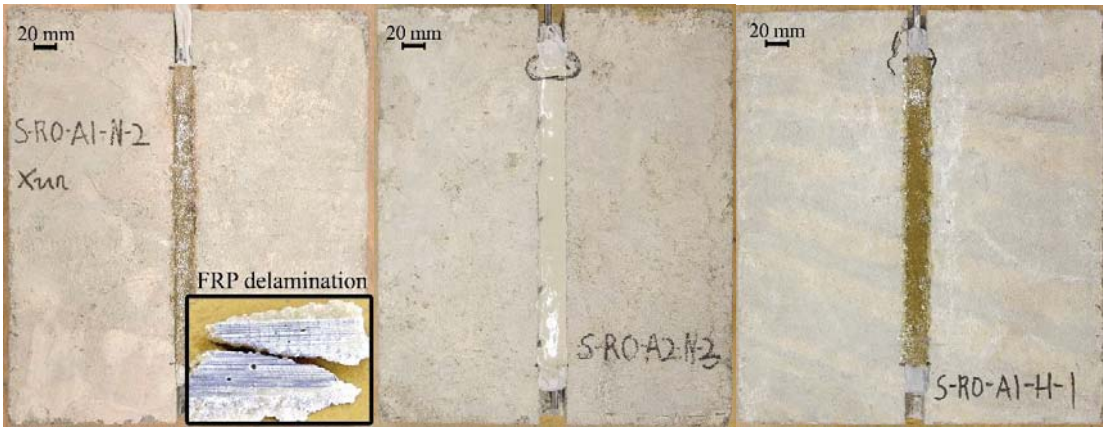

(a) S-RO-A1-N-2 (F/A) (b) S-RO-A2-N-3 (F/A+CEB) (c) S-RO-A1-H-1 (F/A+CB)

Fig. 4.8 Typical failure mode of concrete specimens using CFRP strips under static load

However, unlike the CFRP rod specimens of which the load-carrying capacity depleted after failure, those CFRP strip specimens could still sustain a low residual load capacity after interfacial debonding. This was due to the mechanical friction force existed at the interface between the CFRP strip and epoxy adhesive, and the magnitudes of post-failure residual friction forces of those strip specimens are summarized in Table 4.6, as well as the fatigue specimens. It should be noted that the specimen S-RO-A1-1060-1E3-N-2 is not included because it failed by a different mechanism with both concrete and epoxy damaged and led to an unexpected high pull-out force. One possible explanation is the CFRP strip used in this specimen had a more solid surface texture which enhanced the bond to epoxy adhesive. The average post-failure friction was calculated by the following equation:

$$f = \frac{F_f}{L_p L} \tag{4.1}$$

where F_f = post-failure friction force; L_p = perimeter of failure plane (CFRP strip cross-section); L = bond length (250 mm). It can be seen that the recorded post-failure friction force is proportional to the ultimate pull-out force of the same strip specimen. In short, CFRP strip specimens could sustain approximately 40-60% of its corresponding pull-out force after failure at the interface between FRP and adhesive by a sliding friction mechanism.

Table 4.6 Post-failure residual friction forces for CFRP strip specimens for both monotonic loading case and post-fatigue pull-out testing series

Set	ID	Pull-out force P_f (kN)		Post-failure friction force F_f (kN)		Average post-failure friction f (MPa)	
		Value	Average	Value	Average	Value	Average
4	S-RO-A1-N-1	51.62	54.39	NA[a]	23.87	NA	2.33
	S-RO-A1-N-2	62.92		26.10		2.55	
	S-RO-A1-N-3	48.62		21.65		2.11	
5	S-RO-A2-N-1	50.40	52.91	25.88	23.40	2.52	2.28
	S-RO-A2-N-2	34.11		20.93		2.04	
	S-RO-A2-N-3	74.22		NA[b]		NA	
6	S-RO-A3-N-1	46.18	34.10	20.94	17.56	2.04	1.71
	S-RO-A3-N-2	22.80		14.17		1.38	
	S-RO-A3-N-3	33.32		17.56		1.71	
7	S-RO-A4-N-1	37.53	34.47	16.63	16.72	1.62	1.63
	S-RO-A4-N-2	31.34		16.44		1.60	
	S-RO-A4-N-3	34.55		17.09		1.67	
8	S-RO-A1-H-1	79.01	62.46	35.67	31.45	3.48	3.07
	S-RO-A1-H-2	65.91		26.76		2.61	
	S-RO-A1-H-3	42.46		31.91		3.11	
19	S-RO-A2-1060-F-N-3	50.20	-	29.08	-	2.84	-
20	S-RO-A3-1060-F-N-1	37.47	40.61	17.50	22.14	1.71	2.16
	S-RO-A3-1060-F-N-2	39.04		26.57		2.59	
	S-RO-A3-1060-F-N-3	45.33		22.33		2.18	
21	S-RO-A4-1060-F-N-1	38.31	38.61	18.89	15.66	1.84	1.53
	S-RO-A4-1060-F-N-2	37.98		14.04		1.37	
	S-RO-A4-1060-F-N-3	39.55		14.05		1.37	
23	S-RO-A1-1060-1E1-N-1	43.47	62.20	34.05	31.68	3.32	3.09
	S-RO-A1-1060-1E1-N-2	65.44		29.32		2.86	
	S-RO-A1-1060-1E1-N-3	77.69		NA[b]		NA	
24	S-RO-A1-1060-1E2-N-1	62.85	55.38	23.96	27.19	2.34	2.65
	S-RO-A1-1060-1E2-N-2	40.23		31.07		3.03	
	S-RO-A1-1060-1E2-N-3	63.05		26.55		2.59	
25	S-RO-A1-1060-1E3-N-1	61.62	57.38	29.75	25.56	2.90	2.49
	S-RO-A1-1060-1E3-N-3	53.13		21.36		2.08	
26	S-RO-A1-1060-1E4-N-1	48.08	56.39	31.14	30.05	3.04	2.93
	S-RO-A1-1060-1E4-N-2	50.95		34.60		3.38	
	S-RO-A1-1060-1E4-N-3	70.15		24.40		2.38	
27	S-RO-A1-1050-F-N-1	48.53	52.74	32.18	31.00	3.14	3.02
	S-RO-A1-1050-F-N-2	65.69		28.38		2.77	
	S-RO-A1-1050-F-N-3	44.00		32.44		3.16	

[a]Not available due to loss of data; and
[b]Not available due to concrete and epoxy breakage failure mode.

Fatigue

Noticeable differences in the fatigue bond performance of CFRP rod and strip specimens were observed during the cyclic direct pull-out test, including the local bond characteristics, failure mode, fatigue life, degradation law and post-fatigue behavior. On account of the fact that the magnitudes of the fatigue load range were determined by the static test results, the consistency of

the fatigue bond behavior varied from one set to another for both CFRP rod and strip specimens. As a result, fatigue test results of CFRP rod and strip specimens are reported separately but will be discussed and compared in detail later in this chapter. Note that specimen R-SCSW-A1-1060-F-1 in Set 11 was loaded up to two million cycles instead of one million because it was the very first specimen for the attempt of obtaining its true fatigue life, after which the upper limit was changed to one million cycles for the rest of the specimens for the rationales provided earlier.

For the rod specimens tested for fatigue life (Sets 9-11 and Sets 16-17), failure at the FRP/adhesive interface (F/A) was also experienced in all specimens in addition to the concrete failure with breakage and splitting of epoxy (CEB+ES), which was the predominant failure in the static case. This implies that the fatigue cycles specimens underwent weakened the FRP/adhesive interface at different stages. The specimens using sand-coated and spirally wound (SCSW) rods (Set 11 and 16) survived the loading target of one million cycles and failed during the subsequent monotonic direct pull-up test due to CEB+ES followed by FRP/adhesive interfacial failure (F/A). The same failure mode was also observed in Set 17, specimens using SCSW rods, but failed at an early number of fatigue cycles due to a higher fatigue load range of 10-70%P_f, as presented in Fig 4.9(a). In contrast, the specimens using roughed (RO) and sand-coated (SC) rods (Set 9 and 10, respectively) had the F/A dominated failure mechanism with minor damage in the concrete and epoxy adhesive near the free end (F/A+CEB+ES) [Figs. 4.9(b) and (c)]. Therefore, the weakening effect due to fatigue cycles was more significant in specimens using RO and SC rods than the ones using SCSW rods. This was further confirmed by a close examination of the specimens after failure. For example, the roughened surface of RO specimens and the thin sand coating layer on SC specimens were both smoothed out at fatigue failure, while the SCSW specimens did not show obvious damage after one or two million fatigue cycles under the same load range. This indicated that the sand-coated and spirally wound (SCSW) surface treatment had a better resistance to fatigue degradation than the roughened (RO) or sand-coated (SC) treatment. On the other side, for rod specimens aimed to measure the local bond degradation under fatigue cycles (Sets 12-15), the post-

fatigue failure mode was identical to the static counterpart because of the limited number of fatigue cycles they experienced (i.e., up to 10,000 cycles).

For the strip specimens (Sets 18-28), the failure mechanism was dominated by the failure at the FRP/adhesive interface, similar to their static loading case, as shown in Fig. 4.10 and Table 4.8. In general, no visible crack was observed during the fatigue cycles in either the concrete substrate or the epoxy adhesive. Damage was accumulated at the FRP/adhesive interface under the constant fatigue load range, and the local bond strength at the failure plane degraded with the increase of fatigue cycles. As a result, the load-carrying capacity of the specimen declined gradually until the specimen reached the critical state where the residual capacity was unable to resist the applied fatigue load and the CFRP strip was pulled out from the groove. It is also necessary to clarify that the fatigue bond degradation not only existed at the FRP/adhesive interface but lied in adhesive and substrate concrete as well. But in this test, the FRP/adhesive interface was the weakest link among the CFRP strip-to-concrete bonded joints. Details of the local bond degradation of CFRP strip specimens (Set 23-26) will be discussed later in this chapter.

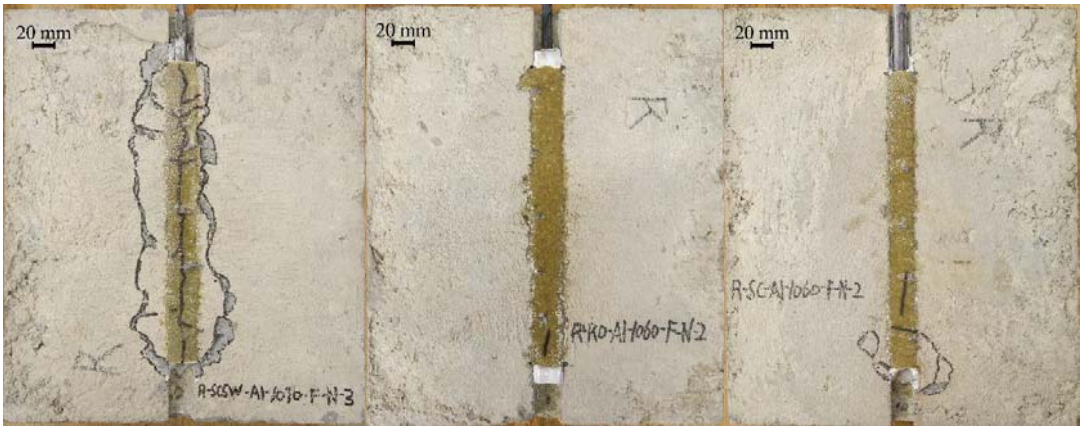

(a) R-SCSW-A1-1070-F-N-3 (CEB+ES+F/A) (b) R-RO-A1-1060-F-N-2 (F/A+ES) (c) R-SC-A1-1060-F-N-2 (F/A+CEB+ES)

Fig. 4.9 Typical failure mode of concrete specimens using CFRP rods under fatigue load

Table 4.7 Direct pull-out test results for CFRP rod specimens under fatigue load

Set	ID	P_{min}[a] (kN)	P_{max}[a] (kN)	Fatigue Life N_f[b]	Post-fatigue pull-out force P_f (kN)		Average bond strength τ_{avg} (MPa)		Local bond strength τ_f (MPa)		Failure mode
					Value	Average	Value	Average	Value	Average	
9	R-RO-A1-1060-F-N-1	8.48	46.40	95,204	-	-	-	-	-	-	F/A+CB
	R-RO-A1-1060-F-N-2	8.50	46.38	79,151	-		-		-		F/A+ES
	R-RO-A1-1060-F-N-3	8.41	46.39	71,774	-		-		-		F/A+CEB
10	R-SC-A1-1060-F-N-1	7.82	41.88	146,605	-	-	-	-	-	-	F/A+ES
	R-SC-A1-1060-F-N-2	7.25	42.10	94,584	-		-		-		F/A+CEB+ES
	R-SC-A1-1060-F-N-3	8.12	41.90	75,987	-		-		-		F/A+CEB+ES
11	R-SCSW-A1-1060-F-N-1	8.78	47.07	2,000,000	80.42	82.26	10.78	11.02	-	-	CB+ES+F/A
	R-SCSW-A1-1060-F-N-2	8.60	46.97	1,000,000	83.17		11.15		-		CEB+ES+F/A
	R-SCSW-A1-1060-F-N-3	8.85	47.08	1,000,000	83.19		11.15		-		CEB+ES+F/A
12	R-SCSW-A1-1060-1E1-N-1	8.71	47.22	-	84.15	83.07	11.28	11.13	16.85	17.16	CEB+ES
	R-SCSW-A1-1060-1E1-N-2	8.96	46.90	-	81.56		10.93		17.37		CEB+ES
	R-SCSW-A1-1060-1E1-N-3	9.00	47.05	-	83.50		11.19		17.27		CEB+ES
13	R-SCSW-A1-1060-1E2-N-1	8.83	46.98	-	106.60	93.28	14.29	12.50	16.03	14.93	CEB+ES
	R-SCSW-A1-1060-1E2-N-2	8.38	46.90	-	90.09		12.07		8.52		CEB+ES
	R-SCSW-A1-1060-1E2-N-3	9.24	46.92	-	83.15		11.14		20.22		CEB+ES
14	R-SCSW-A1-1060-1E3-N-1	8.36	46.99	-	78.69	86.68	10.55	11.62	14.37	14.06	CEB+ES
	R-SCSW-A1-1060-1E3-N-2	9.38	46.83	-	94.78		12.70		9.76		CEB+ES
	R-SCSW-A1-1060-1E3-N-3	8.36	46.97	-	86.58		11.60		18.05		CEB+ES
15	R-SCSW-A1-1060-1E4-N-1	8.72	46.77	-	91.93	94.17	12.32	12.62	8.78	12.41	CEB+ES
	R-SCSW-A1-1060-1E4-N-2	8.76	46.92	-	91.65		12.28		15.99		CEB+ES
	R-SCSW-A1-1060-1E4-N-3	8.96	46.95	-	98.93		13.26		12.47		CEB+ES
16	R-SCSW-A1-1050-F-N-1	8.61	39.29	1,000,000	87.90	79.86	11.78	10.70	-	-	CB+ES+F/A
	R-SCSW-A1-1050-F-N-2	8.26	39.42	1,000,000	71.82		9.63		-		CEB+ES+F/A
	R-SCSW-A1-1050-F-N-3[c]	NA	NA	NA	NA		NA		-		NA
17	R-SCSW-A1-1070-F-N-1	9.20	54.75	16,203	-	-	-	-	-	-	CEB+ES+F/A
	R-SCSW-A1-1070-F-N-2	9.39	54.80	116,181	-		-		-		CB+ES +F/A
	R-SCSW-A1-1070-F-N-3	9.63	54.72	26,072	-		-		-		CEB+ES+F/A

[a]The magnitude of lower and upper limit of the applied fatigue load range, determined by the monotonic counterpart;
[b]The first fatigue specimen (R-SCSW-A1-1060-F-N-1) aimed to obtain the real fatigue life. Since no obvious deterioration was observed up to two million cycles, the upper limit was then changed to one million cycles for the rest of the specimens; and
[c]Not available due to unexpected failure at the first cycle.

Table 4.8 Direct pull-out test results for CFRP strip specimens under fatigue load

Set	ID	P_{min}[a] (kN)	P_{max}[a] (kN)	Fatigue Life N_f	Post-fatigue pull-out force P_f (kN)		Average bond strength τ_{avg} (MPa)		Local bond strength τ_f (MPa)		Failure mode
					Value	Average	Value	Average	Value	Average	
18	S-RO-A1-1060-F-N-1	5.54	32.60	91,917	-	-	-	-	-	-	F/A
	S-RO-A1-1060-F-N-2	5.74	32.61	850,340	-		-		-		F/A
	S-RO-A1-1060-F-N-3	5.91	32.69	1,087,829	-		-		-		F/A+CB+ES
19	S-RO-A2-1060-F-N-1[b]	NA	NA	NA	-	-	-	-	-	-	NA
	S-RO-A2-1060-F-N-2	5.80	31.55	640,385	-		-		-		F/A+CB
	S-RO-A2-1060-F-N-3	5.62	31.55	1,000,000	50.20		4.90		6.86		F/A
20	S-RO-A3-1060-F-N-1	3.46	20.43	1,000,000	37.47	40.61	3.66	3.96	6.60	6.19	F/A
	S-RO-A3-1060-F-N-2	3.34	20.58	1,000,000	39.04		3.81		6.11		F/A
	S-RO-A3-1060-F-N-3[c]	4.13	23.87	1,000,000	45.33		4.42		5.87		F/A
21	S-RO-A4-1060-F-N-1	3.22	20.67	1,000,000	38.31	38.61	3.74	3.77	5.71	6.14	F/A
	S-RO-A4-1060-F-N-2	3.13	20.69	1,000,000	37.98		3.71		6.27		F/A
	S-RO-A4-1060-F-N-3	3.28	20.73	1,000,000	39.55		3.86		6.43		F/A+CB
22	S-RO-A1-1060-F-H-1	7.19	37.41	623,927	-	-	-	-	-	-	F/A+EB[e]
	S-RO-A1-1060-F-H-2	7.29	37.51	1,088,650	-		-		-		F/A+CB
	S-RO-A1-1060-F-H-3	6.98	36.95	125	-		-		-		F/A
23	S-RO-A1-1060-1E1-N-1	6.63	32.53	-	43.47	62.20	4.24	6.07	6.31	8.26	F/A
	S-RO-A1-1060-1E1-N-2	6.53	32.48	-	65.44		6.38		8.55		F/A
	S-RO-A1-1060-1E1-N-3	6.35	32.61	-	77.69		7.58		9.93		F/A+CEB
24	S-RO-A1-1060-1E2-N-1	6.17	32.61	-	62.85	55.38	6.13	5.40	7.57	7.24	F/A
	S-RO-A1-1060-1E2-N-2	6.06	32.49	-	40.23		3.93		5.16		F/A
	S-RO-A1-1060-1E2-N-3	6.29	32.61	-	63.05		6.15		8.99		F/A
25	S-RO-A1-1060-1E3-N-1	6.32	32.62	-	61.62	57.38	6.01	5.60	6.88	6.54	F/A
	S-RO-A1-1060-1E3-N-2[d]	6.18	32.60	-	~~89.42~~		~~8.72~~		~~13.03~~		F/A+CEB
	S-RO-A1-1060-1E3-N-3	6.05	32.46	-	53.13		5.18		6.20		F/A
26	S-RO-A1-1060-1E4-N-1	5.31	32.28	-	48.08	56.39	4.69	5.50	5.61	5.98	F/A+CB
	S-RO-A1-1060-1E4-N-2	6.13	32.57	-	50.95		4.97		5.04		F/A
	S-RO-A1-1060-1E4-N-3	6.22	32.57	-	70.15		6.84		7.30		F/A
27	S-RO-A1-1050-F-N-1	5.23	27.39	1,000,000	48.53	52.74	4.73	5.15	-	-	F/A+CB
	S-RO-A1-1050-F-N-2	5.51	27.40	1,000,000	65.69		6.41		-		F/A+EB
	S-RO-A1-1050-F-N-3	5.50	27.36	1,000,000	44.00		4.29		-		F/A+EB
28	S-RO-A1-1070-F-N-1	6.42	37.90	126,825	-	-	-	-	-	-	F/A
	S-RO-A1-1070-F-N-2	6.00	38.00	54,300	-		-		-		F/A
	S-RO-A1-1070-F-N-3	6.15	37.90	285,504	-		-		-		F/A

[a]The magnitude of lower and upper limit of the applied fatigue load range, determined by the monotonic counterpart;
[b]Not available due to unexpected failure at the first cycle;
[c]P_{max} was determined on the average static pull-out force of S-RO-A3-N-1 and S-RO-A3-N-3 without the weakest specimen S-RO-A3-N-2;
[d]Not included because it failed by a different mechanism (CEB) which led to an unexpected high pull-out force; and [e]EB = epoxy breakage.

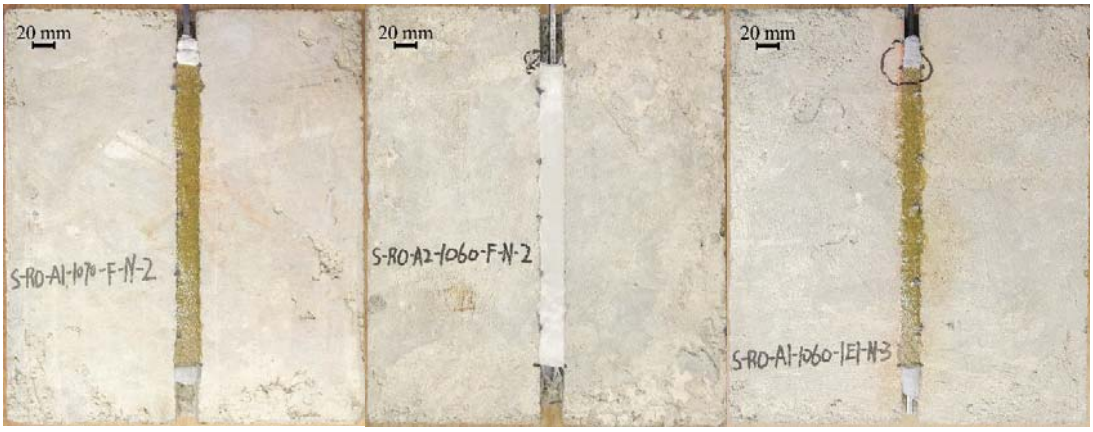

(a)S-RO-A1-1070-F-N-2 (F/A) (b) S-RO-A2-1060-F-N-2 (F/A+CB) (c) S-RO-A1-1060-1E1-N-3 (F/A+CEB)

Fig. 4.10 Typical failure mode of concrete specimens using CFRP strips under fatigue load

4.3.2 FRP Strain distribution

Static

As aforementioned, five strain gauges were installed on the surface of the FRP reinforcement within the bonded region for all the specimens with a constant interval of 50 mm. Assuming zero strain of the FRP reinforcement at the free end of the joint specimen, typical distributions for the strain in both the CFRP rod and strip along the bond length are illustrated in Figs. 4.11 and 4.12, respectively. Each plot contains five curves representing five different load levels with respect to the specimen's corresponding ultimate pull-out force (20-100%P_f). Note that in Figs. 4.11(b) and (c), some data points at 100%P_f were missing because of the strain gauge damage when the specimen was close to failure.

For the CFRP rod specimens, the FRP strain at all locations along the bond length increased proportionally to the load level ranging 20-100%P_f. The strain near the free end (i.e., 150-250 mm away from the loaded end) was negligible at load levels lower than 60%P_f. However, as the increase of the load level from 60%P_f to 100%P_f, strain increased drastically toward the free end. In addition, the slopes of line segments connecting two immediate neighboring strain data points close to loaded end, e.g., 0-50 mm, 50-100 mm, or even 100-150 mm firstly would become steeper

then followed by a trend of getting flatter with the increase of load level. By contrast, for the line segments near free end, e.g., 150-200 mm and 200-250 mm, their slopes were always growing with the increase of load level. Since the slop of a line segment is proportional to the local bond stress, this observation was caused by an uneven local bond strength within the bonded region, where a higher local bond strength was always found to be near the free end. More details will be discussed in the following subchapters. Moreover, comparing these rod specimens to the strip specimens, i.e., S-RO-A1-N-2 in Fig. 4.12(a), the features of strain distribution for strip specimens were almost identical but only smaller in magnitudes due to the premature debonding failure at the FRP/adhesive interface.

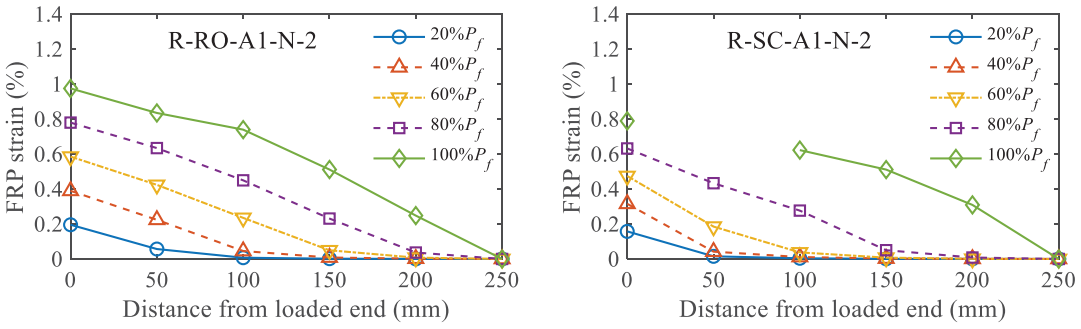

(a) R-RO-A1-N-2 (b) R-SC-A1-N-2

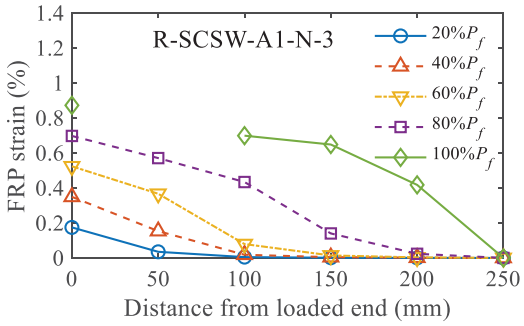

(c) R-SCSW-A1-N-3

Fig. 4.11 Typical FRP strain distributions for CFRP rod specimens under static load

For the CFRP strip specimens, the trend of the FRP strain distribution was consistent with those CFRP rod specimens except for S-RO-A2-N-1 [4.12(b)], of which regions near the free end,

e.g.,150 mm or further away from the loaded end, had almost negligible strain throughout the entire loading process. However, the strain level of specimen S-RO-A2-N-1 at the loaded end was still comparable to that of S-RO-A1-N-2 [Fig. 4.12(a)], indicating similar mechanical properties of epoxy adhesive A2 compared to A1. On the other hand, the development in FRP strain of specimens using epoxy adhesive A3 [Fig. 4.12(c)] and A4 [Fig. 4.12(d)] was similar but smaller in the strain level than the specimens using epoxy adhesive A1 and A2. It can also be seen that adopting a higher strength concrete [Fig. 4.12(e)] was beneficial to the NSM CFRP strip-to-concrete bonded joints, which improved its bond performance even though these specimens did not fail by concrete breakage. These differences in strain distribution for specimens using various types of epoxy adhesive and concrete with higher strength are consistent with their load-carrying capacity as described in Table 4.5.

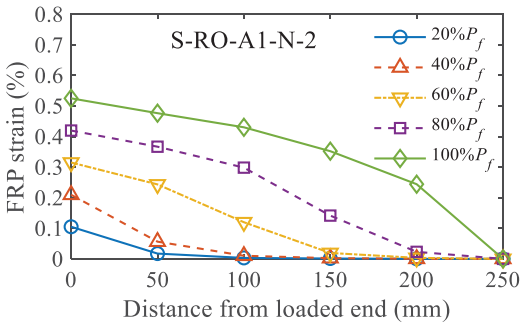

(a) S-RO-A1-N-2

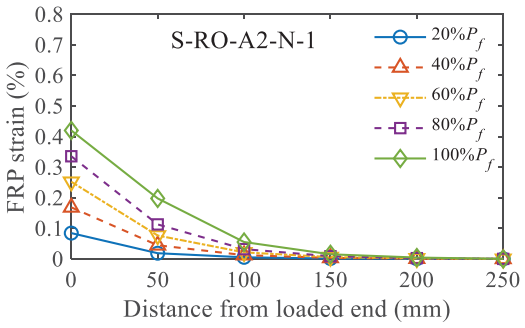

(b) S-RO-A2-N-1

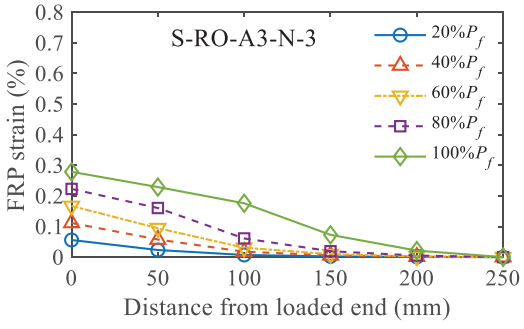

(c) S-RO-A3-N-3

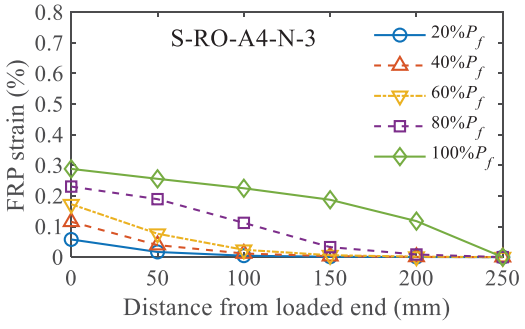

(d) S-RO-A4-N-3

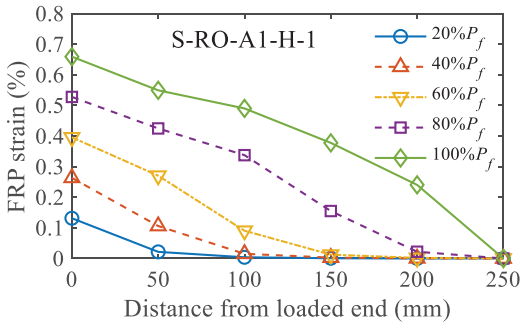

(e) S-RO-A1-H-1

Fig. 4.12 Typical FRP strain distributions for CFRP strip specimens under static load

Post-fatigue

Likewise, typical distributions for the strain in both the CFRP rod and strip along the bond length after 10, 100, 1000 and 10,000 fatigue cycles were recorded and presented in Figs. 4.13 and 4.14, respectively. In Fig. 4.13, some data points were missing at 80% or 100%P_f, especially for specimen R-SCSW-A1-1060-1E4-N-1 [Fig. 4.13(d)] of which the strain gauge at 50 mm away from the free end was damaged at the beginning of post-fatigue DPT due to the higher number of fatigue cycles it experienced.

For the CFRP rod specimens, when compared to the static ultimate pull-out forces recorded in Table 4.5, the fatigue cycles up to 10,000 cycles did not develop much negative effect on the post-fatigue load-carrying capacity. In fact, all the four sets of CFRP rod specimens (Set 12-15 in Table 4.7) reached even higher ultimate pull-out forces on average than their static counterpart (Set 3 in Table 4.5). Two reasons could be provided to explain this phenomenon: (1) the scatter of concrete strength resulted in different load-carrying capacities of specimens of which the failure mode was concrete and epoxy breakage; and (2) the solid sand-coated and spirally wound (SCSW) surface treatment had a good resistance to fatigue degradation, and hence the 10,000 fatigue cycles only had an insignificant effect on the entire load-carrying capacity. Nevertheless, the strain distribution still revealed some evidence of local bond degradation of CFRP rod specimens. For example, under the static loading case, the strain reading at 150mm away from the loaded end was

almost negligible before 80%P_f [Fig. 4.11(c)]. However, after 1000 or 10,000 fatigue cycles [Figs. 4.13(c) and (d)], the strain at the same location was no longer negligible even at 40%P_f. It indicated a higher development of the bonded region closer to the free end than the static loading case. In addition, the slop of the line segment connecting two immediate neighboring strain data points had the tendency of flattening out with the increase of fatigue cycles, e.g., 0-50 mm of R-SCSW-A1-1060-1E3-N-2 [Fig. 4.13(c)].

For the CFRP strip specimens, the fatigue cycles up to 10,000 cycles did not have a negative effect on the post-fatigue load-carrying capacity as well (Set 23-26 in Table 4.8). The post-fatigue ultimate pull-out forces were only slightly higher than that of the static counterpart (Set 4 in Table 4.5) which might be attributed to the further curing of epoxy adhesive in the groove. Unlike the CFRP rod specimens, the increased fatigue cycles did not change the strain level drastically of the bonded region closer to the free end. However, the slope of the line segment connecting two immediate neighboring strain data points was significantly influenced by the number of fatigue cycles. The slope of the line segment 0-50 mm, for instance, was becoming more stable with the increase of applied load from 20%P_f to 100%P_f under higher fatigue cycles, as illustrated in Figs. 4.14(b) and (c). This tendency was even more noticeable for S-RO-A1-1060-1E4-N-2 [Fig. 4.14(d)] and was also extended to the line segment 50-100 mm. On the other hand, the slope of the line segment 100-150 mm or 150-200 mm was flattened out with the increase of fatigue cycles [Figs. 4.14(c) and (d)].

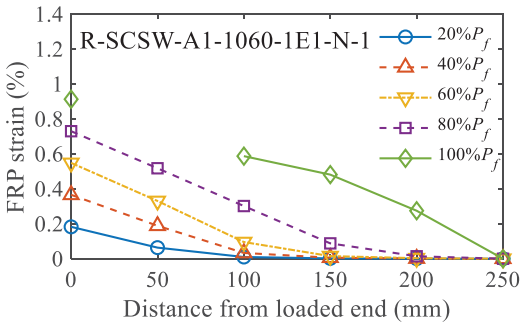

(a) R-SCSW-A1-1060-1E1-N-1

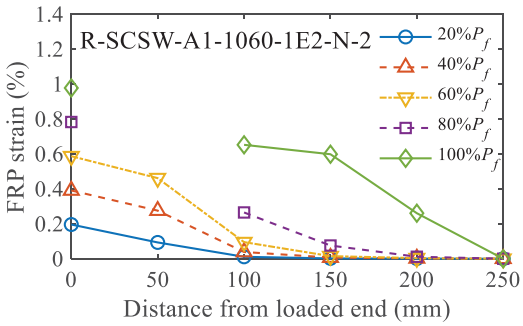

(b) R-SCSW-A1-1060-1E2-N-2

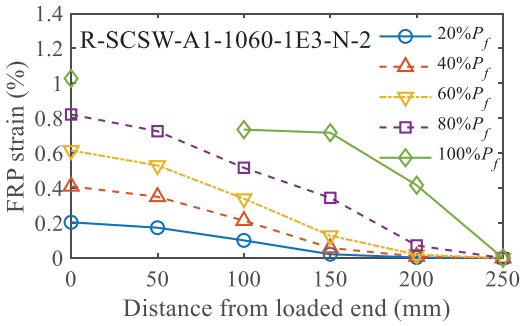

(c) R-SCSW-A1-1060-1E3-N-2

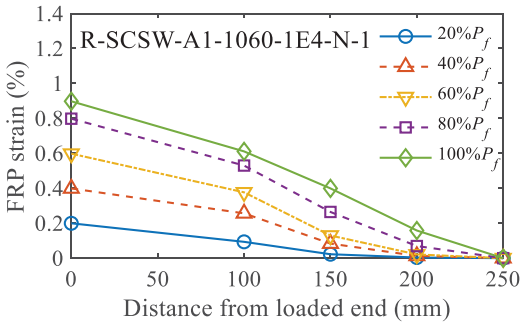

(d) R-SCSW-A1-1060-1E4-N-1

Fig. 4.13 Post-fatigue FRP strain distributions for CFRP rod specimens

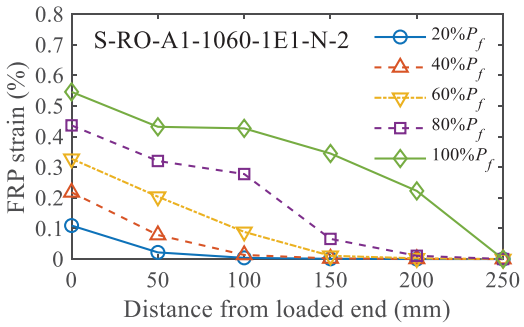

(a) S-RO-A1-1060-1E1-N-2

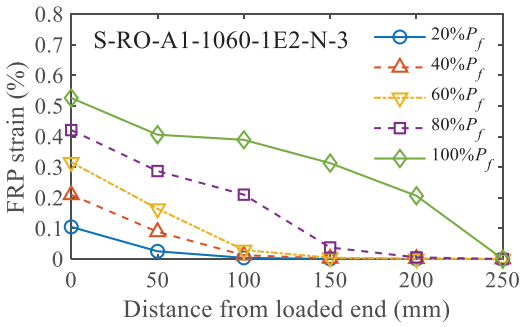

(b) S-RO-A1-1060-1E2-N-3

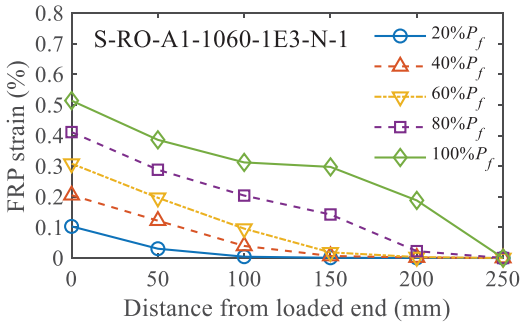

(c) S-RO-A1-1060-1E3-N-1

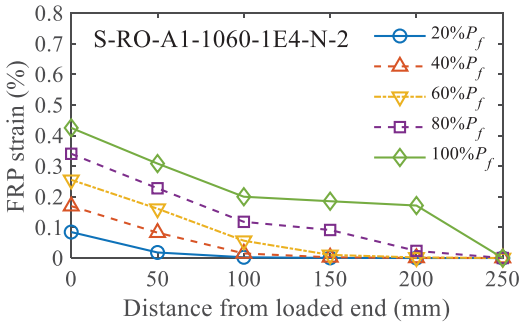

(d) S-RO-A1-1060-1E4-N-2

Fig. 4.14 Post-fatigue FRP strain distributions for CFRP strip specimens

4.3.3 Local bond stress distribution

Assuming a perfect linear elastic behavior for CFRP reinforcement, the average local bond stress τ_i at the FRP/adhesive interface between two consecutive strain gauges can be derived by the following equation (Lee et al. 2013; Chen and Cheng 2015):

$$\tau_i = \frac{A_f E_f}{L_p} \frac{d\varepsilon}{dx} \tag{4.2}$$

where i = location index of local bond stress; A_f = cross-sectional area of NSM reinforcement; E_f = Young's modulus of NSM reinforcement; L_p = perimeter of the failure plane or the NSM reinforcement; $d\varepsilon_i$ = difference in strain readings of two consecutive strain gauges at locations shown in Fig. 4.4(b); and dx = constant interval (50 mm) between two consecutive strain gages. The notations for τ_i (τ_1, τ_2, τ_3, τ_4, and τ_5) represent the local bond stress at locations 25, 75, 125, 175 and 225 mm away from the loaded end, respectively.

Static

Typical distributions for the local bond stress along the bond length for both the CFRP rod and strip specimens are shown in Figs. 4.15 and 4.16, respectively. Following the same labeling scheme of the FRP strain distribution, each plot contains five curves representing five different load levels with respect to the specimen's corresponding ultimate pull-out force (20-100%P_f). Note that in Figs. 4.15(b) and (c), some data points at 100%P_f were missing because of the strain gauge damage when the specimen was close to failure.

For the CFRP rod specimens, as shown in Fig. 4.15, the local bond stress near the free end (125-225 mm on the horizontal axis) was insignificant at lower load levels up to 40%P_f. However, with the increase of the load level from 60%P_f to 100%P_f, the local bond stress was more evenly developed along the bond length with the peak local bond stress migrated quickly towards the free end at failure (100%P_f). In addition, the local bond stress near the loaded end would drop at a higher load level (80%P_f), which was attributed to concrete and epoxy breakage in this region.

Likewise, the development and distribution pattern of the local bond stress for the CFRP strip specimens using the same epoxy adhesive A1 were very similar to that of CFRP rod specimens, regardless of a lower local bond stress due to premature debonding at the FRP/adhesive interface, as presented in Fig. 4.16(a).

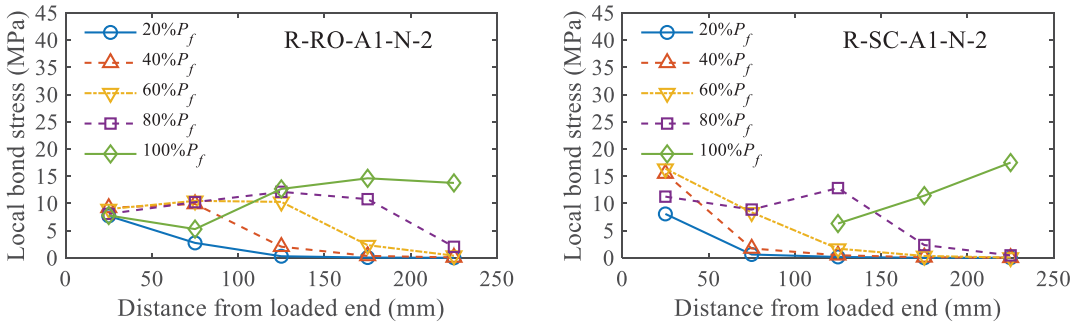

(a) R-RO-A1-N-2 (b) R-SC-A1-N-2

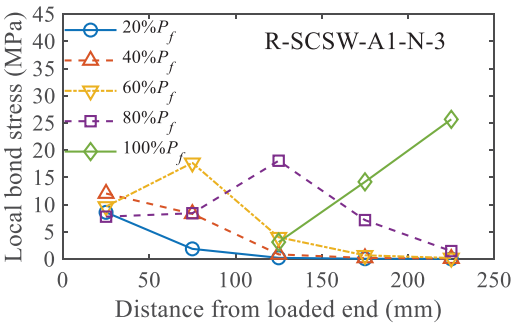

(c) R-SCSW-A1-N-3

Fig. 4.15 Typical local bond stress distributions for CFRP rod specimens under static load

For the CFRP strip specimens under static load, however, the characteristics of the local bond stress distribution varied among specimens using different types of epoxy adhesive. Specimens using epoxy adhesive A1 [Fig. 4.16(a)] performed the best among all, with the highest local bond stress level and evenly developed bonded region represented by the migration of peak local bond stress from the loaded end at a lower load level to the free end at a higher load level. This local bond performance is consistent with the static DPT results (ultimate pull-out forces) as described in Table 4.5 although specimens using epoxy adhesive A2 had almost identical pull-out forces compared to the specimen set S-RO-A1-N. The peak local bond stress was always located at the

loaded end through the entire static loading process. In other words, the bonded region 150 mm or further away from the loaded end provided almost negligible resistance to the applied load, as shown in Fig. 4.16(b). This uneven performance in local bond stress could be caused by either the imperfect casting of epoxy adhesives during specimen construction, e.g., partial leakage of epoxy near the free end because of its high flowability, or the unstable epoxy properties due to the possible deviation in mix proportion. By comparison, the strip specimens using epoxy adhesive A3 and A4 behaved similarly with a much smaller local bond stress within the bonded region and these results agreed with their FRP strain distribution discussed in Chapter 4.3.2, which could be further explained by the weaker shear strength of the used epoxy adhesives (Table 4.3). The pattern of local bond stress distribution for specimen S-RO-A1-H-1 [Fig. 4.16(e)] was almost identical to that of specimen S-RO-A1-N-2 [Fig. 4.16(a)], but the peak local bond stresses at different load levels were slightly higher. Thus, it was safe to conclude that the concrete strength also contributed to the local bond strength of CFRP strip specimens failed by interfacial debonding.

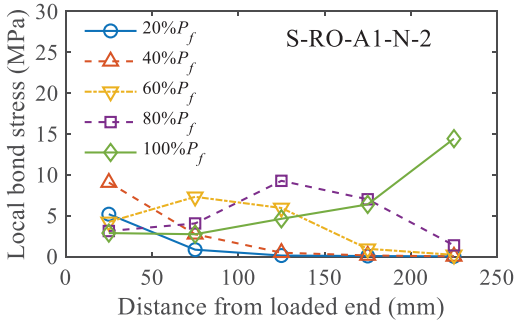

(a) S-RO-A1-N-2

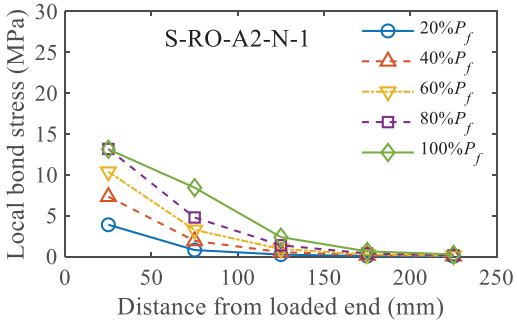

(b) S-RO-A2-N-1

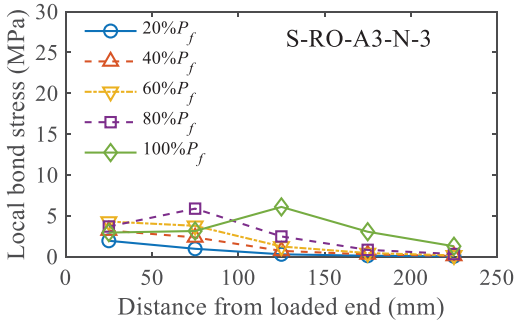

(c) S-RO-A3-N-3

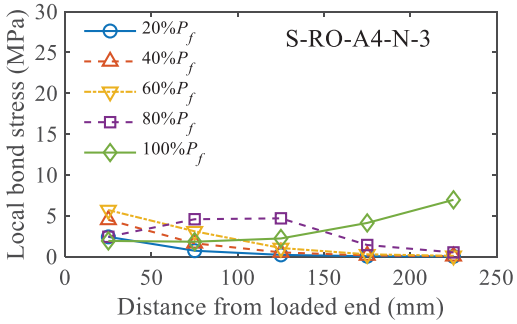

(d) S-RO-A4-N-3

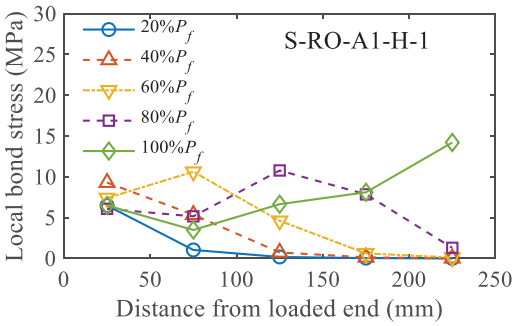

(e) S-RO-A1-H-1

Fig. 4.16 Typical local bond stress distributions for CFRP strip specimens under static load

Post-fatigue

The typical post-fatigue local bond stress distributions for both the CFRP rod and strip specimens after 10, 100, 1000 and 10,000 cycles were measured and illustrated in Figs. 4.17 and 4.18, respectively. Note that the strain gauges of CFRP rod specimens near the loaded end were all damaged when the specimen was close to failure under post-fatigue DPT. Likewise, the strain gauge of specimen R-SCSW-A1-1060-1E4-N-1 at the location 50 mm away from the loaded end was damaged during the experienced fatigue cycles. As a result, some data points were missing at 80% or 100%P_f or through the entire post-fatigue DPT in Fig. 4.17. Furthermore, the data point at 50 mm of Fig. 4.17(d) is the average local bond stress of the bonded region ranging 0-100 mm from the loaded end.

In Fig. 4.17, noticeable difference was observed in the development of bonded regions close to the free end with the increase of fatigue cycles. At the load level less than 80%P_f, the static CFRP rod specimens [Fig. 4.15(c)] and specimens experienced 10 or100 fatigue cycles [Fig. 4.17(a) and (b)] only had an insignificant local bond stress of the bonded region ranging 150-250 mm from the loaded end. However, after 1000 or 10,000 fatigue cycles, the local bond stress of the 150-250 mm bonded region was noticeable even at 40%P_f, indicating a further development of the bonded regions near the free end. Although the post-fatigue load-carrying capacity of the CFRP rod specimens was higher than that of the static counterparts (Table 4.7) due to the scatter of concrete

strength, the local bond stress within the 0-150 mm bonded region presented a slight degradation, as shown in Figs. 4.17(c) and (d).

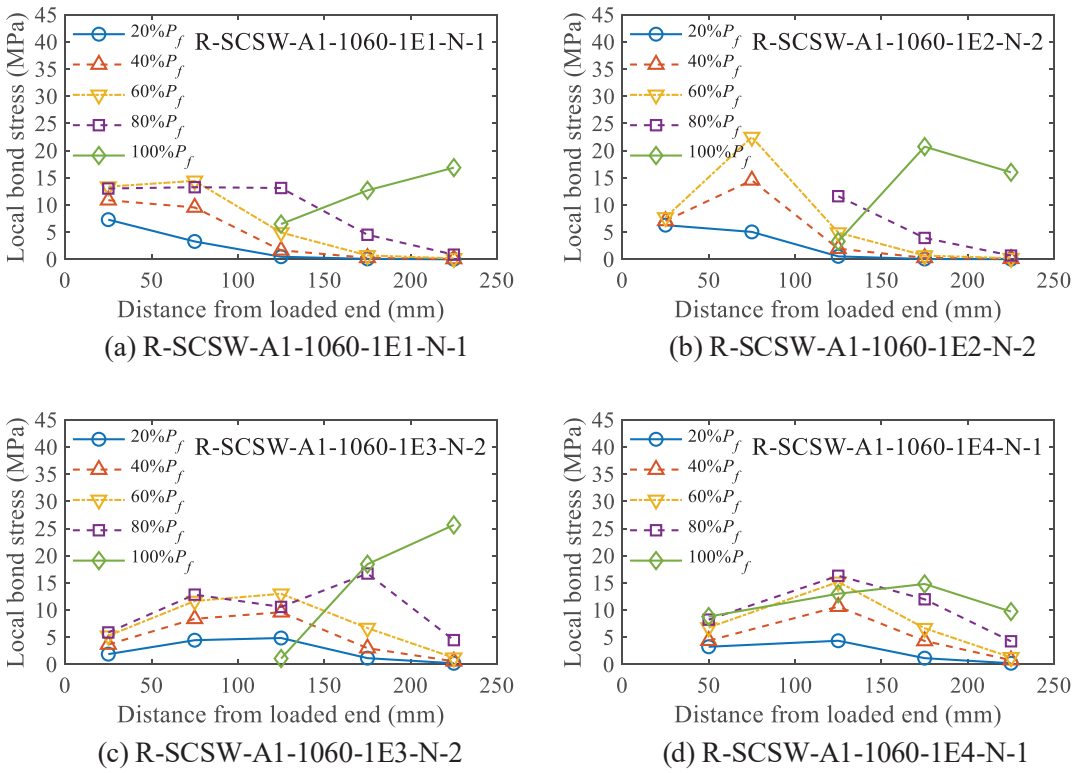

(a) R-SCSW-A1-1060-1E1-N-1 (b) R-SCSW-A1-1060-1E2-N-2

(c) R-SCSW-A1-1060-1E3-N-2 (d) R-SCSW-A1-1060-1E4-N-1

Fig. 4.17 Post-fatigue local bond stress distributions for CFRP rod specimens

On the other side, a significant change in the local bond stress distribution was observed for the CFRP strip specimens, as shown in Fig. 4.18. Except for the region closest to the free end (i.e., 200-250 mm), the peak local bond stress levels along the bond line degraded to different extents especially for the specimens experienced 10,000 fatigue cycles [Fig. 4.18(d)]. Among all these locations, the local bond stress level at the 100-150 mm bonded region dropped the most, whilst the local bond stress level at the 0-100 mm bonded region was relatively stable with only little degradation. This unevenness in the local bond degradation was probably caused by the variation in roughness of the CFRP strip surface treatment and its sliding friction failure mechanism at the FRP/adhesive interface.

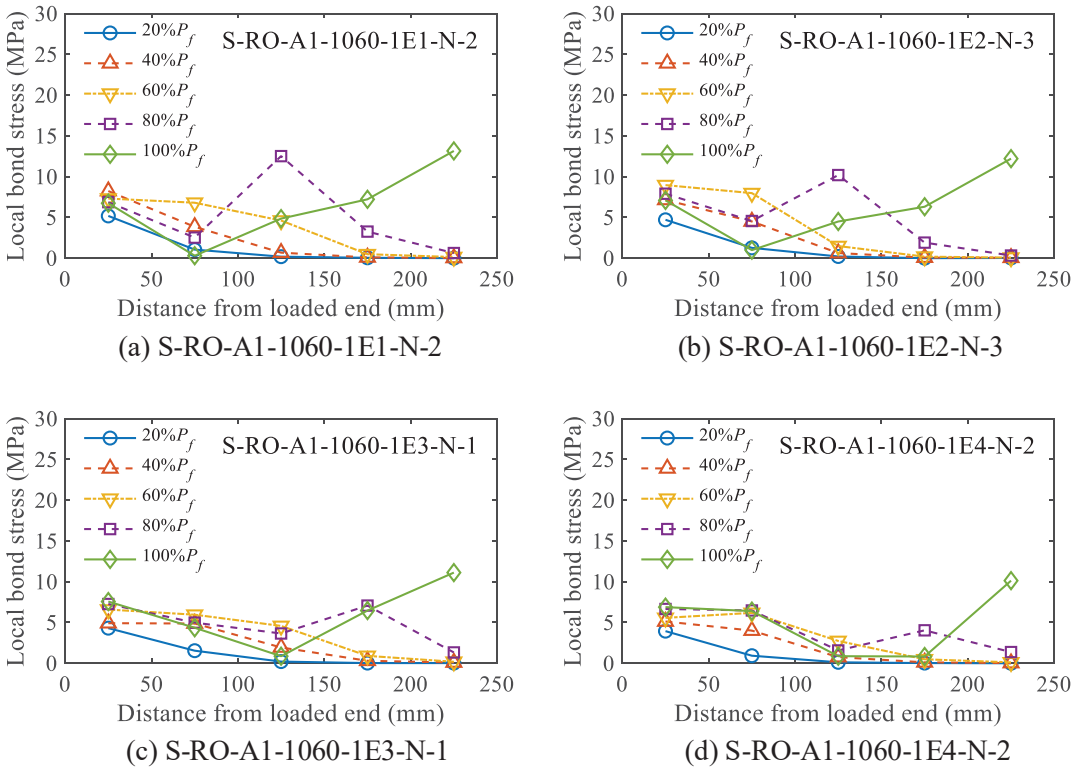

(a) S-RO-A1-1060-1E1-N-2 (b) S-RO-A1-1060-1E2-N-3

(c) S-RO-A1-1060-1E3-N-1 (d) S-RO-A1-1060-1E4-N-2

Fig. 4.18 Post-fatigue local bond stress distributions for CFRP strip specimens

4.3.4 Local bond stress-slip relationship

The local bond stress-slip relationship is featured as the constitutive law for NSM FRP-to-concrete joints under direct pull-out test, as previously discussed in Chapter 3. The area under the local bond stress-slip curve is usually detonated as the interfacial fracture energy, G_f, required for the bond to fail in shear per unit area (Blaschko 2003; Seracino et al. 2007b; Barros and Costa 2010; Soliman et al. 2010; Palmieri et al. 2012; Lee et al. 2013) since the load at failure is reported to be a function of the interfacial fracture energy (Yuan et al. 2004). In general, the pull-out force is transferred from the FRP reinforcement at the loaded end to the concrete substrate in conjunction with the deformation of intermediate adhesive. The intensity of load transferred is quantified as the local bond stress (Eq. 4.2). In addition, the relative slip at the free end was measured by a linear potentiometer (LP), as illustrated in Fig. 4.6(b). Assuming the deformation of the concrete block is negligible as compared to the elongation of the FRP reinforcement, the relative slip between FRP

reinforcement and concrete at different locations can be calculated by integrating the experimental strain readings along the bond line plus the relative slip at the free end as follows (Ceroni et al. 2012; Palmieri et al. 2012; Lee et al. 2013; Chen and Cheng 2015):

$$\delta_i = \sum_{k=i+1}^{6} \frac{1}{2}\left(\varepsilon_{k-1} + \varepsilon_k\right)\left(x_k - x_{k-1}\right) + \delta_{fe} \tag{4.3}$$

where δ_i = relative slip between FRP reinforcement and concrete; δ_{fe} = relative slip at the free end; $\varepsilon_{k\text{-}1}$, ε_k = strain readings from immediate neighboring strain gauges [Fig. 4.4(b)]; ε_6 = strain at the free end (zero); x_k, $x_{k\text{-}1}$ = coordinates of immediate neighboring strain gauges measured from the loaded end; and x_6 = coordinate at the free end (i.e., 250 mm).

Static

By combining Eq. 4.2 and Eq. 4.3, the local bond stress-slip relationships under DPT for both the CFRP rod and CFRP strip in concrete were obtained, as illustrated in Figs. 4.19 and 4.20, respectively. Each plot contains five curves representing the responses at five locations, each at the midpoint of two consecutive strain gage locations, i.e., τ_1, τ_2, τ_3, τ_4 and τ_5 at locations 25, 75, 125, 175 and 225 mm away from the loaded end, respectively [Fig. 4.4(b)]. It should be noted that not all the curves were able to reach the final failure stage due to the loss of some damaged strain gages upon specimen failure especially near the loaded end. Additionally, SG-5 near the free end of R-SCSW-A1-N-1 was damaged during epoxy casting and thus τ_5 was missing [Fig. 4.19(g)].

In Figs. 4.19 and 4.20, the local bond stress-slip relationships for both the CFRP rod and strip cases are characterized by a general three-stage development, similar to other studies (De Lorenzis 2004; Lee et al. 2013; Al-Saadi et al. 2018). At the beginning stage, the local bond stress increased with the slow increase of the relative slip in a mostly linear elastic manner. After the local bond stress reached its peak magnitude, it gradually decreased with further increase of the relative slip, which is considered as the second softening stage. The decrease rate of the local bond stress then slowed down until it reached a plateau (residual bond stress), indicating the initiation of the local

debonding at the interface, referring to the last debonding stage. The magnitude of the governing parameters such as the peak local bond stress (τ_f), residual bond stress (τ_r) and stress changing rate in both the elastic and softening stages depended on the type of materials used in the joints (i.e., NSM FRP reinforcement, concrete and adhesive).

For the CFRP rod specimens, the average local bond strength of the specimen set R-RO-A1-N (Set 1), R-SC-A1-N (Set 2) and R-SCSW-A1-N (Set 3) was 13.18 MPa, 16.61 MPa and 17.30 MPa, respectively, as presented in Table 4.5. Note that the local bond strength was calculated based on the perimeter of CFRP rod cross-section, yet all the CFRP rod specimens failed by concrete breakage under the direct pull-out force. Although the average local bond strength of R-RO-A1-N was lower than that of R-SC-A1-N, the pull-out force of R-RO-A1-N was approximately 10% higher. This result could be explained by a more gradual softening behavior of R-RO-A1-N in the second stage rather than the steep drop of the local bond stress observed for R-SC-A1-N, as well as a higher residual bond strength of R-RO-A1-N, as shown in Figs. 4.19(a)-4.19(f). In addition, it can be seen that the local bond strengths at different locations of the bond length were not identical. The local bond strength was generally higher at the bonded region closer to the free end (i.e., τ_5) than that at the loaded end (i.e., τ_1). However, this conclusion of variation in local bond strength was not always true. For example, specimen R-SC-A1-N-2 [Fig. 4.19(e)] and specimen R-SCSW-A1-N-2 [Fig. 4.19(h)] were two exceptions in which τ_1 and τ_4 was the peak number, respectively. The uneven distribution of the local bond strength might be influenced by various factors including, but not limited to, difference in confinement of surrounding concrete, scatter of material properties, uncertainty induced by manual mixing and casting of epoxy adhesive, and changing in environmental conditions, etc. Nevertheless, among the specimens using the same type of concrete (N) and adhesive (A1) [Fig. 4.19 and Figs. 4.20(a)-4.20(c)], the specimens using sand-coated and spirally wound (SCSW) CFRP rods [Figs. 4.19(g)-4.19(i)] overall showed a higher local bond stress than the other specimens using roughened (RO) rods [Figs. 4.19(a)-4.19(c)], sand-coated (SC) rods [Figs. 4.19(d)-4.19(f)] and roughened (RO) strips [Figs. 4.20(a)-4.20(c)].

Among all the CFRP strip specimens, on the other hand, the average local bond strength of the specimen set S-RO-A1-N (Set 4), S-RO-A2-N (Set 5), S-RO-A3-N (Set 6), S-RO-A4-N (Set 7), and S-RO-A1-H (Set 8) was 10.42 MPa, 11.35 MPa, 5.77 MPa, 6.22 MPa and 11.11 MPa, respectively, as reported in Table 4.5. The type of adhesive epoxy had a significant influence on the local bond strength where the specimens using A1 prevailed over all other specimens with a strong local bond strength and the best ductile behavior during softening stage. In addition, the specimens using A2 reached the highest local bond strength but was weaker in uniformity of the local bond performance along the bond length. The specimens using A3 and A4 performed similarly to the specimens using A1 with a consistent three-stage local bond stress-slip relationship, however, both the local bond strength and residual bond strength were much smaller than that using A1 or A2. Furthermore, the NSM FRP strip-to-concrete bonded joints took the benefit of adopting a higher strength concrete [Figs. 4.20(m)-4.20(o)], which enhanced both the local bond strength and the load-carrying capacity.

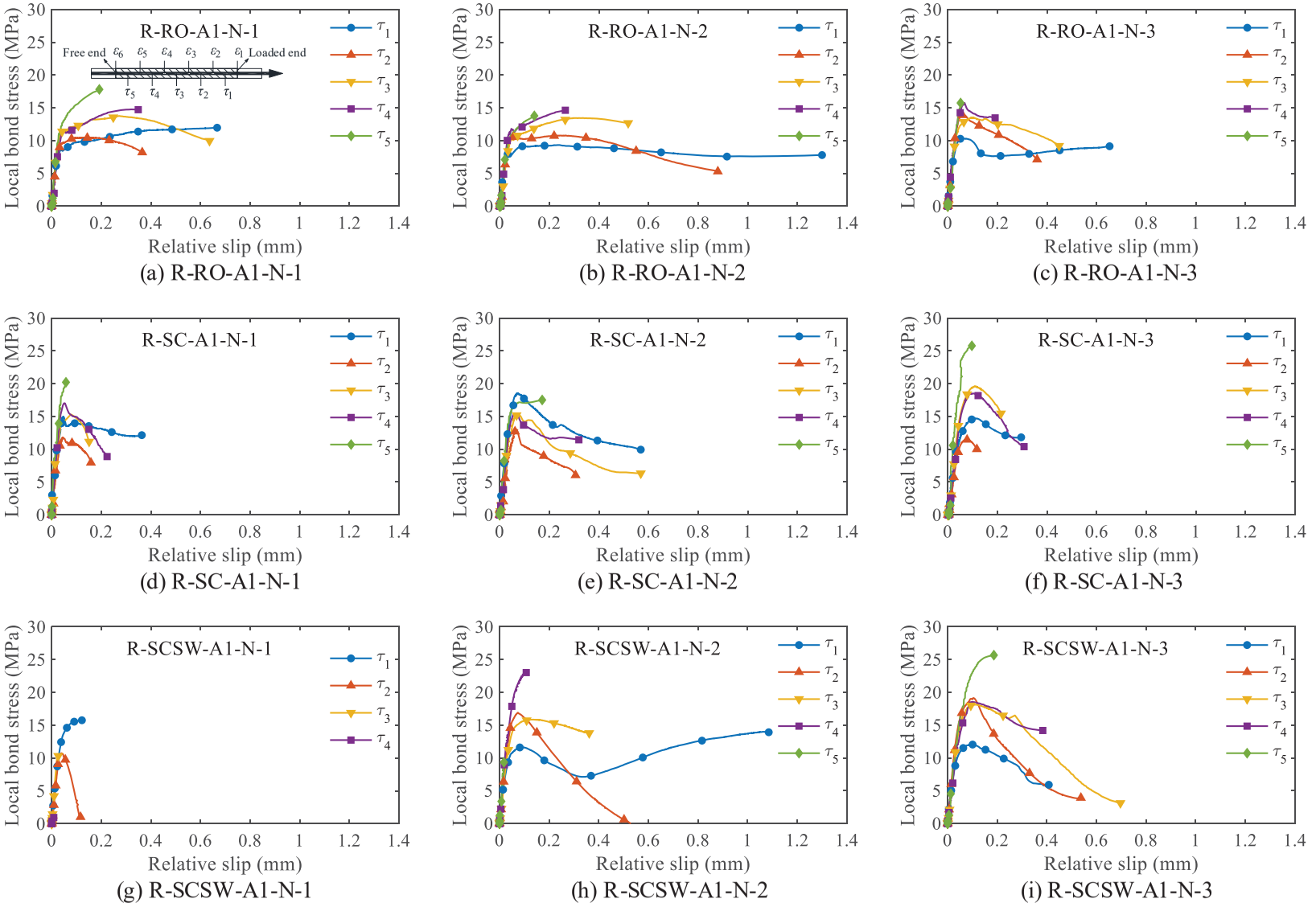

(a) R-RO-A1-N-1 (b) R-RO-A1-N-2 (c) R-RO-A1-N-3

(d) R-SC-A1-N-1 (e) R-SC-A1-N-2 (f) R-SC-A1-N-3

(g) R-SCSW-A1-N-1 (h) R-SCSW-A1-N-2 (i) R-SCSW-A1-N-3

Fig. 4.19 Local bond stress-slip relationships for CFRP rod specimens under static load

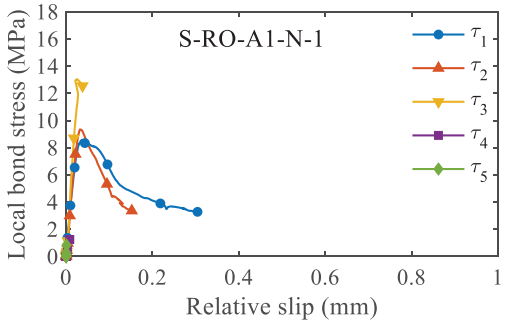

(a) S-RO-A1-N-1

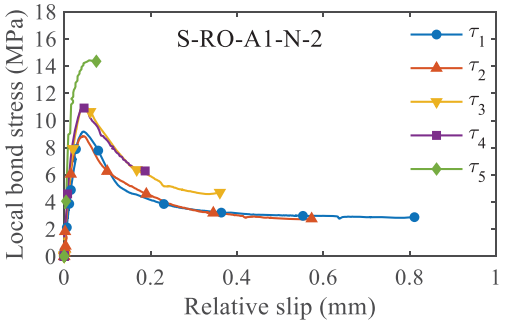

(b) S-RO-A1-N-2

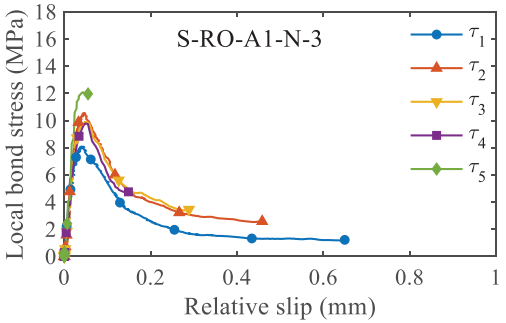

(c) S-RO-A1-N-3

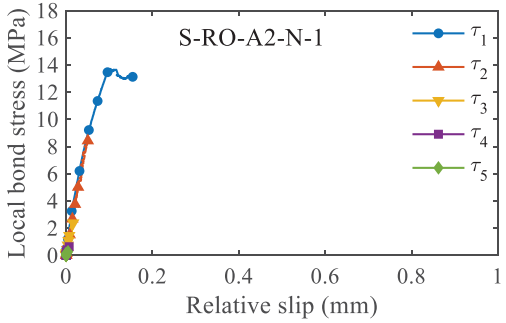

(d) S-RO-A2-N-1

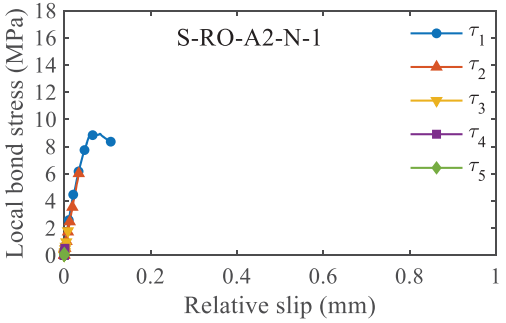

(e) S-RO-A2-N-2

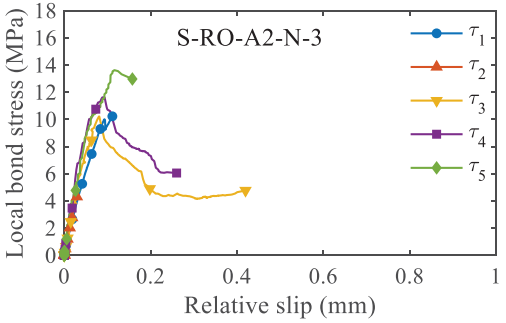

(f) S-RO-A2-N-3

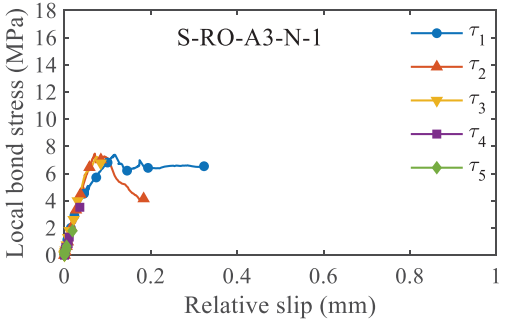

(g) S-RO-A3-N-1

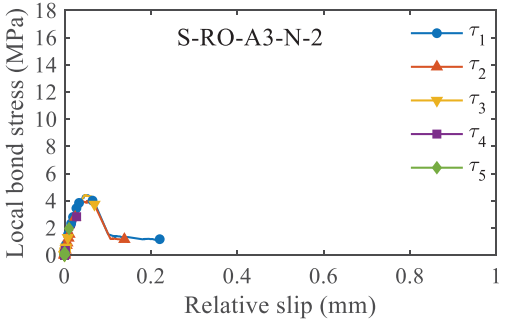

(h) S-RO-A3-N-2

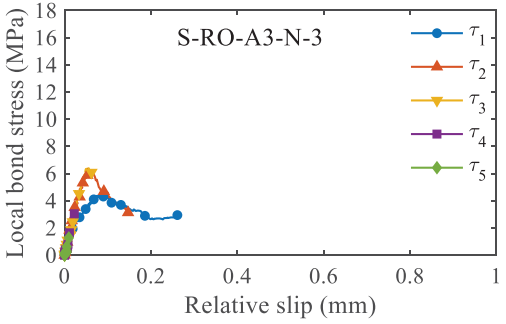

(i) S-RO-A3-N-3

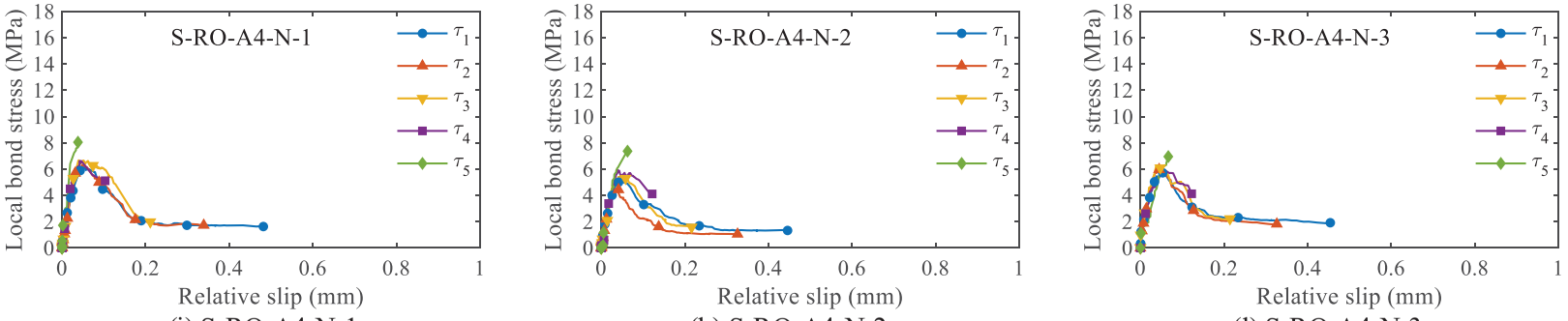

(j) S-RO-A4-N-1 (k) S-RO-A4-N-2 (l) S-RO-A4-N-3

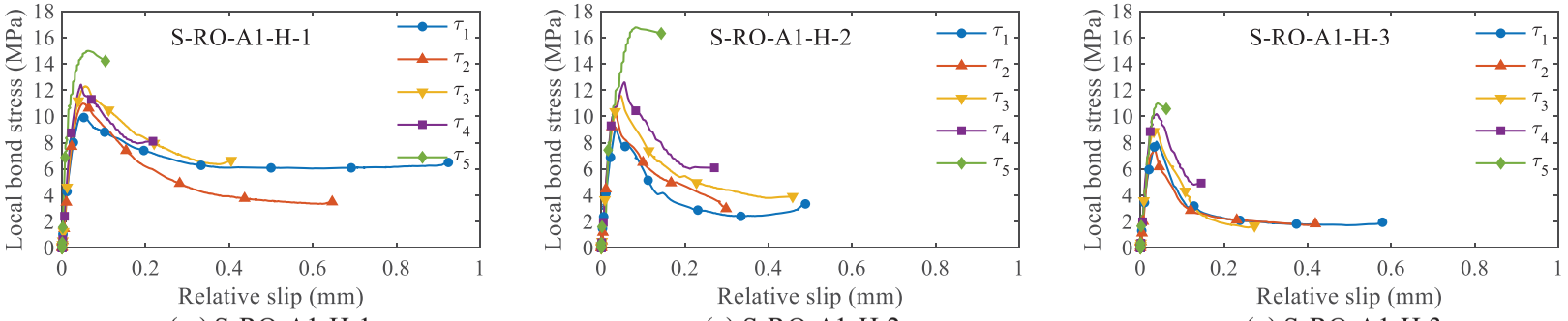

(m) S-RO-A1-H-1 (n) S-RO-A1-H-2 (o) S-RO-A1-H-3

Fig. 4.20 Local bond stress-slip relationships for CFRP strip specimens under static load

Post-fatigue

The post-fatigue local bond stress-slip relationships for both the CFRP rod and strip specimens after 10, 100, 1000, and 10,000 fatigue cycles are shown in Figs. 4.21 and 4.22, respectively, as well as their static counterparts for direct comparison. Note that for the CFRP rod specimens, when the experienced fatigue cycles were close to 10,000, the strain gauge near the loaded was damaged and thus the data of τ_1 was missing during the post-fatigue DPT [Fig. 4.21(m)-4.21(o)]. In addition, the average post-fatigue local bond strengths (τ_{avg}) and the local bond strengths (τ_f) for both the CFPR rod and strip specimens are summarized in Tables 4.7 and 4.8, respectively. The local bond strengths were calculated from the strain gauge readings only within the bonded regions that experienced softening stage (i.e., post-peak stress stage) during the fatigue cycles. It is assumed in this study that if the bond region sustained within the linear elastic stage during the fatigue cycles, its local bond performance was intact under the fatigue load.

In Fig. 4.21, with the increase of the experienced fatigue cycles, the local bond strength near the loaded end degraded to different extents for some rod specimens, e.g., τ_1 of R-SCSW-A1-1060-1E2-N-2 [Fig. 4.21(h)] and R-SCSW-A1-1060-1E3-N-2 [Fig. 4.21(k)], τ_2 of R-SCSW-A1-1060-1E4-N-1 [Fig. 4.21(m)] and τ_3 of R-SCSW-A1-1060-1E4-N-2 [Fig. 4.21(n)]. However, no substantial degradation in average bond strength was observed and the post-fatigue pull-out forces were even higher than that of their static counterparts because of the growth in concrete strength.

For the CFRP strip specimens, however, more significant degradation in local bond strength was observed, as illustrated in Fig. 4.22. Although inconsistency still existed within the same testing set of three identical specimens, the local bond strength of S-RO-A1-1060-1E1-N-1 [Fig. 4.22(d)] was only approximately half of that of S-RO-A1-1060-1E1-N-3 [Fig. 4.22(f)]. The local bond strength of S-RO-A1-1060-1E3-N-2 [Fig. 4.22(k)] was exceptionally high after 1000 fatigue cycles. Specimen S-RO-A1-1060-1E4-N-3 [Fig. 4.22(o)] still had a comparable local bond strength compared to the static counterparts, and the average local bond strength overall dropped

with the increase of fatigue cycles. Additionally, after a specific number of fatigue cycles, the local bond stress at the location near the loaded end was prone to keeping stable after reaching its peak magnitude with only minor softening behavior if not negligible, for instance, τ_1 after 100 fatigue cycles [Figs. 4.22(g)-4.22(o)] and τ_2 after 1000 fatigue cycles [Figs. 4.22(j)-4.22(o)]. The probable reason was the sliding friction failure mechanism of CFRP strip specimens. As the fatigue cycles increased, the relative slip near the loaded end at the FRP/adhesive interface accumulated until it reached a threshold where the interfacial debonding finally occurred, however, residual friction still existed at the interface and sustained the local bond stress with slow degradation under fatigue load.

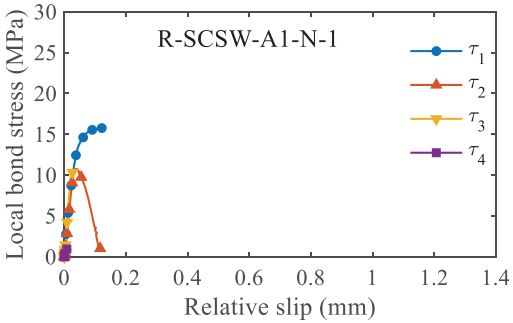

(a) R-SCSW-A1-N-1

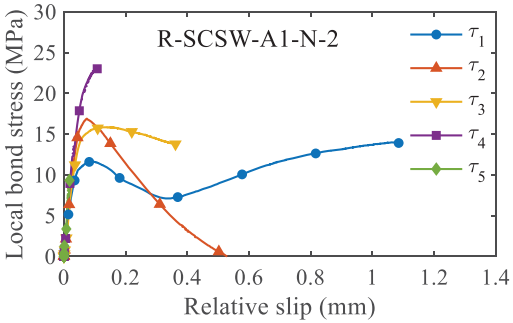

(b) R-SCSW-A1-N-2

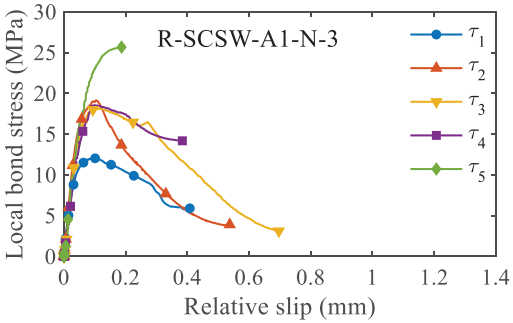

(c) R-SCSW-A1-N-3

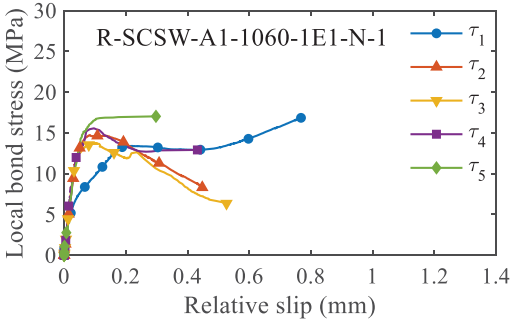

(d) R-SCSW-A1-1060-1E1-N-1

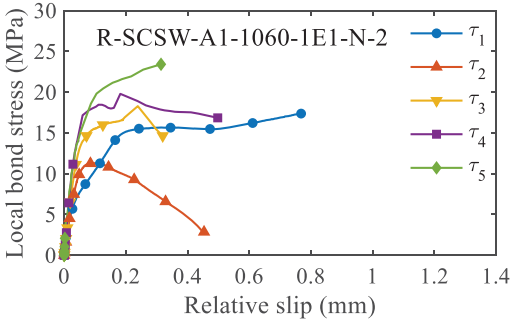

(e) R-SCSW-A1-1060-1E1-N-2

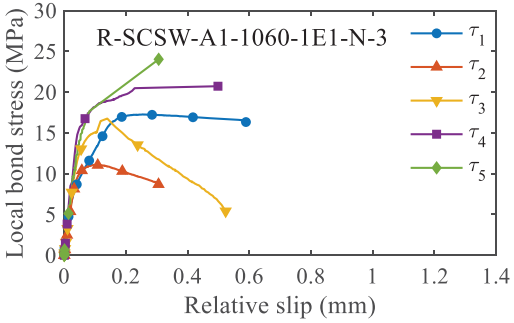

(f) R-SCSW-A1-1060-1E1-N-3

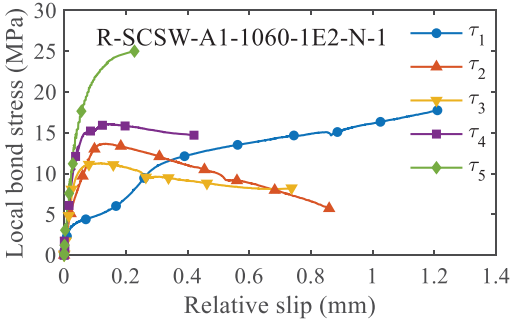

(g) R-SCSW-A1-1060-1E2-N-1

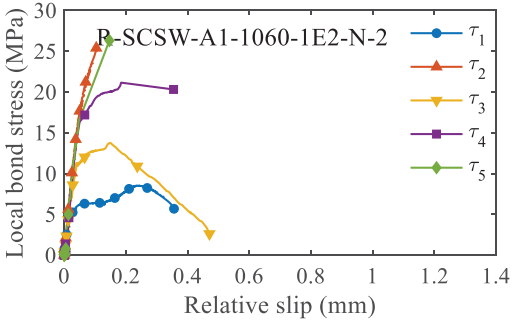

(h) R-SCSW-A1-1060-1E2-N-2

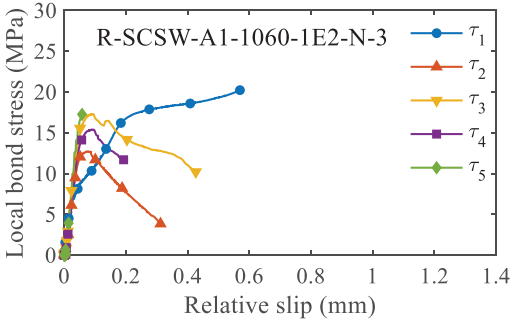

(i) R-SCSW-A1-1060-1E2-N-3

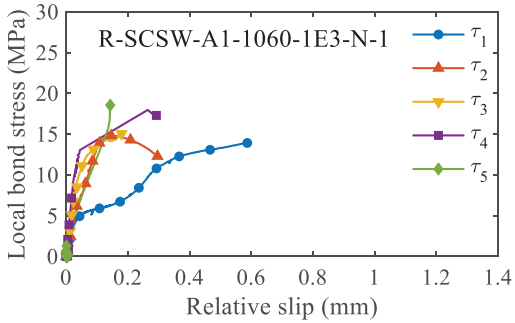

(j) R-SCSW-A1-1060-1E3-N-1

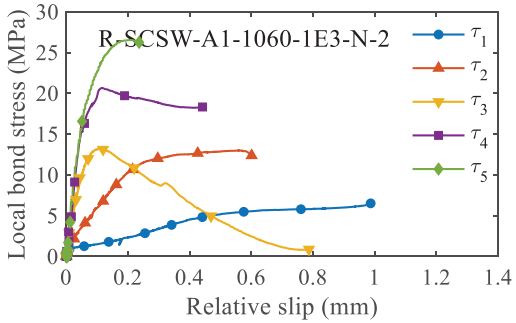

(k) R-SCSW-A1-1060-1E3-N-2

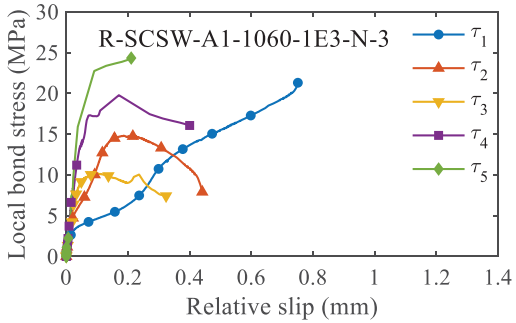

(l) R-SCSW-A1-1060-1E3-N-3

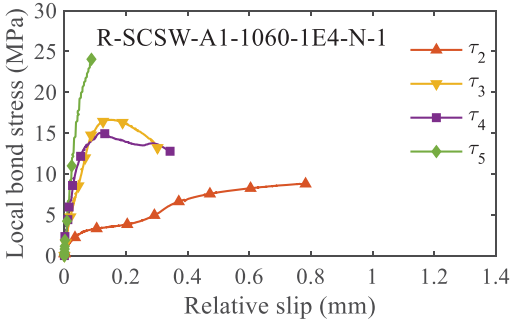

(m) R-SCSW-A1-1060-1E4-N-1

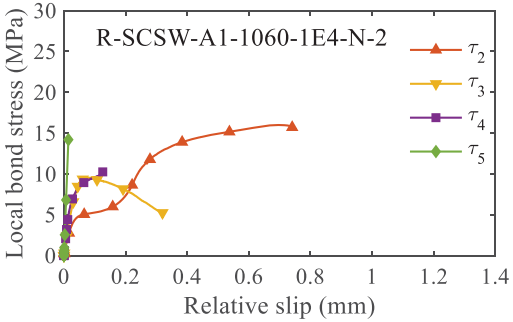

(n) R-SCSW-A1-1060-1E4-N-2

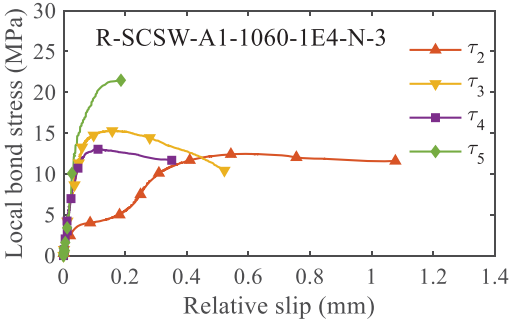

(o) R-SCSW-A1-1060-1E4-N-3

Fig. 4.21 Post-fatigue local bond stress-slip relationships for CFRP rod specimens

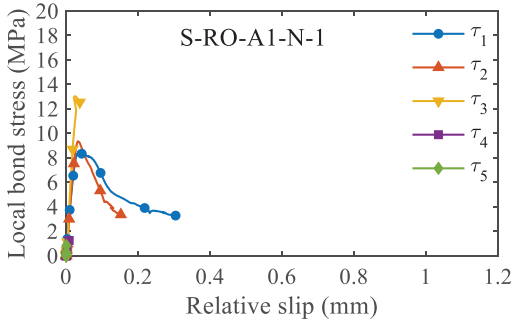

(a) S-RO-A1-N-1

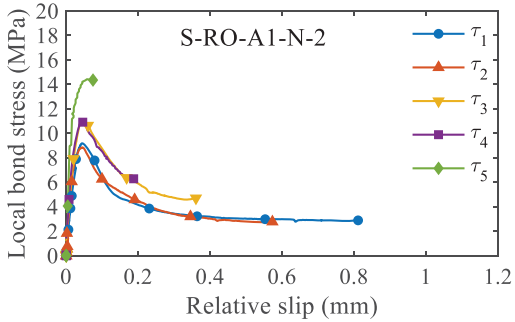

(b) S-RO-A1-N-2

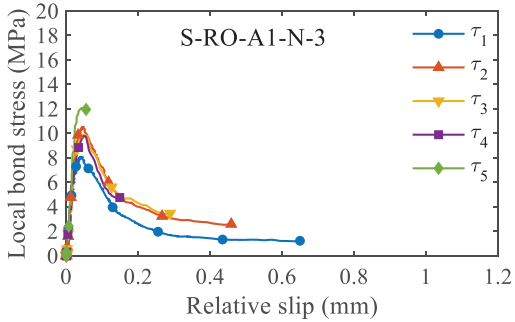

(c) S-RO-A1-N-3

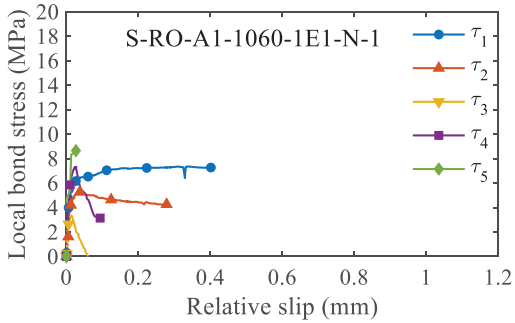

(d) S-RO-A1-1060-1E1-N-1

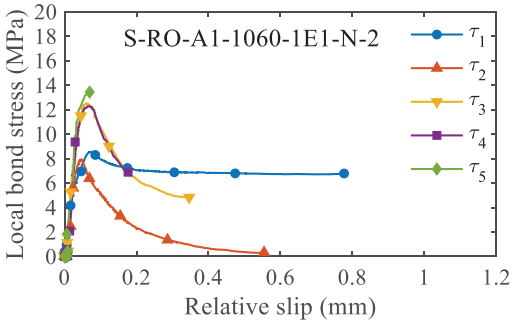

(e) S-RO-A1-1060-1E1-N-2

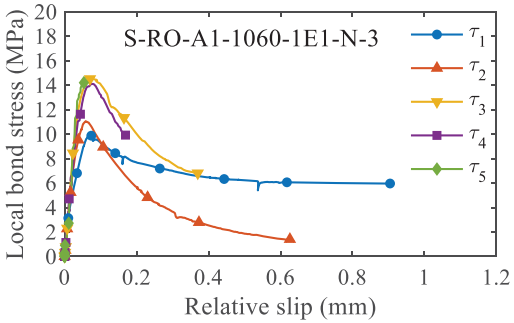

(f) S-RO-A1-1060-1E1-N-3

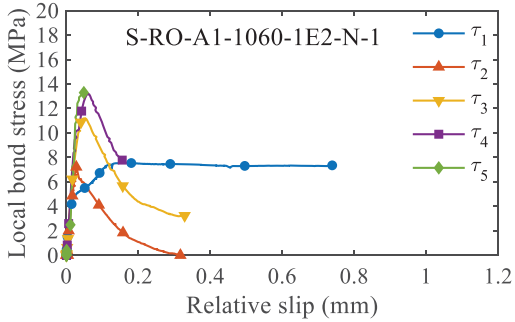

(g) S-RO-A1-1060-1E2-N-1

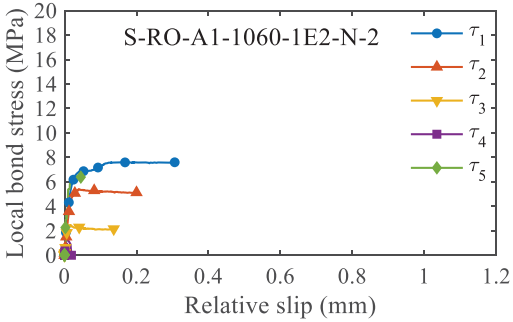

(h) S-RO-A1-1060-1E2-N-2

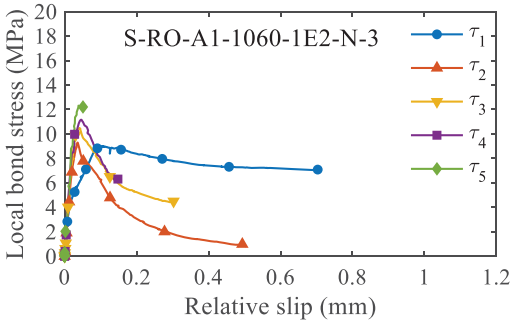

(i) S-RO-A1-1060-1E2-N-3

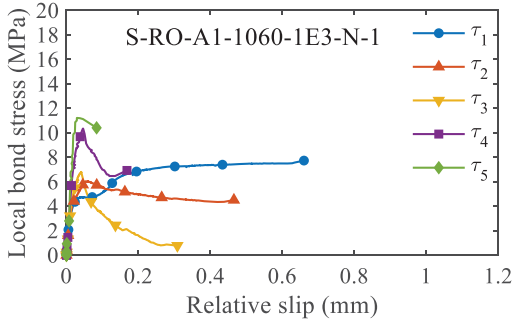

(j) S-RO-A1-1060-1E3-N-1

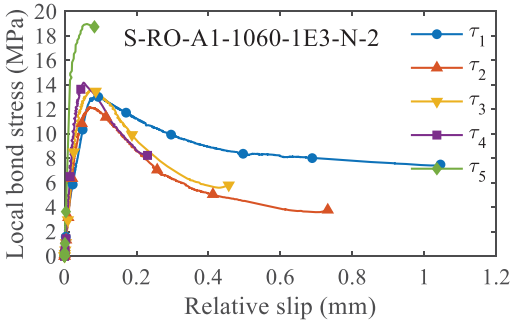

(k) S-RO-A1-1060-1E3-N-2

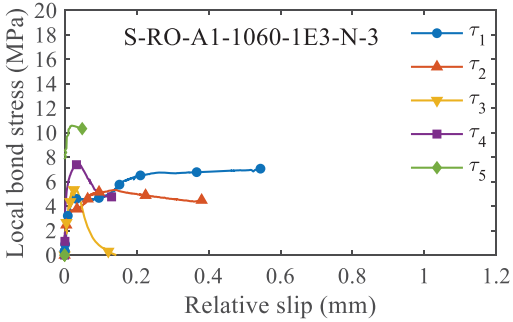

(l) S-RO-A1-1060-1E3-N-3

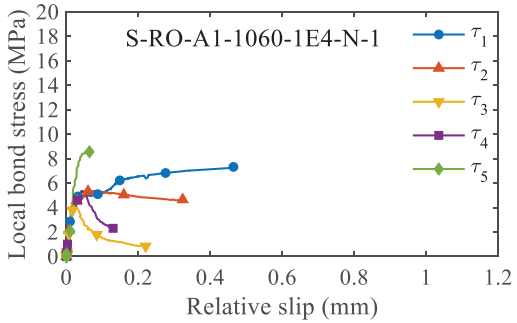

(m) S-RO-A1-1060-1E4-N-1

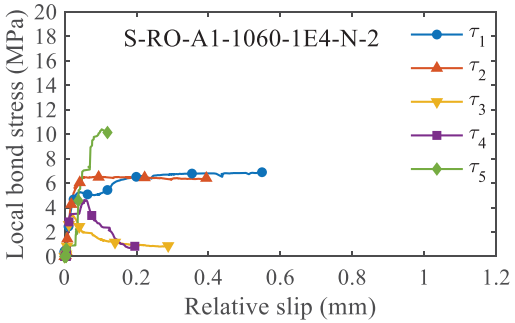

(n) S-RO-A1-1060-1E4-N-2

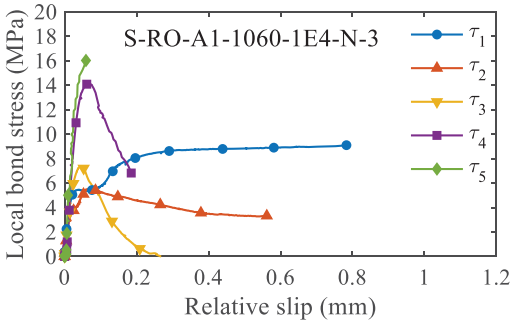

(o) S-RO-A1-1060-1E4-N-3

Fig. 4.22 Post-fatigue local bond stress-slip relationships for CFRP strip specimens

4.4 Local bond performance during fatigue cycles

Readings from the five strain gauges and linear potentiometer were recorded throughout the fatigue cycles until specimen failure or the one million cycles threshold for those specimens tested for fatigue life. To visualize the development of the local bond stress (τ_i) under the maximum applied fatigue load (P_{max}) during the fatigue cycles, as well as the degradation in stiffness of the concrete specimen, the test results are plotted for both the CFRP rod and strip specimens and are categorized by different cross-sectional shape, surface treatment, adhesive epoxy, fatigue load range and concrete strength, as presented in Figs. 4.23-4.46. The local bond stress was calculated by using Eq. 4.2, and the relative slip between the FRP reinforcement and concrete at the loaded end during the fatigue cycles was derived from Eq. 4.3.

In addition, the development of the local bond stress τ_i at different locations along the bond line during the entire fatigue loading process is presented in a semilogarithmic scale, e.g., Fig. 4.23, where the five curves in each plot represent the local bond stress τ_1-τ_5 throughout the fatigue cycles (with a logarithmic base of 10 in the x axis for the number of fatigue cycles). Note that some of the strain gages near the loaded end was damaged at earlier cycles while those near the free end survived a much larger number of fatigue cycles. The logarithmic scale is commonly adopted in representing the number of fatigue cycles when relating the stress or load range to the fatigue life.

Moreover, for the illustrations of the development in the local bond stress distribution during the fatigue cycles (e.g., Fig. 4.24) and the applied fatigue load range vs. relative slip at the loaded end during the fatigue cycles (e.g., Fig. 4.25), the multiple curves in each plot represent the test results corresponding to different percentages of the fatigue life (N_f) with a logarithmic base of 10, i.e., 0-100%logN_f with a 10% interval. The distribution of the local bond stress helps indicating the utilization of the bond length under the fatigue cycles, whilst the change in the relative slip within each fatigue cycle marks the accumulated fatigue bond damage or degradation.

4.4.1 Influence of cross-sectional shape

Test results for specimen set R-RO-A1-1060-F-N (Set 9 in Table 4.7) and set S-RO-A1-1060-F-N (Set 18 in Table 4.8) are illustrated and compared in Figs. 4.23-4.26. Except for the cross-sectional shape, these two specimen sets were mostly identical with the same cross-section area, surface characteristics, epoxy adhesive, concrete material and applied fatigue load range corresponding to their static counterpart. Notice that even though the bond performance of set R-RO-A1-N exceeded set S-RO-A1-N in almost every aspect, e.g., higher average pull-out force, higher local bond strength and better utilization of concrete material with no premature sliding at the FRP/adhesive interface. Its fatigue behavior under the same percentage range (10-60%P_f) was not comparable to that of the roughened CFRP strip specimen.

In terms of the local bond stress development under P_{max} as shown in Fig. 4.23, specimen set R-RO-A1-1060-F-N degraded much faster than set S-RO-A1-1060-F-N with the increase of fatigue cycles though the local bond stress level of R-RO-A1-1060-F-N was still higher on average. This was mainly caused by a weaker roughened texture on the CFRP rod which was worn out more rapidly than that of the CFRP strip during the fatigue cycles. As a result, the specimens using roughened CFRP rod failed with an average fatigue life of 82,043 cycles while the specimens using roughened CFRP strip failed on average at 969,085 cycles (excluding the first specimen in the set that failed much earlier due to its a noticeable poor quality in the surface treatment).

For the development in local bond stress distribution under P_{max}, these two sets had similar behavior in many aspects, as illustrated in Fig. 4.24. They both followed the distribution pattern that the peak local bond stress gradually migrated from the region near loaded end to the regions near free end. Besides, the stress level at each location along the bond line decreased to a low magnitude if not zero after reaching its peak stress. Except for the local bond stress τ_5 which remained relatively high near the fatigue failure, all the other local bond stresses (i.e., τ_1 - τ_4) dropped significantly comparing to their peak stress magnitudes. It implied that the 250 mm bond

length had almost been fully utilized through the fatigue cycles and a good consistency of bond performance along the bond length for both two sets. However, the initial stress distribution of these two specimen sets were not the same. At the first fatigue cycle (labeled by 0% in the diagram), the peak local bond stress of set S-RO-A1-1060-F-N was located at 25 mm away from the loaded end, by contrast, it appeared at 75 mm away from the loaded end for set R-RO-A1-1060-F-N. This meant that a longer bond length had to be developed to balance the applied 60%P_f for set R-RO-A1-1060-F-N than set S-RO-A1-1060-F-N at the first fatigue cycle, which also contributed to the shorter fatigue life of the former specimen set.

Moreover, the relative slip at the loaded end under both P_{min} and P_{max} within one fatigue cycle is plotted in Fig. 4.25, along with their applied fatigue load range through the fatigue cycles for both two specimen sets. It could be seen that the magnitude of the relative slip of set R-RO-A1-1060-F-N was only slightly larger than that of set S-RO-A1-1060-F-N before 80%logN_f, however, the difference in the relative slip rapidly increased after 80%logN_f, and the maximum slip of set R-RO-A1-1060-F-N was almost triple of that of set S-RO-A1-1060-F-N. This indicated a larger relative slip close to failure at the FRP/adhesive interface of set R-RO-A1-1060-F-N and the result was consistent with its interfacial debonding failure mechanism. Meanwhile, in Fig. 4.25, the slope of each line represents the overall stiffness of the NSM FRP-to-concrete bonded joints during the fatigue cycles and is further illustrated in Fig. 4.26. Two represented specimens were selected to compare the stiffness change under the fatigue loading. It is obvious that, the stiffness of set R-RO-A1-1060-F-N was always smaller than that of set S-RO-A1-1060-F-N even though these two sets had the same trend of reduction in bond stiffness. This phenomenon was not surprising because the set R-RO-A1-1060-F-N had a much shorter fatigue life. This was caused by the change in failure mechanism from cohesive failure in substrate concrete under static load to failure at the FRP/adhesive interface under cyclic load.

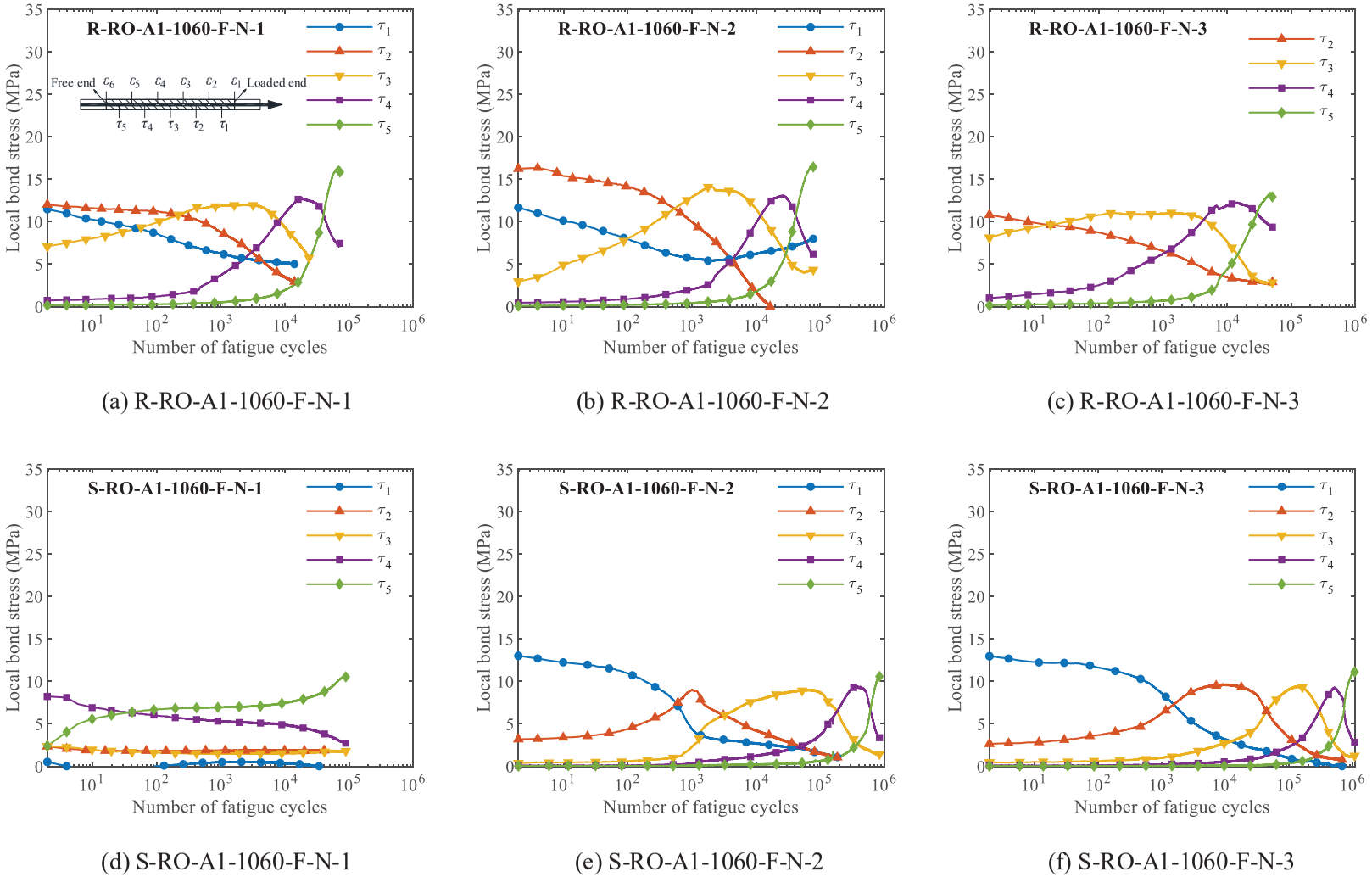

(a) R-RO-A1-1060-F-N-1 (b) R-RO-A1-1060-F-N-2 (c) R-RO-A1-1060-F-N-3

(d) S-RO-A1-1060-F-N-1 (e) S-RO-A1-1060-F-N-2 (f) S-RO-A1-1060-F-N-3

Fig. 4.23 Local bond stress development under P_{max} during the fatigue cycles for CFRP specimens of different cross-section

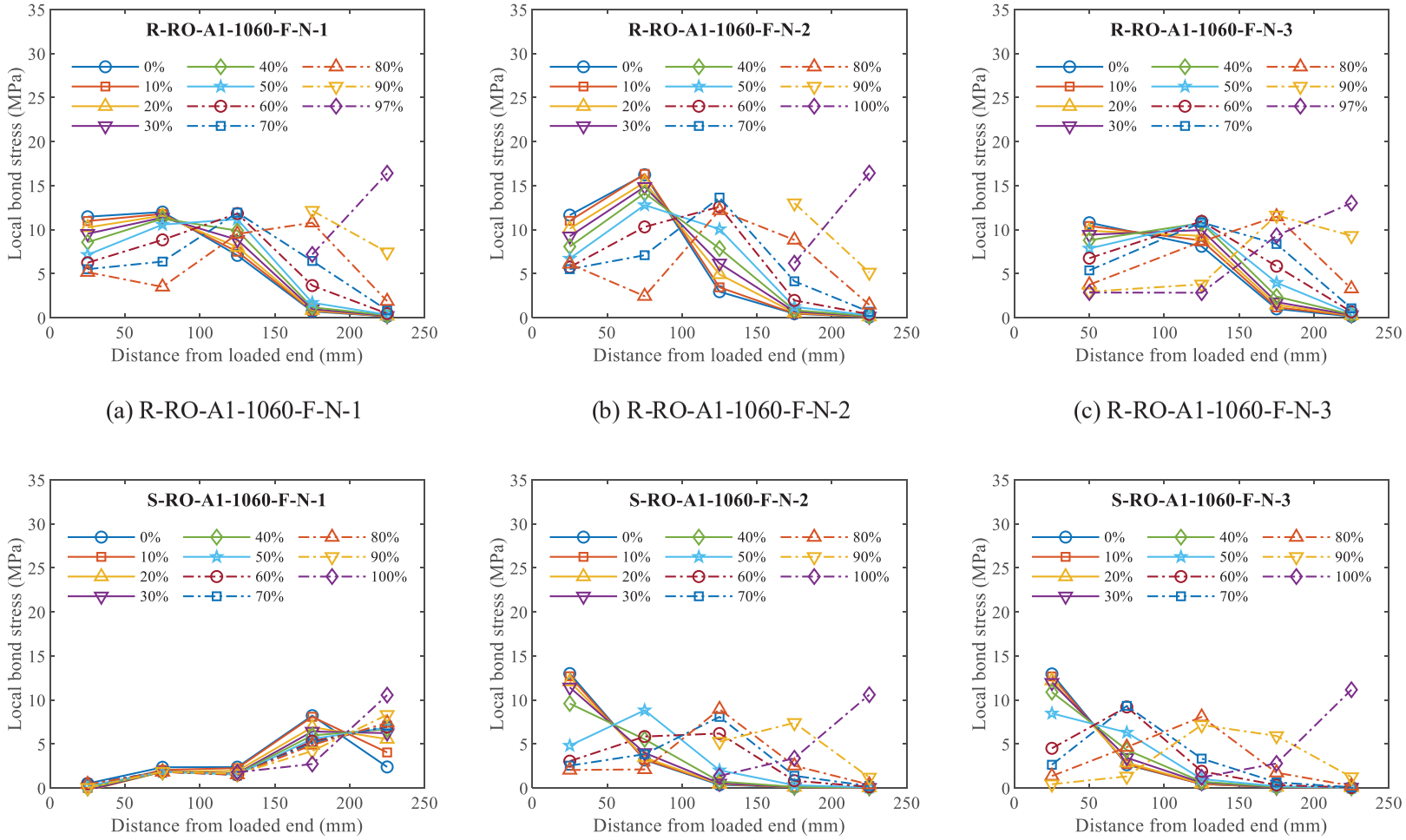

(a) R-RO-A1-1060-F-N-1 (b) R-RO-A1-1060-F-N-2 (c) R-RO-A1-1060-F-N-3

(d) S-RO-A1-1060-F-N-1 (e) S-RO-A1-1060-F-N-2 (f) S-RO-A1-1060-F-N-3

Fig. 4.24 Development in local bond stress distribution under P_{max} during the fatigue cycles for CFRP specimens of different cross-section

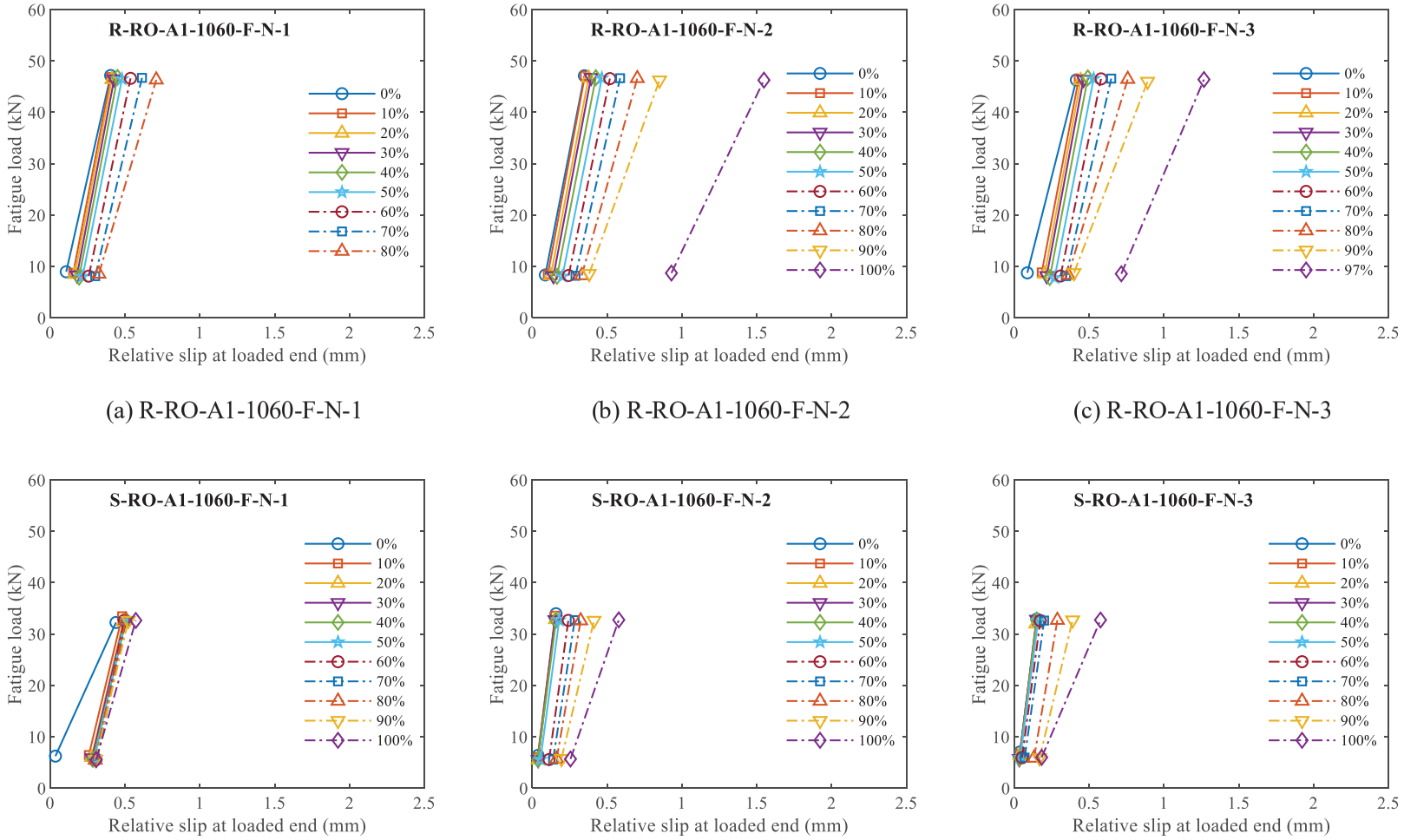

(a) R-RO-A1-1060-F-N-1 (b) R-RO-A1-1060-F-N-2 (c) R-RO-A1-1060-F-N-3

(d) S-RO-A1-1060-F-N-1 (e) S-RO-A1-1060-F-N-2 (f) S-RO-A1-1060-F-N-3

Fig. 4.25 Applied fatigue load range vs. relative slip at the loaded end during the fatigue cycles for CFRP specimens of different cross-section

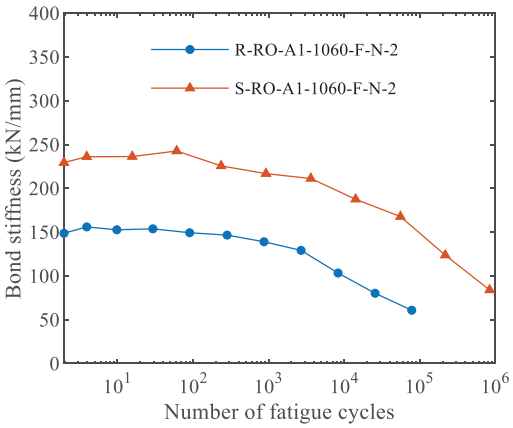

Fig. 4.26 Stiffness of NSM FRP-to-concrete bonded joints during the fatigue cycles for CFRP specimens of different cross-section

4.4.2 Influence of surface treatment

Figs. 4.27-4.30 show the effect of different types of surface treatment of the NSM CFRP rod (RO, SC, SCSW) on the fatigue bond behavior of the rod specimens (Sets 9-11 in Table 4.7) that used the same adhesive type under the same fatigue load range, respectively. As previously discussed in Chapter 4.3.1, these three sets of CFRP rod specimens varied in failure mechanism under fatigue cycles. Both specimen sets R-RO-A1-1060-F-N (set 9) and R-SC-A1-1060-F-N (set 10) failed much earlier under fatigue load because their textured or sand-coated surface were worn out quickly and, hence, interfacial sliding occurred. Specimen set R-SCSW-A1-1060-F-N (set 11), however, survived much longer and reached the predefined upper limit of fatigue cycles without significant degradation at the FRP/adhesive interface. This difference in failure mechanism was again confirmed and quantified by their local bond stress development under P_{max} during the fatigue cycles, as presented in Fig. 4.27. Herein, the local bond stress development for specimen set R-RO-A1-1060-F-N and R-SC-A1-1060-F-N were similar in terms of degradation pattern and rate, as well as the peak local bond stress at approximately 15 MPa under the fatigue cycles. By comparison, the peak local bond stress of specimen set R-SCSW-A1-1060-F-N was about 20 MPa on average. Although τ_1 and τ_2 of specimen set R-SCSW-A1-1060-F-N dropped rapidly in the

early cycles before 10^4, similar to that of the other two sets, the development of τ_3, τ_4 and τ_5 were all much slower. For example, τ_5 of specimen sets R-RO-A1-1060-F-N and R-SC-A1-1060-F-N reached their peak at around 10^5 fatigue cycles or earlier while τ_5 of set R-SCSW-A1-1060-F-N were still in the process of climbing, especially for R-SCSW-A1-1060-F-N-1 in which τ_5 had just started to increase [Fig. 4.27(g)].

As for the development in the local bond stress distribution under P_{max} during the fatigue cycles (Fig. 4.28), all the three specimen sets behaved similarly. At the beginning of the fatigue loading (the first cycle), the peak local bond stress occurred at a location between 50 mm and 100 mm away from the loaded end. Then the peak magnitude gradually migrated toward the free end until the residual bond strength was unable to resist the applied fatigue load. The only difference existed in the degradation rate and the magnitude value of the peak local bond stress. With a slower degradation rate and a higher local bond stress level especially within the region between 200 and 250 mm away from the loaded end, the specimen set R-SCSW-A1-1060-F-N reached a much higher fatigue life than the other two sets.

In addition, the applied fatigue load range vs. relative slip at the loaded end during the fatigue cycles for these three sets are illustrated with a constant 10%logN_f interval in Fig .4.29. It should be noted that all the data were derived and plotted up to the failure of the embedded strain gauges. Therefore, not all the curves could reach 100% fatigue life. It could be seen that specimen set R-RO-A1-1060-F-N had the largest relative slip increase at the loaded end over 90%logN_f [Figs. 4.29(b) and (c)]. This sudden increase in the relative slip of set R-RO-A1-1060-F-N implied the switch in failure mode from concrete breakage to interfacial sliding when the textured surface was mostly worn out. But due to the lack of data beyond 90%logN_f of specimen set R-SC-A1-1060-F-N and beyond 70%logN_f of specimen set R-SCSW-A1-1060-F-N, it is difficult to compare the severity of relative slip at the loaded end for these three sets. Nevertheless, the typical development in stiffness of these three types of NSM FRP-to-concrete bonded joints could still be derived and compared in Fig. 4.30. The plot presented a very close bond stiffness and degradation rate of these

specimens which was not surprising because they only differed in the surface treatment of CFRP reinforcement. It implied a low relevance between the bond stiffness and surface treatment of CFRP reinforcement though the type of surface treatment was proved to be important in the fatigue bond behavior of NSM FRP-to-concrete bonded joints.

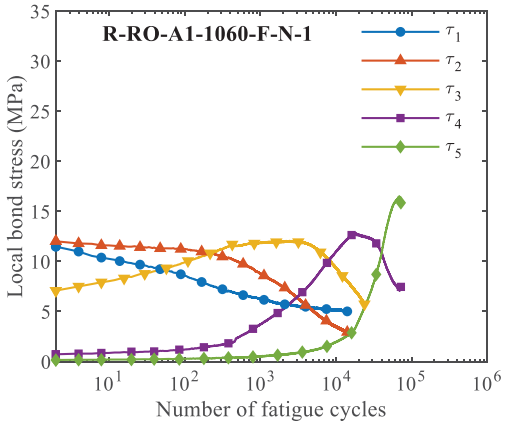

(a) R-RO-A1-1060-F-N-1

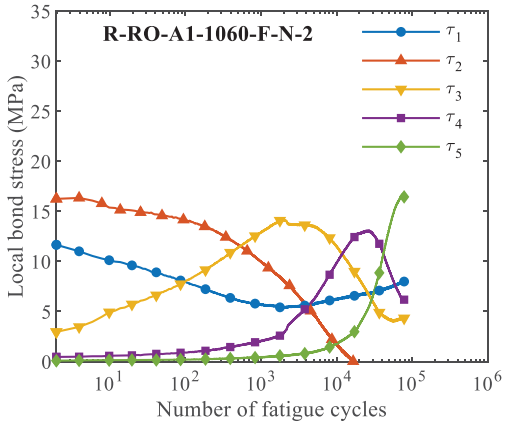

(b) R-RO-A1-1060-F-N-2

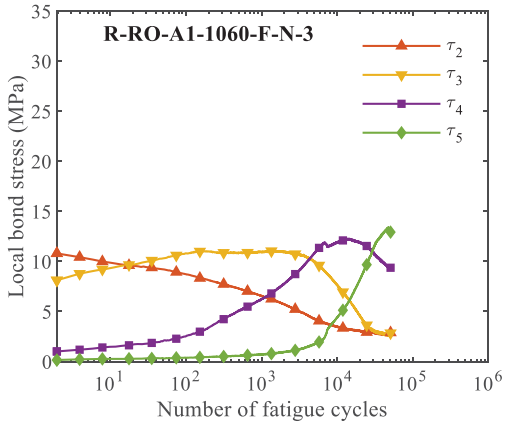

(c) R-RO-A1-1060-F-N-3

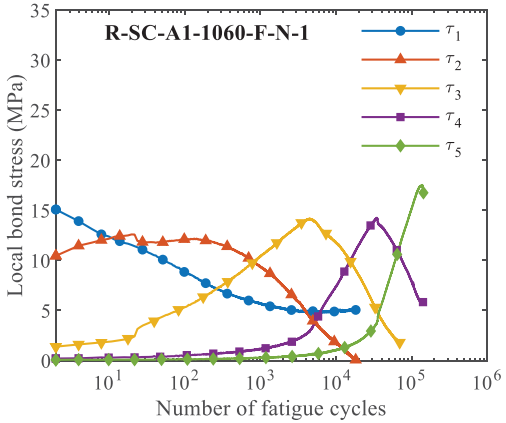

(d) R-SC-A1-1060-F-N-1

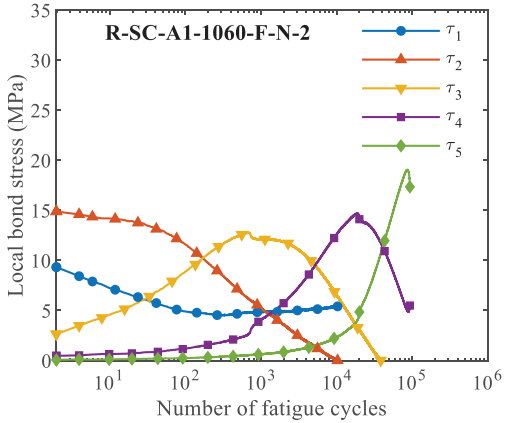

(e) R-SC-A1-1060-F-N-2

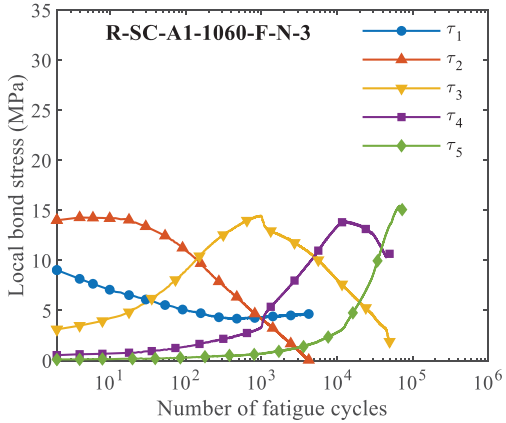

(f) R-SC-A1-1060-F-N-3

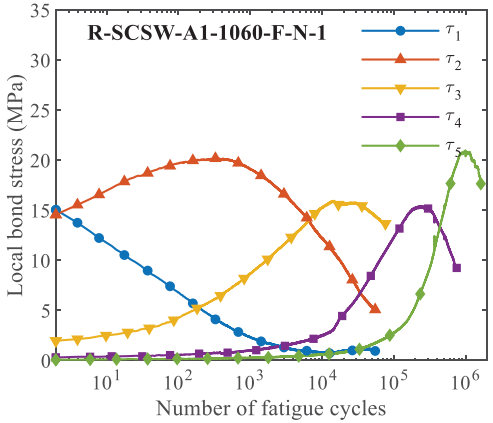

(g) R-SCSW-A1-1060-F-N-1

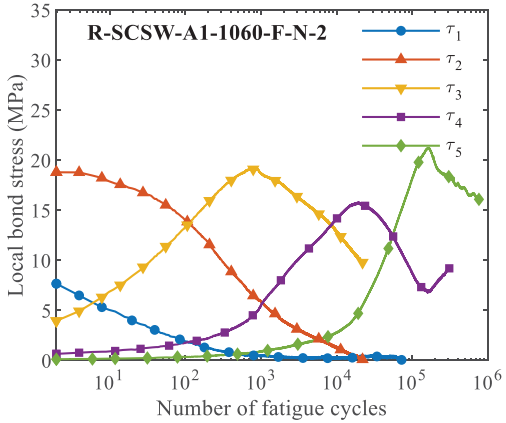

(h) R-SCSW-A1-1060-F-N-2

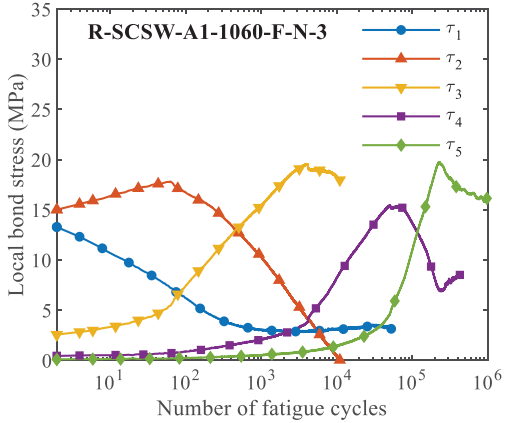

(i) R-SCSW-A1-1060-F-N-3

Fig. 4.27 Local bond stress development under P_{max} during the fatigue cycles for CFRP rod specimens of different surface treatment

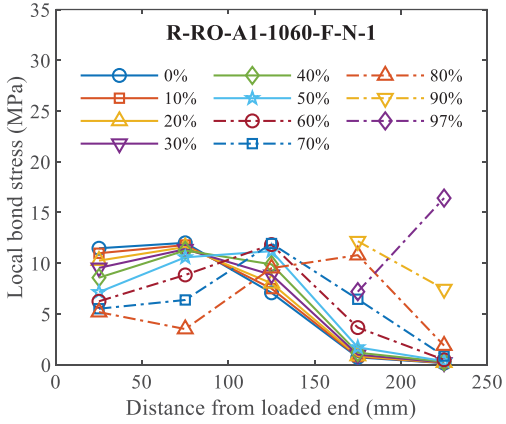

(a) R-RO-A1-1060-F-N-1

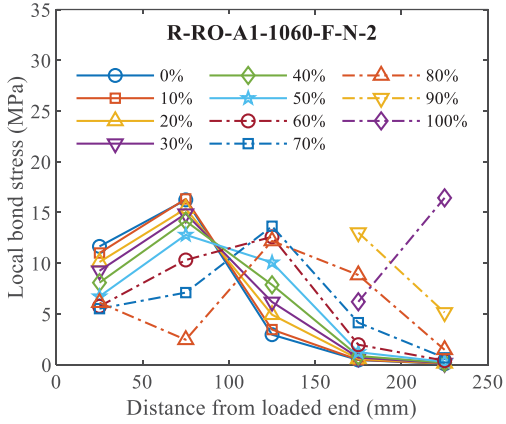

(b) R-RO-A1-1060-F-N-2

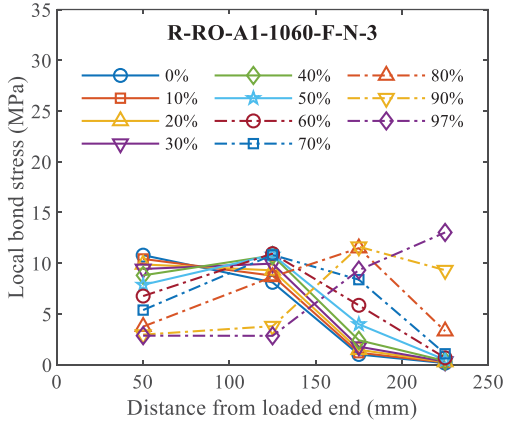

(c) R-RO-A1-1060-F-N-3

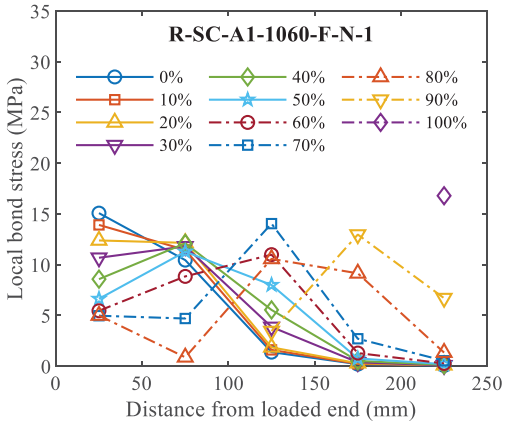

(d) R-SC-A1-1060-F-N-1

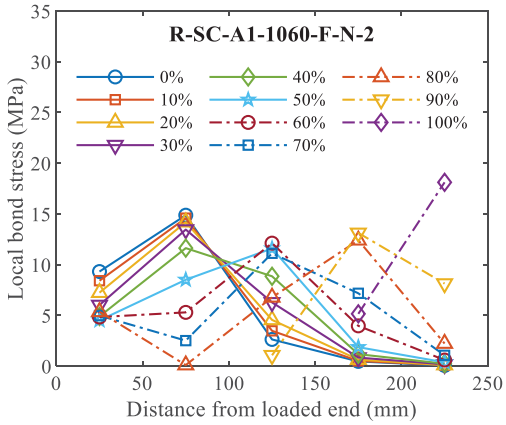

(e) R-SC-A1-1060-F-N-2

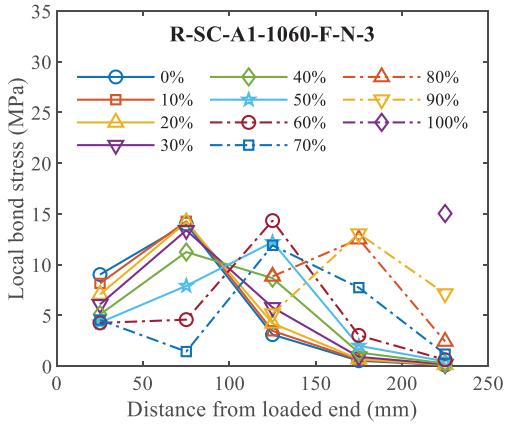

(f) R-SC-A1-1060-F-N-3

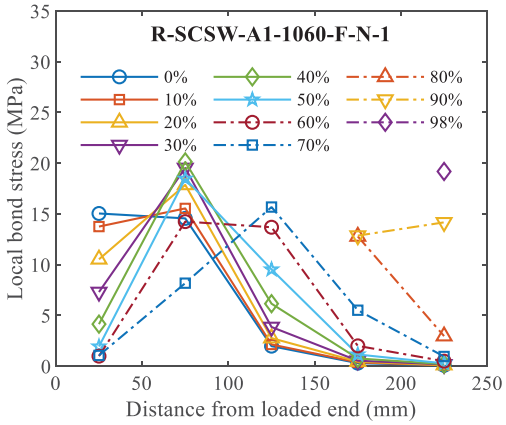

(g) R-SCSW-A1-1060-F-N-1

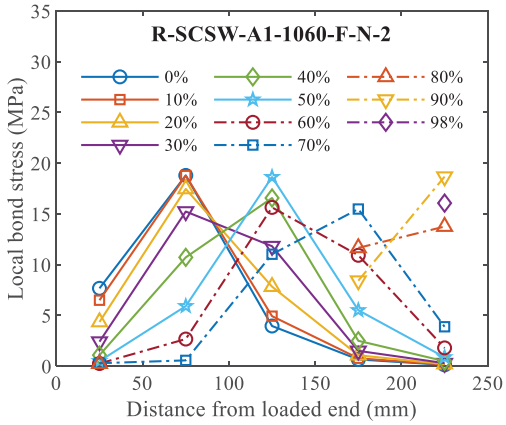

(h) R-SCSW-A1-1060-F-N-2

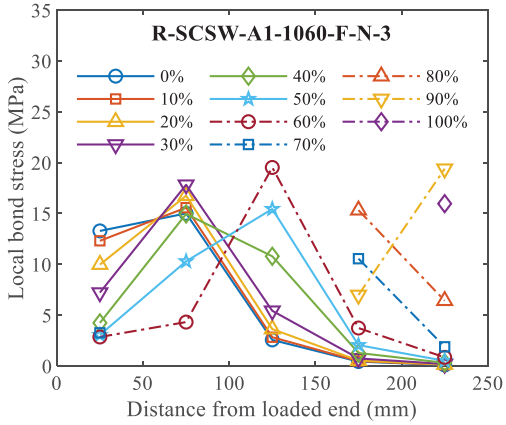

(i) R-SCSW-A1-1060-F-N-3

Fig. 4.28 Development in local bond stress distribution under P_{max} during the fatigue cycles for CFRP rod specimens of different surface treatment

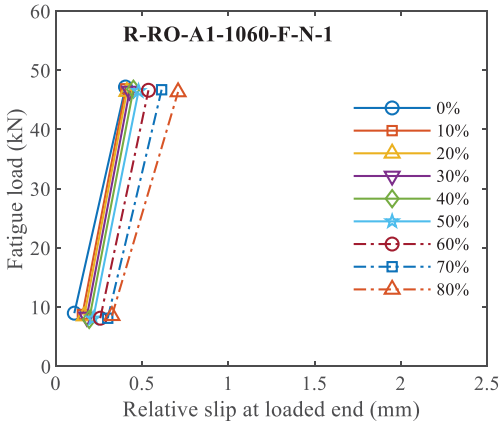

(a) R-RO-A1-1060-F-N-1

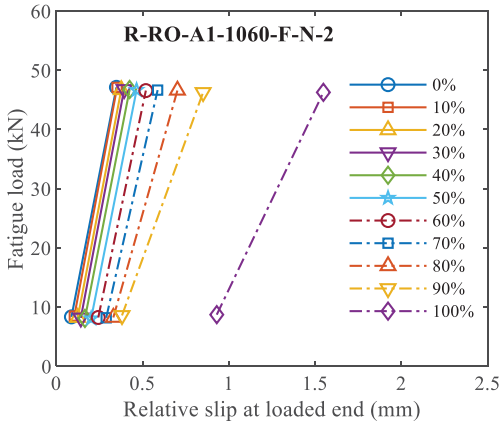

(b) R-RO-A1-1060-F-N-2

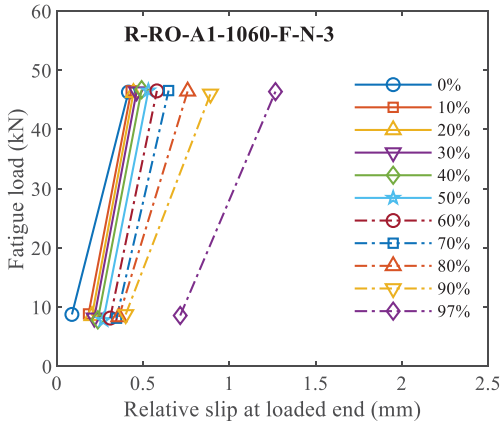

(c) R-RO-A1-1060-F-N-3

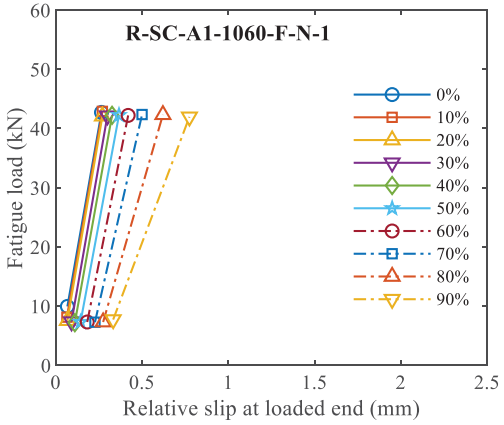

(d) R-SC-A1-1060-F-N-1

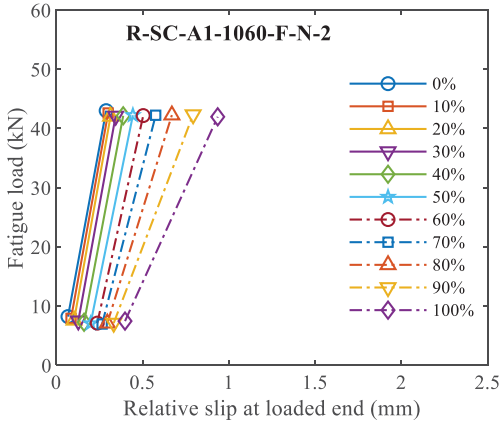

(e) R-SC-A1-1060-F-N-2

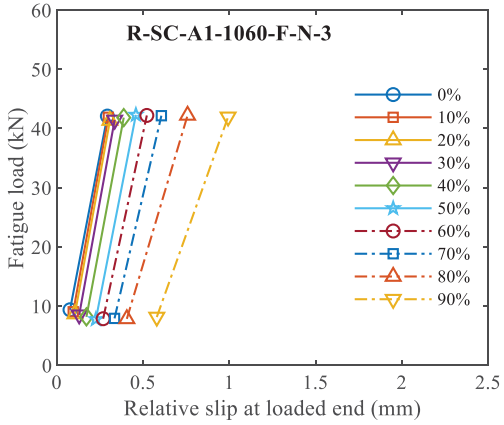

(f) R-SC-A1-1060-F-N-3

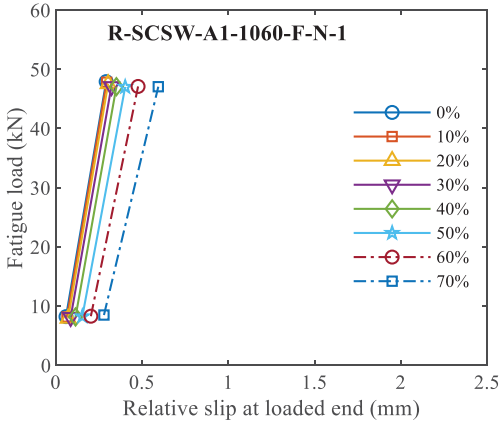

(g) R-SCSW-A1-1060-F-N-1

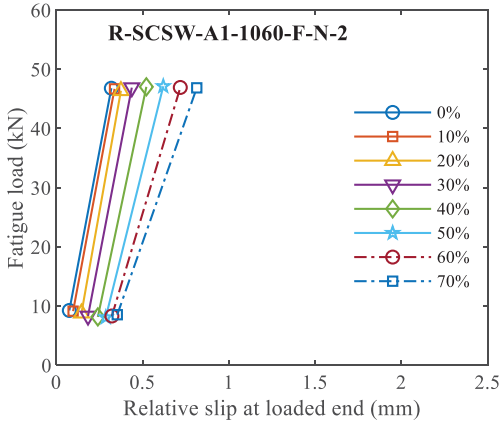

(h) R-SCSW-A1-1060-F-N-2

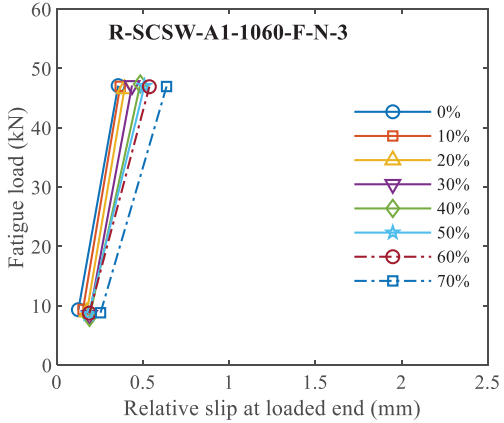

(i) R-SCSW-A1-1060-F-N-3

Fig. 4.29 Applied fatigue load range vs. relative slip at the loaded end during the fatigue cycles for CFRP rod specimens of different surface treatment

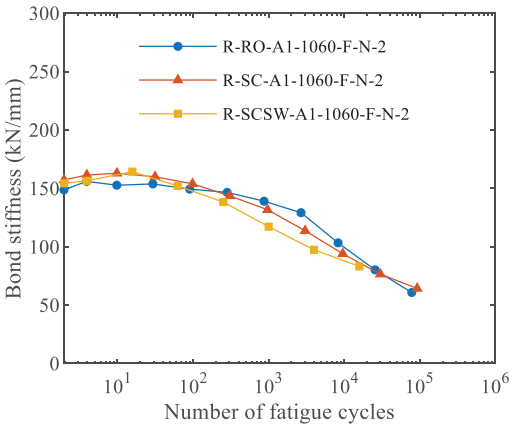

Fig. 4.30 Stiffness of NSM FRP-to-concrete bonded joints during the fatigue cycles for CFRP specimens of different surface treatment

4.4.3 Influence of epoxy adhesive

Figs. 4.31-4.34 show the effect of epoxy-based adhesive type (A1, A2, A3 and A4) on the fatigue bond behavior of the strip specimens (Sets 18-21 in Table 4.8) that had the same surface treatment of the CFRP strip under the same fatigue load range. It should be noted that specimen S-RO-A2-1060-F-N-1 failed unexpectedly at the first cycle of the fatigue loading. Specimen S-RO-A1-1060-F-N-1 showed relatively low local bond stress for the region near the loaded end (0-150 mm) at the first cycle of fatigue loading [Fig. 4.32(a)], which led to a much earlier failure as compared to the other specimens in the same set. This inconsistency and variation in local bond strength did exist when deviation of product quality, including epoxy adhesive and CFRP reinforcement, was relatively high and could become more significant with improper construction process. These two specimens are therefore excluded from the comparison discussed herein. Of course, with proper mix proportion of epoxy adhesive and meticulous embedment process, specimen set S-RO-A2-1060-F-N could still reach fatigue life as high as those of set S-RO-A1-1060-F-N, e.g., S-RO-A2-1060-F-N-2 and S-RO-A2-1060-F-N-3 as summarized in Table 4.8.

The specimen set using epoxy adhesive A1 (Pilgrim-Magmaflow Grout-Pak CF) showed a smooth increase followed by a gradual decrease pattern in the development of the local bond stress

at all locations within the bond length [Figs. 4.31(b) and (c)]. The local bond stress of specimen set using epoxy adhesive A2 (Sikadur-32 Hi-Mod), however, behaved more stagewise with either a sudden drop or increase during the fatigue cycles [Figs. 4.31(e) and (f)], indicating a more brittle behavior of the bond under fatigue as compared to the specimen set using epoxy A1. Note that this specimen set could still survive up to one million cycles with a considerable post-fatigue load-carrying capacity, i.e., 50.20 kN for S-RO-A2-1060-F-N-3. On the other hand, the specimen sets using epoxy adhesive A3 (Simpson-ETI-GV) and A4 (BASF-MasterEmaco ADH 327) both survived the targeted one million cycles, after which they were loaded statically up to failure for their post-fatigue or residual capacity. It can be seen that the development of their local bond stress during the one million cycles were fairly steady [Figs. 4.31(g)-4.31(l)]. Except for the location near the loaded end (τ_1) where some minor degradation was observed, all other regions showed only small increase in the stress level, indicating insignificant deterioration of the bond along the bond length. Although it is noted that the post-fatigue capacity of some specimens was slightly higher than their static counterpart as shown in Table 4.8, it could be due to the variation of material and construction quality in addition to the 3-month time difference between the static and fatigue test during which additional curing allowed the gain of some extra strength in the materials. Regardless, it consistently supported the insignificant degradation of the bond under fatigue as previously discussed. Interestingly, in comparison with the epoxy type A1 and A2, A3 and A4 have a lower shear strength (Table 4.3), attributing to a weaker local bond strength in the specimens but also slower degradation of the bond under the same fatigue load range.

In Fig. 4.32, the development in the local bond stress distribution under P_{max} during the fatigue cycles was consistent with the results of the fatigue life observed for those CFRP strip specimens. For example, the peak local bond stress of the specimen sets using epoxy adhesive A1 and A2 migrated from the loaded end to the locations near the free end, showing a full utilization of the bond length under the applied fatigue load range [Figs. 4.32(a)-4.32(f)]. By contrast, except for S-RO-A4-1060-F-N-1, the local bond stress distribution of specimens using epoxy adhesive A3

and A4 were relatively stable throughout the entire one million cycles. The peak local bond stress did not show much evolvement toward the free end under the applied 10-60% fatigue load range [Fig. 4.32(g)-4.32(l)].

On the other hand, the relationship of the applied fatigue load range vs. the relative slip at the loaded end at both upper and lower limit in one fatigue cycle for the CFRP strip specimens is plotted in Fig. 4.33. The relative slips at both upper and lower limit gradually increased during the fatigue cycles regardless of the type of epoxy adhesives. By comparison, specimen sets using either epoxy adhesive A1 or A2 had higher growth rate in relative slip at the loaded end than sets using A3 or A4. Neither specimen set using A3 or A4 had maximum relative slip larger than 0.2 mm at one million cycles while specimen set using A1 or A2 could reach approximately 0.6 mm at fatigue failure. This result reconfirmed a more significant degradation in bond for specimen set using A1 or A2 than specimen set using A3 or A4. Moreover, the overall stiffness of the NSM FRP-to-concrete bonded joints during the fatigue cycles for those CFRP strip specimens are derived and compared in Fig. 4.34. It should be noted that only one representative specimen in each set was plotted for concise illustration. The overall stiffness of specimen set S-RO-A3-1060-F-N and S-RO-A4-1060-F-N were close in magnitude and higher than that of specimen set S-RO-A1-1060-F-N and S-RO-A2-1060-F-N. Among these four CFRP specimen sets, only minor decrease in stiffness was observed for specimen set S-RO-A3-1060-F-N and S-RO-A4-1060-F-N, while specimen set S-RO-A1-1060-F-N presented the most significant drop in stiffness especially after 10^4 fatigue cycles.

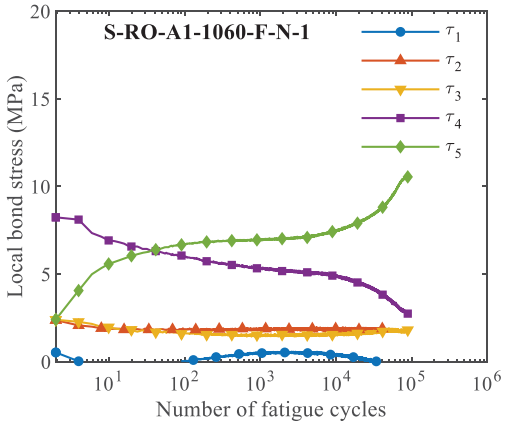

(a) S-RO-A1-1060-F-N-1

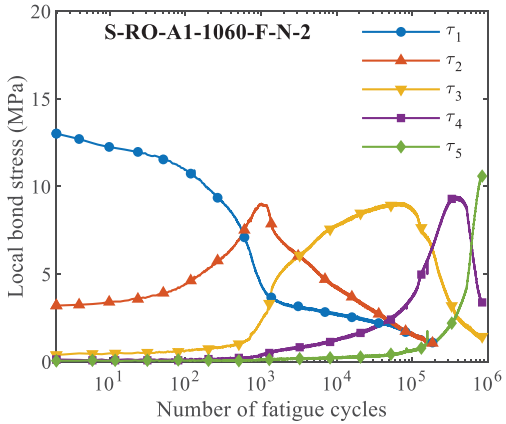

(b) S-RO-A1-1060-F-N-2

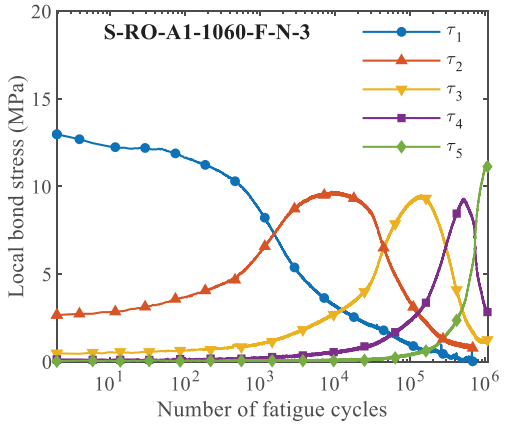

(c) S-RO-A1-1060-F-N-3

N/A because of sliding failure

(d) S-RO-A2-1060-F-N-1

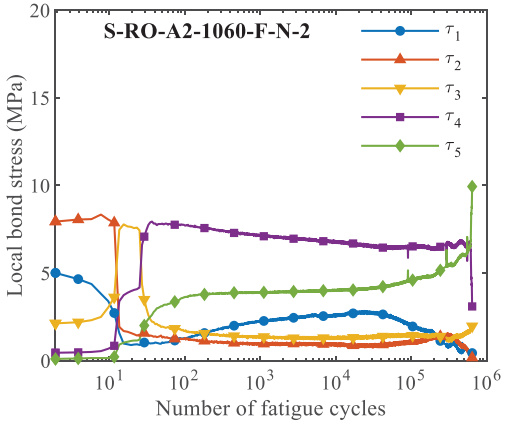

(e) S-RO-A2-1060-F-N-2

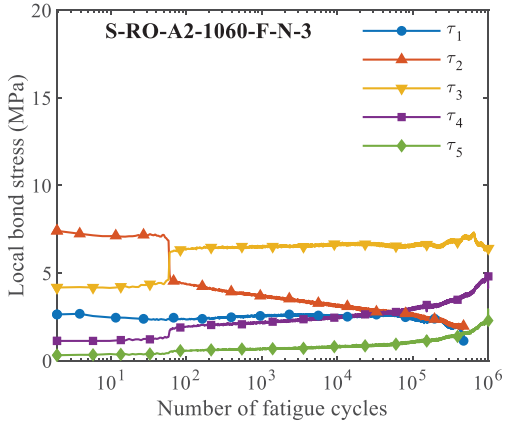

(f) S-RO-A2-1060-F-N-3

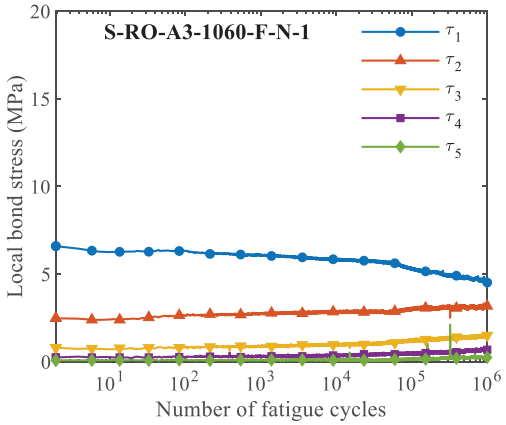

(g) S-RO-A3-1060-F-N-1

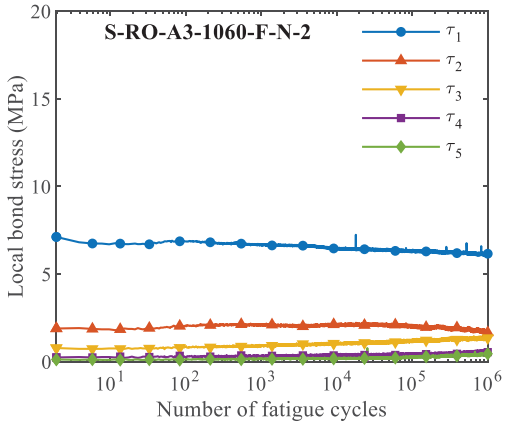

(h) S-RO-A3-1060-F-N-2

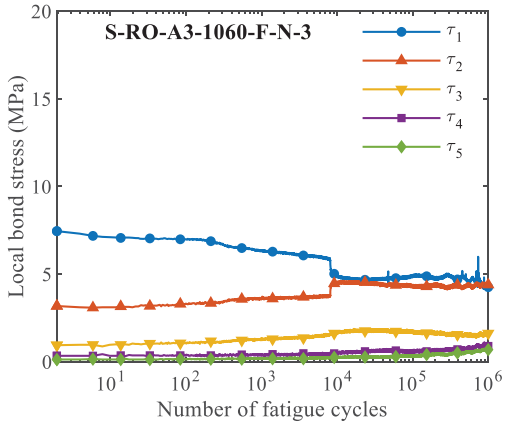

(i) S-RO-A3-1060-F-N-3

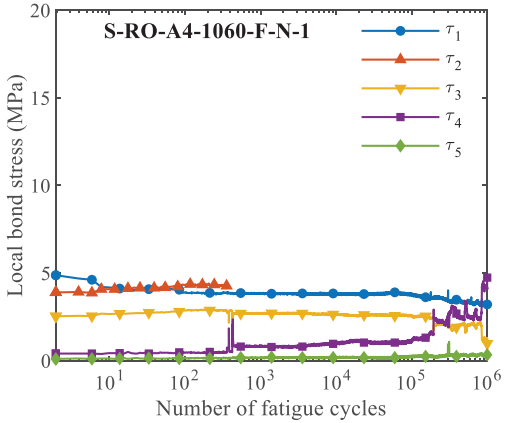

(j) S-RO-A4-1060-F-N-1

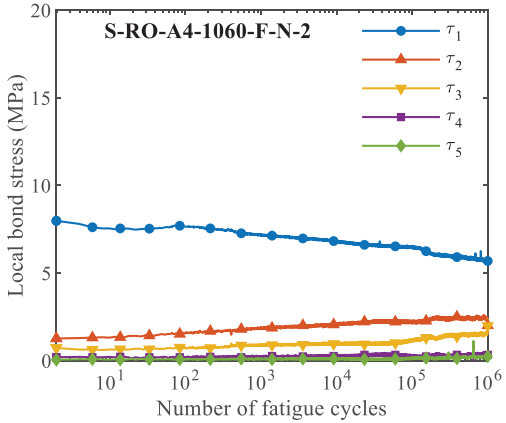

(k) S-RO-A4-1060-F-N-2

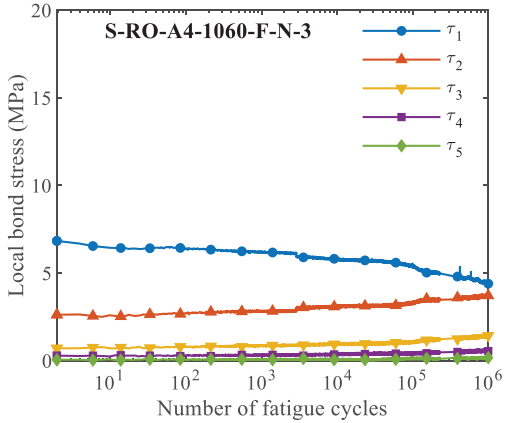

(l) S-RO-A4-1060-F-N-3

Fig. 4.31 Local bond stress development under P_{max} during the fatigue cycles for CFRP strip specimens using different epoxy adhesives

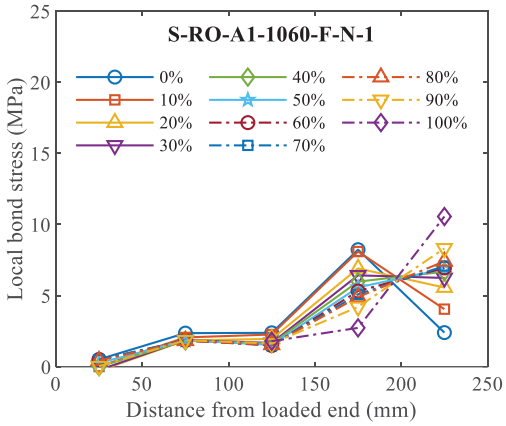

(a) S-RO-A1-1060-F-N-1

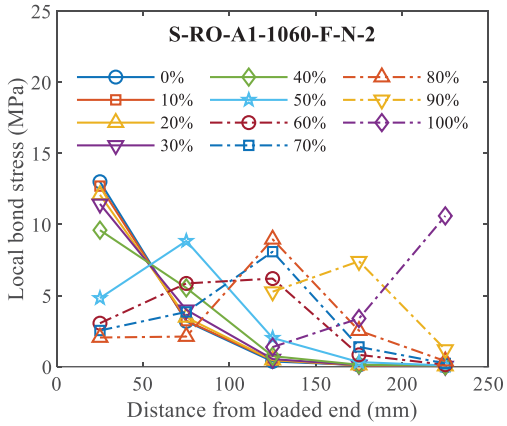

(b) S-RO-A1-1060-F-N-2

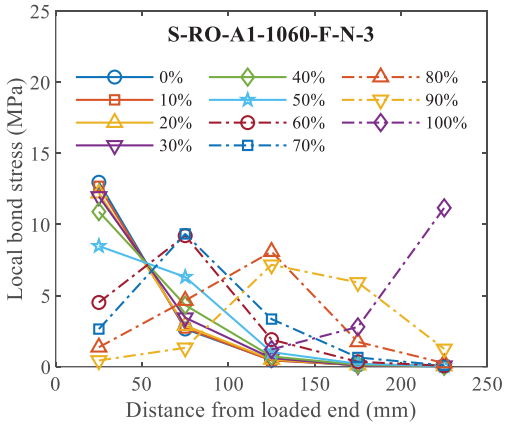

(c) S-RO-A1-1060-F-N-3

N/A because of sliding failure

(d) S-RO-A2-1060-F-N-1

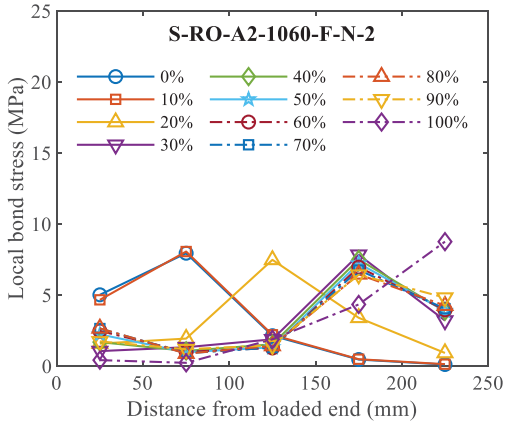

(e) S-RO-A2-1060-F-N-2

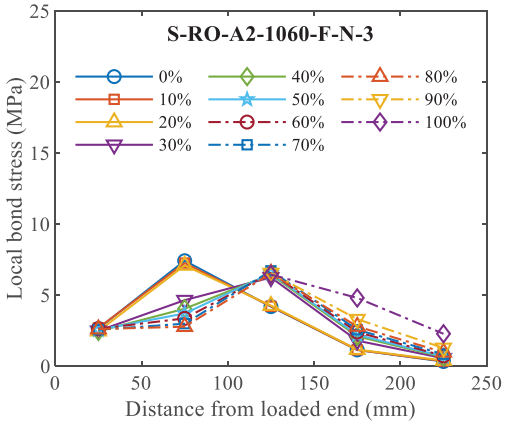

(f) S-RO-A2-1060-F-N-3

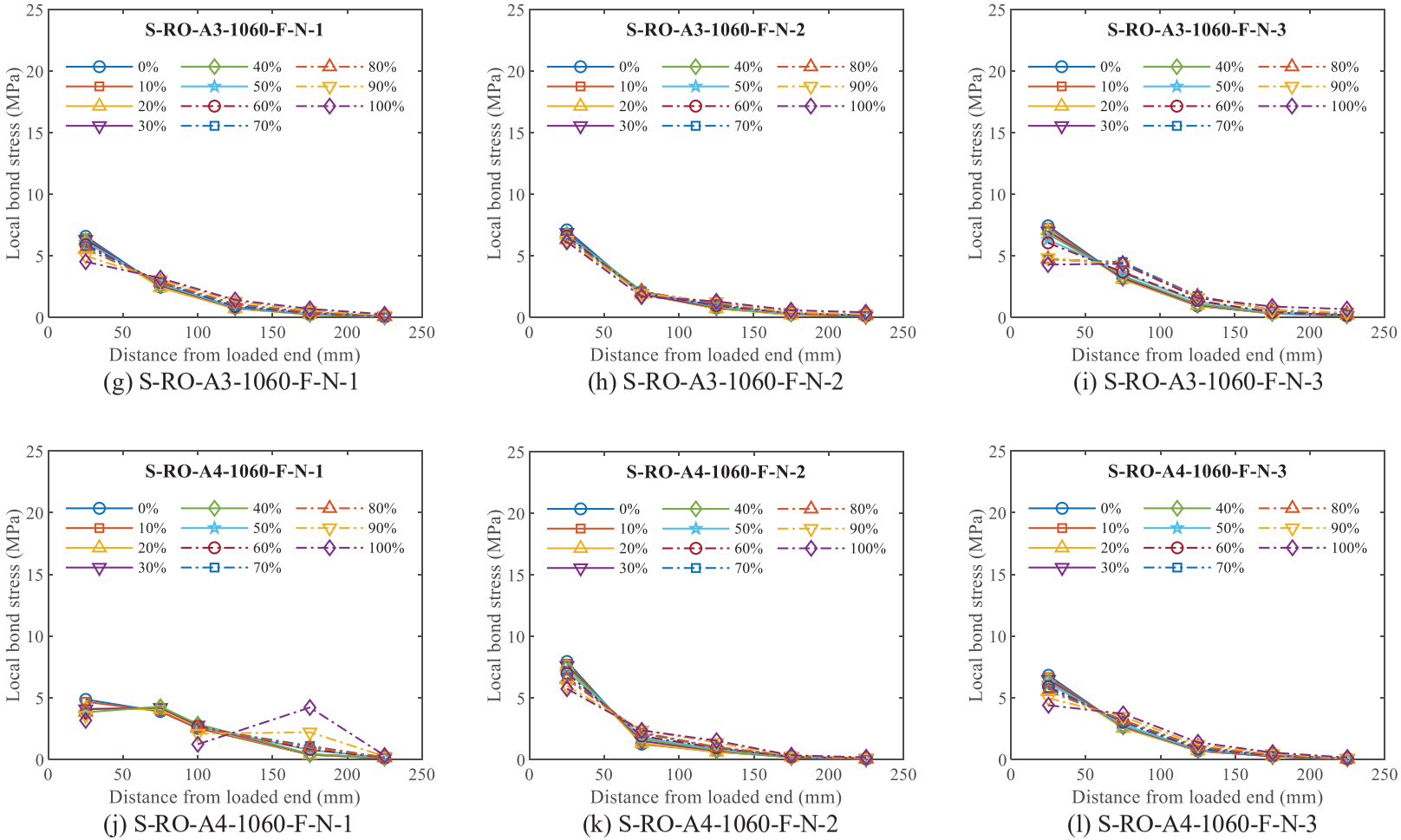

(g) S-RO-A3-1060-F-N-1 (h) S-RO-A3-1060-F-N-2 (i) S-RO-A3-1060-F-N-3

(j) S-RO-A4-1060-F-N-1 (k) S-RO-A4-1060-F-N-2 (l) S-RO-A4-1060-F-N-3

Fig. 4.32 Development in local bond stress distribution under P_{max} during the fatigue cycles for CFRP strip specimens using different epoxy adhesives

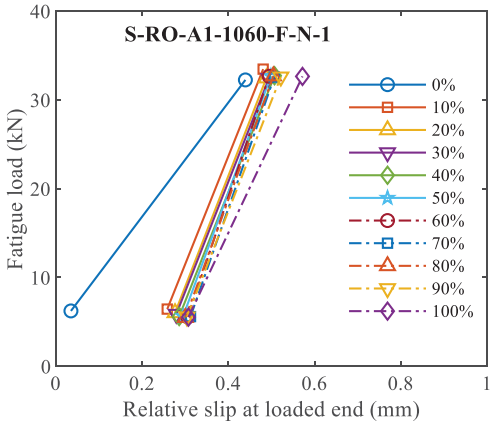

(a) S-RO-A1-1060-F-N-1

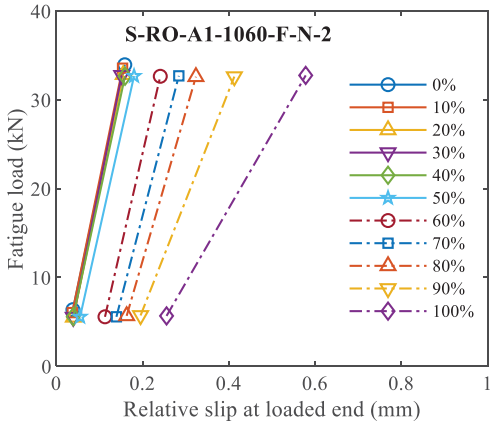

(b) S-RO-A1-1060-F-N-2

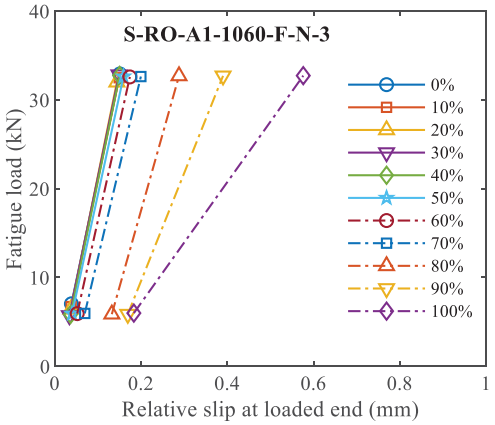

(c) S-RO-A1-1060-F-N-3

N/A because of sliding failure

(d) S-RO-A2-1060-F-N-1

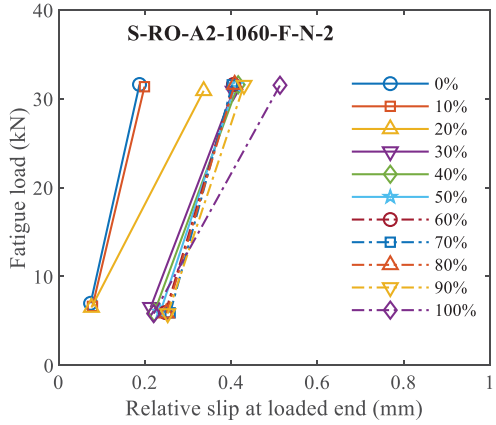

(e) S-RO-A2-1060-F-N-2

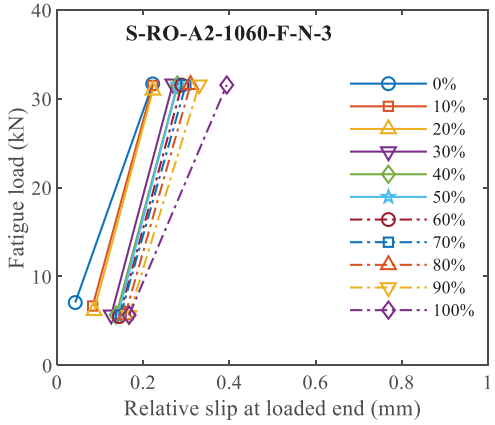

(f) S-RO-A2-1060-F-N-3

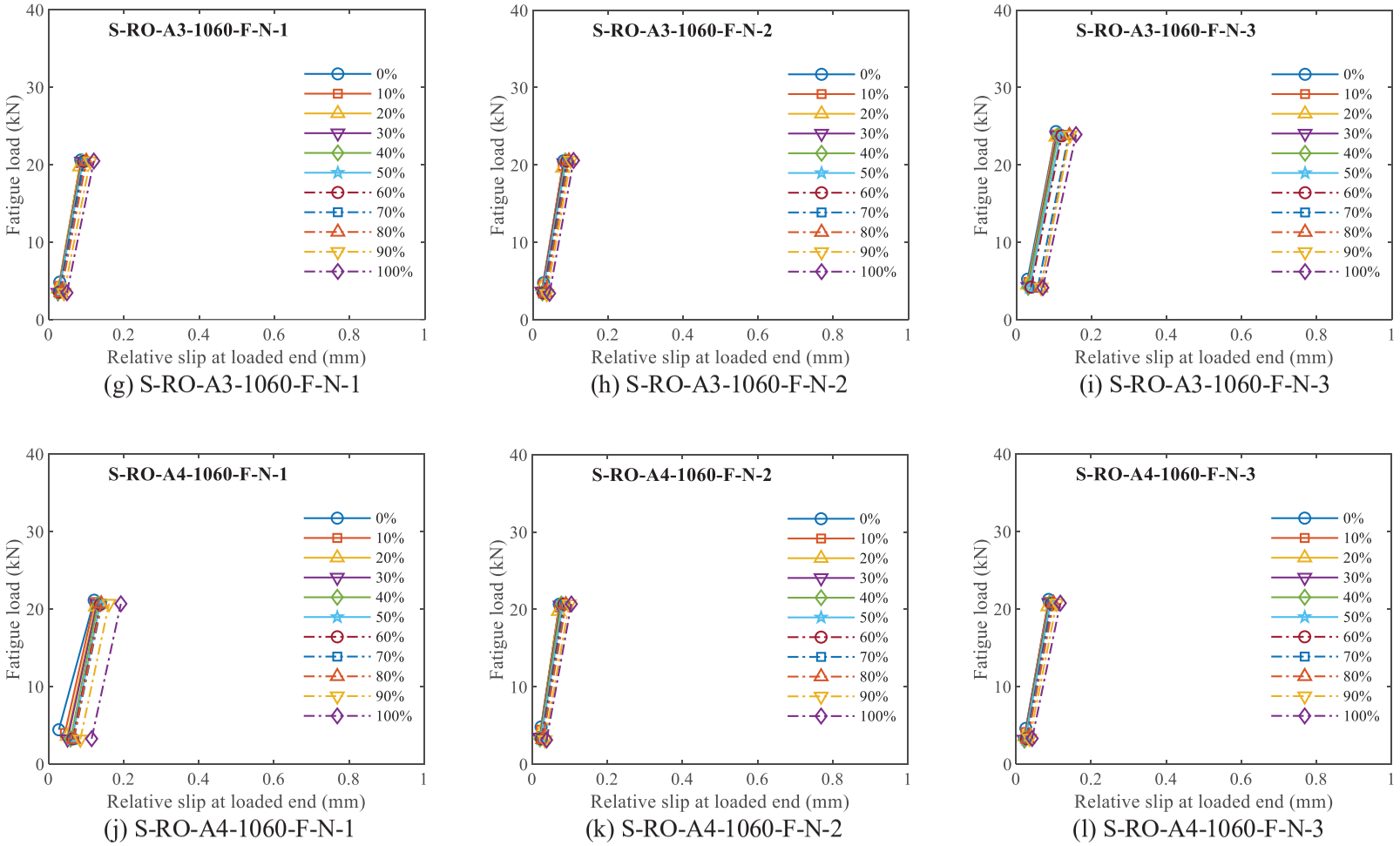

(g) S-RO-A3-1060-F-N-1 (h) S-RO-A3-1060-F-N-2 (i) S-RO-A3-1060-F-N-3

(j) S-RO-A4-1060-F-N-1 (k) S-RO-A4-1060-F-N-2 (l) S-RO-A4-1060-F-N-3

Fig. 4.33 Applied fatigue load range vs. relative slip at the loaded end during the fatigue cycles for CFRP strip specimens using different epoxy adhesives

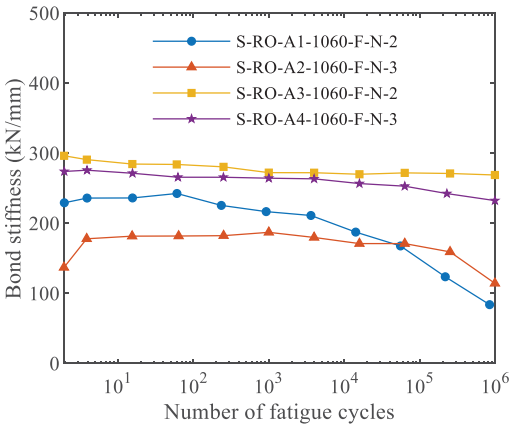

Fig. 4.34 Stiffness of NSM FRP-to-concrete bonded joints during the fatigue cycles for CFRP specimens of different epoxy adhesives

4.4.4 Influence of fatigue load range

Test results of the CFRP rod and strip specimens under fatigue loading case for different fatigue load ranges are illustrated and compared in Figs. 4.35-4.37 and Figs. 4.38-4.40, respectively. The experimental data are collected up to the failure of the strain gauges to ensure the accuracy of the readings. It is obvious that the higher fatigue load range accelerated the local bond stress degradation, especially for the local bond stress near the loaded end. For example, τ_2 of the CFRP rod specimens dropped down to zero much faster under 10-70% fatigue load range at approximately 10^3 cycles [Figs. 4.35(g)-4.35(i)] while it reached zero at around 10^4 cycles under 10-60% [Figs. 4.35(e) and (f)] or even at 10^5 cycles under 10-50% fatigue load range [Fig. 4.35(b)]. The same trend was observed for the CFRP strip specimens, for example, the magnitude of τ_1 and τ_2 were both less than 3 MPa at 10^4 cycles [Figs. 4.38(g)-4.38(i)] under 10-70% fatigue load range but τ_2 was still as high as about 10 MPa under 10-60% fatigue load range [Fig. 4.38(f)]. Of course, due to the scatter of material properties and inevitable variation in both the groove size and the roughness of CFRP strip, the test results within the same set were not identical. But it is undoubtable that the fatigue load range had a significant effect on the local bond performance of NSM FRP-to-concrete bonded joints. In terms of the local bond stress distribution, the bond length

was fully developed for all the three sets of CFRP rod specimens when the specimen failed or reached one million cycles (Fig. 4.36). The difference mainly lied in the extent of bond development of τ_5. For example, τ_5 of the CFRP rod specimen sets under both 10-60% and 10-70% fatigue load range experienced a stress decline, whilst τ_5 of specimen set R-SCSW-A1-1050-F-N was still growing or remaining stable. It also implied that the bonded region close to the free end (200 mm away from the loaded end or further) had a stronger resistance to fatigue degradation under lower fatigue load range. This observation was consistent with the fact that τ_5 usually had the largest local bond strength during the static pull-out test. However, no decrease in τ_5 was noticed for the CFRP strip specimens near fatigue failure and the stress level of τ_5 was still low for specimen set S-RO-A1-1050-F-N, indicating the bonded region was not fully developed yet [Fig. 4.39(a)-4.39(c)]. It appeared that the CFRP strip specimens were more sensitive to the fatigue load range in the aspect of the local bond degradation rate which could be explained by their interfacial sliding failure mechanism.

Figs. 4.37 and 4.40 present the relationship between the fatigue load range and the corresponding relative slip at the loaded end throughout the fatigue cycles for the CFRP rod and strip specimens, respectively. For the CFRP rod specimens, the difference in magnitude of maximum slip at 70%logN_f were small between the fatigue load range 10-50% and 10-60% cases. However, when the fatigue load range increased to 10-70%, the maximum slip reached as high as over 1.5 mm. For the CFRP strip specimens, on the other hand, the maximum slip at failure for both fatigue load range 10-60% and 10-70% were almost equivalent at about 0.6 mm. But the maximum slip at 100%logN_f under fatigue load range 10-50% was less than 0.4 mm. This result confirmed that sand-coated and spirally wound CFRP rod specimens were more resistant to fatigue degradation with a better ductility at failure and could still sustain considerable bond strength at one million fatigue cycles under the 10-60% fatigue load range. By contrast, the safety threshold of fatigue load range for the roughened CFRP strip specimens should be 10-50% to ensure a fatigue life of at least one million. In addition, the typical development of bond stiffness during the fatigue

cycles are shown in Figs. 4.41 and 4.42 for both the CFRP rod and strip specimens, respectively. It is not surprising that with a higher fatigue load upper limit, the bond stiffness was smaller because more bonded regions would develop into softening stage to resist the larger applied load. For the CFRP rod specimens, the decline rate of bond stiffness increased with the increase of fatigue load range. But for the CFRP strip specimens, all the three curves are almost paralleling to each other, indicating a similar decrease rate in bond stiffness. Moreover, the stiffness of CFRP strip specimens were mostly larger than that of CFRP rod specimens under the same fatigue load range, which could be attributed to the more ductile bond behavior of CFRP rod specimens.

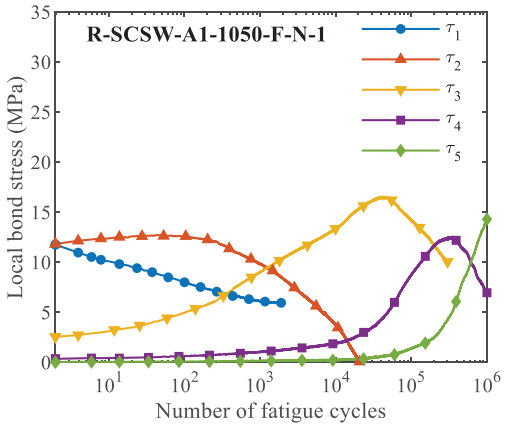

(a) R-SCSW-A1-1050-F-N-1

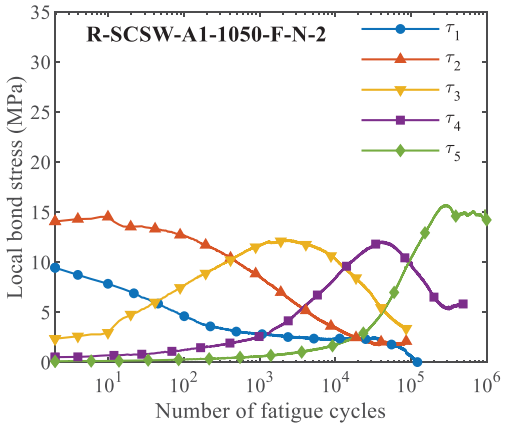

(b) R-SCSW-A1-1050-F-N-2

N/A because of FRP fracture

(c) R-SCSW-A1-1050-F-N-3

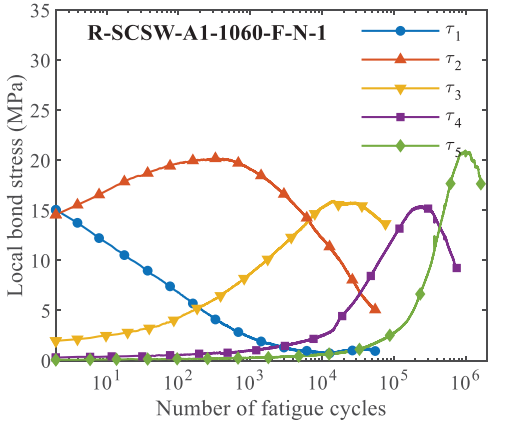

(d) R-SCSW-A1-1060-F-N-1

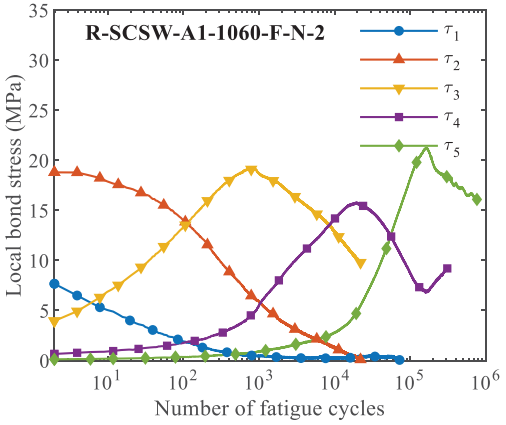

(e) R-SCSW-A1-1060-F-N-2

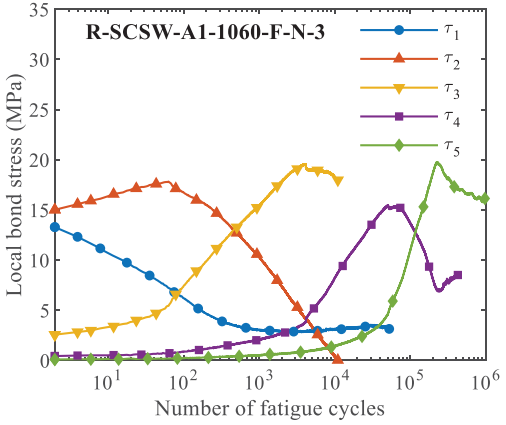

(f) R-SCSW-A1-1060-F-N-3

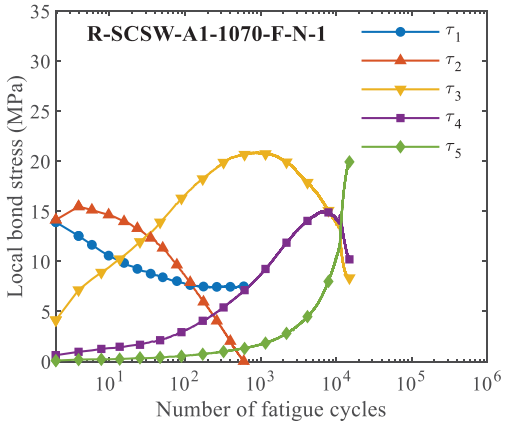

(g) R-SCSW-A1-1070-F-N-1

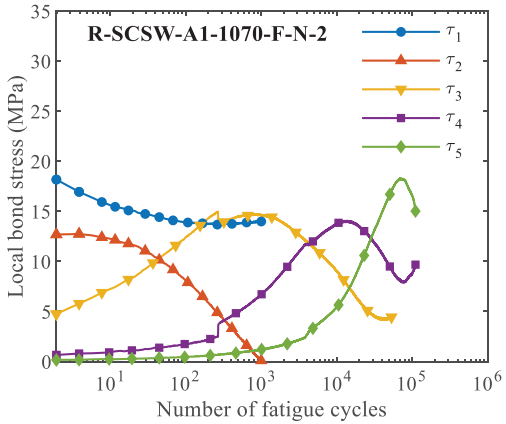

(h) R-SCSW-A1-1070-F-N-2

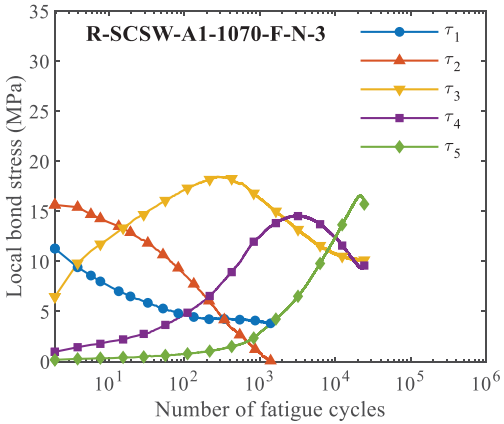

(i) R-SCSW-A1-1070-F-N-3

Fig. 4.35 Local bond stress development under P_{max} during the fatigue cycles for CFRP rod specimens of different fatigue load range

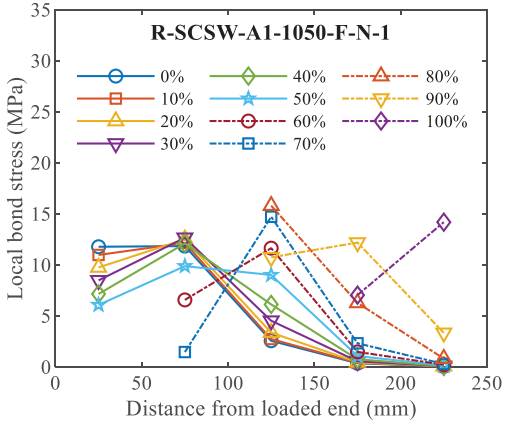

(a) R-SCSW-A1-1050-F-N-1

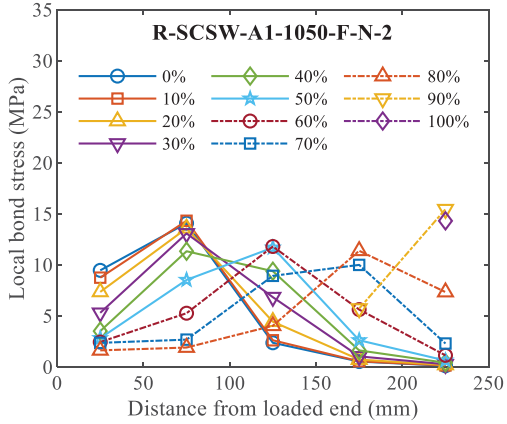

(b) R-SCSW-A1-1050-F-N-2

N/A because of FRP fracture
(c) R-SCSW-A1-1050-F-N-3

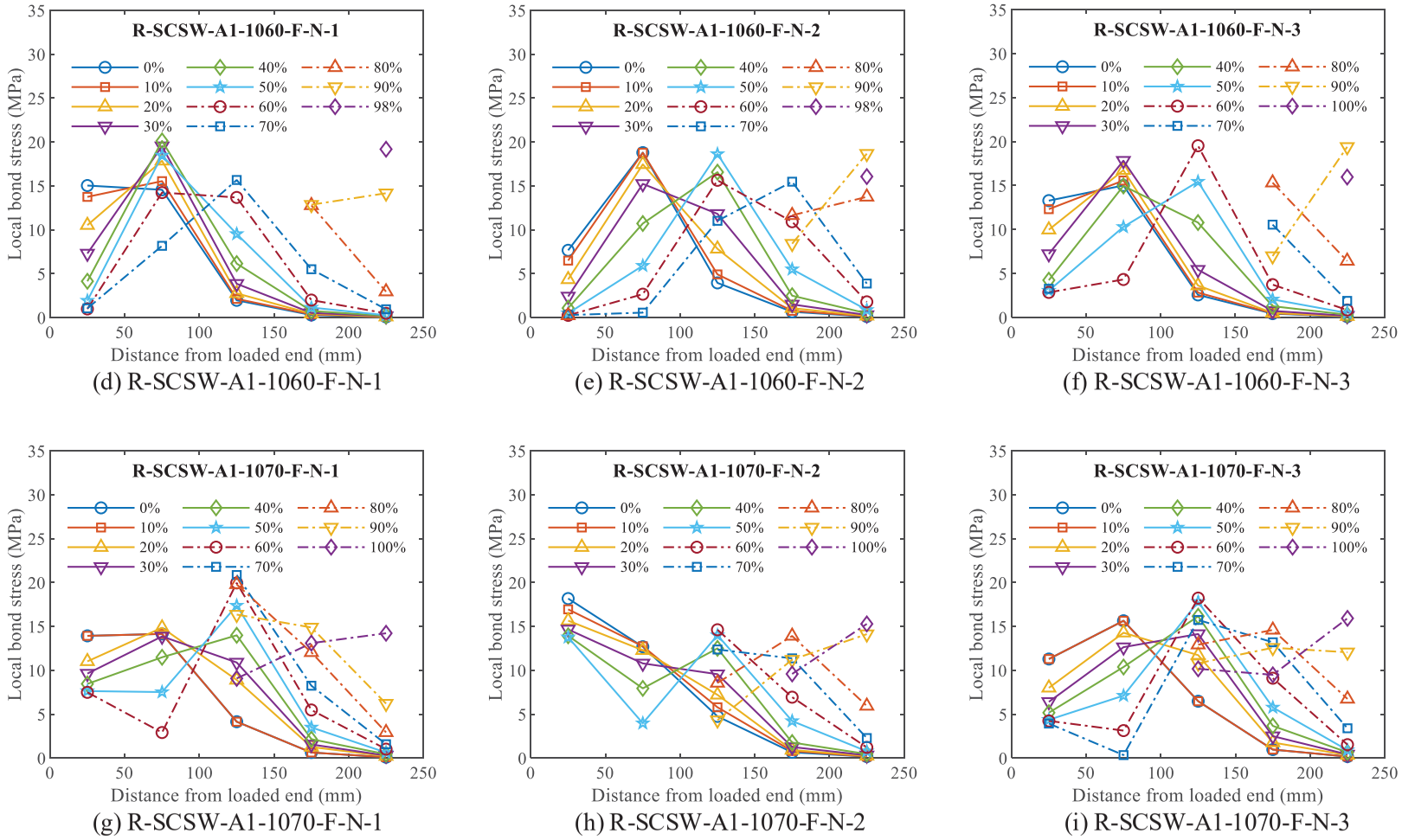

(d) R-SCSW-A1-1060-F-N-1 (e) R-SCSW-A1-1060-F-N-2 (f) R-SCSW-A1-1060-F-N-3

(g) R-SCSW-A1-1070-F-N-1 (h) R-SCSW-A1-1070-F-N-2 (i) R-SCSW-A1-1070-F-N-3

Fig. 4.36 Development in local bond stress distribution under P_{max} during the fatigue cycles for CFRP rod specimens of different fatigue load range

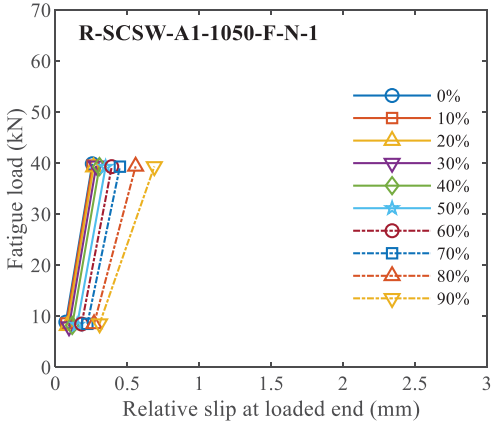

(a) R-SCSW-A1-1050-F-N-1

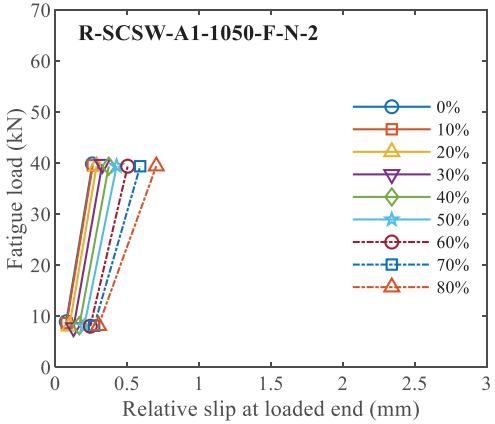

(b) R-SCSW-A1-1050-F-N-2

N/A because of FRP fracture

(c) R-SCSW-A1-1050-F-N-3

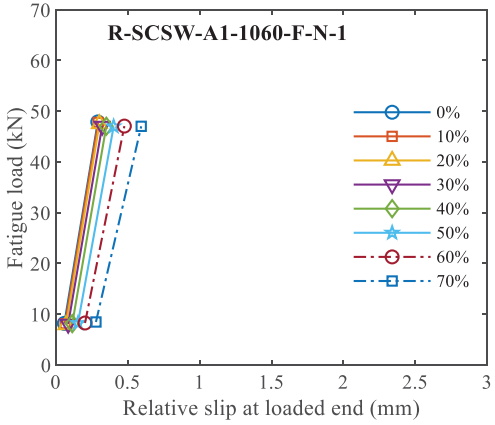

(d) R-SCSW-A1-1060-F-N-1

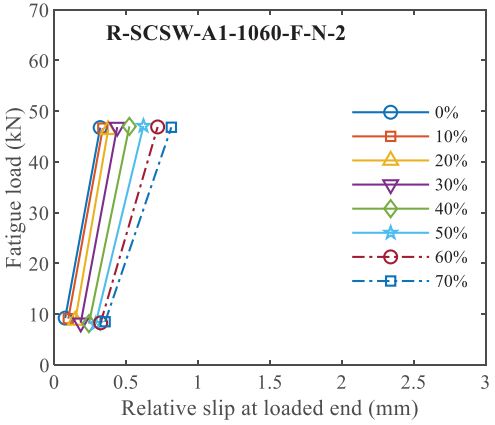

(e) R-SCSW-A1-1060-F-N-2

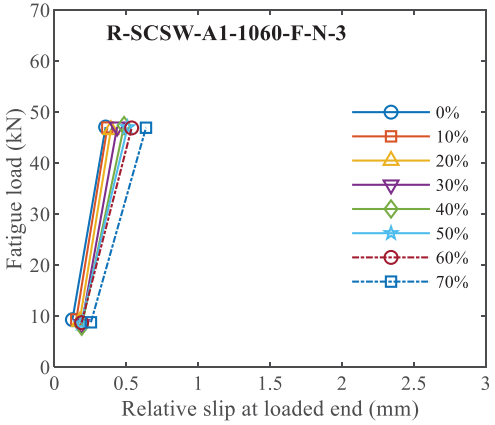

(f) R-SCSW-A1-1060-F-N-3

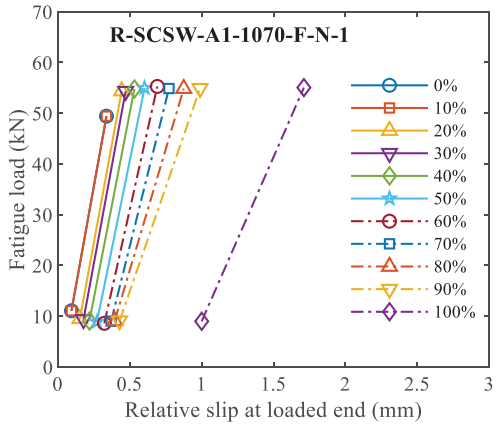

(g) R-SCSW-A1-1070-F-N-1

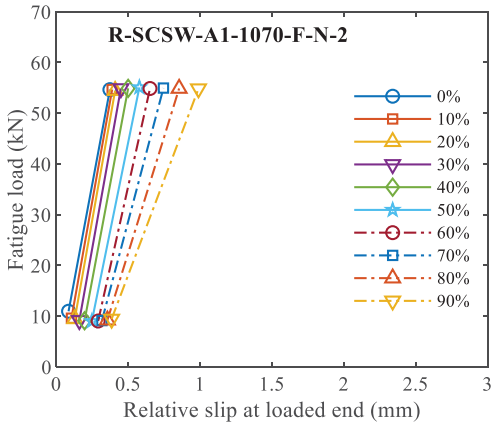

(h) R-SCSW-A1-1070-F-N-2

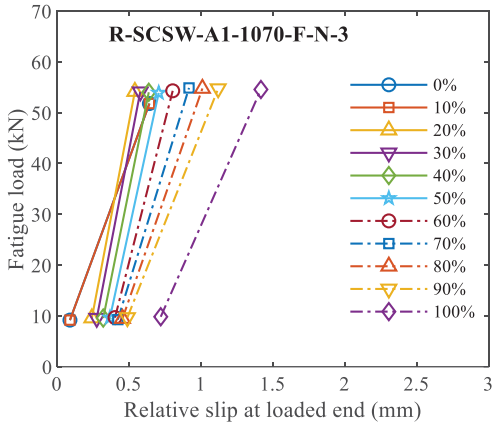

(i) R-SCSW-A1-1070-F-N-3

Fig. 4.37 Applied fatigue load range vs. relative slip at the loaded end during the fatigue cycles for CFRP rod specimens of different fatigue load range

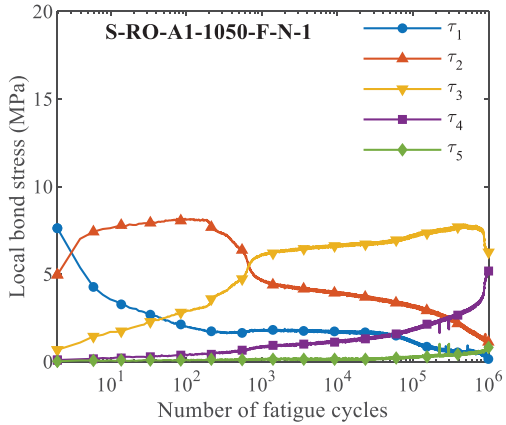

(a) S-RO-A1-1050-F-N-1

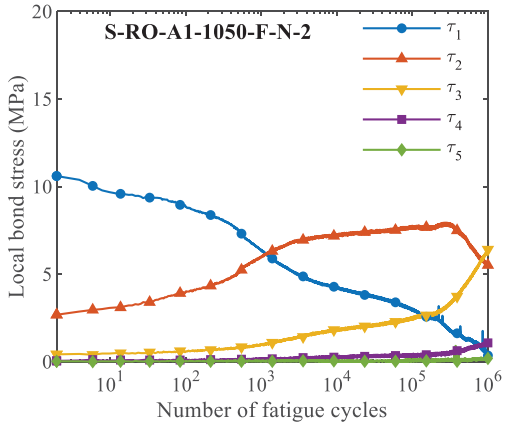

(b) S-RO-A1-1050-F-N-2

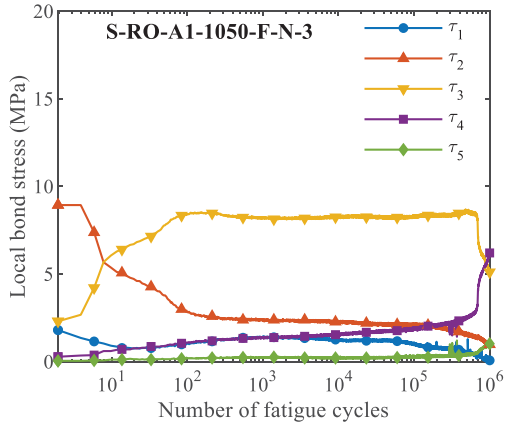

(c) S-RO-A1-1050-F-N-3

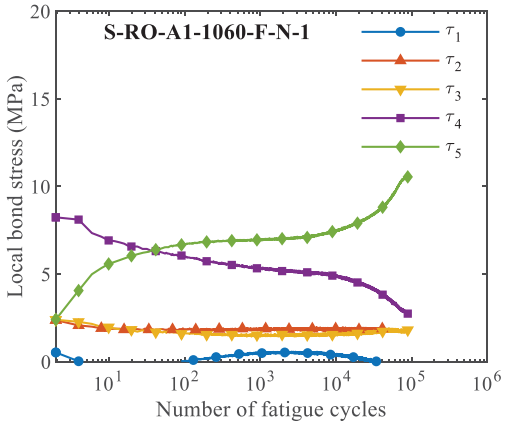

(d) S-RO-A1-1060-F-N-1

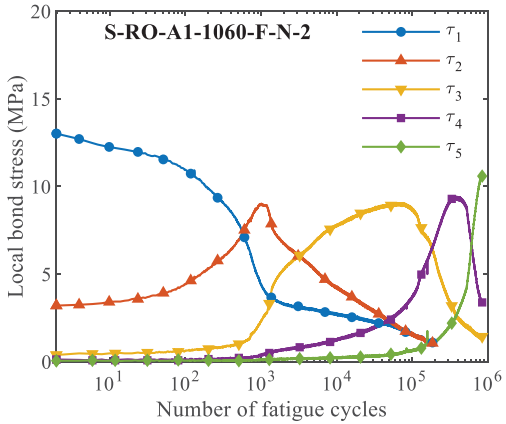

(e) S-RO-A1-1060-F-N-2

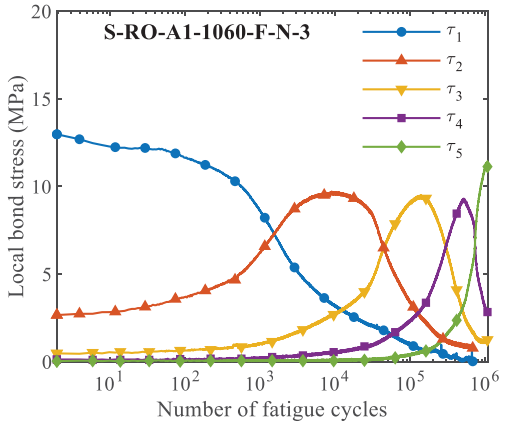

(f) S-RO-A1-1060-F-N-3

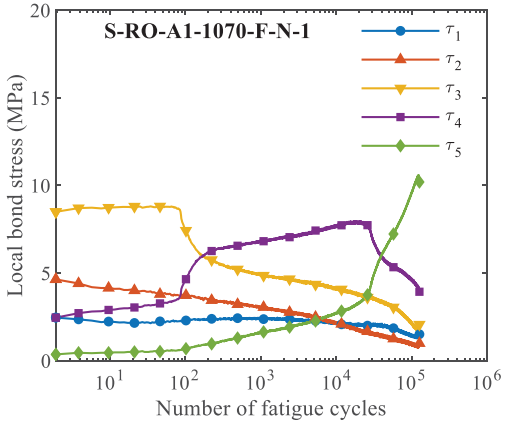

(g) S-RO-A1-1070-F-N-1

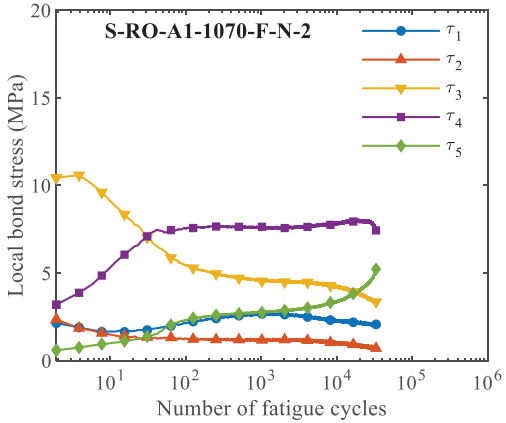

(h) S-RO-A1-1070-F-N-2

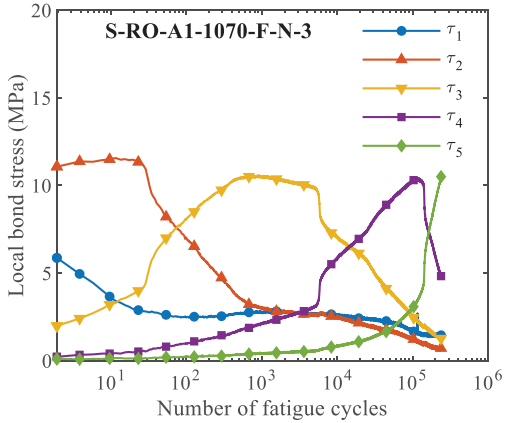

(i) S-RO-A1-1070-F-N-3

Fig. 4.38 Local bond stress development under P_{max} during the fatigue cycles for CFRP strip specimens of different fatigue load range

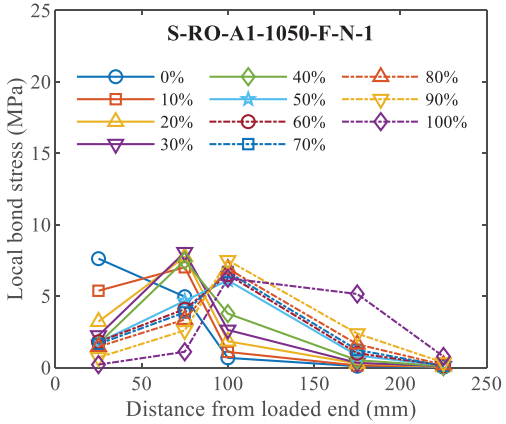

(a) S-RO-A1-1050-F-N-1

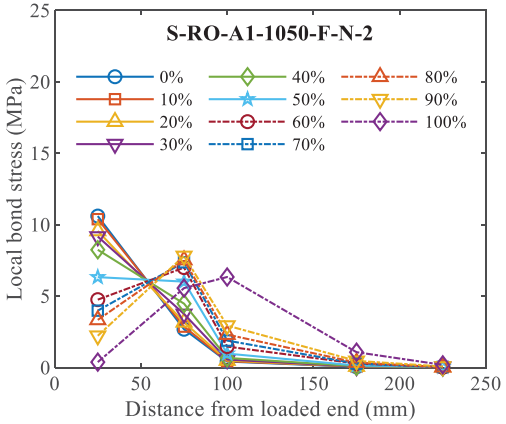

(b) S-RO-A1-1050-F-N-2

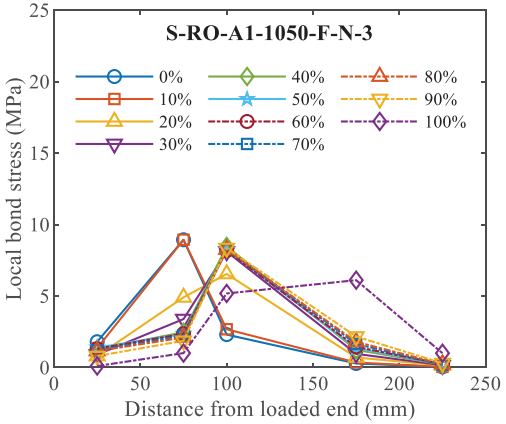

(c) S-RO-A1-1050-F-N-3

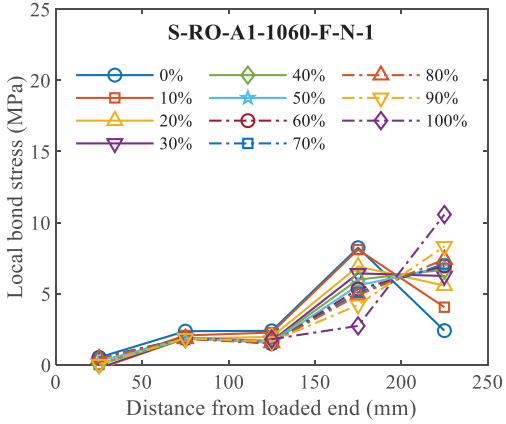

(d) S-RO-A1-1060-F-N-1

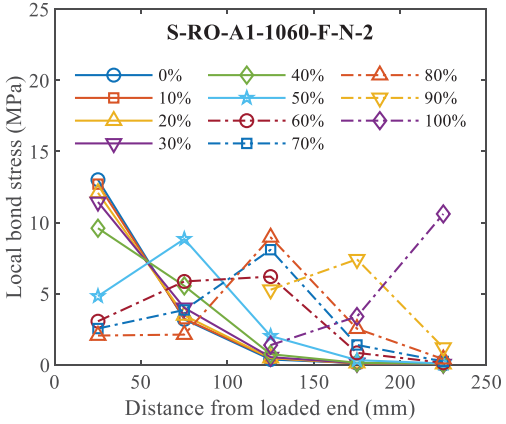

(e) S-RO-A1-1060-F-N-2

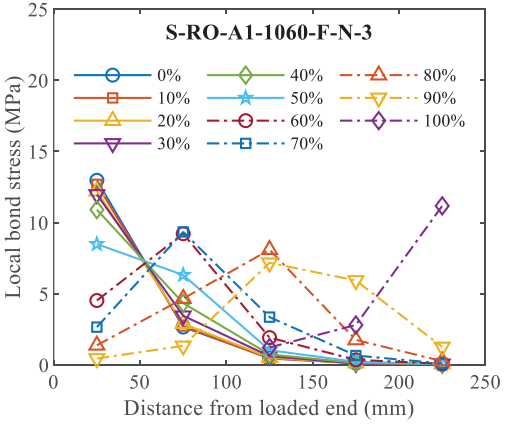

(f) S-RO-A1-1060-F-N-3

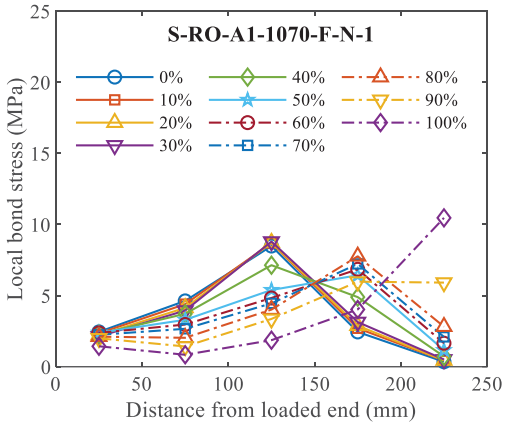

(g) S-RO-A1-1070-F-N-1

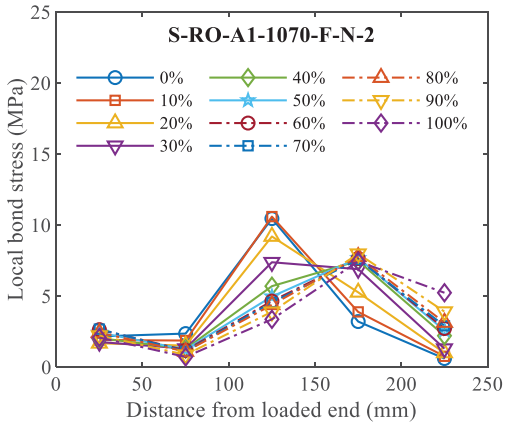

(h) S-RO-A1-1070-F-N-2

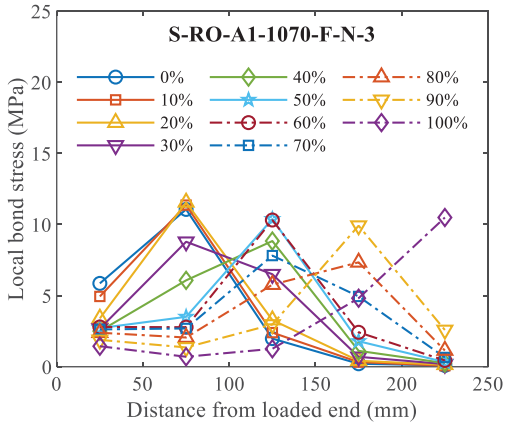

(i) S-RO-A1-1070-F-N-3

Fig. 4.39 Development in local bond stress distribution under P_{max} during the fatigue cycles for CFRP strip specimens of different fatigue load range

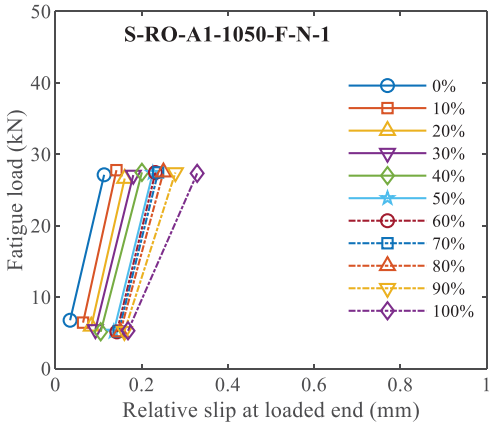

(a) S-RO-A1-1050-F-N-1

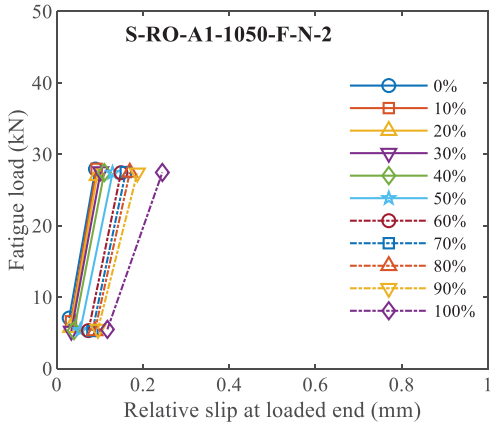

(b) S-RO-A1-1050-F-N-2

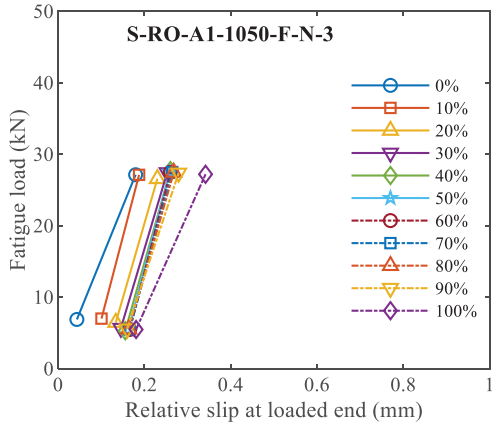

(c) S-RO-A1-1050-F-N-3

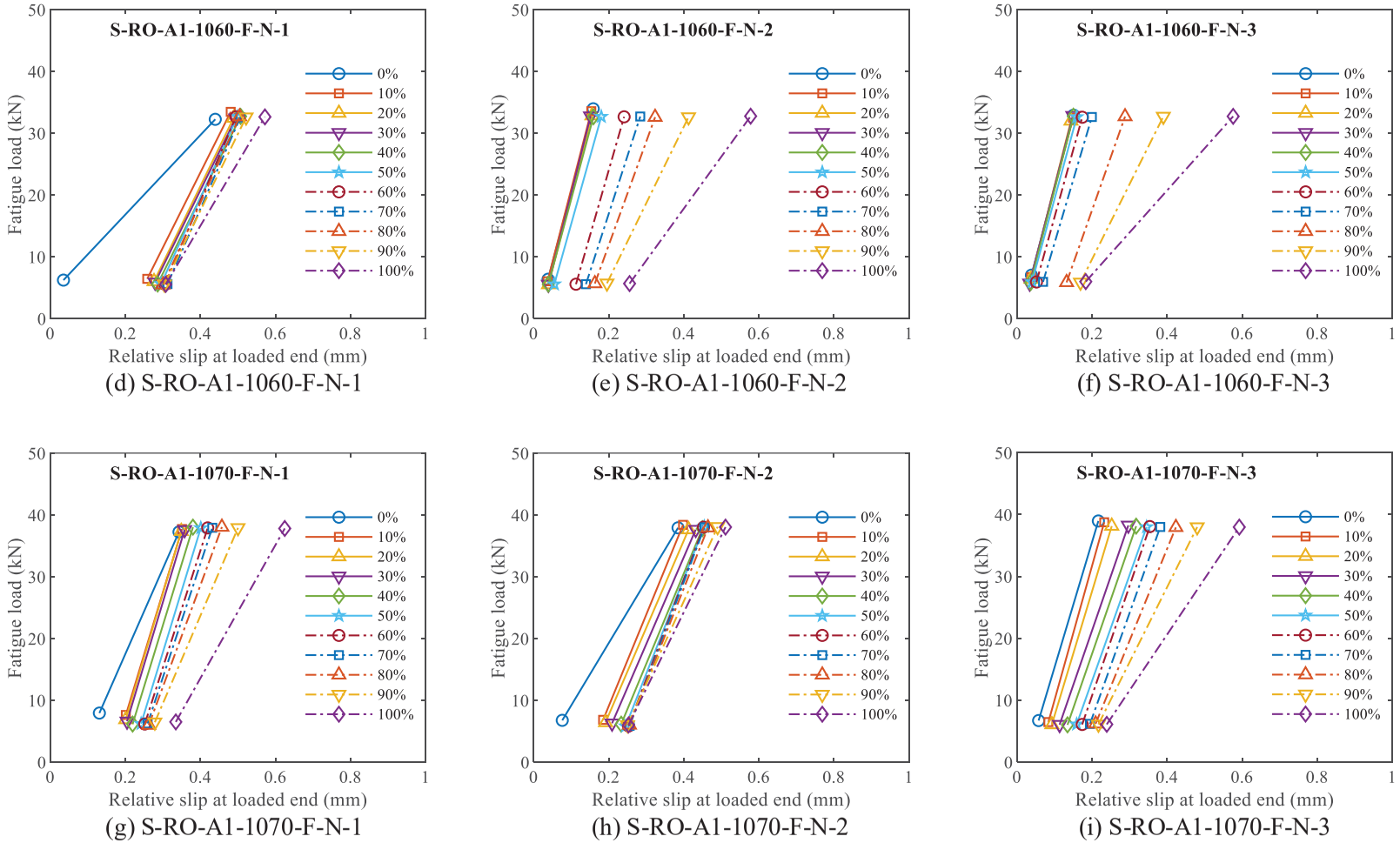

(d) S-RO-A1-1060-F-N-1 (e) S-RO-A1-1060-F-N-2 (f) S-RO-A1-1060-F-N-3

(g) S-RO-A1-1070-F-N-1 (h) S-RO-A1-1070-F-N-2 (i) S-RO-A1-1070-F-N-3

Fig. 4.40 Applied fatigue load range vs. relative slip at the loaded end during the fatigue cycles for CFRP strip specimens of different fatigue load range

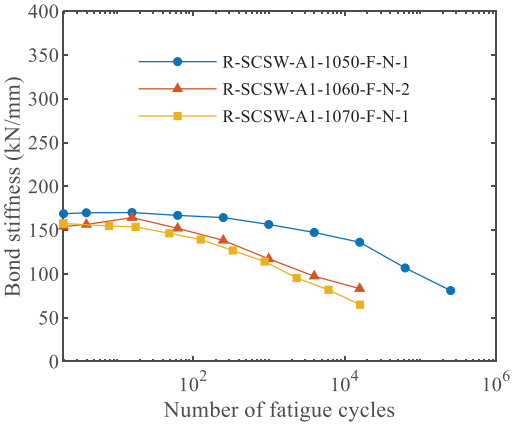

Fig. 4.41 Stiffness of NSM FRP-to-concrete bonded joints during the fatigue cycles for CFRP rod specimens of different fatigue load range

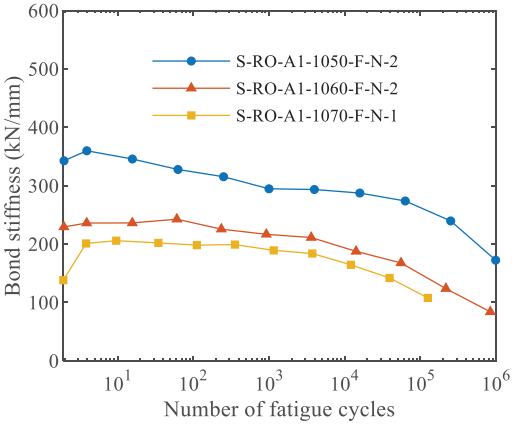

Fig. 4.42 Stiffness of NSM FRP-to-concrete bonded joints during the fatigue cycles for CFRP strip specimens of different fatigue load range

4.4.5 Influence of concrete strength

Test results for the CFRP strip specimen sets S-RO-A1-1060-F-N and S-RO-A1-1060-F-H are presented and compared in Figs. 4.43-4.46. These specimens were cast by two batches of concrete with different mix proportions and ended up with about 9% difference in strength on average over the 7.5-month fatigue testing period (45.02 MPa and 49.11 MPa, respectively). It should be noted that specimen S-RO-A1-1060-F-H-3 performed an early interfacial sliding failure between the FRP and epoxy under fatigue loading (125 cycles, Table 4.8). Meanwhile, as

illustrated in Fig. 4.44(f), the peak local bond stress under P_{max} for S-RO-A1-1060-F-H-3 started from the free end at the first fatigue cycle, which was similar to specimen S-RO-A1-1060-F-N-1 as described above. This phenomenon indicated a poor bond resistance for most regions along the bond line of this specimen, and a significant interfacial sliding already existed at the first fatigue cycle (0.6 mm in relative slip under P_{max}) as shown in Fig. 4.45(f). The unexpected premature failure was caused by the inconsistency in the quality of the CFRP strip textured (roughened) surface, because delamination of the top surface was confirmed in post-test inspection by cutting open the epoxy groove. Thus, both specimen S-RO-A1-1060-F-N-1 and S-RO-A1-1060-F-H-3 were disregarded in the following discussion.

The general trends of the local bond stress development under P_{max} for both specimen sets were similar where τ_1 remained decreasing since the start of the fatigue cycles, and τ_2- τ_4 increased gradually followed by stress decline as the fatigue cycles went up (Fig. 4.43). They all failed by interfacial debonding not long after τ_5 reached the maximum followed by a rapid plunge. Both the results of peak local bond stress level (approximately 10-12 MPa) and the average fatigue life (969,085 and 856,289 cycles) were close for the two specimen sets under the same percentage range (10-60%P_f). In terms of the development of the local bond stress distribution under P_{max}, as shown in Fig. 4.44, the migration of the peak local bond stress from the loaded end at early cycles to the free end near failure was noticed for both specimen sets. The slight difference exited in the location of peak local bond stress at initial fatigue cycles, where it was 25 mm away from loaded end for specimen set S-RO-A1-1060-F-N but was further (75 mm) for specimen set S-RO-A1-1060-F-H. It was probably caused by a larger applied fatigue load magnitude for specimen set S-RO-A1-1060-F-H under the same percentage range (10-60%P_f) due to its higher static bond strength, hence, more bonded regions were developed.

In addition, test results for the applied fatigue load range vs. relative slip at the loaded end during the fatigue cycles were plotted for both specimen sets, as illustrated in Fig. 4.45. Although relative slip data for specimen set S-RO-A1-1060-F-H was unavailable near failure (100%logN_f),

the magnitude of the relative slip for both specimen sets were very close up to 90%logN_f. Moreover, it seemed reasonable from the observations that 0.6 mm in the relative slip between the FRP and concrete block was the threshold beyond which fatigue life would be reached shortly. The slope of each subplot in Fig. 4.45 represents the equivalent bond stiffness at a specific fatigue cycle, and it was evident that, with the increase of fatigue cycles, the bond stiffness gradually decreased. Representative curves of the bond stiffness vs. fatigue cycle from the two specimen sets were plotted in Fig. 4.46, where both specimens revealed comparatively stable stiffness before 10^3 fatigue cycles with only minor drop in magnitude. However, the rate of stiffness deterioration sped up after 10^4 fatigue cycles or so, and it dropped down to less than half of the original bond stiffness at failure. All in all, these two specimen sets behaved very alike with respect to the bond stiffness and degradation rate. It appeared that, except for the higher static bond strength by using the higher strength concrete, there is no significant difference in the fatigue bond behavior by using the two different batches of concrete under the same percentage range. This conclusion was reasonable since both specimen sets failed at the FRP/adhesive interface because of interfacial sliding under fatigue loading case, concrete strength did not contribute much to the fatigue bond performance especially with such small difference in strength.

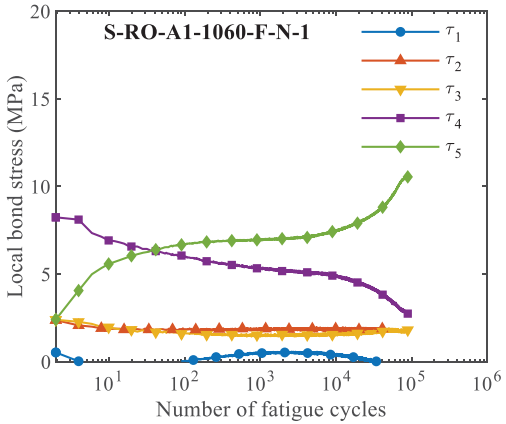

(a) S-RO-A1-1060-F-N-1

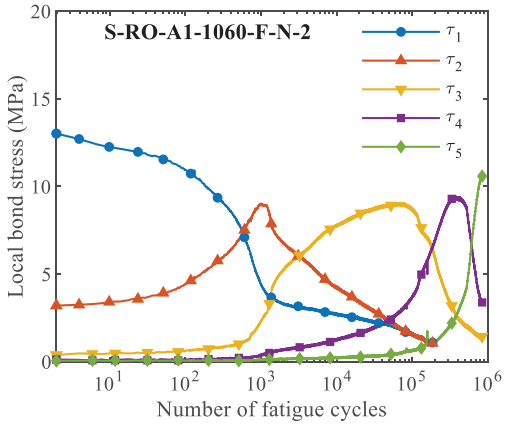

(b) S-RO-A1-1060-F-N-2

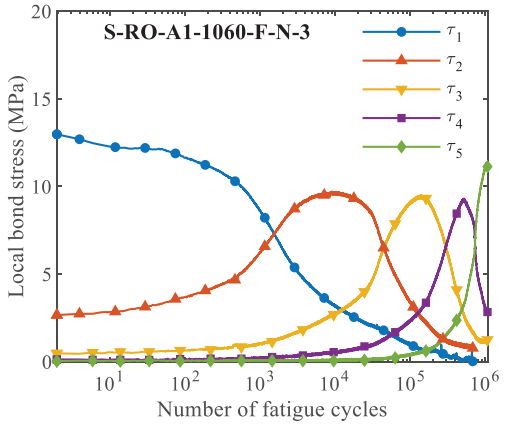

(c) S-RO-A1-1060-F-N-3

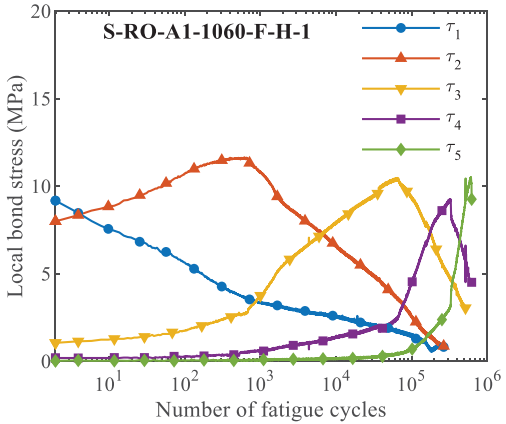

(d) S-RO-A1-1060-F-H-1

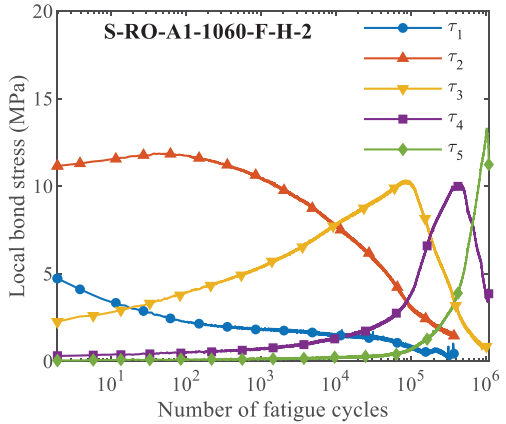

(e) S-RO-A1-1060-F-H-2

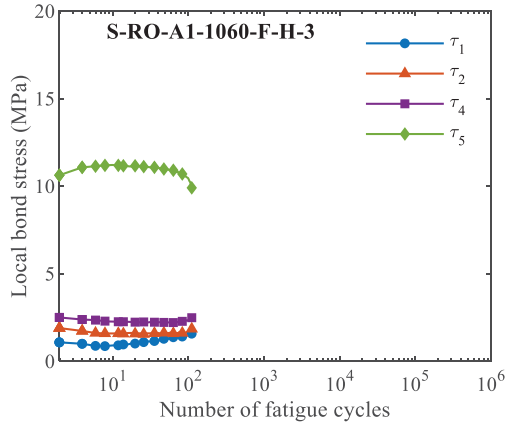

(f) S-RO-A1-1060-F-H-3

Fig. 4.43 Local bond stress development under P_{max} during the fatigue cycles for CFRP specimens of different concrete strength

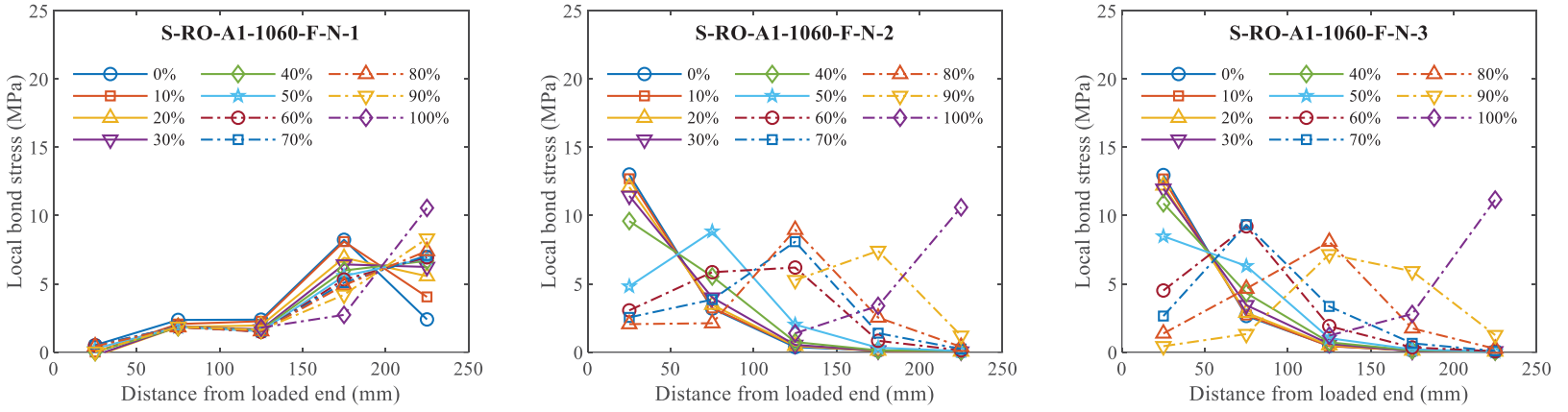

(a) S-RO-A1-1060-F-N-1 (b) S-RO-A1-1060-F-N-2 (c) S-RO-A1-1060-F-N-3

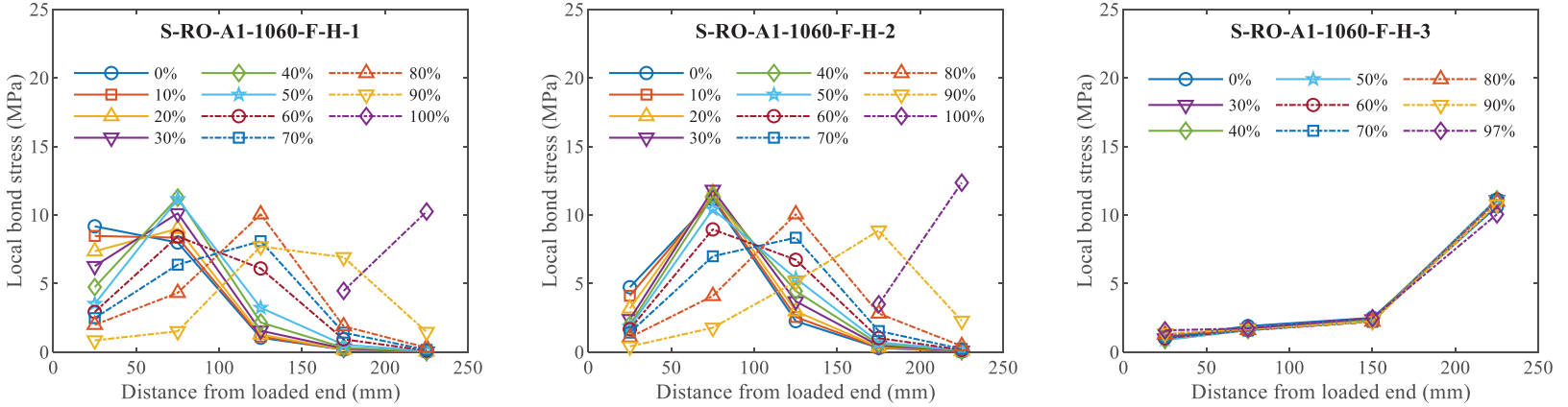

(d) S-RO-A1-1060-F-H-1 (e) S-RO-A1-1060-F-H-2 (f) S-RO-A1-1060-F-H-3

Fig. 4. 44 Development in local bond stress distribution under P_{max} during the fatigue cycles for CFRP specimens of different concrete strength

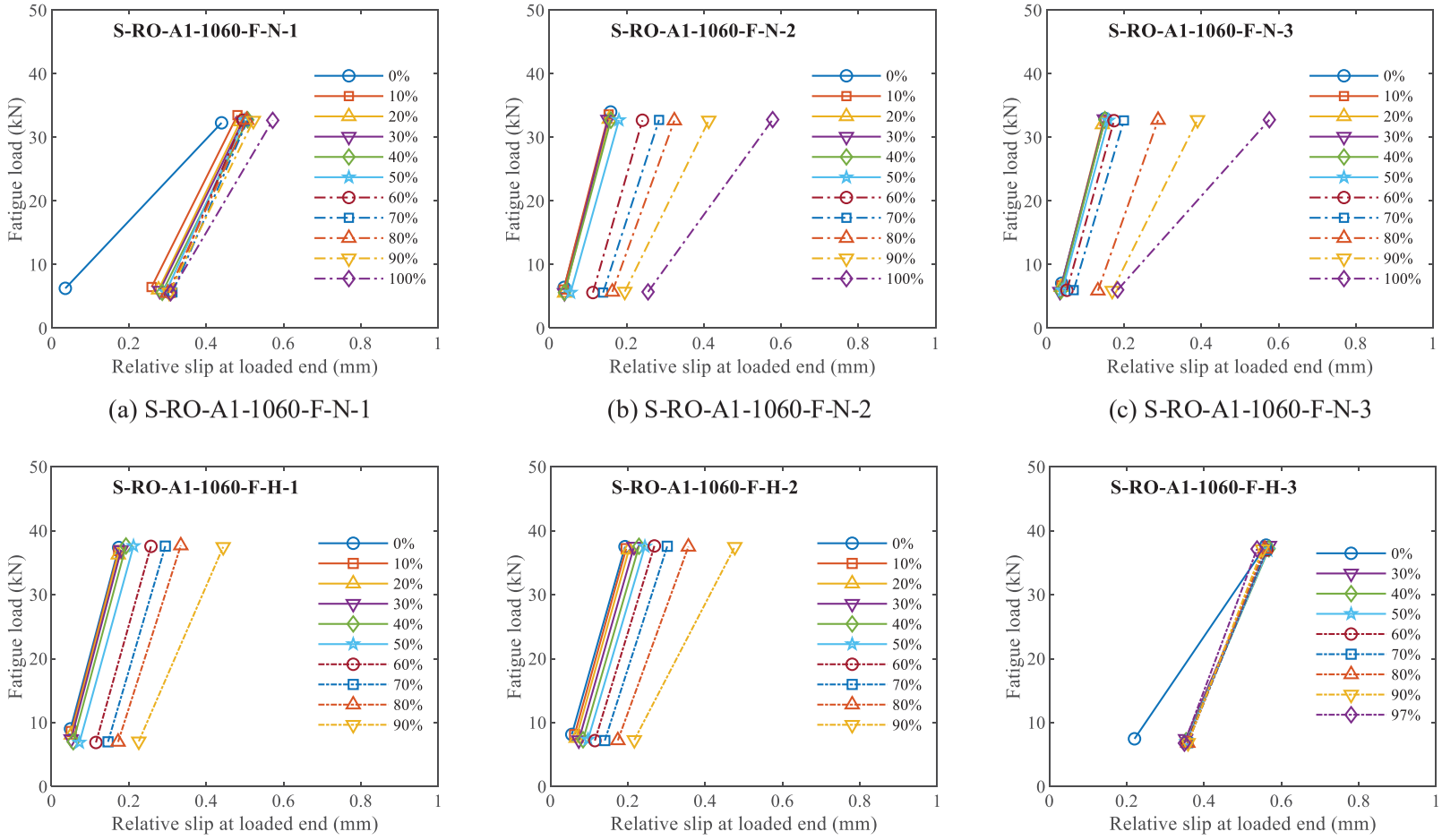

(a) S-RO-A1-1060-F-N-1 (b) S-RO-A1-1060-F-N-2 (c) S-RO-A1-1060-F-N-3

(d) S-RO-A1-1060-F-H-1 (e) S-RO-A1-1060-F-H-2 (f) S-RO-A1-1060-F-H-3

Fig. 4.45 Applied fatigue load range vs. relative slip at the loaded end during the fatigue cycles for CFRP specimens of different concrete strength

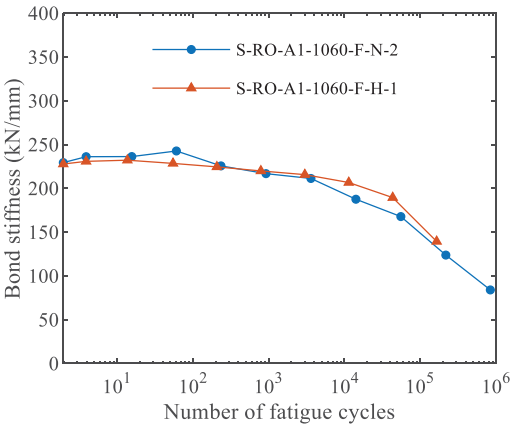

Fig. 4.46 Stiffness of NSM FRP-to-concrete bonded joints during the fatigue cycles for CFRP strip specimens of different concrete strength

4.5 Local bond degradation

From the fatigue test results discussed in this chapter, especially those specimen sets (Sets 12-15 and Sets 23-26) intended to obtain the post-fatigue local bond stress-slip relationships after a specific number of fatigue cycles, degradation of the local bond strength was observed for both the CFRP rod and strip specimens under fatigue cycles. Although the variation in the local bond strength existed within the same set, especially the range of its fluctuation was sometimes too large to differentiate it from the bond degradation of CFRP rod specimens (Sets 12-15), test results from Section 4.4 still confirmed the gradual declining tendency in the local bond strength of the CFRP rod specimens, as shown in Figs. 4.27(g)-4.27(i). To quantify the rate of the degradation in the local bond strength for both the CFRP rod and strip specimens under the same 10-60% fatigue load range, the normalized local bond strength at arbitrary number of fatigue cycles after degradation was derived from the experiment results by using the regression analysis, as presented in Fig. 4.47 and Fig. 4.48, respectively.

For the CFRP rod specimens (Sets 12-15), the post-fatigue local bond strength was measured after 10, 100, 1000 and 10,000 fatigue cycles, respectively, and the magnitude recorded in Table 4.7 was the average of designated peak local bond stress τ_i (i = 1, 2 or 3) along the bond line, where

the selected τ_i must had bond degradation throughout the entire past fatigue cycles (Fig. 4.21). In other words, only the local bond strength of regions near the loaded end was included to obtain the post-fatigue local bond strength. Besides, because the actual fatigue life of specimen set R-SCSW-A1-1060-F-N was not reached and the strain gauges were unable to survive the upper limit of fatigue cycles, the average bond strength obtained from the post-fatigue test at one million fatigue cycles was selected as the data point to derive the degradation law. As shown in Fig. 4.47(a), the logarithmic function using a base of 10 for the local bond strength fits perfectly with the test results, yielding a R^2 factor equals to 0.9595. However, unlike the local bond strength which could be directly obtained from experiment by strain gauges, the residual bond stress needs to be calibrated from the full-range local bond behavior predicted by the analytical model. As a result, a similar logarithmic degradation law is proposed for the residual bond strength of CFRP rod specimens because the local bond stress τ_1 dropped rapidly in early cycles but was able to hold a relatively low value for a long fatigue period, as observed in the experiment [Figs. 4.27(g)-4.27(i)].

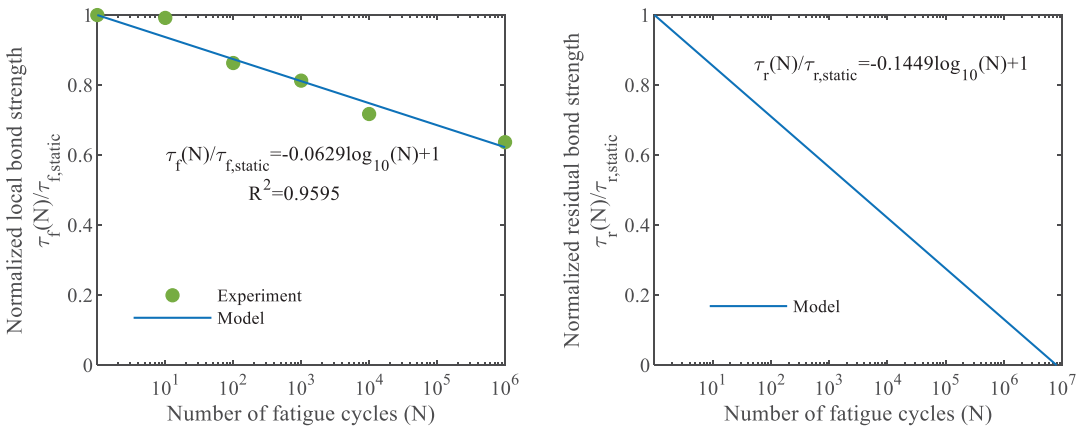

(a) Local bond strength (b) Residual bond strength

Fig. 4.47 Local bond degradation law for CFRP rod specimens (R-SCSW-A1-1060)

For the CFRP strip specimens (Sets 23-26), a similar strategy was adopted to derive the degradation law for the local bond strength. The post-fatigue local bond strength after 10, 100, 1000, and 10,000 fatigues was collected and summarized in Table 4.8, respectively. According to

the test results from specimen set S-RO-A1-1060-F-N, an average fatigue life of 969,085 was obtained, neglecting the first specimen which failed prematurely because of the delamination of its pretreated roughened surface. The average post-failure residual friction of those CFRP strip specimens using epoxy adhesive A1 (Table 4.6) is selected as the ultimate local bond strength at 969,085 fatigue cycles, which equals to 2.7 MPa. Herein, the degradation law proposed for CFRP strip specimens is the same logarithmic function used by the CFRP rod specimens, but it is characterized by a more rapid degradation rate with a R^2 factor equals to 0.9507. On the other hand, a linear interpolation function is proposed as the degradation law for the residual bond strength of CFRP strip specimens, assuming the residual bond strength will vanish completely when fatigue failure occurs. The linear function is determined by the nature of degradation for local bond stress τ_1 during the fatigue cycles, where it dropped steadily up to near fatigue failure as illustrated in Figs. 4.23(e) and (f).

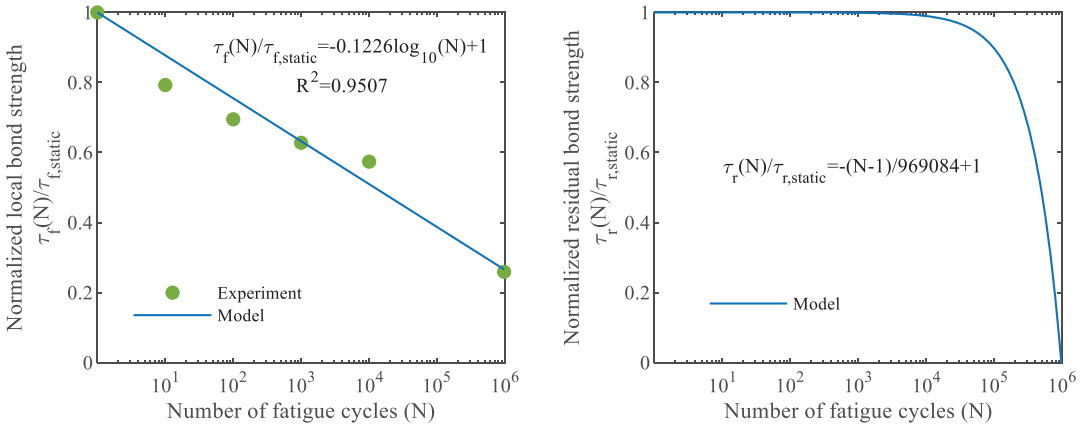

(a) Local bond strength (b) Residual bond strength

Fig. 4.48 Local bond degradation law for CFRP strip specimens (S-RO-A1-1060)

The local bond degradation law proposed for both the rod and strip specimens quantify the local bond deterioration of the NSM FRP-to-concrete bonded joints under fatigue cycles, which agrees well with the experiment results. Besides, it provides the basis for theoretical analysis which aims to explain the fundamental mechanism of local bond development under fatigue cycles.

Assumptions and derivation process of this analytical model will be introduced in detail in the next chapter.

4.6 Summary

This chapter systematically introduces the experimental study of fatigue bond performance of NSM FRP-to-concrete bonded joints through the direct poll-out test, which contains preparation and construction of 84 test specimens, test setup, data acquisition, test observations and test results. Failure mechanism of both static and fatigue DPT of NSM FRP-to-concrete bonded joints has been elaborated. Representative test results measured by embedded strain gauges have been presented under both static and fatigue loading cases, including FRP strain distribution, local bond stress distribution and local bond stress-slip relationship. In addition, the effects on the local bond performance under fatigue cycles due to cross-sectional shape, surface treatment of CFRP, epoxy adhesive type, fatigue load range and concrete strength have been comprehensively discussed. Lastly, the local bond degradation laws under fatigue cycles have been proposed for both the CFRP rod and strip specimens. The following conclusions can be made based on this chapter:

- The static bond strength of the CFRP rod specimens prevailed over the CFRP strip specimens, indicating a more efficient utilization of CFRP material of round cross-section, under the circumstance that the test setup only restrained the loaded end of concrete block;
- For the CFRP rod specimens, the fatigue cycles under the applied load ranges changed the failure mechanism from concrete and epoxy breakage as observed in the static case to slippage/debonding at the FRP/adhesive interface by different extents. However, the strip specimens experienced similar failure mechanism (F/A) in both loading cases;
- Under the same fatigue load range (10-60%P_f), the CFRP strip specimens could resist more fatigue cycles than CFRP rod specimens;
- For the CFRP rod specimens, all the three typical surface treatments including roughened (RO), sand-coated (SC) and sand-coated and spirally wound (SCSW) provided reliable mechanical

interlocking to prevent interfacial sliding between FRP and adhesive under static loading case. Among the three surface conditions, sand-coated and spirally wound (SCSW) had been confirmed as the most efficient with both higher local bond strength and better utilization of concrete material;

- The rod specimens with sand-coated and spirally wound (SCSW) surface treatment showed higher local bond strength and slower degradation rate as compared with the ones with roughened (RO) or sand-coated (SC) treatment under fatigue loading case. The roughened texture and sand coating on those specimens were worn out quickly during the fatigue cycles, leading to a much shorter fatigue life;
- The shear strength of epoxy adhesive had a significant influence on the bond strength. For the CFRP strip specimens of which failure was the interfacial sliding, the pull-out force was proportional to the material property of epoxy adhesive under static loading case. The three-component epoxy adhesive A1 (Pilgrim-Magmaflow Grout-Pak CF) had been verified as the most reliable adhesive with its highest bond strength, good consistency in material property and satisfying fatigue performance of specimens;
- Concrete strength had a positive effect on the local bond strength and the load-carrying capacity of the NSM FRP-to-concrete bonded joints under static loading case. Even if the failure did not occur in concrete substrate, the bond performance took the benefit of using a higher strength concrete. However, it did not noticeably affect the fatigue bond behavior under the same fatigue load range (10-60%P_f); and
- The fatigue load range had significant influence on the local bond behavior. The higher fatigue load range (e.g., 10-70%P_f) accelerated the local bond degradation drastically which resulted in a much shorter fatigue life for both CFRP rod and strip specimens.

CHAPTER FIVE

5 BOND DEGRADATION MODEL OF NSM FRP IN CONCRETE UNDER FATIGUE LOADING

5.1 Overview

The local bond stress-slip model describes the relationship between the local bond stress and the relative slip between concrete and FRP reinforcement at the failure plane under DPT. This is the fundamental law to predict the bond behvior of NSM FRP-to-concrete bonded joints. As presented in Chapter 3.4, the full range bond behavior based on the bilinear local bond stress-slip model was developed by revising the analytical model for the FRP-adhesive-concrete bonded joints initially proposed by Yuan et al. (2001). However, observations from both previous bond tests (Soliman et al. 2011; Lee et al. 2013; Al-Saadi et al. 2018) and static direct pull-out tests conducted in this research (Figs. 4.19 and 4.20) verified that residual bond stress existed after the local debonding occurred. Yet, most reported studies (Seracino et al. 2007a; Oehlers et al. 2008; Bilotta et al. 2011) adopted either the linear descending or the bilinear local bond stress-slip model for their analytical predictions rather than the more representative trilinear model. To this end, a trilinear local bond stress-slip model was proposed based on the test results for different specimen sets. The analytical full-range local bond behavior was then derived and assessed using experimental results.

In addition, although some efforts have been made to correlate the relationship between the fatigue life and the fatigue load range (ratio) or the maximum fatigue load (ratio), the accuracy of the empirical models derived from regression analyses were unsatisfactory as pointed out in Chapter 2.6.3 for NSM FRP-to-concrete bonded joints. Regarding the experimental and analytical research on the more essential local bond stress degradation under fatigue loading, Chen and Cheng (2015, 2016) are the only available references in the open literature. Therefore, this chapter aims at developing the trilinear local bond stress-slip model that is adaptable to fatigue cycles and predict

the local bond behavior of the NSM FRP-to-concrete bonded joints under fatigue. Analytical results based the one-dimensional finite element (FE) model are also presented and compared with the fatigue test results, which included the FRP strain distribution, local bond stress distribution and relative slip, etc.

5.2 Bond model for NSM FRP under static loading case

5.2.1 Trilinear local bond stress-slip model

As mentioned in Chapter 4.3.4, the local bond stress-slip relationship recorded in this experimental research could be featured as a three-stage development. Therefore, to simulate the full-range local bond behavior of NSM FRP-to-concrete bonded joints, the local bond stress-slip relationship for each specimen was idealized as the trilinear model expressed by Eq. 5.1 and Fig. 5.1 below.

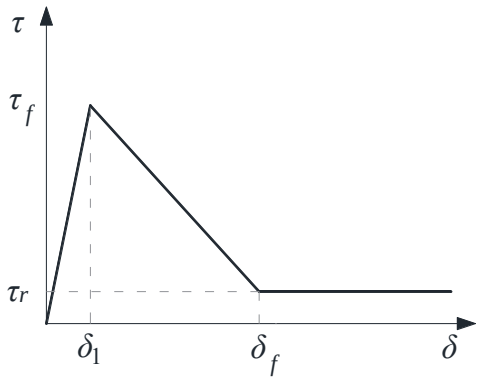

Fig. 5.1 Trilinear local bond stress-slip model

$$\tau(\delta)=\begin{cases}\dfrac{\delta}{\delta_1}\tau_f & for\ 0\le\delta\le\delta_1 \quad (a)\\ \dfrac{\delta_f-\delta}{\delta_f-\delta_1}(\tau_f-\tau_r)+\tau_r & for\ \delta_1<\delta\le\delta_f \quad (b)\\ \tau_r & for\ \delta>\delta_f \quad (c)\end{cases} \tag{5.1}$$

where τ = local bond stress; δ = relative slip between FRP reinforcement and concrete block; τ_f = peak local bond stress; δ_1 = relative slip at peak stress; τ_r = residual bond strength and δ_f = relative slip at debonding. The latter four key parameters were calibrated from the experimental local bond

stress-slip results from the DPT in this study (Figs. 4.19 and 4.20) and are summarized in Table 5.1 for each type of applicable specimen. In addition, the governing equation for the NSM FRP-to-concrete bonded joints under single pull-out force is derived as Eqs. 5.2 and 5.3 below, i.e.,

$$\frac{d^2\delta}{dx^2} - \lambda^2\tau(\delta) = 0 \tag{5.2}$$

$$\lambda = \sqrt{L_p\left(\frac{1}{A_f E_f} + \frac{1}{A_c E_c}\right)} \tag{5.3}$$

where A_c = cross-sectional area of concrete block; and E_c = Young's modulus of concrete. By substituting Eq. 5.1 into Eq. 5.2 and applying appropriate boundary conditions, such as the external boundary conditions and the internal continuities for the relative slip (the first derivative of the relative slip and FRP stress), an analytical solution to this ordinary differential equation (ODE) can be obtained at different stages of the bond development. Details of the mathematical derivation procedure can refer to the theoretical model based on the bilinear local bond stress-slip relationship, which have already been elaborated in Chapter 3.4 and hence are not repeated herein. The major difference lies in the debonding stage where the residual local bond strength τ_r is adopted in this study, and hence the debonding region still contribute to the bond resistance after debonding occurs.

5.2.2 Full range local bond behavior

Based on the trilinear local bond stress-slip model, the distribution along the bond line of the relative slip between FRP and concrete block δ, the local bond stress τ, and the FRP stress σ_f at different bond development stages under pull-out force are derived in the expressions by Eqs. 5.4-5.23 below.

Linear elastic stage I – This stage starts with the beginning of monotonic loading under the pull-out force P and develops to the elastic-softening stage II when $\delta(L) = \delta_1$.

$$\delta = \frac{P\delta_1\lambda_1}{L_p\tau_f}\frac{\cosh(\lambda_1 x)}{\sinh(\lambda_1 L)} \qquad for\ x \in [0, L] \tag{5.4}$$

$$\tau = \frac{P\lambda_1}{L_p}\frac{\cosh(\lambda_1 x)}{\sinh(\lambda_1 L)} \qquad for\ x \in [0, L] \tag{5.5}$$

$$\sigma_f = \frac{P}{A_f}\frac{\sinh(\lambda_1 x)}{\sinh(\lambda_1 L)} \qquad for\ x \in [0, L] \tag{5.6}$$

where

$$\lambda_1 = \sqrt{\frac{\tau_f}{\delta_1}L_p\left(\frac{1}{A_f E_f} + \frac{1}{A_c E_c}\right)} \tag{5.7}$$

Elastic-softening stage II

$$\delta = \begin{cases} \delta_1 \dfrac{\cosh(\lambda_1 x)}{\cosh\left[\lambda_1 (L - L_s)\right]} & for\ x \in [0, L - L_s] \\ \dfrac{\tau_f (\delta_f - \delta_1)}{\tau_f - \tau_r} \left\{ \begin{array}{l} \dfrac{\lambda_2}{\lambda_1}\tanh\left[\lambda_1 (L - L_s)\right] \\ \bullet\ sin\left[\lambda_2 (x - L + L_s)\right] \\ -\cos\left[\lambda_2 (x - L + L_s)\right] \\ + \dfrac{\tau_f \delta_f - \tau_r \delta_1}{\tau_f (\delta_f - \delta_1)} \end{array} \right\} & for\ x \in [L_s, L] \end{cases} \tag{5.8}$$

$$\tau = \begin{cases} \tau_f \dfrac{\cosh(\lambda_1 x)}{\cosh\left[\lambda_1 (L - L_s)\right]} & for\ x \in [0, L - L_s] \\ -\tau_f \left\{ \begin{array}{l} \dfrac{\lambda_2}{\lambda_1}\tanh\left[\lambda_1 (L - L_s)\right] \\ \bullet\ sin\left[\lambda_2 (x - L + L_s)\right] \\ -\cos\left[\lambda_2 (x - L + L_s)\right] \end{array} \right\} & for\ x \in [L_s, L] \end{cases} \tag{5.9}$$

$$\sigma_f = \begin{cases} \dfrac{L_p \tau_f}{A_f \lambda_1} \dfrac{\sinh(\lambda_1 x)}{\cosh\left[\lambda_1 (L - L_s)\right]} & for\ x \in [0, L - L_s] \\ \dfrac{L_p \tau_f}{A_f \lambda_2} \left\{ \begin{array}{l} \dfrac{\lambda_2}{\lambda_1} \tanh\left[\lambda_1 (L - L_s)\right] \\ \bullet cos\left[\lambda_2 (x - L + L_s)\right] \\ + sin\left[\lambda_2 (x - L + L_s)\right] \end{array} \right\} & for\ x \in [L_s, L] \end{cases} \tag{5.10}$$

where

$$\lambda_2 = \sqrt{\frac{\tau_f - \tau_r}{\delta_f - \delta_1} L_p \left(\frac{1}{A_f E_f} + \frac{1}{A_c E_c} \right)} \tag{5.11}$$

Elastic-softening-debonding stage III – The elastic-softening stage II keeps developing until the boundary condition $\delta(L) = \delta_f$ is reached which indicates the start of the elastic-softening-debonding stage III.

$$\delta = \begin{cases} \delta_1 \dfrac{\cosh(\lambda_1 x)}{\cosh\left[\lambda_1 (L - L_d - L_s)\right]} & for\ x \in [0, L - L_d - L_s] \\ \dfrac{\tau_f (\delta_f - \delta_1)}{\tau_f - \tau_r} \left\{ \begin{array}{l} \dfrac{\lambda_2}{\lambda_1} \tanh\left[\lambda_1 (L - L_d - L_s)\right] \\ \bullet sin\left[\lambda_2 (x - L + L_d + L_s)\right] \\ - \cos\left[\lambda_2 (x - L + L_d + L_s)\right] \\ + \dfrac{\tau_f \delta_f - \tau_r \delta_1}{\tau_f (\delta_f - \delta_1)} \end{array} \right\} & for\ x \in [L - L_d - L_s, L - L_d] \\ 0.5 \lambda_3 x^2 + A_1 x + B_1 & for\ x \in [L - L_d, L] \end{cases} \tag{5.12}$$

$$\tau = \begin{cases} \tau_f \dfrac{\cosh(\lambda_1 x)}{\cosh\left[\lambda_1 (L - L_d - L_s)\right]} & for\ x \in [0, L - L_d - L_s] \\ -\tau_f \left\{ \begin{array}{l} \dfrac{\lambda_2}{\lambda_1} \tanh\left[\lambda_1 (L - L_d - L_s)\right] \\ \bullet\, sin\left[\lambda_2 (x - L + L_d + L_s)\right] \\ -\cos\left[\lambda_2 (x - L + L_d + L_s)\right] \end{array} \right\} & for\ x \in [L - L_d - L_s, L - L_d] \\ \tau_r & for\ x \in [L - L_d, L] \end{cases} \quad (5.13)$$

$$\sigma_f = \begin{cases} \dfrac{L_p \tau_f}{A_f \lambda_1} \dfrac{\sinh(\lambda_1 x)}{\cosh\left[\lambda_1 (L - L_d - L_s)\right]} & for\ x \in [0, L - L_d - L_s] \\ \dfrac{L_p \tau_f}{A_f \lambda_2} \left\{ \begin{array}{l} \dfrac{\lambda_2}{\lambda_1} \tanh\left[\lambda_1 (L - L_d - L_s)\right] \\ \bullet\, cos\left[\lambda_2 (x - L + L_d + L_s)\right] \\ +sin\left[\lambda_2 (x - L + L_d + L_s)\right] \end{array} \right\} & for\ x \in [L - L_d - L_s, L - L_d] \\ \dfrac{L_p \tau_r}{A_f} \left(x - L + \dfrac{P}{L_p \tau_r} \right) & for\ x \in [L - L_d, L] \end{cases} \quad (5.14)$$

where

$$A_1 = \frac{\lambda_2 \tau_f (\delta_f - \delta_1)}{(\tau_f - \tau_r)} \frac{\left[1 - \dfrac{\tau_r}{\tau_f} \cos(\lambda_2 L_s)\right]}{\sin(\lambda_2 L_s)} - \lambda_3 (L - L_d) \quad (5.15)$$

$$B_1 = -0.5 \lambda_3 (L - L_d)^2 - A_1 (L - L_d) + \delta_f \quad (5.16)$$

$$\lambda_3 = \tau_r L_p \left(\frac{1}{A_f E_f} + \frac{1}{A_c E_c} \right) \quad (5.17)$$

Softening-debonding stage IV – When the bonded region at the free end further develops and reaches the critical local bond strength, i.e., $\tau(0) = \tau_f$, the softening-debonding stage IV initiates in conjunction with a rapid drop in the residual bond strength until complete failure.

$$\delta = \begin{cases} -\dfrac{\tau_r\left(\delta_f - \delta_1\right)}{\left(\tau_f - \tau_r\right)}\dfrac{\cos\left(\lambda_2 x\right)}{\cos\left(\lambda_2 L_s\right)} + \dfrac{\delta_f \tau_f - \delta_1 \tau_r}{\tau_f - \tau_r} & \text{for } x \in \left[0, L_s\right] \\ 0.5\lambda_3 x^2 + A_2 x + B_2 & \text{for } x \in \left[L_s, L\right] \end{cases} \tag{5.18}$$

$$\tau = \begin{cases} \tau_r \dfrac{\cos\left(\lambda_2 x\right)}{\cos\left(\lambda_2 L_s\right)} & \text{for } x \in \left[0, L_s\right] \\ \tau_r & \text{for } x \in \left[L_s, L\right] \end{cases} \tag{5.19}$$

$$\sigma_f = \begin{cases} \dfrac{L_p \tau_r}{A_f \lambda_2}\dfrac{\sin\left(\lambda_2 x\right)}{\cos\left(\lambda_2 L_s\right)} & \text{for } x \in \left[0, L_s\right] \\ \dfrac{L_p \tau_r}{A_f}\left(x - L + \dfrac{P}{L_p \tau_r}\right) & \text{for } x \in \left[L_s, L\right] \end{cases} \tag{5.20}$$

where

$$P = L_p \tau_r \left[L - L_s + \frac{1}{\lambda_2}\tan\left(\lambda_2 L_s\right) \right] \tag{5.21}$$

$$A_2 = \frac{\lambda_2 \tau_r \left(\delta_f - \delta_1\right)}{\left(\tau_f - \tau_r\right)}\tan\left(\lambda_2 L_s\right) - \lambda_3 L_s \tag{5.22}$$

$$B_2 = -0.5\lambda_3 {L_s}^2 - A_2 L_s + \delta_f \tag{5.23}$$

where x = distance measured from the free end; L = bond length; L_s = bond length within the softening stage; and L_d = debonding length that is close to the loaded end.

5.2.3 Comparison between bilinear and trilinear model in full range load-slip behavior

Based on the full range local bond behavior of the trilinear local bond stress-slip model, the representative curve of the load vs. relative slip at the loaded end is presented in Fig. 5.2. The theoretical solution based on the bilinear local bond stress-slip model is illustrated in the same figure. Both curves are derived by providing the same appropriate material properties and sufficiently long bond length, where the residual bond stress τ_r is set as 20% of the local bond strength τ_f for the trilinear model.

It is obvious that both curves are featured as linear elastic at lower load level and then develop nonlinearly with the increase of the relative slip, indicating the softening mechanism of the material beyond the elastic limit. The major difference between these two models lies in the bond behavior after debonding occurs (stage III) where steady drop in applied load is observed for bilinear model whilst extra load is obtained for the trilinear model because of the residual bond strength. Theoretically, the bonded joints will fail not long after reaching the load-carrying capacity under the displacement-control mode, which has been confirmed by the test observations in this research. Therefore, the stage III and IV of the bilinear model only exist under the ideal loading scenario. However, the full-range behavior based on the trilinear model has the advantage of considering the contribution by the residual bond strength, which is closer to the actual load-slip response recorded during the monotonic DPT. In addition, because of the further increase in the applied load in stage III for the trilinear model, the bonded joints will reach its maximum capacity later with some debonding region exists already. This feature is highly consistent with the static DPT result and make the trilinear model more appropriate for the analytical development of the predictive model, which will be discussed in detail in the following chapters.

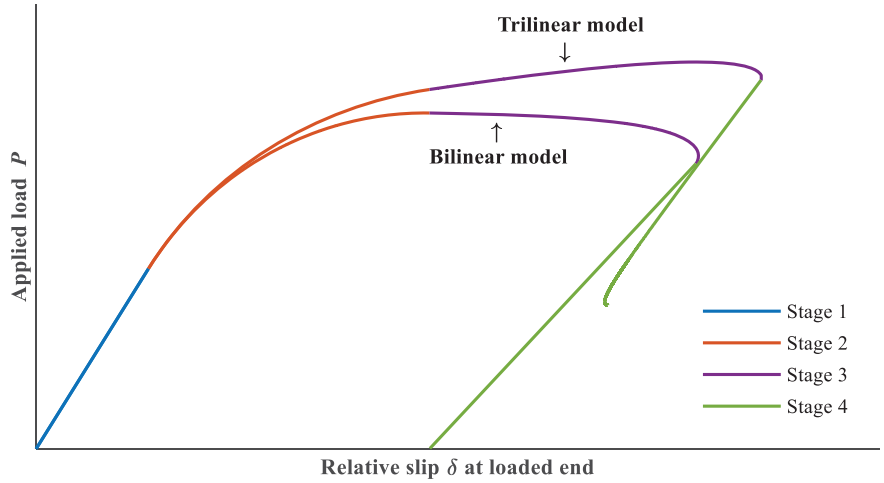

Fig. 5.2 Full-range load-slip behaviors for both bilinear and trilinear local bond stress-slip model

5.3 Model verification

The comparison for the pull-out force between the analytical predictions using the proposed trilinear local bond stress-slip relationship and the experimental data is summarized in Table 5.1. It can be seen that good correlations were obtained for all specimens with the absolute differences less than or equal to 1%, where the difference was calculated by $(P_{f\_model} - P_{f\_exp})/P_{f\_exp} \times 100$, provided that the average key parameters of the trilinear model, i.e., τ_f, δ_1, τ_r and δ_f, were set properly for each set. Variations of these parameters certainly existed within the same set due to the fluctuation of material properties, CFRP surface roughness and groove qualities etc. More effort should be taken to ensure a better consistency of the local bond performance during the construction procedure.

Table 5.1 Comparison between analytical predictions and experimental results.

Set	ID	Local bond strength τ_f (MPa)	δ_1 (mm)	Residual bond strength τ_r (MPa)	δ_f (mm)	Pull-out force P_{f_exp}[a] (kN)	P_{f_model}[b] (kN)	Difference[c] (%)
1	R-RO-A1-N	13.2	0.08	9.44	0.30	77.7	77.8	0.07
2	R-SC-A1-N	16.6	0.06	6.39	0.30	70.5	70.6	0.05
3	R-SCSW-A1-N	17.3	0.08	7.18	0.45	78.5	77.7	-1.02
4	S-RO-A1-N	10.4	0.05	3.37	0.21	54.4	54.1	-0.50
5	S-RO-A2-N	11.4	0.09	3.24	0.19	52.9	52.3	-1.09
6	S-RO-A3-N	5.77	0.06	2.47	0.13	34.2	33.9	-0.96
7	S-RO-A4-N	6.22	0.04	1.92	0.19	34.5	34.6	0.31
8	S-RO-A1-H	11.1	0.08	4.47	0.22	62.5	62.9	0.63

[a]Average pull-out force of specimen set obtained from bond test.
[b]Pull-out force of specimen set predicted by the analytical model.
[c]Difference = $(P_{f\_model} - P_{f\_exp})/P_{f\_exp.} \times 100$.

Figs. 5.3 and 5.4 show the comparison for the CFRP strain distribution and the local bond stress distribution along the bond length, respectively, under different load levels (25, 50, 75 and 100%P_f) using specimen set R-RO-A1-N for rod case (4 plots on the left-hand side) and set S-RO-A4-N for strip case (4 plots on the right-hand side) as an example. It can be seen that the predictions using the proposed model that considered the contribution of the residual bond stress well captured the overall physical performance of the specimens during the direct pull-out tests except for some small discrepancy in the rod case when the load level approached 100%P_f.

For the load vs. relative slip response at the loaded end, Fig. 5.5 shows the typical comparison between the analytical predictions and the experimental results for both the CFRP rod case (specimen sets R-SC-A1-N and R-SCSW-A1-N on the left-hand side) and strip case (specimen sets S-RO-A1-N and S-R0-A1-H on the right-hand side). It can be seen that the proposed model was able to capture the entire development trend of the load vs. relative slip response although it underestimated the relative slip at failure for some of the specimens.

However, it should be noted that the bond behavior, e.g., the CFRP strain distribution and the local bond stress distribution, of specimen set S-RO-A2-N and S-RO-A3-N was not represented by the proposed model. Because the local bond strength at different locations along the bond length, which were directly measured from the DPT, varied drastically for these two specimen sets. For example, τ_3-τ_5 of specimen S-RO-A2-N-3 [Fig. 4.20(e)] and τ_5 of specimen S-RO-A3-N-3 [Fig. 4.20(i)] were exceptionally small compared to the rest of the local bond strength. This significant inconsistency of the local bond strength along the bond line violated the fundamental assumptions of this analytical model (Yuan et al. 2004) and thus the corresponding theoretical predictions were not applicable. This phenomenon should be attributed to two probable factors including: (a) these two epoxy adhesives were sensitive to mix proportion and minor deviation might lead to a significant fluctuation in material properties; (b) slight leakage of epoxy adhesive at both ends of bonded region due to their higher flowability. Nevertheless, the overall accuracy of the predicted pull-out forces and bond behaviors based on the trilinear local bond stress-slip relationship was still high for most test specimens.

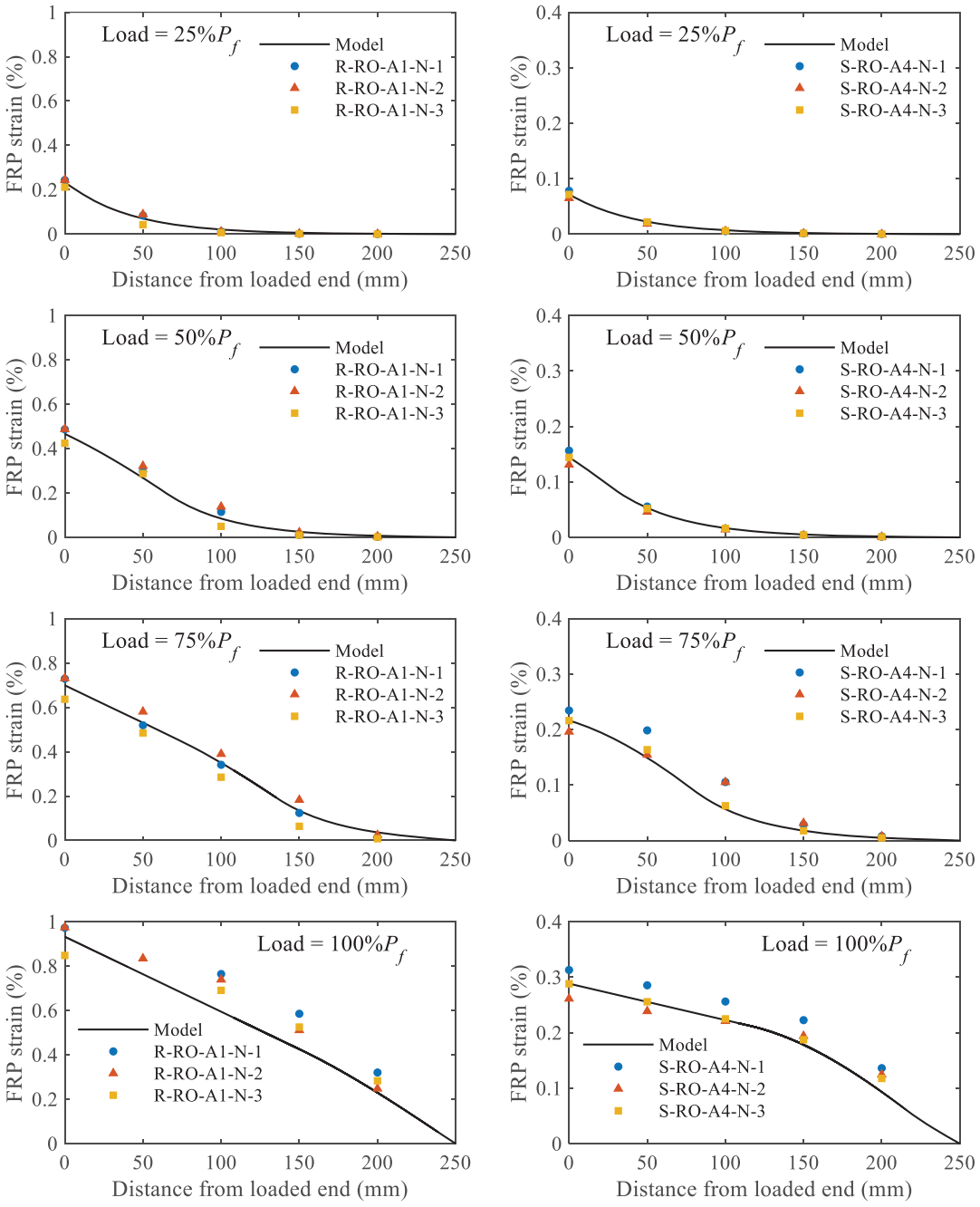

(a) R-RO-A1-N

(b) S-RO-A4-N

Fig. 5.3 Comparison of CFRP strain distribution between analytical predictions and experimental results

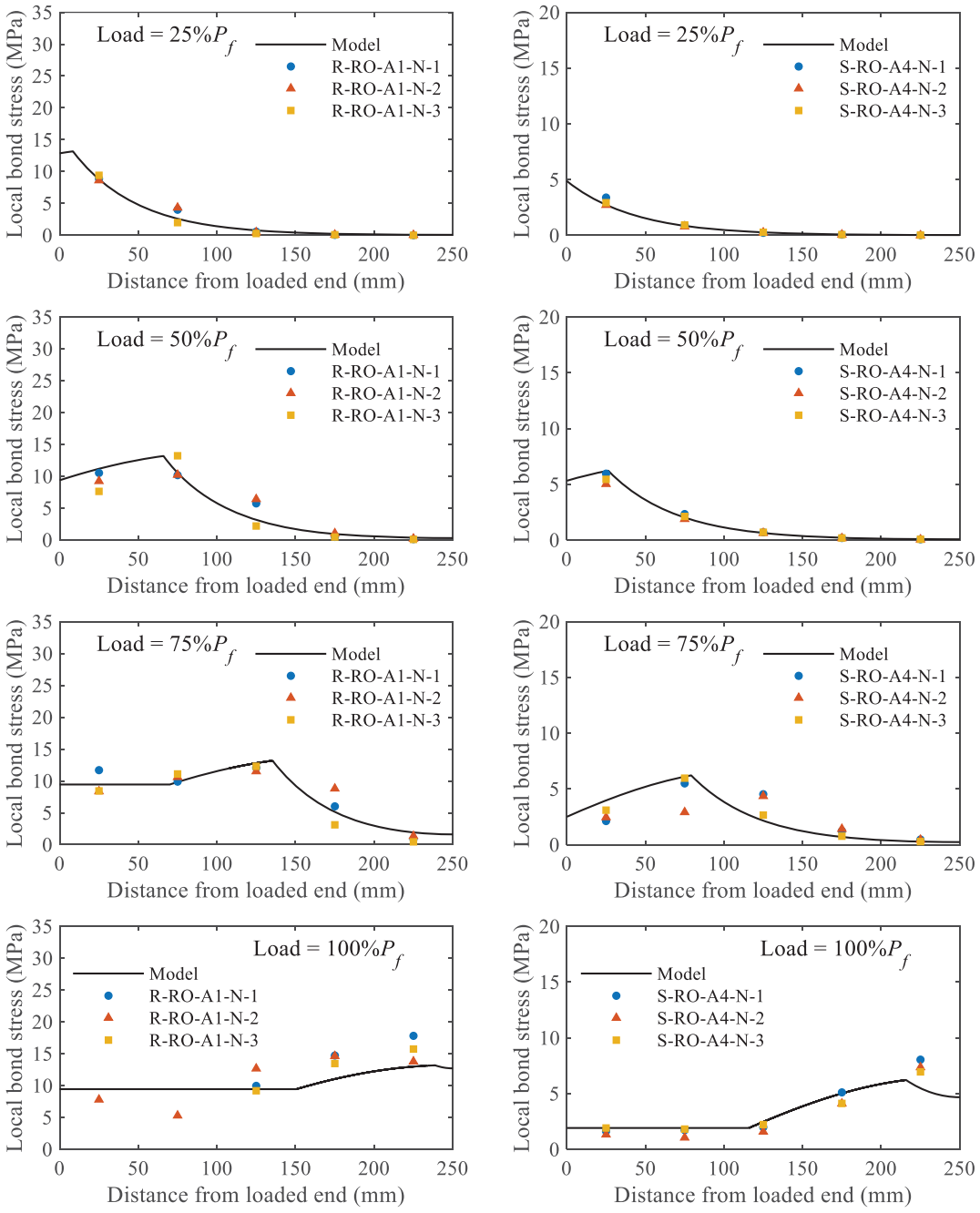

(a) R-RO-A1-N

(b) S-RO-A4-N

Fig. 5.4 Comparison of local bond stress distribution between analytical predictions and experimental results

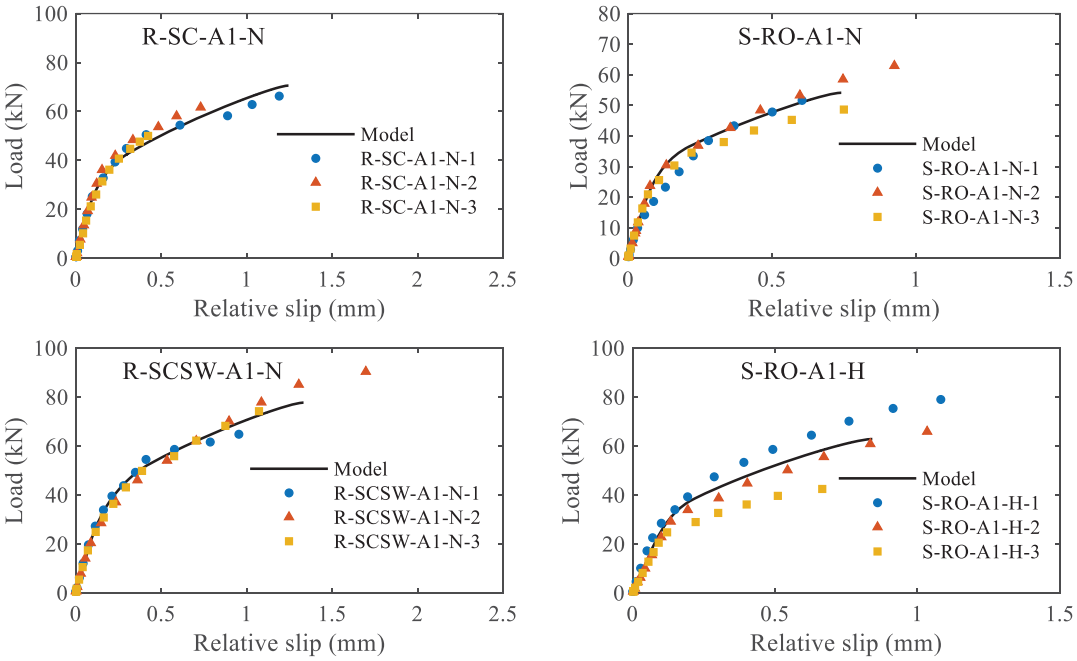

(a) CFRP rod case (b) CFRP strip case

Fig. 5.5 Comparison of load-slip response at loaded end between analytical predictions and experimental results

5.4 Finite element model for bond degradation under fatigue loading

As mentioned in Chapter 4.5, the local bond strength τ_f of the NSM FRP-to-concrete bonded joints will gradually degrade with the increase of the fatigue cycles and the tendency of degradation can be approximated by the logarithmic function based on the test results for both CFRP rod (Sets 12-15 in Table 4.7) and strip (Sets 23-26 in Table 4.8) specimens, as presented below.

$$\frac{\tau_f(N)}{\tau_{f,static}} = -0.0629\log_{10}(N)+1 \quad \text{for CFRP rod specimens} \tag{5.24}$$

$$\frac{\tau_r(N)}{\tau_{r,static}} = -0.1449\log_{10}(N)+1 \quad \text{for CFRP rod specimens} \tag{5.25}$$

$$\frac{\tau_f(N)}{\tau_{f,static}} = -0.1226\log_{10}(N)+1 \quad \text{for CFRP strip specimens} \tag{5.26}$$

$$\frac{\tau_r(N)}{\tau_{r,static}} = -(N-1)/969084 + 1 \text{ for CFRP strip specimens} \quad (5.27)$$

Because the trilinear local bond stress-slip model adopted has three stages including the linear elastic stage, the softening stage and the debonding stage for the local bond behavior, the bonded regions of different stages will coexist and develop under the applied pull-out force along the bond line. In addition, the general derivation procedure of the theoretical solutions to the governing equation (Eq. 5.2) based on the trilinear model can refer to Chapter 3.4 to obtain the relative slip $\delta(x)$, local bond stress $\tau(x)$ and FRP stress $\sigma_f(x)$ at different stages as presented in Chapter 5.2.2. Thereafter, the finite element method (FEM) has been used to discretize the entire bond line into continuous elements provided that each element still complies with the fundamental governing equation and the trilinear local bond stress-slip model. The benefit of applying the FEM is that each bond element can be manipulated individually and make it adaptable to the degradation law of the NSM FRP-to-concrete bonded joints under fatigue loading case.

5.4.1 Model and assumptions

The general configuration of a single shear direct pull-out test (DPT) for NSM FRP-to-concrete bonded joints is illustrated in Fig. 5.6, which also shows a typical local bond stress distribution including all three different bonded regions. The bond length can be categorized by three different regions: the elastic region ($0 \le x \le L-L_d-L_s$); the softening region ($L-L_d-L_s \le x \le L-L_d$); and the debonding region ($L-L_d \le x \le L$), where x measures the distance from the free end of the bonded joints as mentioned above. Next, apply a one-dimensional mesh to partition the bond length into the designated number of segments, i.e., n_1 elastic elements, (n_2-n_1) softening elements and (n_3-n_2) debonding elements under the first cycle of the fatigue load. The number of elements of different regions is intended for controlling the accuracy of the numerical analysis. As a result, the length for each element is not identical for different regions and will further be updated upon each fatigue

cycle. Prior to the detailed derivation process, some important assumptions are adopted as follows to insure the validity of this FEM model:

- Both the FRP reinforcement and concrete are homogenous and linear elastic;
- The axial stress is uniformly distributed over the cross-section for both FRP reinforcement and concrete block;
- Epoxy adhesive is homogeneous, linear elastic and constant in dimensions along the bond length and it transfers load from FRP reinforcement to the surrounding concrete as an intermediate. Thus, the thickness of epoxy adhesive is neglected.
- Bending or twisting effect is neglected in the analytical model, i.e., the bonded region is subjected to pure tension; and
- The weakest part of the NSM bonded joints is the interface between FRP and epoxy adhesive as observed during the experiments, which is considered as the failure plane.

The local bond stress of each bond finite element within the elastic region follows the trilinear model as presented in Fig. 5.1 with no degradation. However, for those bond finite elements within the softening region under the current fatigue cycle, of which the relative slip δ is beyond δ_1, their local bond strength τ_f and the residual bond strength τ_r will degrade in accordance with the empirical Eqs. 5.24-5.27 during the following fatigue cycles, as presented in Fig. 5.7.

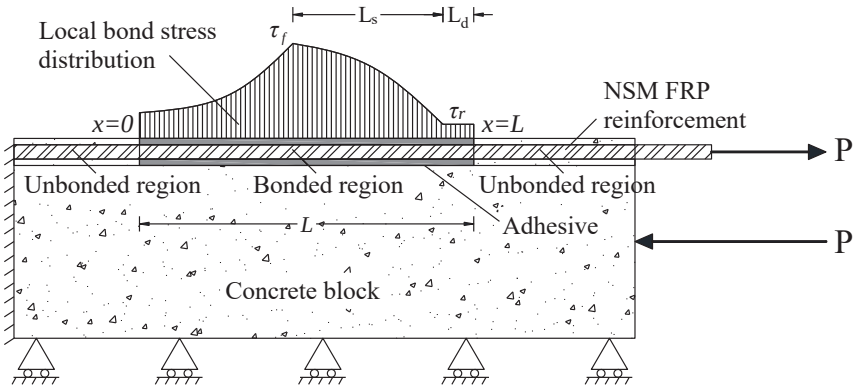

Fig. 5.6 Single shear DPT configuration for NSM FRP-to-concrete bonded joints under pull-out force

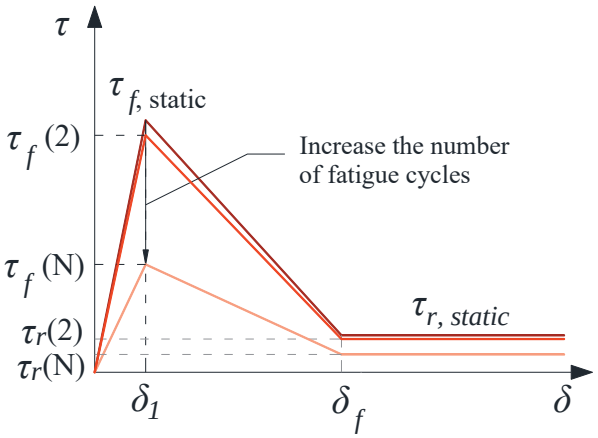

Fig. 5.7 Trilinear local bond stress-slip model under fatigue cycles

The concept of adopting the FEM method to simulate the local bond degradation under fatigue cycles is illustrated in Fig. 5.8. During the first cycle of fatigue load, three bonded regions (elastic, softening and debonding) are developed to balance the applied pull-out force (P_{max}). It should be noted that the local bond stress distribution depends on the magnitude of the applied fatigue load. Based on the assumption defined above, if P_{max} is too low to develop the softening region on the bond line, no degradation will even occur, leading to an infinite fatigue life. Therefore, a sufficiently large P_{max} is assumed to ensure at least partial region of the bond line develops into the inelastic stage. Under the applied P_{max}, a total number of n_3 finite elements are developed alone with (n_3+1) nodes, detonated by x_0, x_1, x_2, …, x_{n3}, among which x_{n1} is the boundary between the elastic and the softening region and x_{n2} is the boundary between the softening and the debonding region [Fig. 5.8(a)]. After one more fatigue cycle, damages occur for elements from both softening and debonding regions through the unloading and loading process and their local bond stress will slightly drop accordingly, see the dashed line in Fig. 5.8 (b). To compensate for the loss of the local bond stress of these degraded regions and to resist the same P_{max}, the elastic region is further developed with larger relative slip and higher local bond stress. As a result, one more softening element is created to the right of x_{n1} since its relative slip δ increases to be larger than δ_1. In the meantime, the peak of the local bond stress distribution ($\tau_{f,static}$) moves leftwards. Similarly, another

debonding element is developed since its relative slip δ grows to be larger than δ_f. The same procedure will repeat for the next fatigue cycle, while the peak local bond stress remains migrating towards the free end until it reaches the critical situation, where the residual bond strength is unable to resist P_{max}, leading to the fatigue failure of the bond [Fig. 5.8(c)].

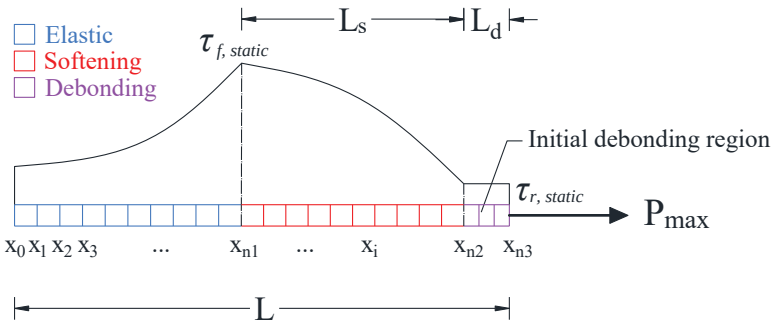

(a) Local bond stress distribution and bond finite element under the 1st fatigue cycle

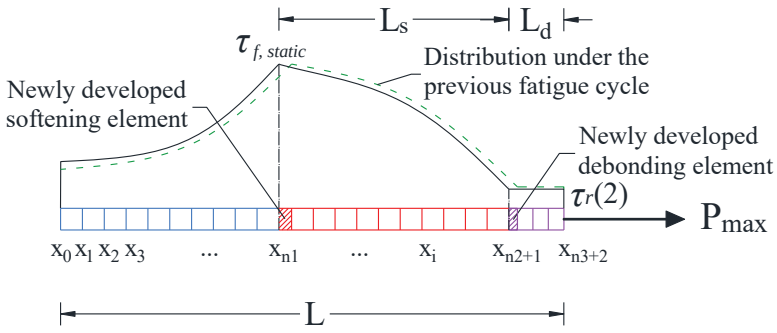

(b) Local bond stress distribution and bond finite element under the 2nd fatigue cycle

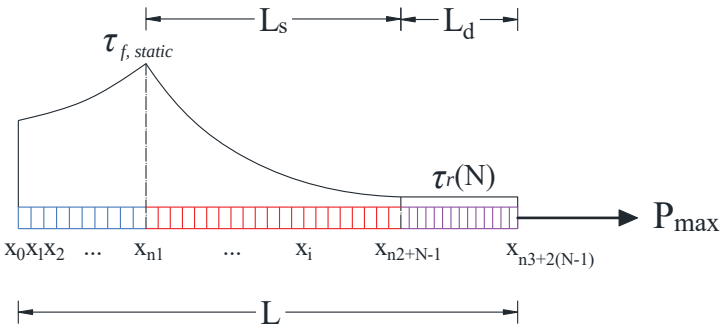

(c) Local bond stress distribution and bond finite element under the N^{th} fatigue cycle

Fig. 5.8 Illustration of FEM model for NSM FRP-to-concrete bonded joints under fatigue cycles

5.4.2 Governing equation and general solutions

Although the bond line has been discretized into finite elements, the fundamental interactions within the NSM FRP-adhesive-concrete joints are still the same as the analytical model introduced in Chapter 3. Thus, the governing equation for the i^{th} finite element can be represented as follows regardless of the bonded region to which it belongs:

$$\frac{d^2\delta}{dx^2} - \lambda^2 \tau_i(\delta) = 0 \quad for\ x_{i-1} \le x \le x_i \tag{5.28}$$

where λ can be referred to Eq. 5.3; $\tau_i(\delta)$ = local bond stress-slip relationship for the i^{th} finite element; x_{i-1}, x_i = start and end coordinate of the element, where $x_0 = 0$ (free end of the bond line); and all other variables are the same as previously defined.

The theoretical solutions to this governing equation depend on the type of bond finite elements (i.e., elastic, softening and debonding) [Fig. 5.8(a)], and their solutions are derived respectively as follows:

(a) For elements within the elastic region ($0 \le x \le L - L_d - L_s$), the general solution can be obtained by firstly substituting Eq. 5.1(a) into Eq. 5.28, which yields the following equation:

$$\frac{d^2\delta}{dx^2} - \left(\lambda_1^{\,i}\right)^2 \delta = 0 \tag{5.29}$$

where

$$\lambda_1^{\,i} = \sqrt{\frac{\tau_f^{\,i}}{\delta_1} L_p \left(\frac{1}{A_f E_f} + \frac{1}{A_c E_c} \right)} \tag{5.30}$$

where $\tau_f^{\,i}$ = local bond strength for the i^{th} finite element.

Then it could be further derived by solving this homogeneous linear second-order ODE as shown below:

$$\delta = C_1^{\,i} \cosh\left(\lambda_1^{\,i} x\right) + C_2^{\,i} \sinh\left(\lambda_1^{\,i} x\right) \tag{5.31}$$

The local bond stress τ and FRP stress σ_f can be easily obtained through Eq. 5.1(a) and Eq. 3.1, respectively, as presented below:

$$\tau = \frac{{\tau_f}^i}{\delta_1}\left[{C_1}^i \cosh\left({\lambda_1}^i x \right) + {C_2}^i \sinh\left({\lambda_1}^i x \right) \right] \tag{5.32}$$

$$\sigma_f = \frac{L_p {\tau_f}^i}{A_f \delta_1 {\lambda_1}^i}\left[{C_1}^i \sinh\left({\lambda_1}^i x \right) + {C_2}^i \cosh\left({\lambda_1}^i x \right) \right] + {C_3}^i \tag{5.33}$$

where ${C_1}^i$, ${C_2}^i$ and ${C_3}^i$ = constants of the i^{th} element remain to be solved by boundary conditions.

(b) For elements within the softening region (L-L_d-$L_s \le x \le L$-L_d), the general equation of the relative slip δ can be derived similarly by solving the following nonhomogeneous ODE, which is obtained by substituting Eq. 5.1(b) into Eq. 5.28 as:

$$\frac{d^2\delta}{dx^2} + \left({\lambda_2}^i \right)^2 \delta = \frac{\delta_f {\tau_f}^i - \delta_1 {\tau_r}^i}{\delta_f - \delta_1} \lambda^2 \tag{5.34}$$

where

$${\lambda_2}^i = \sqrt{\frac{{\tau_f}^i - {\tau_r}^i}{\delta_f - \delta_1} L_p \left(\frac{1}{A_f E_f} + \frac{1}{A_c E_c} \right)} \tag{5.35}$$

where ${\tau_r}^i$ = residual bond strength for the i^{th} finite element.

The explicit solution to Eq. 5.33 is thus derived as:

$$\delta = {C_1}^i \cos\left[{\lambda_2}^i \left(x - L + L_d + L_s \right) \right] + {C_2}^i \sin\left[{\lambda_2}^i \left(x - L + L_d + L_s \right) \right] + \frac{\delta_f {\tau_f}^i - \delta_1 {\tau_r}^i}{{\tau_f}^i - {\tau_r}^i} \tag{5.36}$$

Then the local bond stress τ and the FRP stress σ_f can be obtained as well in the following:

$$\tau = -\frac{{\tau_f}^i - {\tau_r}^i}{\delta_f - \delta_1}\left\{ {C_1}^i \cos\left[{\lambda_2}^i \left(x - L + L_d + L_s \right) \right] + {C_2}^i \sin\left[{\lambda_2}^i \left(x - L + L_d + L_s \right) \right] \right\} \tag{5.37}$$

$$\sigma_f = -\frac{L_p \left({\tau_f}^i - {\tau_r}^i \right)}{A_f \left(\delta_f - \delta_1 \right) {\lambda_2}^i}\left\{ {C_1}^i \sin\left[{\lambda_2}^i \left(x - L + L_d + L_s \right) \right] - {C_2}^i \cos\left[{\lambda_2}^i \left(x - L + L_d + L_s \right) \right] \right\} + {C_3}^i \tag{5.38}$$

(c) For elements within the debonding region (L-$L_d \le x \le L$), the same procedure is conducted by substituting Eq. 5.1(c) into Eq. 5.28, which leads to the following expression:

$$\frac{d^2\delta}{dx^2} = \lambda_3^{\,i} \tag{5.39}$$

$$\lambda_3 = \tau_r^{\,i} L_p \left(\frac{1}{A_f E_f} + \frac{1}{A_c E_c} \right) \tag{5.40}$$

Thus, the general solution of relative slip δ, the local bond stress τ and the FRP stress σ_f are derived as:

$$\delta = 0.5\lambda_3^{\,i} x^2 + C_1^{\,i} x + C_2^{\,i} \tag{5.41}$$

$$\tau = \tau_r^{\,i} \tag{5.42}$$

$$\sigma_f = \frac{L_p}{A_f} \tau_r^{\,i} x + C_3^{\,i} \tag{5.43}$$

5.4.3 Boundary conditions

For a total number of n finite elements on the bond line, $3n$ unknown constants ($C_1^{\,i}$, $C_2^{\,i}$ and $C_3^{\,i}$, i = 1, 2, …, n) need to be determined to generate the complete solutions of the relative slip δ, the local bond stress τ and the FRP stress σ_f. In addition, both the softening length L_s and the debonding length L_d are unknown under the applied fatigue load P_{max}, which add up the total unknown constants to ($3n$+2). For the sake of internal continuity among these finite elements, the relative slip δ, the first derivative of δ and the FRP stress σ_f are required to remain continuous at the node between two neighboring elements. On the other hand, the external boundary conditions are required to be satisfied at both free and loaded end.

Internal boundary conditions

(a) For the interior nodes of the elastic region ($0<x<L-L_d-L_s$):

$$C_1^{\,i} \cosh\left(\lambda_1^{\,i} x_i\right) + C_2^{\,i} \sinh\left(\lambda_1^{\,i} x_i\right) = C_1^{\,i+1} \cosh\left(\lambda_1^{\,i+1} x_i\right) + C_2^{\,i+1} \sinh\left(\lambda_1^{\,i+1} x_i\right) \tag{5.44}$$

$$C_1^{\,i} \lambda_1^{\,i} \sinh\left(\lambda_1^{\,i} x_i\right) + C_2^{\,i} \lambda_1^{\,i} \cosh\left(\lambda_1^{\,i} x_i\right) = C_1^{\,i+1} \lambda_1^{\,i+1} \sin\left(\lambda_1^{\,i+1} x_i\right) + C_2^{\,i+1} \lambda_1^{\,i+1} \cosh\left(\lambda_1^{\,i+1} x_i\right) \tag{5.45}$$

$$\frac{L_p {\tau_f}^i}{A_f \delta_1 {\lambda_1}^i}\left[{C_1}^i \sinh\left({\lambda_1}^i x_i\right)+{C_2}^i \cosh\left({\lambda_1}^i x_i\right)\right]+{C_3}^i$$
$$=\frac{L_p {\tau_f}^{i+1}}{A_f \delta_1 {\lambda_1}^{i+1}}\left[{C_1}^{i+1} \sinh\left({\lambda_1}^{i+1} x_i\right)+{C_2}^{i+1} \cosh\left({\lambda_1}^{i+1} x_i\right)\right]+{C_3}^{i+1} \tag{5.46}$$

(b) For node between the elastic and softening region ($x = L\text{-}L_d\text{-}L_s$):

$${C_1}^{n_1} \cosh\left[{\lambda_1}^{n_1}\left(L-L_d-L_s\right)\right]+{C_2}^{n_1} \sinh\left[{\lambda_1}^{n_1}\left(L-L_d-L_s\right)\right]$$
$$={C_1}^{n_1+1}+\frac{\delta_f {\tau_f}^{n_1+1}-\delta_1 {\tau_r}^{n_1+1}}{{\tau_f}^{n_1+1}-{\tau_r}^{n_1+1}} \tag{5.47}$$

$${C_1}^{n_1}{\lambda_1}^{n_1} \sinh\left[{\lambda_1}^{n_1}\left(L-L_d-L_s\right)\right]+{C_2}^{n_1}{\lambda_1}^{n_1} \cosh\left[{\lambda_1}^{n_1}\left(L-L_d-L_s\right)\right]={C_2}^{n_1+1}{\lambda_2}^{n_1+1} \tag{5.48}$$

$$\frac{L_p {\tau_f}^{n_1}}{A_f \delta_1 {\lambda_1}^{n_1}}\left\{{C_1}^{n_1} \sinh\left[{\lambda_1}^{n_1}\left(L-L_d-L_s\right)\right]+{C_2}^{n_1} \cosh\left[{\lambda_1}^{n_1}\left(L-L_d-L_s\right)\right]\right\}+{C_3}^{n_1}$$
$$=\frac{L_p\left({\tau_f}^{n_1+1}-{\tau_r}^{n_1+1}\right)}{A_f\left(\delta_f-\delta_1\right){\lambda_2}^{n_1+1}}{C_2}^{n_1+1}+{C_3}^{n_1+1} \tag{5.49}$$

(c) For interior nodes of the softening region ($L\text{-}L_d\text{-}L_s<x<L\text{-}L_d$):

$${C_1}^i \cos\left[{\lambda_2}^i\left(x_i-L+L_d+L_s\right)\right]+{C_2}^i \sin\left[{\lambda_2}^i\left(x_i-L+L_d+L_s\right)\right]+\frac{\delta_f {\tau_f}^i-\delta_1 {\tau_r}^i}{{\tau_f}^i-{\tau_r}^i}$$
$$={C_1}^{i+1} \cos\left[{\lambda_2}^{i+1}\left(x_i-L+L_d+L_s\right)\right]+{C_2}^{i+1} \sin\left[{\lambda_2}^{i+1}\left(x_i-L+L_d+L_s\right)\right]+\frac{\delta_f {\tau_f}^{i+1}-\delta_1 {\tau_r}^{i+1}}{{\tau_f}^{i+1}-{\tau_r}^{i+1}} \tag{5.50}$$

$$-{C_1}^i{\lambda_2}^i \sin\left[{\lambda_2}^i\left(x_i-L+L_d+L_s\right)\right]+{C_2}^i{\lambda_2}^i \cos\left[{\lambda_2}^i\left(x_i-L+L_d+L_s\right)\right]$$
$$=-{C_1}^{i+1}{\lambda_2}^{i+1} \sin\left[{\lambda_2}^{i+1}\left(x_i-L+L_d+L_s\right)\right]+{C_2}^{i+1}{\lambda_2}^{i+1} \cos\left[{\lambda_2}^{i+1}\left(x_i-L+L_d+L_s\right)\right] \tag{5.51}$$

$$-\frac{L_p\left({\tau_f}^i-{\tau_r}^i\right)}{A_f\left(\delta_f-\delta_1\right){\lambda_2}^i}\left\{{C_1}^i \sin\left[{\lambda_2}^i\left(x_i-L+L_d+L_s\right)\right]-{C_2}^i \cos\left[{\lambda_2}^i\left(x_i-L+L_d+L_s\right)\right]\right\}+{C_3}^i$$
$$=-\frac{L_p\left({\tau_f}^{i+1}-{\tau_r}^{i+1}\right)}{A_f\left(\delta_f-\delta_1\right){\lambda_2}^{i+1}}\left\{{C_1}^{i+1} \sin\left[{\lambda_2}^{i+1}\left(x_i-L+L_d+L_s\right)\right]-{C_2}^{i+1} \cos\left[{\lambda_2}^{i+1}\left(x_i-L+L_d+L_s\right)\right]\right\}+{C_3}^{i+1} \tag{5.52}$$

(d) For node between the softening and debonding region ($x = L\text{-}L_d$) under the N^{th} fatigue cycle:

$$C_1^{n_2+N-1}\cos\left(\lambda_2^{n_2+N-1}L_s\right)+C_2^{n_2+N-1}\sin\left(\lambda_2^{n_2+N-1}L_s\right)+\frac{\delta_f\tau_f^{n_2+N-1}-\delta_1\tau_r^{n_2+N-1}}{\tau_f^{n_2+N-1}-\tau_r^{n_2+N-1}} = 0.5\lambda_3^{n_2+N}\left(L-L_d\right)^2+C_1^{n_2+N}\left(L-L_d\right)+C_2^{n_2+N} \tag{5.53}$$

$$-C_1^{n_2+N-1}\lambda_2^{n_2+N-1}\sin\left(\lambda_2^{n_2+N-1}L_s\right)+C_2^{n_2+N-1}\lambda_2^{n_2+N-1}\cos\left(\lambda_2^{n_2+N-1}L_s\right) = \lambda_3^{n_2+N}\left(L-L_d\right)+C_1^{n_2+N} \tag{5.54}$$

$$-\frac{L_p\left(\tau_f^{n_2+N-1}-\tau_r^{n_2+N-1}\right)}{A_f\left(\delta_f-\delta_1\right)\lambda_2^{n_2+N-1}}\left[C_1^{n_2+N-1}\sin\left(\lambda_2^{n_2+N-1}L_s\right)-C_2^{n_2+N-1}\cos\left(\lambda_2^{n_2+N-1}L_s\right)\right]+C_3^{n_2+N-1} = \frac{L_p}{A_f}\tau_r^{n_2+N}\left(L-L_d\right)+C_3^{n_2+N} \tag{5.55}$$

(e) For interior nodes of the debonding region (L-L_d<x<L):

$$0.5\lambda_3^{i}x_i^2+C_1^{i}x_i+C_2^{i} = 0.5\lambda_3^{i+1}x_i^2+C_1^{i+1}x_i+C_2^{i+1} \tag{5.56}$$

$$\lambda_3^{i}x_i+C_1^{i} = \lambda_3^{i+1}x_i+C_1^{i+1} \tag{5.57}$$

$$\frac{L_p}{A_f}\tau_r^{i}x_i+C_3^{i} = \frac{L_p}{A_f}\tau_r^{i+1}x_i+C_3^{i+1} \tag{5.58}$$

External boundary conditions

(a) FRP stress $\sigma_f = 0$ when $x = 0$:

$$\frac{L_p\tau_f^{1}}{A_f\delta_1\lambda_1^{1}}C_2^{1}+C_3^{1} = 0 \tag{5.59}$$

(b) Concrete stress $\sigma_c = 0$ when $x = 0$ which leads to $d\delta/dx = 0$ at the free end:

$$C_2^{1}\lambda_1^{1} = 0 \tag{5.60}$$

(c) Relative slip $\delta = \delta_1$ when $x = L$-L_d-L_s:

$$C_1^{n_1}\cosh\left[\lambda_1^{n_1}\left(L-L_d-L_s\right)\right]+C_2^{n_1}\sinh\left[\lambda_1^{n_1}\left(L-L_d-L_s\right)\right] = \delta_1 \tag{5.61}$$

(d) Relative slip $\delta = \delta_f$ when $x = L$-L_d under the N^{th} fatigue cycle:

$$C_1^{n_2+N-1}\cos\left(\lambda_2^{n_2+N-1}L_s\right)+C_2^{n_2+N-1}\sin\left(\lambda_2^{n_2+N-1}L_s\right)+\frac{\delta_f\tau_f^{n_2+N-1}-\delta_1\tau_r^{n_2+N-1}}{\tau_f^{n_2+N-1}-\tau_r^{n_2+N-1}} = \delta_f \tag{5.62}$$

(e) FRP stress $\sigma_f = P_{max}/A_f$ when $x = L$ under the N^{th} fatigue cycle:

$$\frac{L_p}{A_f}\tau_r^{\,n_3+2(N-1)}L + C_3^{\,n_3+2(N-1)} = \frac{P_{max}}{A_f} \tag{5.63}$$

The number of internal boundary conditions described in Eqs. 5.44-5.58 is (3n-3) provided that n finite elements are partitioned within the bond length. Besides, by adding the five external boundary conditions described by Eqs. 5.59-5.63, the total number of independent equations becomes (3n+2), which equals to the number of unknown constants. However, both the softening length L_s and the debonding length L_d are implicit parameters since all other unknown constants, $C_1^{\,i}$, $C_2^{\,i}$ and $C_3^{\,i}$ (i = 1, 2, …, n), are explicitly solvable via linear algebra on the premise that both L_s and L_d are known in advance. Therefore, an iteration process in conjunction with calculation algorithm is required to reach the stable solutions to the finite element problem.

5.4.4 Algorithm framework

The strategy of solving this one-dimensional FEM problem with a changing number of elements, which depends on the number of fatigue cycles, has been streamlined into the flow chart as illustrated in Fig. 5.9.

1. The slip tolerance T_{slip} and the force tolerance T_{force} are preset to control the convergency of the iteration algorithm. The bond failure limit L_f controls the extent of the bond development towards failure. Of course, smaller tolerance leads to higher accuracy at the expense of longer calculating time;
2. Assuming the maximum applied load P_{max} is large enough to develop at least softening stage of the NSM FRP-to-concrete bonded joints, i.e., $\delta > \delta_1$ at the loaded end, two situations should be considered: (a) debonding already exists; or (b) debonding does not occur at the first fatigue cycle. These two cases can be easily determined by the analytical bond model under the static loading case described in this chapter since no degradation will happen for the first fatigue cycle.

In the same sense, both L_s^1 and L_d^1 can be calculated by the analytical model as well at the beginning of the loop.

Fig. 5.9 Flow chart of the finite element model for NSM FRP-to-concrete bonded joints

3. For both cases, the local bond properties of each element, i.e., τ_f^i and τ_r^i, should be updated cycle by cycle as per the degradation law (Eqs. 5.24-5.27). It is also important to note that the newly developed elements created in each cycle, as illustrated in Fig. 5.8(b), should have less degradation than those softening or debonding elements that already exist before the current cycle. In principle, both the local bond strength τ_f^i and the residual bond strength τ_r^i of a specific element depend solely on the number of fatigue cycles that this element experienced rather than the current number of fatigue cycles;
4. Starting from the 2nd fatigue cycle, an iteration process is required to solve the implicit parameters L_s^k and L_d^k for case (a), and L_s^k for case (b) under the current k^{th} fatigue cycle. As shown in Fig. 5.9, the force (traction) boundary condition (Eq. 5.63) and the displacement boundary condition (Eq. 5.62) are applied to obtain L_s^k and L_d^k. respectively. The speed and accuracy of this iteration process depend mainly on the magnitude of the preset tolerances and the algorithm adopted to update L_s^k and L_d^k in the loop, e.g., the method of bisection is used in this study for its simplicity and good accuracy. For case (b), if the displacement boundary condition $\delta > \delta_f$ at the loaded end is reached before the target number of fatigue cycles N, which means the softening stage should be developed, it shall be automatically switched to case (a) and the process continues to the next cycle; and
5. This algorithm can lead to the FEM solutions, including the relative slip δ, the local bond stress τ and the FRP stress σ_f, etc., along the bond line at the target number of fatigue cycles N if the NSM FRP joint still survives. Otherwise, the debonding failure and fatigue life will be obtained whilst the softening length L_s developing all the way to the free end, yet the joint is still unable to balance the applied P_{max}.

5.4.5 FEM model predictions

A MATLAB subroutine was programmed to generate the finite element model based on the trilinear local bond stress-slip relationship and the degradation law as described above.

Experimental variables such as material properties, geometric detailing of NSM FRP-to-concrete bonded joints and maximum fatigue load P_{max} are provided as input parameters of the model, along with the target number of fatigue cycles N and the tolerances of convergency. The numerical predictions of the FRP strain distribution and the local bond stress distribution are illustrated compared to the test results in Figs. 5.10-5.13 for both FRP rod and strip specimens, respectively. Among these figures, comparisons are made at 10, 100, 1000, 10,000 and 100,000 fatigue cycles respectively to present the overall performance of the model during the fatigue cycles. Also, it should be noted that all applicable experiment data points have been collected and plotted on the diagram to reveal the most authentic local bond performance of NSM FRP-to-concrete bonded joints. To ensure the contents of the plots are concise and visible, IDs of specimen sets are simplified to a combination of the CFRP cross-sectional shape and the number of fatigue cycles, e.g., R-1E2 represents R-SCSW-A1-1060-1E2-N and S-F represents S-RO-A1-1060-F-N, since the influence of parameters such as cross-sectional shape, surface treatment and so on is not a concern here. Besides, regardless of the fluctuation of bond behavior, data within the same specimen set are not distinguished from each other by different labels because the overall discrepancy between the numerical predictions and test results should draw more attention.

In general, the model well captured the entire local bond degrading behavior under the fatigue loading scenario. As the number of fatigue cycles becomes larger, the utilization of FRP material from regions near the loaded end develops higher which is featured by a flatter distribution of the FRP strain [Fig. 5.10(e) and Fig. 5.12(e)]. This phenomenon is consistent with the gradual migration of the peak local bond stress towards the free end, as a result of accumulated bond damage within the debonding and the softening regions. Of course, fluctuations of test results are undeniably high which leads to such scattered data points, and hence the model is unable to fit the local bond behavior of any specific specimen set because the degradation law was derived on the average test results of these specimen sets. In this context, it is natural to expect a model of higher accuracy if the bond consistency and construction quality can be improved.

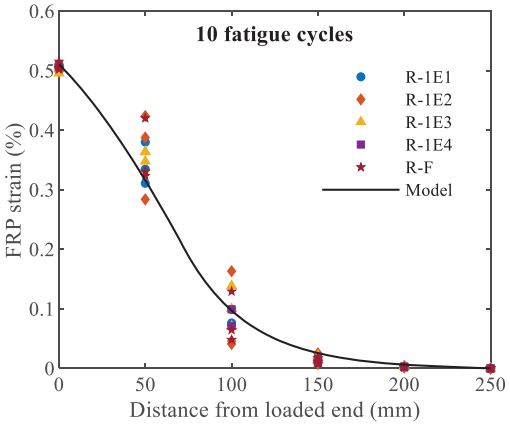

(a) $N = 10$

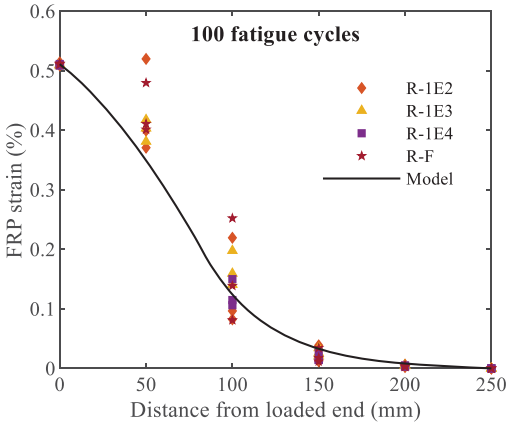

(b) $N = 100$

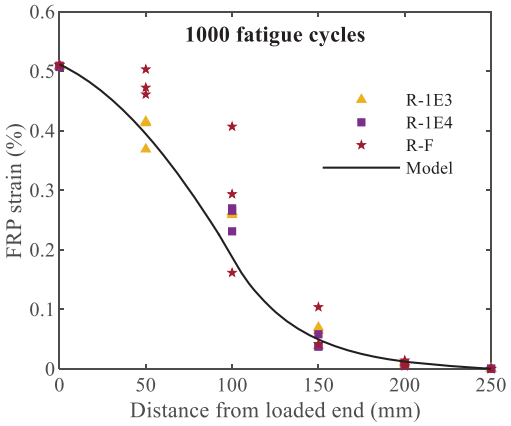

(c) $N = 1000$

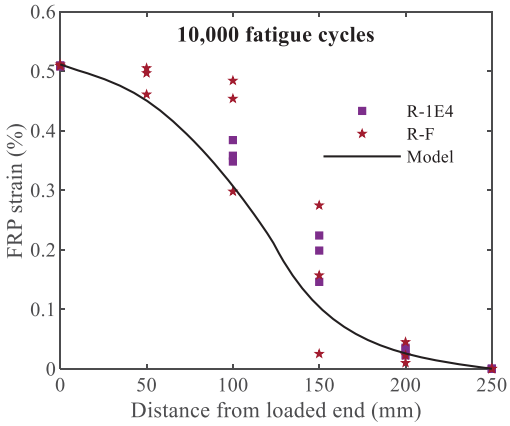

(d) $N = 10{,}000$

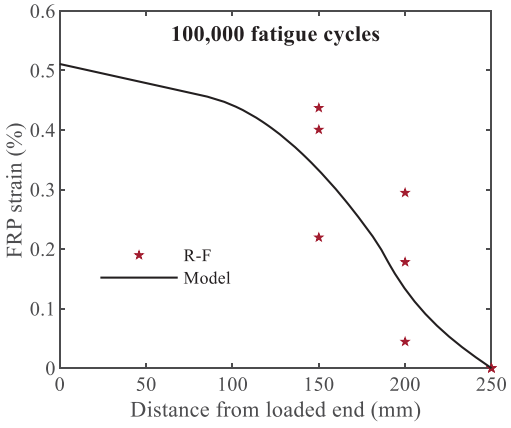

(e) $N = 100{,}000$

Fig. 5.10 Comparison between test results and FEM model predictions for FRP strain distribution of CFRP rod specimens

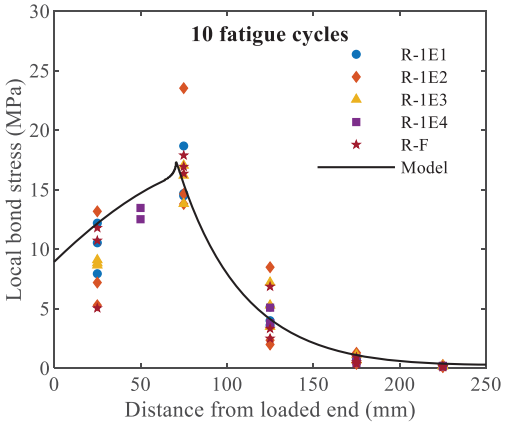

(a) $N = 10$

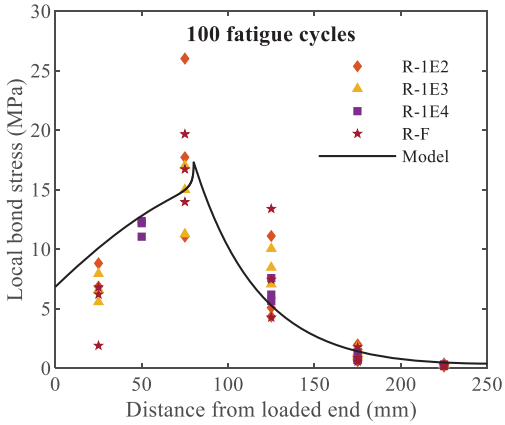

(b) $N = 100$

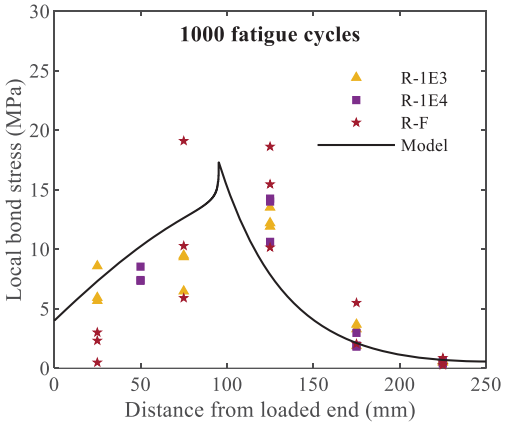

(c) $N = 1000$

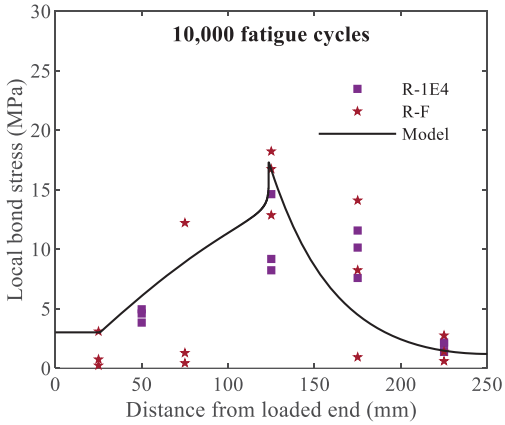

(d) $N = 10{,}000$

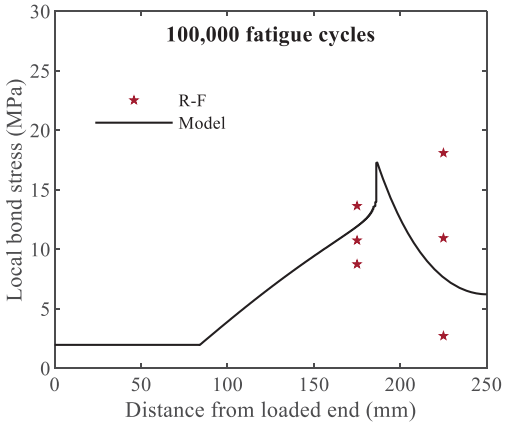

(e) $N = 100{,}000$

Fig. 5.11 Comparison between test results and FEM model predictions for local bond stress distribution of CFRP rod specimens

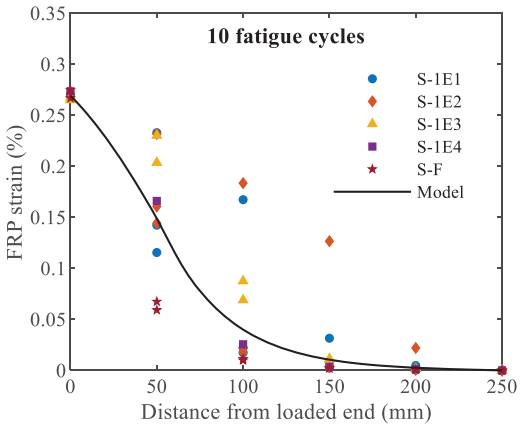

(a) $N = 10$

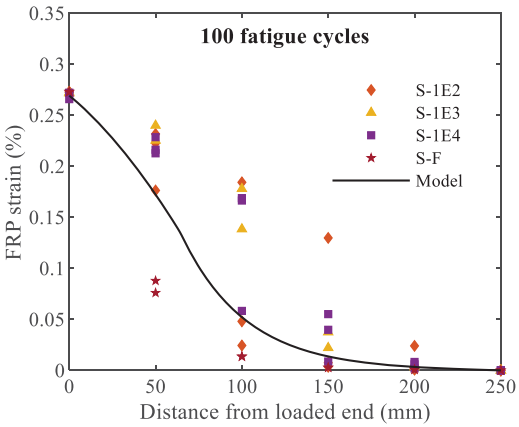

(b) $N = 100$

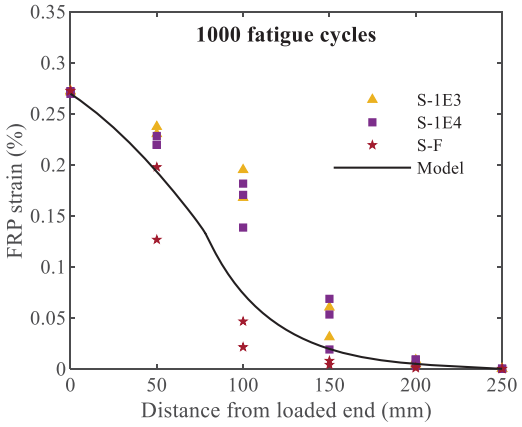

(c) $N = 1000$

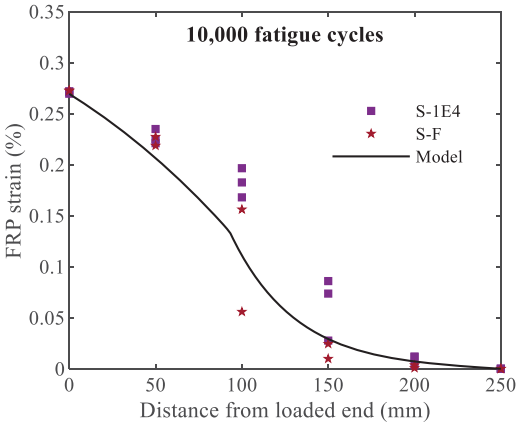

(d) $N = 10{,}000$

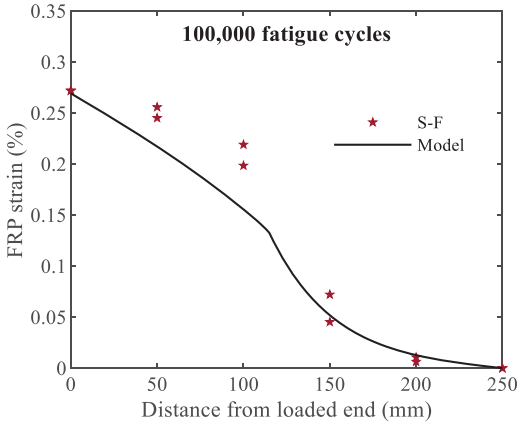

(e) $N = 100{,}000$

Fig. 5.12 Comparison between test results and FEM model predictions for FRP strain distribution of CFRP strip specimens

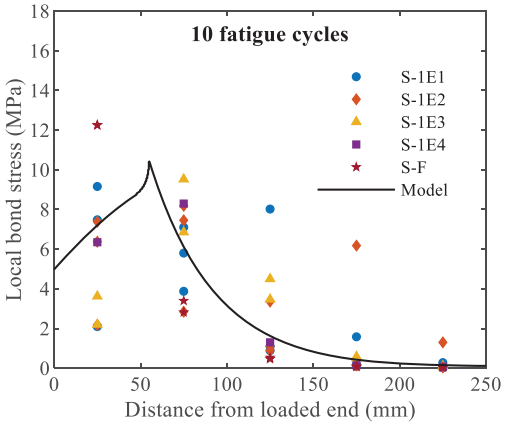

(a) $N = 10$

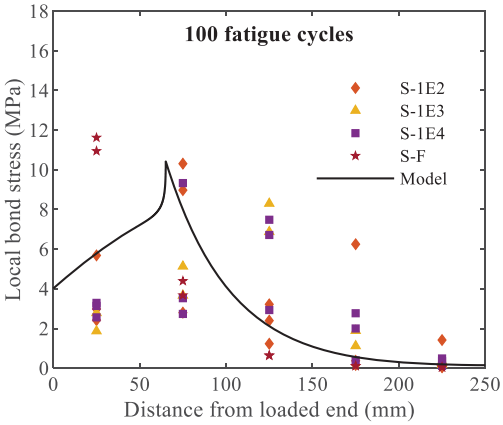

(b) $N = 100$

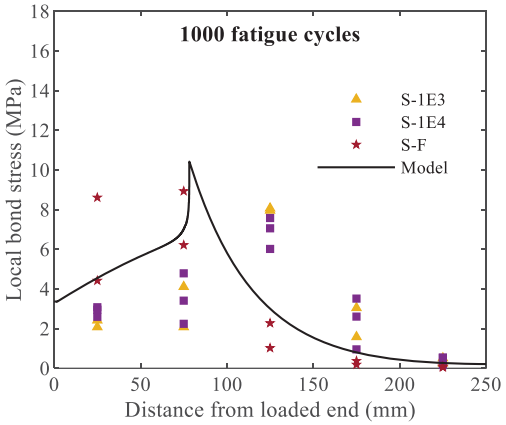

(c) $N = 1000$

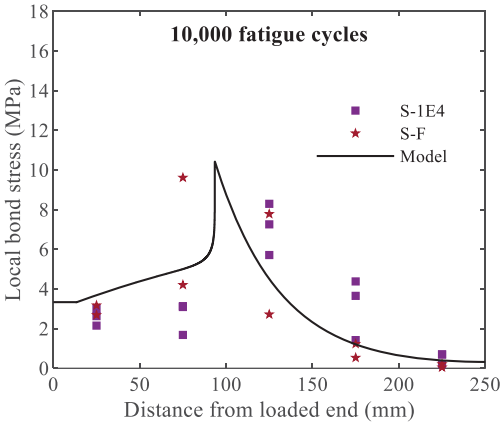

(d) $N = 10{,}000$

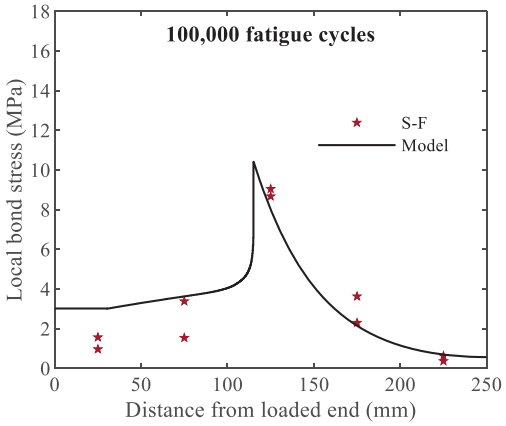

(e) $N = 100{,}000$

Fig. 5.13 Comparison between test results and FEM model predictions for local bond stress distribution of CFRP strip specimens

Other than that, models for both CFRP rod and strip specimens appear to overestimate the residual bond strength after debonding occurs, especially for situations over 10,000 fatigue cycles. This is a measure of compensation for underestimating both local bond strengths and resistance to bond degradation of regions near the free end. Because from the test observations, regions near the free end usually have higher local bond strength as discussed in Chapter 4.3.4 and they were proved to be much more resistant to degradation as well as described in Chapter 4.4. However, the fundamental assumption of the analytical model, hypothesizing a uniform local bond strength along the bond line under static loading case and a same degradation law during the fatigue cycles, is a prerequisite of the FEM model for practical reasons and deviates from the test results inevitably to some extents. Therefore, the residual bond strength has to be slightly over estimated. Alternatively, the degradation of the residual bond strength shall be slower than that in the physical experiment to balance the applied fatigue load magnitude and keep the pace with the overall development of the bond.

Moreover, the comparison between the test results and the analytical predictions in terms of the relative slip at the loaded end is shown in Fig. 5.14. The data points included in the plots are derived from specimen set R-SCSW-A1-1060-F-N (Set 11) and S-RO-A1-1060-F-N (Set 18) since they experienced more fatigue cycles and hence the records of the relative slip are more representative. Being scaled on the semi-logarithmic plot, the model undoubtedly captures the overall trend of the slip increment throughout the fatigue life of selected specimens sets, including (1) the initial relative slip obtained under the first fatigue cycle; (2) the steady increase of the relative slip with the number of fatigue cycles rises; and (3) the rapid climbing of the relative slip close to failure. Observation of this typical three-stage development has also been reported by other researchers as mentioned in Chapter 2.4.5. However, because bonded regions near the free end had unexpectedly high endurance limit as discussed above, the model is unable to reach the exact fatigue life as obtained in the experiment by adopting the same local bond stress-slip model and degradation law for all elements along the bond line. This regional enhancement of the bond

strength is possibly caused by the type of loading setup and boundary conditions of the concrete block, which requires further investigation in the future.

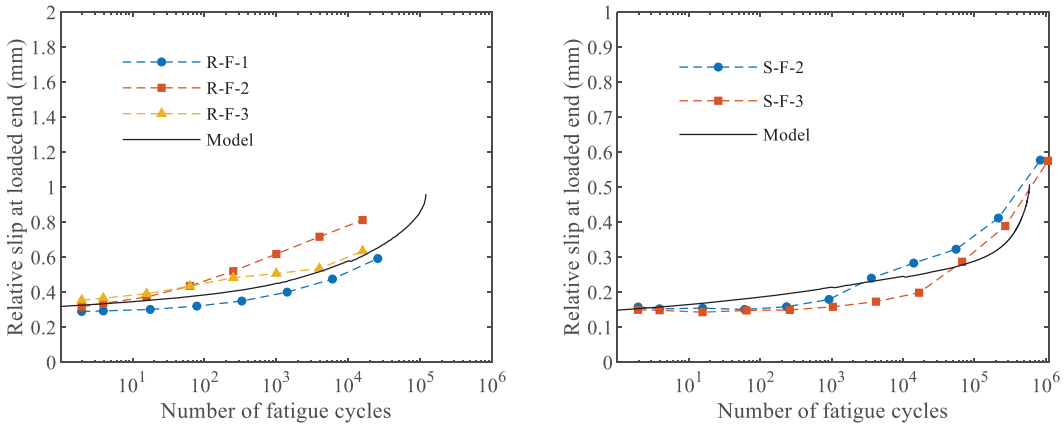

(a) CFRP rod specimens (b) CFRP strip specimens

Fig. 5.14 Comparison between test results and FEM model predictions for relative slip at the loaded end of both CFRP rod and strip specimens

5.5 Parametric study

Based on the proposed FEM model, three parameters were selected to further investigate their contribution to the local bond behavior under the fatigue cycles: (1) local bond strength τ_f with a fixed residual bond strength ratio τ_r/τ_f; (2) residual bond strength ratio τ_r/τ_f; and (3) Young's modulus of FRP reinforcement. The former two parameters are crucial to the bond performance of NSM FRP-to-concrete bonded joints and they can be affected by FRP surface treatment, concrete strength, epoxy strength and groove dimensions, etc. The last parameter determines the axial stiffness of the FRP material (assuming equivalent cross-sectional area) and depends mainly on the type of FRP reinforcement being used. The Young's modulus of concrete is not a concern here because previous research had verified its negligible influence on the bond behavior under fatigue (Chen and Cheng 2016). To make the parametric study more realistic, numerical results are calculated based on the same geometric information, material properties and degradation law adopted by the CFRP strip specimens discussed in the previous chapter.

5.5.1 Local bond strength

The bond development of the NSM FRP is sensitive to the local bond strength during the fatigue cycles. To ensure a complete comparison by using different local bond strength up to 100,000 cycles, a ±20% range of variation is selected based on the original local bond strength of τ_f = 10.42 MPa. The same fatigue load range, i.e., 10-60% of the static pull-out force (P_{max} = 32.6 kN), is applied to the analysis. In addition, the original residual bond strength ratio τ_r/τ_f = 0.32 remains constant for all cases. The results of the local bond stress distribution by using various local bond strength are illustrated in Fig. 5.15. The comparison indicates a substantial difference in the bond development caused by different local bond strengths under fatigue cycles. Analytical results of 120% τ_f case represent the strongest resistance to the fatigue degradation with no debonding region occurring before 100,000 fatigue cycles, and the length of damaged bonded region has the minimum increase from 39.07 mm under 10 cycles to 84.44 mm under 100,000 cycles. By comparison, the analytical results of 80% τ_f case have debonding region occurred from the very beginning and its damaged bonded region has the maximum increases from 88.55 mm under 10 cycles to 166.8 mm under 100,000 cycles [Figs. 5.15(a) and (e)]. Thus, it can be concluded that the NSM FRP-to-concrete bonded joints will greatly benefit from a higher local bond strength with the damaged zone more localized to the loaded end, and a slower bond development under fatigue cycles.

5.5.2 Residual bond strength ratio

The residual bond strength ratio τ_r/τ_f affects the post-softening behavior of the bond development based on the trilinear local bond stress-slip model. By changing the residual bond strength ratio τ_r/τ_f to 80, 90, 100, 110 and 120% of its original magnitude (which is 0.32 for CFRP strip specimens) while all other parameters remained unchanged, the local bond stress distribution throughout the fatigue cycles up to 100,000 of these cases is shown in Fig. 5.16. The difference in the local bond stress distribution between the analytical cases is very small under 10 fatigue cycles

[Fig. 5.16(a)] and increases slightly under 100 fatigue cycles [Fig. .5.16(b)]. However, after debonding region occurs over 1000 fatigue cycles, the difference becomes more significant and increases as the increase of the fatigue cycles. At 100,000 fatigue cycles, the subplot of $80\%\tau_r/\tau_f$ case has a damaged region of 131.6 mm while the $120\%\tau_r/\tau_f$ case has a smaller length of 104 mm [Fig. 5.16(e)]. The result reveals that the residual bond strength ratio τ_r/τ_f has less influence on the local bond behavior than the local bond strength τ_f especially at early fatigue cycles but it affects more on the post-softening behavior of the bonded joints after debonding.

5.5.3 Young's modulus of FRP reinforcement

To compare the significance of different parameters on the local bond performance, the same FRP reinforcement with 80, 90, 100, 110 and 120% of its original Young's modulus E_f (168.22 GPa) is adopted for the parametric study herein. The numerical results of the local bond stress distribution during the fatigue cycles for all these cases are plotted in Fig. 5.17. It could be seen that although the influence on the bond behavior due to E_f is less significant than the local bond strength τ_f, it is still greater than the effect due to the residual bond stress ratio τ_r/τ_f. In addition, the influence caused by E_f is relatively stable throughout the fatigue cycles. For example, the distance between the peak local bond stress of $80E_f$ and $120E_f$ case is 23.45 mm at 10 fatigue cycles and increases only slightly to 28.6 mm at 100,000 fatigue cycles [Figs. 5.17(a) and (e)]. This observation is expected since unlike the local bond strength τ_f and the residual bond strength τ_r which degrade under the fatigue cycles, E_f is assumed to be constant in the model; therefore, its influence on the bond performance should be less dependent on the number of fatigue cycles.

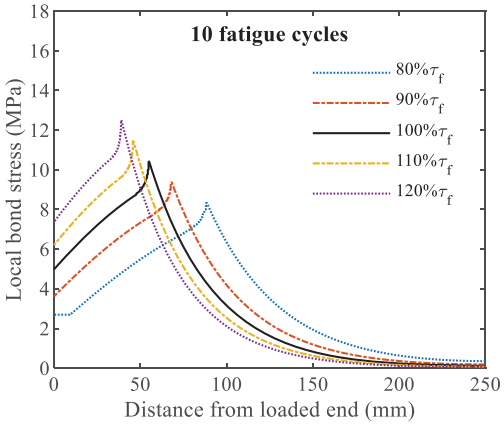

(a) $N = 10$

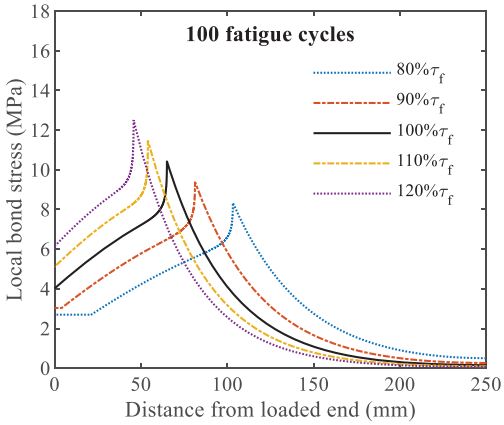

(b) $N = 100$

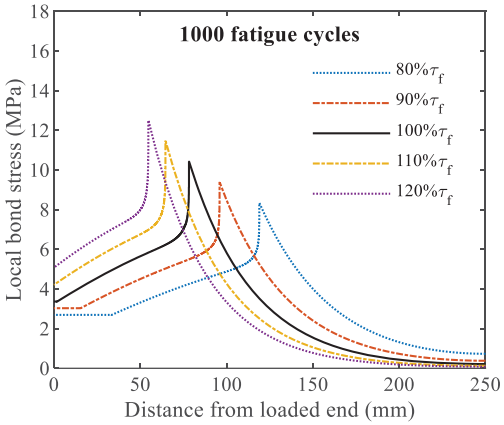

(c) $N = 1000$

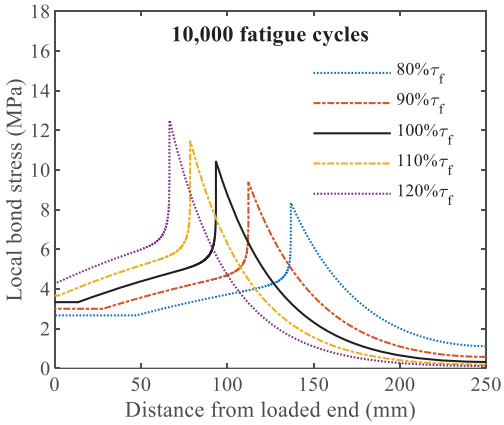

(d) $N = 10{,}000$

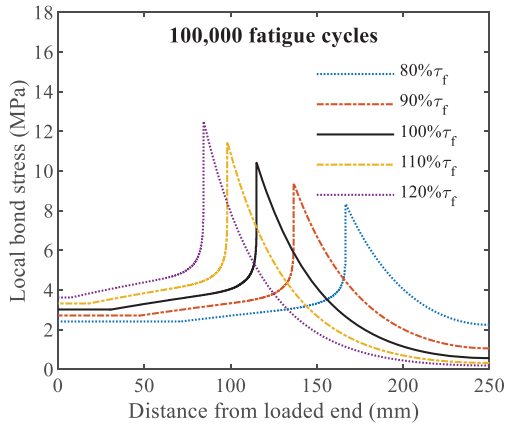

(e) $N = 100{,}000$

Fig. 5.15 Influence of local bond strength on the bond behavior under fatigue cycles

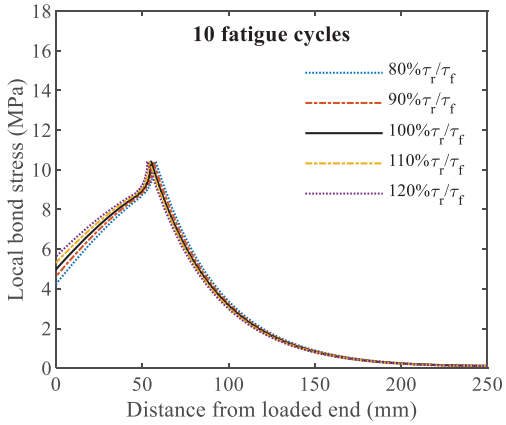

(a) $N = 10$

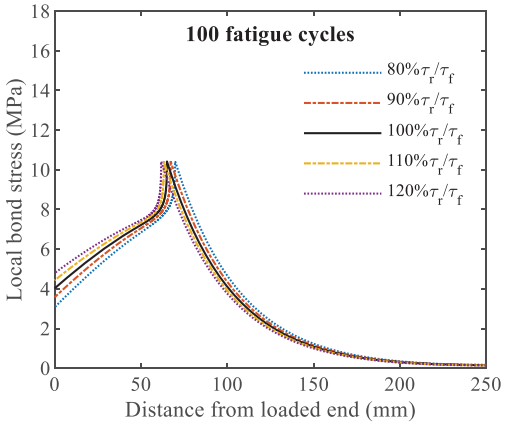

(b) $N = 100$

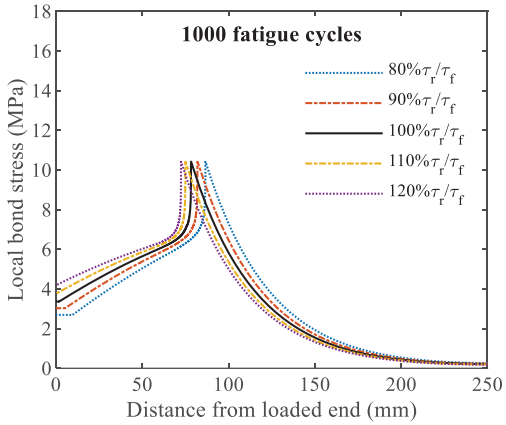

(c) $N = 1000$

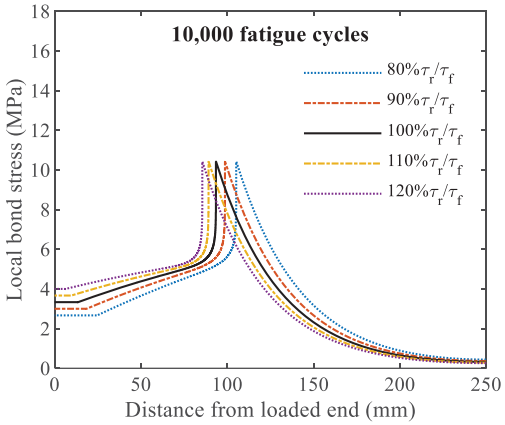

(d) $N = 10{,}000$

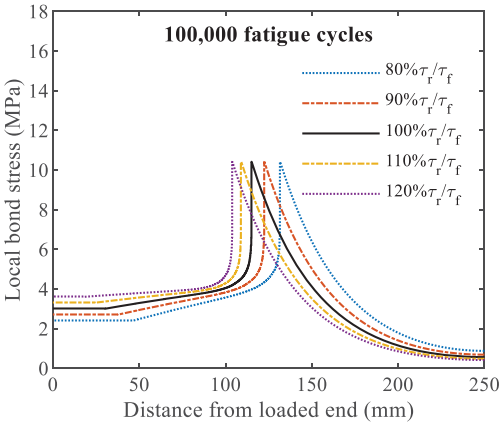

(e) $N = 100{,}000$

Fig. 5.16 Influence of residual bond strength ratio on the bond behavior under fatigue cycles

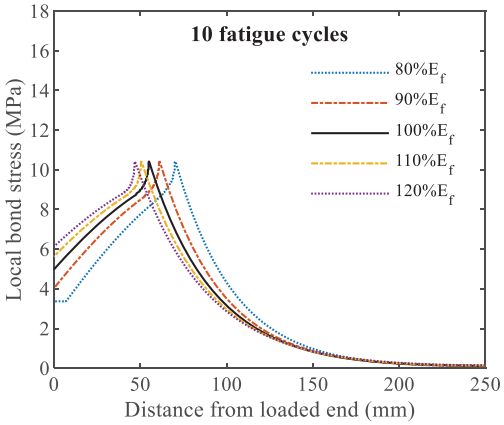

(a) $N = 10$

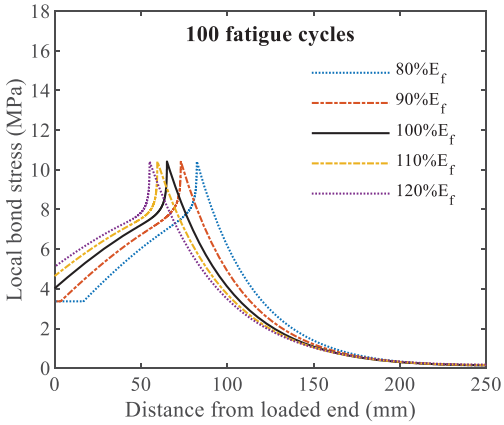

(b) $N = 100$

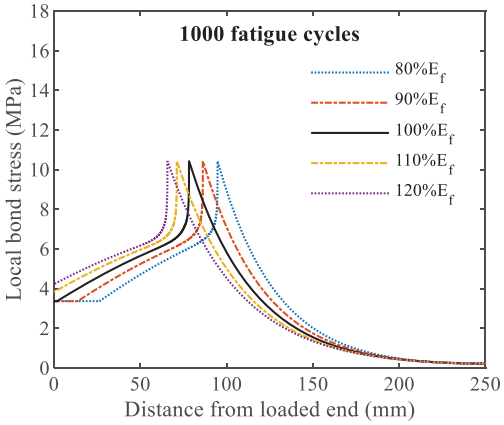

(c) $N = 1000$

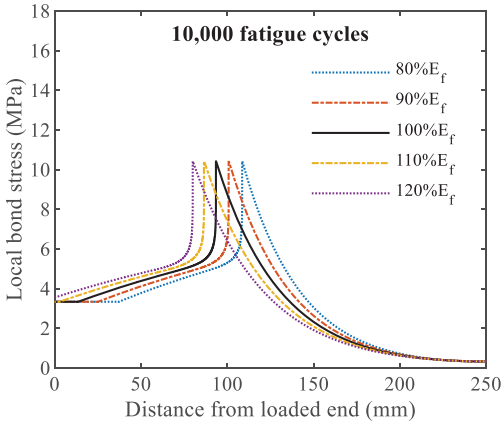

(d) $N = 10{,}000$

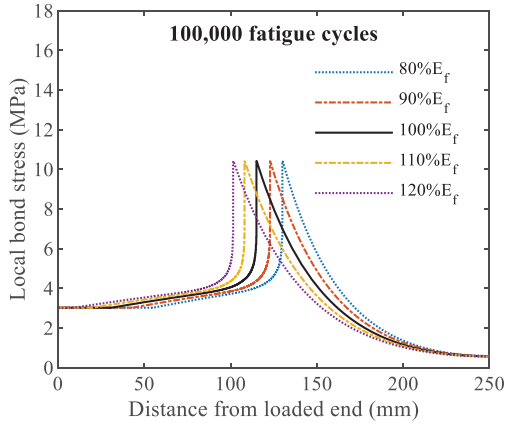

(e) $N = 100{,}000$

Fig. 5.17 Influence of Young's modulus of NSM FRP reinforcement on the bond behavior under fatigue cycles

5.6 Summary

This chapter proposes a trilinear local bond stress-slip relationship based on the test observations and derives the close-form solutions to the governing equation. The full range local bond behavior by adopting the trilinear model has been presented. Key parameters including peak local bond stress τ_f, relative slip δ_1 at peak stress, residual bond strength τ_r and relative slip δ_f at debonding are calibrated from the static pull-out test results. A comparison between the theoretical predictions and the experimental results under static loading case has been conducted to verify the validity of the proposed model. On the other hand, in light of the advantage of adopting the trilinear local bond stress-slip relationship, a FEM analytical model has been proposed to simulate the local bond behavior under fatigue cycles. Degradation laws of the local bond strength for both CFRP rod and strip specimens derived from the fatigue DPT results have been adopted to provide the fundamental principle of the bond development under fatigue loading case. The mechanism of the propagation of the damaged bonded region and the migration of the peak local bond stress has been elaborated in conjunction with an algorithm framework. Analytical predictions obtained from a MATLAB program using the FEM model are compared with the test results. The following conclusions can be drawn based on this study:

- The trilinear local bond stress-slip model is proved to be ideal of representing the actual behavior during the test. The prediction model based on the trilinear local bond stress-slip relationship presents a good agreement with the experimental data in terms of the pull-out force, CFRP strain distribution, local bond stress distribution and load-slip relationship at the loaded end. However, the analytical model is only valid for a stable local bond stress-slip relationship and hence more work is still needed to ensure the quality and consistency of NSM FRP-to-concrete bonded joints;
- The discretization of the bond line into finite elements provides the maximum flexibility of manipulating the local bond properties at different stages of bond development. The proposed

FEM model based on the trilinear local bond stress-slip relationship has been proved to be efficient in predicting the overall local bond degradation behavior under fatigue cycles. Analytical results of bond development in terms of FRP strain, local bond stress and relative slip at the loaded end reach a satisfying agreement with the experimental data. However, the model is unable to provide a perfect agreement with the test results, where it overestimates the local bond performance near the loaded end and generally fails earlier than the practical specimens under fatigue loading. Because the fundamental assumptions of the FEM model hypothesize the same degradation laws for all bond elements for practical reasons, but bonded regions near the free end are usually more resistant to degradation and hence more sustainable under fatigue cycles; and

- Three important parameters including the local bond strength τ_f, residual bond strength ratio τ_r/τ_f and Young's modulus E_f of FRP reinforcement, are studied based on the FEM model to investigate their influence on the fatigue bond behavior of NSM FRP-to-concrete bonded joints. The result indicates the local bond strength has the most significant effect on the local bond development throughout the fatigue life of specimens. The residual bond strength ratio influences more on the post-softening behavior of the bond. Consequently, it affects more at a higher number of fatigue cycles. In contrast, the Young's modulus of FRP reinforcement has a relatively stable influence on the local bond behavior but it is less sensitive to the number of fatigue cycles.

CHAPTER SIX

6 THREE-DIMENSIONAL FINITE ELEMENT MODELING OF NSM FRP-TO-CONCRETE BONDED JOINTS

6.1 Overview

The bond behavior of NSM FPR-to-concrete bonded joints is intrinsically more complicated than that of the EB FRP-to-concrete bonded joints because the former technique requires the embedment of FRP reinforcement in the concrete substrate by means of grooves cutting on the surface of concrete, whilst the latter applies FRP laminates or fabrics to the pretreated concrete surface using adhesives externally. The creation of the concrete groove and accordingly a thicker adhesive layer between FRP reinforcement and concrete adds to the complexity of the NSM FRP-to-concrete bonded joints. Its bond performance depends on parameters encompassing the size, cross-sectional shape and surface treatment of the NSM FRP reinforcement, the shape and size of the groove, and the material properties of adhesive and concrete. Although experimental studies can assist on the investigation of the influence of those parameters on the bond behavior of NSM FRP-to-concrete bonded joints, e.g., the series of direct pull-out tests (DPT) conducted in this research (as discussed in the previous chapters), the data collected for the local bond behavior reles on the strain gauges attached to the surface of the FRP reinforcement and their existence inevitably affect the efficiency of the stress transfer from FRP to concrete. Unlike the EB FRP in which strain gauges can be installed on the surface to monitor the local bond behavior, the number of strain gauges installed are limited for the NSM FRP-to-concrete bonded joints to minimize its influence on the local bond performance. Those strain gages are also vulnerable under fatigue loading case since most strain gauges of CFRP rod cases were unable to survive a large number of fatigue cycles. Based on these difficulties, using the finite element (FE) method to supplement the experimental studies in understanding the bond performance and failure mechanism of NSM FRP-to-concrete bonded joints has been an attractive option.

Research efforts on adopting the FE model to study the NSM FRP-to-concrete bonded joints is rather limited up to date. Cruz and Barros (2004) implemented an interface element between the CFRP and concrete to simulate the interfacial local bond behavior based on the calibrated bond stress-slip relationship from the experimental study. But the bonded joints was simplified as a two-dimensional FE model, i.e., plane stress problem, assuming both concrete and CFRP material as linear elastic without the inclusion of adhesive layer. Teng et al. (2013) proposed a three-dimensional meso-scale FE model for NSM CFRP strip-to-concrete bonded joints using FE software package MSC.MARC. This model well predicted the failure mechanism of the concrete block comparing to the experimental results and was also capable of providing the local bond-slip relationship, assuming a perfect bond between CFRP strip and epoxy adhesive. Zhang et al. (2013; 2014) used the same modeling strategy to propose both the local bond-slip model and the bond strength model of the NSM CFRP strip-to-concrete bonded joints. Zhang et al. (2017; 2018) also investigate the effect due to groove spacing and concrete edge distance on this bond strength model by means of introducing two reduction factors. Some other numerical studies were also conducted using software package ATENA 3D, e.g., Sasmal et al. (2013) (ribbed CFRP rod case) and Al-Saadi et al. (2016) (smooth and roughened CFRP strip case), where a three-dimensional contact element was defined to simulate the interfacial bond behavior between the FRP reinforcement and epoxy adhesive for the bonded joints.

In this context, to comprehensively understand the failure mechanism of NSM FRP-to-concrete bonded joints observed in the experiment conducted by this research, as well as the effect caused by the material properties such as concrete and epoxy adhesive, a three-dimensional FE model using software package ABAQUS is proposed in this chapter. The failure process of the concrete specimens reinforced by both CFRP strip and rod reinforcement is simulated and compared with the experiment results. Some parameters of the adopted concrete model and epoxy adhesives, and different local bond stress-slip models are focused to reveal their influence on the overall bond behavior of the FRP-to-concrete bonded joints.

6.2 Strategy of finite element modeling

6.2.1 General

The three-dimensional FE model was constructed using the universal engineering simulation software package ABAQUS (version 6.13). To simplify the modeling process and take advantage of symmetry, the FE model consisted of half of the specimen illustrated in Fig. 4.4 of Chapter 4. The boundary conditions applied to the FE model was slightly different from the test setup configuration shown in Fig. 4.5 to ease the modeling effort and improve the convergency of the solver. In Fig. 6.1(a), using the strip specimen as an example, the right-hand side surface of the concrete block was restrained to represent the fixed reaction beam applied to the loaded end as illustrated in Fig. 4.5. The bottom of the concrete block was restrained as well to balance the moment produced by the eccentric single shear pull-out force, and this boundary condition was equivalent to the two pairs of push bolts adopted in the experiment. In addition, the horizontal displacement of the left-hand side surface in Fig. 6.1(b), i.e., displacement in *X* direction, was prevented to ensure symmetry. The numerical CFRP-to-concrete bonded joints was loaded by applying a displacement increment in each time step at the loaded end of the CFRP reinforcement. Note that the coordinate system indicated in Fig. 6.1 represent the orientation of the model built in ABAQUS, and the boundary conditions were identical to both CFRP rod and strip specimen cases.

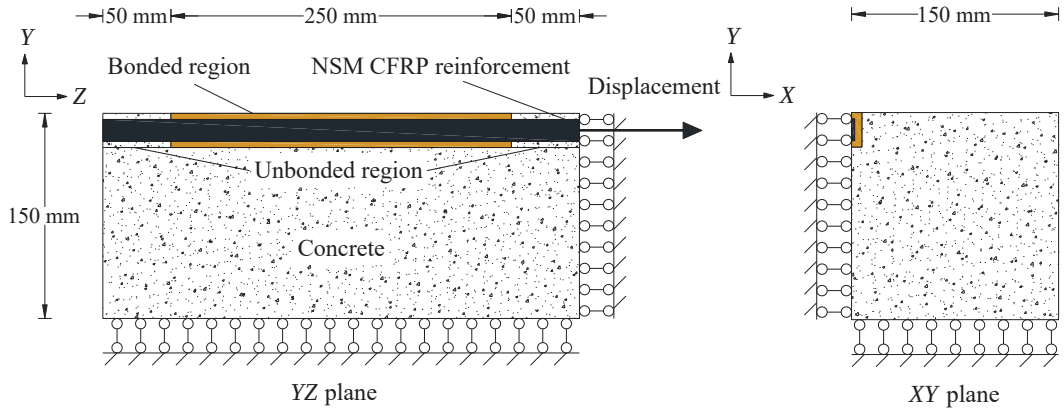

(a) *YZ* plane view (b) *XY* plane view

Fig. 6.1 Boundary conditions of the three-dimensional FE model (CFRP strip specimen case)

Test results of the experimental study in this research indicated major failure modes of the NSM CFRP-to-concrete bonded joints due to concrete and epoxy breakage (CEB) plus epoxy splitting (ES) for CFRP rod specimens and interfacial debonding between FRP and concrete (F/A) for CFRP strip specimens. However, given the test observation that the epoxy breakage only occurred after the concrete cracking when the specimen was about to fail, it was less significant to the overall bond behavior. Hence, the failure of epoxy adhesive was not considered in this FE model to simplify the numerical calculation and for better convergency. In this case, the modeling of concrete become extremely important and thus small size elements were used to reflect the entire failure process of the specimen. The eight-node 3D solid linear hexahedral element with reduced integration (C3D8R element) was used to model CFRP, epoxy adhesive and concrete material to save computational time, in conjunction with hourglass control automatically activated to prevent the zero energy modes (ABAQUS 2013). The eight-node 3D cohesive element (COH3D8) was used to construct the interface between the CFRP and epoxy adhesive to simulate the interfacial debonding phenomenon observed in the test. The mesh scheme was determined by means of a sensitivity study and calibrated by the test results, as to be described later, as follows: (1) the mesh size for the CFRP rod was 1.19 mm in its radial direction (4 elements), 1.24 mm in its circumferential direction (12 elements) and 1.25 mm in its longitudinal direction (280 elements); (2) the mesh size for the CFRP strip was 1.13 mm in its transverse direction (2 elements), 1.33 mm in its height direction (12 elements) and 1.25 mm in its longitudinal direction (280 elements); (3) the mesh size for the epoxy adhesive layer was 1.38 mm in its transverse direction (8 elements) for the CFRP rod case and 1.25 mm (6 elements) for the CFRP strip case, 1.11 mm in its height direction (18 elements) for the CFRP rod case and 1.45 mm (20 elements) for the CFRP strip case, and 1.25 mm in its longitudinal direction (200 elements); (4) the mesh size for concrete was mostly the same as 5 mm but was slightly adjusted to accommodate the groove shape within the regions including one groove depth away from the top surface and half the groove thickness away from the symmetric plane. It should be noted that the groove dimension adopted in the FE model was

measured from the actual testing specimen, i.e., 22 mm in width and 20 mm in depth for the CFRP rod case, 15 mm in width and 29 mm in depth for the CFRP strip case, which was different from the design dimension due to the imperfect manipulation in the process of the groove cutting.

6.2.2 Modeling of concrete

The failure in the concrete substrate of the NSM FRP-to-concrete bonded joints requires a proper concrete constitutive model to characterize the nonlinear cracking process. ABAQUS provides a concrete damaged plasticity (CDP) model based on the theoretical framework proposed by Lubliner et al. (1989) to reflect the nonlinearity in both compressive and tensile stress toward failure. The mechanical behavior of the CDP model depends primarily on the uniaxial tensile and compressive stress-strain relationship, damage variable of the elastic stiffness, and concrete plasticity properties.

Uniaxial compressive stress-strain relationship

The uniaxial compressive behavior of the concrete adopted in this research was based on the model proposed by Elwi and Murray (1979), which was modified from Saenz (1964) and can be described as follows (Fig. 6.2):

$$\sigma_c = \frac{E_0 \varepsilon_c}{1 + \left(R + \frac{E_0}{E_s} - 2 \right) \left(\frac{\varepsilon_c}{\varepsilon_0} \right) - (2R - 1) \left(\frac{\varepsilon_c}{\varepsilon_0} \right)^2 + R \left(\frac{\varepsilon_c}{\varepsilon_0} \right)^3} \tag{6.1}$$

$$R = \frac{E_0 / E_s \left(\sigma_0 / \sigma_u - 1 \right)}{\left(\varepsilon_u / \varepsilon_0 - 1 \right)^2} - \frac{\varepsilon_0}{\varepsilon_u} \tag{6.2}$$

where σ_c = concrete compressive stress (MPa); σ_0 = maximum concrete compressive stress (45.02 MPa, equals to the average concrete compressive strength f_c from the cylinder test); σ_u = ultimate concrete stress at crushing failure (38.27 MPa, equals to 0.85 f_c referring to Hognestad (1951)); ε_c = concrete compressive strain; ε_0 = concrete compressive strain corresponding to σ_0 (equals to 0.002 referring to Mander et al. (1988)); ε_u = ultimate concrete strain at crushing failure (equals to 0.0038

referring to Hognestad (1951)) after which the concrete stress drops to zero; E_0 = initial concrete elastic modulus (equals to $4700\sqrt{f_c}$ per ACI 318-19); and E_s = secant modulus at σ_0 (equals to σ_0/ε_0).

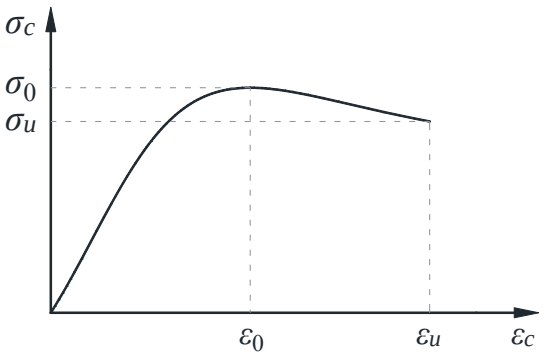

Fig. 6.2 Uniaxial compressive stress-strain relationship for the concrete

However, the material definition in ABAQUS for the CDP model assumes a linear elastic stress-strain relationship before the initial compressive yielding in the concrete. As a result, only the inelastic portion of the stress-strain relationship described in Eq. 6.1 and Eq. 6.2 was applied to the CDP model to determine the post yielding behavior of the concrete in compression. The slight difference within the elastic range of the compressive stress-strain relationship for the concrete material is illustrated in Fig. 6.3 and both curves are calculated based on the assumed model parameters.

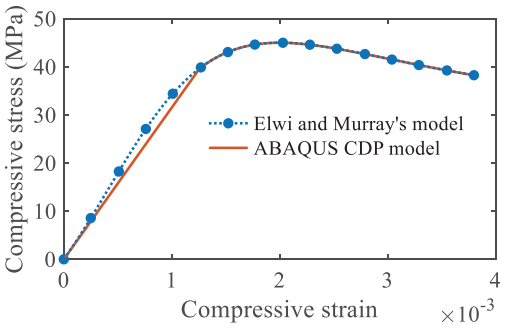

Fig. 6.3 Comparsion between theorectical and adopted compressive stress-strain relationship for the concrete

Uniaxial tensile stress-strain relationship

The uniaxial tensile stress-strain relationship adopted in this research was referring to Hordijk (1991), in which an exponential tensile stress-crack opening model was proposed and calibrated from a series of deformation-controlled uniaxial tensile tests. That same model was also used by Jendele and Cervenka (2006) and Chen et al. (2011) to describe the post-cracking tension-softening behavior of concrete in numerical analysis, as follows (Fig. 6.4):

$$\frac{\sigma_t}{f_t}=\left(1+\left(c_1\frac{w}{w_c}\right)^3\right)\exp\left(-c_2\frac{w}{w_c}\right)-\frac{w}{w_c}\left(1+c_1^3\right)\exp\left(-c_2\right) \tag{6.3}$$

$$w_c=5.14\frac{G_F}{f_t} \tag{6.4}$$

where σ_t = concrete tensile stress (MPa); f_t = concrete tensile strength (2.07 MPa, assumed to be the average concrete splitting tensile strength from the cylinder test); c_1 = 3 and c_2 = 6.93 = constants determined from concrete tensile tests; w = concrete crack opening displacement (mm); w_c = critical concrete crack opening displacement (mm); and G_F = fracture energy absorbed per unit crack area in widening the crack from zero to w_c (N·m/m^2, Hillerborg et al. 1976). In the case of lacking test data for the concrete material, the magnitude of G_F may be estimated from the CEB-FIP (1993) equation as follows:

$$G_F=\left(0.0469d_a{}^2-0.5d_a+26\right)\left(\frac{f_c}{10}\right)^{0.7} \tag{6.5}$$

where d_a = maximum aggregate size (mm) and 25.4 mm (1 inch) size was used according to the concrete batch data provided by the manufacturer in this study.

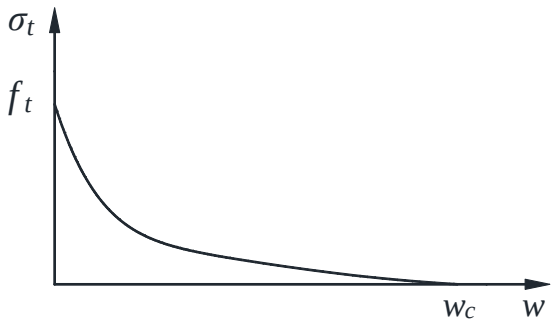

Fig. 6.4 Post-cracking tension softening model for the concrete

However, the implementation of this stress-displacement concept in ABAQUS requires the definition of a crack band width or characteristic crack length to convert the stress-displacement relationship into a stress-strain relationship for FE simulation. The crack band width h_c, over which the cracking strain ε_t^{ck} accumulates due to concrete microcracking (Bažant et al. 1983), is typically measured as the length of a line across an element for a first-order element in ABAQUS and thus it can be calculated as

$$\varepsilon_t^{ck} = \frac{w}{h_c} \tag{6.6}$$

Because the direction of concrete crack is unknown in advance for the numerical model, and also the elements with large aspect ratios will perform differently in post-cracking behavior depending on the direction in which they crack. Some mesh sensitivity exists due to this effect, therefore, the elements with aspect ratios close to one are recommended by ABAQUS (2013). Meanwhile, to further minimize this mesh dependency, the crack band width was defined as a function of the element size, i.e., $h_c = \sqrt{3}l_e$, where l_e is the edge length of a concrete element. The equivalent stress-cracking strain relationships of 5 mm, 7.5 mm and 10 mm concrete element adopted in this research, for example, are presented in Fig. 6.5.

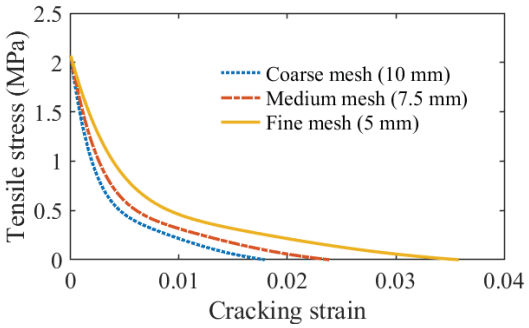

Fig. 6.5 Stress-cracking strain relationships for the concrete elements with different sizes

Definition of damage variables

Two damage variables, d_t and d_c are defined in the CDP model to characterize the extent of concrete damage in tensile and compressive behavior, respectively, within the plastic regime after material yielding. They are directly related to the cracking strain ε_{ck} in tension or inelastic strain ε_{in} in compression as follows:

$$d_t = d_t\left(\varepsilon_t^{ck}\right) \quad \left(0 \le d_t \le 1\right) \tag{6.7}$$

$$d_c = d_c\left(\varepsilon_c^{in}\right) \quad \left(0 \le d_t \le 1\right) \tag{6.8}$$

where $d_t = 0$ = no damage in tension; $d_t = 1$ = complete tensile failure in concrete; $d_c = 0$ = no damage in compression; and $d_c = 1$ = complete crushing failure in concrete.

The post-failure behaviors in both tension and compression for concrete will be significantly affected with the inclusion of damage variables. Figs. 6.6 and 6.7 display the loading (solid line) and unloading (dashed line) branches of the stress-strain relationship for both concrete tensile and compressive behaviors. For concrete tensile strain develops into softening stage, the elastic modulus degrades gradually in accordance with the tensile damage d_t. The cracking strain ε_t^{ck} presented in the plot is defined by the total strain subtracting the elastic strain corresponding to the undamaged concrete, i.e., $\varepsilon_t^{ck} = \varepsilon_t - \varepsilon_{0t}^{el}$ where $\varepsilon_{0t}^{el} = \sigma_t/E_0$. On the other hand, the plastic strain ε_t^{pl} can be calculated by the total strain subtracting the elastic strain corresponding to the damaged concrete, i.e., $\varepsilon_t^{pl} = \varepsilon_t - \varepsilon_t^{el}$ where $\varepsilon_t^{el} = \sigma_t/[(1\text{-}d_t)E_0]$. Because the definitions for both post-cracking

softening behavior and tensile damage variable of the CDP model in ABAQUS are provided in terms of the cracking strain ε_t^{ck}. The plastic strain ε_t^{pl} in tension will be automatically calculated by the following equation:

$$\varepsilon_t^{pl} = \varepsilon_t^{ck} - \frac{d_t}{1-d_t}\frac{\sigma_t}{E_0} \tag{6.9}$$

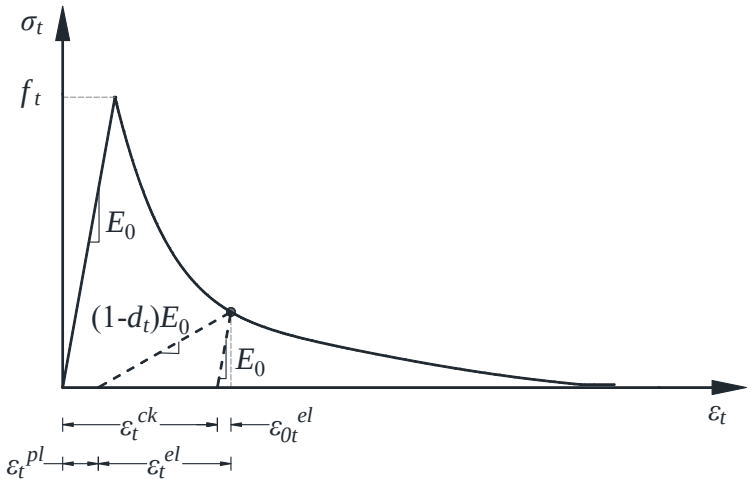

Fig. 6.6 Loading and unloading behavior of damaged concrete in tension

The damaged concrete compressive behavior is provided following the same strategy and the plastic strain ε_c^{pl} in compression is given by:

$$\varepsilon_c^{pl} = \varepsilon_c^{in} - \frac{d_c}{1-d_c}\frac{\sigma_c}{E_0} \tag{6.10}$$

where, as illustrated in Fig. 6.7, σ_{c0} = initial concrete yield stress in compression (MPa); $\varepsilon_c^{in} = \varepsilon_c - \varepsilon_{0c}^{el}$ in which $\varepsilon_{0c}^{el} = \sigma_c/E_0$; and $\varepsilon_c^{el} = \sigma_c/[(1\text{-}d_c)E_0]$. However, the definition of damage parameters requires some modeling practice through trial and error or calibration on the test data, which is not consistent and depending on the different purpose of FE model. For example, Chen et al. (2011) deduced the equation for tensile damage variable d_t by assuming a constant zero plastic strain ε_t^{pl} during the entire post-cracking behavior of concrete, indicating the unloading path of tensile stress-strain curve always passes through the origin shown in Fig. 6.6. Lopez-Almansa et al. (2014) used an exponential function to define the damage variables which required a calibration from concrete

cylinder tests. Alfarah et al. (2017) proposed a new methodology to calculate the damage variables for CDP model and it was suitable for describing the monotonic behavior of reinforced concrete structures. On the other hand, Genikomsou and Polak (2015) and Genikomsou (2016) systematically investigated the influence by both the compressive and tensile damage variable for the reinforced concrete slab-column connection under punching shear, and it was concluded that the damage variables are more important for cyclic or dynamic loadings but not for monotonic loading and thus could be neglected. A similar strategy was also adopted by Mercan et al. (2010) earlier for the FE modeling of a prestressed concrete spandrel beam. Consequently, the damage variables are not considered in this research because of the one-time pull-out procedure of the CFRP-to-concrete bonded joints under monotonic loading.

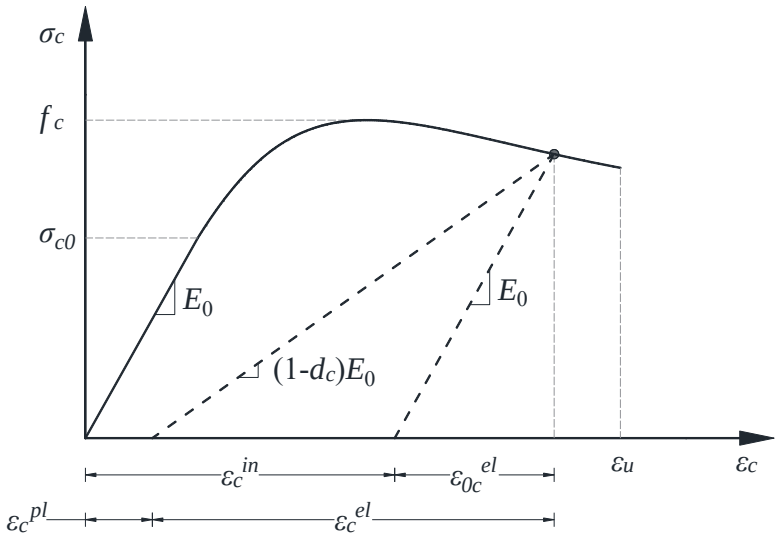

Fig. 6.7 Loading and unloading behavior of damaged concrete in compression

Yield surface

The yield function of the CDP model used in ABAQUS is based on Lubliner et al. (1989), with the modifications proposed by Lee and Fenves (1998) to provide the different strength evolutions in various loading conditions. Depending on the hardening variables, the plastic strains and effective stresses, the evolution of the yield function takes the form as follows:

$$F = \frac{1}{1-\alpha}\left(\bar{q} - 3\alpha\bar{p} + \beta\left(\varepsilon^{pl}\right)\left\langle\bar{\sigma}_{\max}\right\rangle - \gamma\left\langle-\bar{\sigma}_{\max}\right\rangle\right) - \bar{\sigma}_c\left(\varepsilon_c^{pl}\right) = 0 \tag{6.11}$$

$$\alpha = \frac{\left(\sigma_{b0}/\sigma_{c0}\right)-1}{2\left(\sigma_{b0}/\sigma_{c0}\right)-1}; \quad 0 \le \alpha \le 0.5 \tag{6.12}$$

$$\beta = \frac{\bar{\sigma}_c\left(\varepsilon_c^{pl}\right)}{\bar{\sigma}_t\left(\varepsilon_t^{pl}\right)}\left(1-\alpha\right) - \left(1+\alpha\right) \tag{6.13}$$

$$\gamma = \frac{3\left(1-K_c\right)}{2K_c - 1} \tag{6.14}$$

where $\bar{p}$ = hydrostatic pressure stress (MPa); $\bar{q}$ = Mises equivalent effective stress (MPa); $\langle\cdot\rangle$ = Macaulay bracket which yields the number inside the bracket only if it is positive otherwise yields zero; $\bar{\sigma}_{\max}$ = maximum principal effective stress (MPa); σ_{b0}/σ_{c0} = ratio of the initial biaxial compressive yield stress to the initial uniaxial compressive yield stress (default value = 1.16 per ABAQUS 2013); $\bar{\sigma}_t\left(\varepsilon_t^{pl}\right) = \sigma_t\left(\varepsilon_t^{pl}\right)/\left(1-d_t\right)$ = effective tensile cohesion stress (MPa); $\bar{\sigma}_c\left(\varepsilon_c^{pl}\right) = \sigma_c\left(\varepsilon_c^{pl}\right)/\left(1-d_c\right)$ = effective compressive cohesion stress (MPa); and K_c = ratio of the second stress invariant on the tensile meridian, $q_{(TM)}$, to that on the compressive meridian, $q_{(CM)}$, and determines the shape of the yield surface in the deviatoric plane ($0.5 < K_c \le 1$ per ABAQUS 2013, and the default value = 2/3), as illustrated in Fig. 6.8.

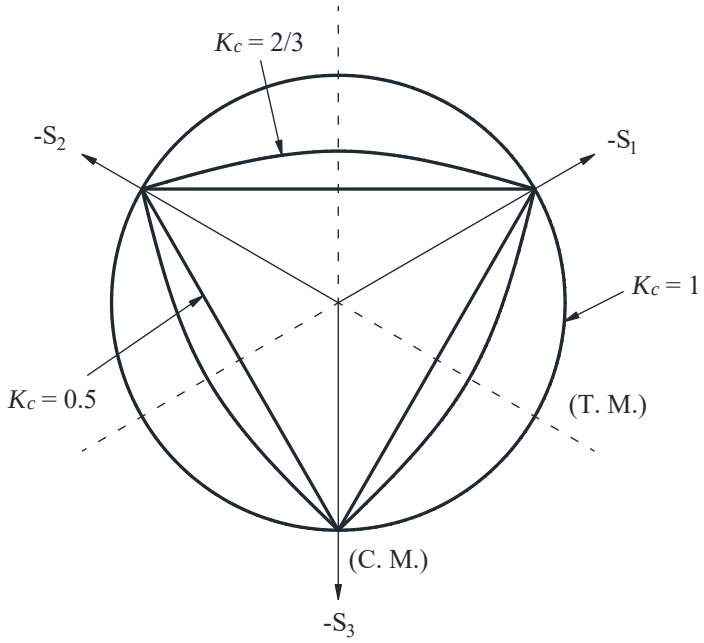

Fig. 6.8 Yield surfaces in the deviatoric plane for different values of K_c

Plastic flow

A non-associated potential plastic flow G is adopted in the CDP model and takes the form of the Drucker-Prager hyperbolic function as follows (Fig. 6.9):

$$G = \sqrt{\left(\varepsilon \sigma_{t0} \tan\varphi\right)^2 + \bar{q}^2} - \bar{p}\tan\varphi \tag{6.15}$$

where ε = eccentricity, which determines the rate at which the function approaches the asymptote (default value = 0.1 per ABAQUS 2013); σ_{t0} = uniaxial tensile stress at failure (MPa); and φ = dilation angle of the concrete measured in the meridian plane at high confining (hydrostatic) pressure.

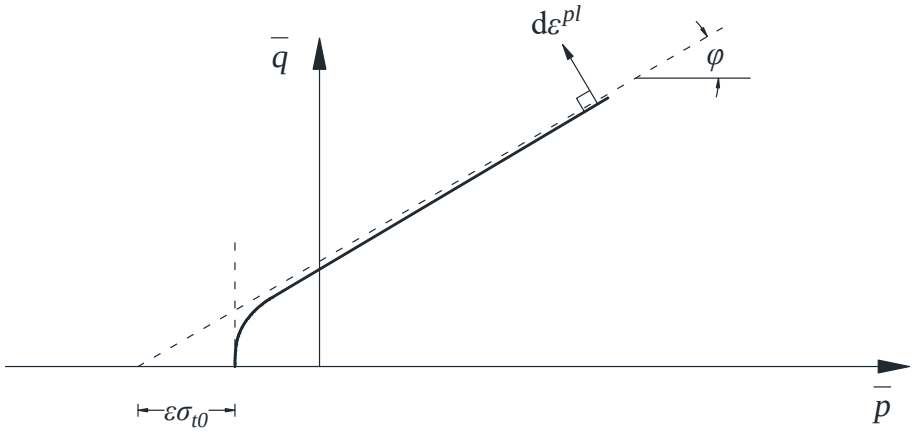

Fig. 6.9 The non-associated hyperbolic flow potential in the meridian plane

In Fig. 6.9, the hyperbolic flow potential approaches the linear Drucker-Prager flow potential asymptotically with the increase of confining pressure, and it intersects the horizontal axis at 90°. A small magnitude of eccentricity, e.g., ε = 0.1, keeps almost the same dilation angle φ of the concrete over a wide range of the confining pressure values. However, values of eccentricity that are significantly smaller than 0.1 is not recommended because of the possible convergence problem at low confining pressures. It should also be noted that the dilation angle is crucial to the plastic behavior of concrete since it determines the direction in which the plastic strain increases. For plain concrete, a dilation angle of 13° is recommended according to Vermeer and Borst (1984).

6.2.3 Modeling of epoxy adhesive and CFRP

The breakage of epoxy adhesive observed in the experiment was considered more like a collateral damage caused by the breakage of surrounding concrete, and it usually occurred close to the specimen failure. On the other hand, as described in Table 4.3, the mechanical performance of those adopted epoxies in this research all prevailed over that of the two batches of concrete. In such a case, to ease the modeling process and alleviate the possible convergency issue of the numerical model, the epoxy adhesive was idealized as an isotropic linear elastic material and assumed to be perfectly bonding to the substrate concrete. CFRP reinforcement was also modeled as linear elastic material since the orientation of carbon fibers was in line with the applied load

(tension), the effect caused by transverse deformation of the CFRP material was thus almost negligible. In addition, because the utilizations of CFRP reinforcements were all reported as much lower than their ultimate capacities based on the test results. The rupture of the CFRP reinforcement as a failure mode was not a concern in this numerical simulation. Two CFRP reinforcement cases were studied in this analysis, including the sand-coated and spirally wound (SCSW) rod specimen (R-SCSW-A1-N, Set 3 in Table 4.5) and the roughened (textured) strip specimen (S-RO-A1-N, Set 4 in Table 4.5). Details of material definitions in ABAQUS for these two cases are summarized in Table 6.1, along with the key parameters of the adopted CDP model.

Table 6.1 Summary of material definitions in ABAQUS for both CFRP rod and strip cases

Specimen cases	CFRP rod	CFRP strip
Groove dimensions (width × depth, mm)[a]	22 × 20	15 × 29
CFRP sizes (diameter or width × depth mm)	9.5	4.5 × 16
Young's modulus of CFRP (GPa)	129	168
Tensile strength of CFRP (MPa)	2372	2532
Poisson's ratio of CFRP[b]	0.2	
Young's modulus of epoxy (MPa)	12411	
Poisson's ratio of epoxy[b]	0.35	
Young's modulus of concrete (MPa)	31536	
Poisson's ratio of concrete[b]	0.18	
Concrete compressive strength (MPa)	45.02	
Concrete tensile strength (MPa)	2.07	
Dilation angle φ (°)	13	
Eccentricity ε	0.1	
σ_{b0}/σ_{c0}	1.16	
K_c	2/3	
μ[c]	0.0005	

[a]Average measured dimensions based on testing specimens; [b]Assumed value for modeling; [c]Viscosity parameter defined in the CDP model to improve the rate of convergence of the model without compromising results (ABAQUS 2013).

6.2.4 Modeling of cohesive element

To reproduce the interfacial debonding failure mode observed in the test for strip specimens, a special cohesive element (COH3D8) was defined and a thin cohesive layer was built between the CFRP strip and epoxy adhesive material, as presented in Fig. 6.10. The mesh size for cohesive layer was 1.13 mm in its transverse direction (2 elements), 1.33 mm in its height direction (12 elements) and 1.25 mm in its longitudinal direction (200 elements). The inner and outer surface of

the cohesive layer was tied to the CFRP strip and epoxy, respectively. Thus, the relative translation and rotation between CFRP strip and epoxy was governed by the intermediate cohesive layer.

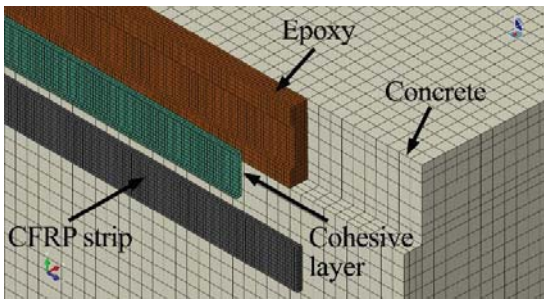

Fig. 6.10 Meshed cohesive layer between CFRP strip and epoxy adhesive

The objective of adopting cohesive element was to model the delamination (or debonding) behavior at interfaces by means of a traction-separation (or local bond stress-slip) relationship. ABAQUS provides a linear elastic traction-separation behavior (step 1) for cohesive material followed by the initiation and evolution of damage (step 2), as presented in Fig. 6.11. The universal constitutive relationship between the traction stress vector **t** and the strain vector **ε** for the cohesive element could be presented as follows:

$$\mathbf{t} = \begin{Bmatrix} t_n \\ t_s \\ t_t \end{Bmatrix} = \begin{bmatrix} E_{nn} & E_{ns} & E_{nt} \\ E_{ns} & E_{ss} & E_{st} \\ E_{nt} & E_{st} & E_{tt} \end{bmatrix} \begin{Bmatrix} \varepsilon_n \\ \varepsilon_s \\ \varepsilon_t \end{Bmatrix} = \mathbf{E}\boldsymbol{\varepsilon} \tag{6.16}$$

where t_n = normal traction (MPa, along the local 3-direction in 3D); t_s, t_t = shear traction (MPa, along the local 1- and 2-direction, respectively); E_{nn}, E_{ss} and E_{tt} = elastic tensile or shear stiffness (MPa); E_{ns}, E_{nt} and E_{st} = coupling stiffness term (zero for uncoupled traction-separation behavior); ε_n = normal strain; ε_s, ε_t = shear strain. Assuming an uncoupled traction-separation behavior of the cohesive element in this research, values of E_{nn}, E_{ss} and E_{tt} need to be provided to define the cohesive material. However, because the actual thickness of the cohesive layer is usually very small, e.g., 0.001 mm in this research, ABAQUS uses a unit length 1.0 as the constitutive thickness of the cohesive element to ensure that the strain is the same as the displacement (ABAQUS 2013).

As a result, the stiffness that relates the nominal stress (traction) to the displacement of the cohesive element, i.e., K_{nn}, K_{ss} and K_{tt}, are used and defined in the following (Rezazadeh et al. 2017):

$$K_{nn} = \frac{K_{nn}^{a} K_{nn}^{f}}{K_{nn}^{a} + K_{nn}^{f}} \tag{6.17}$$

$$K_{ss} = \frac{t_s^0}{\delta_s^0} \tag{6.18}$$

$$K_{tt} = \frac{t_t^0}{\delta_t^0} \tag{6.19}$$

where $K_{nn}^{a} = E_a/t_a$ = stiffness of epoxy adhesive in the normal direction (MPa/mm), in which E_a = Young's modulus of epoxy adhesive (MPa) and t_a = thickness of epoxy adhesive layer (mm); $K_{nn}^{f} = E_f/t_f$ = stiffness of CFRP strip in the normal direction (MPa/mm), in which E_f = Young's modulus of CFRP strip (MPa) and t_f = half width of CFRP strip (mm); t_n^0 = peak value of the nominal stress in the normal direction to the interface (mm); δ_n^0 = relative displacement between the top and bottom of the cohesive layer corresponding to t_n^0 (mm); t_s^0, t_t^0 = peak value of the nominal stress in the first and second shear direction (MPa), respectively; and δ_s^0, δ_t^0 = relative displacement corresponding to t_s^0 and t_t^0 (mm), respectively. It should be noted that the bracket presented in Fig. 6.11, e.g., K_{nn} (K_{ss}, K_{tt}), simply represents that the concept of separation-traction relationship is the same in all three local directions. Calculated values of these stiffnesses are summarized in Table 6.2.

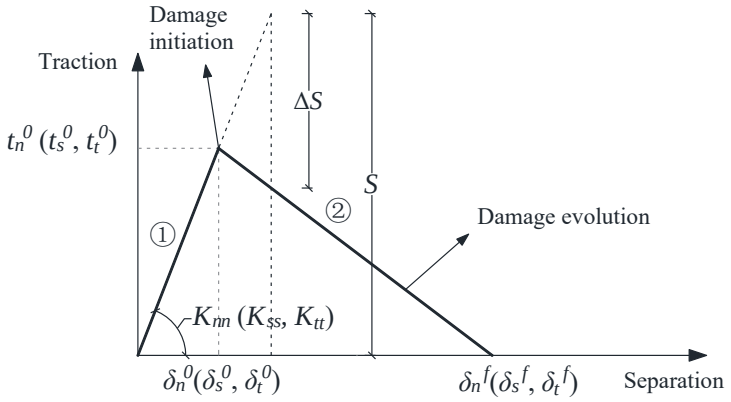

Fig. 6.11 Typical separation-traction relationship with linear damage evolution

As illustrated in Fig. 6.11, the stiffness keeps constant for the entire separation-traction relationship, but a damage variable *D* needs to be introduced when the specified damage initiation criterion has been reached. The maximum nominal stress criterion was used in this research to indicate the initiation of damage in cohesive element as follows:

$$\max\left\{\frac{\langle t_n \rangle}{t_n^0}, \frac{\langle t_s \rangle}{t_s^0}, \frac{\langle t_t \rangle}{t_t^0}\right\} = 1 \tag{6.20}$$

It should be noted that the first term of Eq. 6.20 is almost negligible by assuming the linear elastic response in the normal direction to the interface between CFRP strip and epoxy when the tensile strength of epoxy was used as the damage initiation limit. The value of peak shear traction (t_s^0 and t_t^0) was taken as the local bond strength τ_f measured from the previous DPT experiment for the CFRP strip case, i.e., set S-RO-A1-N (Table 6.2). On the other hand, as shown in step 2, the softening behavior after damage initiation is controlled by the damage variable D in the following format:

$$t_n, t_s, t_t = (1-D)S \tag{6.21}$$

where *S* = predicted stress by the linear elastic traction-separation relationship for the current strain without damage (MPa); ΔS = difference between the predicted stress and actual softening stress (MPa); and $D = \Delta S/S$. Details of defining the damaged behavior of the cohesive elements will be elaborated in the following chapter.

Table 6.2 Summary of cohesive material defined in ABAQUS for the CFRP strip case

K_{nn} (MPa/mm)	K_{ss} (MPa/mm)	K_{tt} (MPa/mm)	t_n^0 (MPa)	t_s^0 (MPa)	t_t^0 (MPa)
2291.5	208.4	208.4	14.8	10.42	10.42

6.3 FE model calibration

6.3.1 Calibration of the CDP model by Barr et al. (2003)'s beam test

To verify the accuracy of the CDP model and present how the FE model is calibrated based on the test specimen and loading setup, the round-robin beam bending test conducted by Barr et al.

(2003) was simulated as an example in ABAQUS by using the CDP model. The series of tests were aimed to evaluate the applicability and robustness of the test method recommended by the RILEM TC 162-TDF (2003) for steel fiber reinforced concrete. However, the two cases of plain concrete beams, i.e., C25/30 and C70/85, which served as the control specimens in the testing series were ideal for the calibrating of the CDP model. The concrete beam tested had a dimension of 150×150 mm in cross-section and 600 mm in length, and a 3 mm wide notch with 25 mm in length was cut by rotating diamond blades at the mid-span of the beam, as illustrated in Fig. 6.12. Two roller supports were placed at a distance of 50 mm away from the beam end, respectively, and a concentrated load was applied at the mid-span by displacement control. The values of concentrated load, mid-span displacements and crack mouth opening displacement (CMOD) were recorded throughout the test by gauges. The material properties of the beam for both normal strength concrete (NSC) and high strength concrete (HSC) are summarized in Table 6.3, which were also used for the definition of the CDP model.

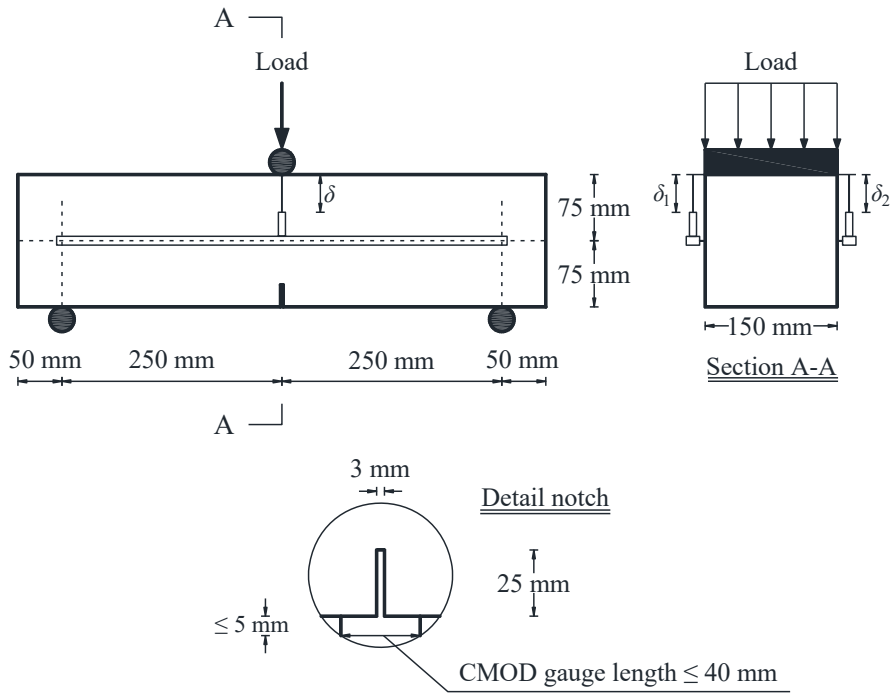

Fig. 6.12 Beam bending test set-up (Barr et al. 2003)

Table 6.3 Properties of concrete material used for the beam bending test

Concrete grade	Density[a] (kg/m^3)	Young's modulus of concrete[b] (MPa)	Compressive strength[a] (MPa)	Flexural strength[c] (MPa)
C25/30 (NSC)	2367	27924	35.3	4.2
C70/85 (HSC)	2395	45032	91.8	6.7

[a]Data was collected from Barr et al. (2003); [b]Calculated by $4700\sqrt{f_c}$ per ACI 318-19; [c]Calculated by $0.7\sqrt{f_c}$ per ACI 318-19.

In ABAQUS, the beam was modeled by using the plane stress element CPS4R for simplicity and a mesh size of 3 mm was adopted because of the small notch cut in the mid-span. Under the circumstance that the concrete cracking direction of the beam specimen was predictable (parallel to the notch, or vertical), the tensile stress-cracking strain relationship was thus determined based on a characteristic crack length of 3 mm by using Eq. 6.6. The variables for the definition of the concrete plasticity were the same as aforementioned in Table 6.1, where $\varphi = 13°$; $\varepsilon = 0.1$; $\sigma_{b0}/\sigma_{c0} = 1.16$; and $K_c = 2/3$. The cracking pattern and maximum principal stress distribution of the FE model for the NSC case at the peak load is presented in Fig. 6.13 (deformation is scaled up by 100 times), while the comparisons of load vs. mid-span deflection and load vs. CMOD between the FE model and experiment are illustrated in Fig. 6.14. For the load vs. mid-span deflection [Fig. 6.14(a)], the FE model captures the overall development of the load-deflection relationship recorded during the experiment. However, the deflections at peak load for both the NSC and HSC cases are slightly smaller than that of the experiment. The peak load capacity of HSC case is also underestimated by the FE model. These differences might be explained by the measuring error of the gauge in vertical direction and the fluctuation of the concrete material. It should be noted that the selected curve for the experiment was the typical test result and the variation in peak load between test specimens in the same set was 8% and 10% for NSC and HSC case, respectively (Barr et al. 2003). By contrast, the load vs. CMOD curves have a better consistency between the FE model and experiment [Fig. 6.14(b)], and it proves the validity of adopting the CDP model to simulate the cracking behavior of plain concrete specimens.

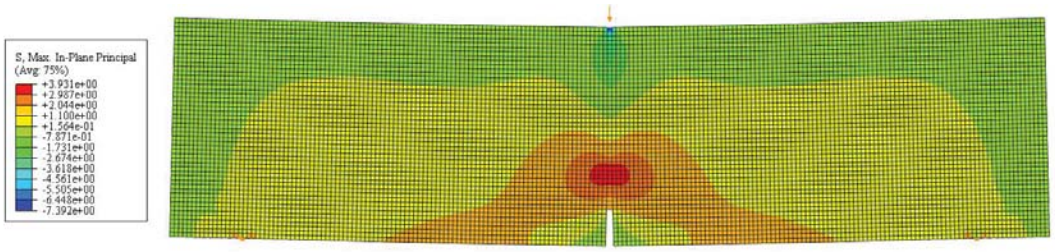

Fig. 6.13 In-plane principal stress contours at peak load of the FE model (NSC case, unit: MPa)

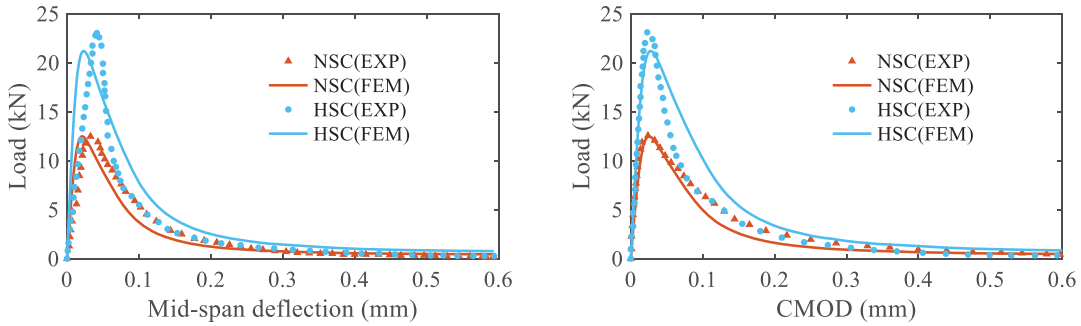

(a) Load-deflection curve (b) Load-CMOD curve

Fig. 6.14 Comparison between the FE model and experiment for the plain concrete beam

6.3.2 Mesh sensitivity

The results of FE analysis always vary with the change in mesh size especially for concrete material in the current study, though a mesh-dependent strategy was introduced for the definition of concrete in tensile stress-strain relationship by using the concept of crack band width to minimize the mesh sensitivity. Three mesh scenarios were studied for CFRP rod case to determine the mesh scheme of the FE analysis because the specimen using CFRP rod predominately failed in concrete and thus was more sensitive to the change in mesh size, including:

(1) Coarse mesh: Most concrete had a mesh size of 10 mm but will be slightly adjusted in the regions close to the groove, epoxy adhesive had 4 elements in its thickness direction and 6 elements in its height direction, and CFRP rod had 2 elements in its radial direction and 6 elements in its circumferential direction;

(2) Medium mesh: Most concrete had a mesh size approximately 7.5 mm and was slightly adjusted in the regions close to the groove, epoxy adhesive had 6 elements in its thickness direction and 12 elements in its height direction, and CFRP rod had 3 elements in its radial direction and 8 elements in its circumferential direction; and

(3) Fine mesh: Most concrete had a mesh size of 5 mm but will be slightly adjusted in the regions close to the groove, epoxy adhesive had 8 elements in its thickness direction and 18 elements in its height direction, and CFRP rod had 4 elements in its radial direction and 12 elements in its circumferential direction.

These three meshes were illustrated in Fig. 6.15 for the CFRP rod case, note that the CFRP rod was tied to the surrounding epoxy adhesive, the same as the epoxy adhesive was tied to the substrate concrete at the surface of contact. The load-displacement curves at the loaded end of the FE analysis based on these three meshes were presented in Fig. 6.16, where the experimental data from DPT of the specimen set R-SCSW-A1-N was plotted as well as references. All the three meshes had a very close behavior below 50 kN because of the same definition of concrete material within the linear elastic stage regardless of the mesh size. However, the difference in bond development of these three meshes was much larger in the post-cracking stage of concrete, where strong non-linear behavior was observed. The coarse mesh had the most significant fluctuation of pull-out force to maintain the same displacement increase rate at the loaded end, which was as expected because of the fewer elements used, and led to a less reliable result. Both the medium and fine meshes presented a more stable development during the non-linear stage of concrete after cracking though a difference of 6.8% was still observed for the peak pull-out force, where the fine mesh could reach a higher value of 68.2 kN compared to the lower 63.6 kN of the medium mesh. In addition, the FE result seemed to underestimate the bond strength compared to the test results, which had a pull-out force of 78.5 kN on average. Because the tensile strength 2.07 MPa adopted to define the concrete tensile behavior was the average value of 9 concrete cylinders during the 7.5-month testing series, where a standard deviation of 0.44 MPa was recorded. As a result, the large

fluctuation in concrete tensile strength led to a lower numerical prediction when an average tensile strength was used especially under the circumstance that the dominate failure mode was concrete breakage. Nevertheless, the fine mesh was selected by the current research for the CFRP rod specimen, as well as for the CFRP strip specimen, because it was more coincided with the experimental data. It should be noted that a finer mesh of concrete (e.g., 1.25 or 2.5 mm) was applicable and expected to be more accurate, yet due to the high computation cost it was beyond the scope of current research. Besides, the main purpose of this FE analysis was to reproduce the failure procedure observed in the experiment and study the different failure mechanism of CFRP rod and strip specimens. In such a case, a mesh size of 5 mm for the concrete block was acceptable.

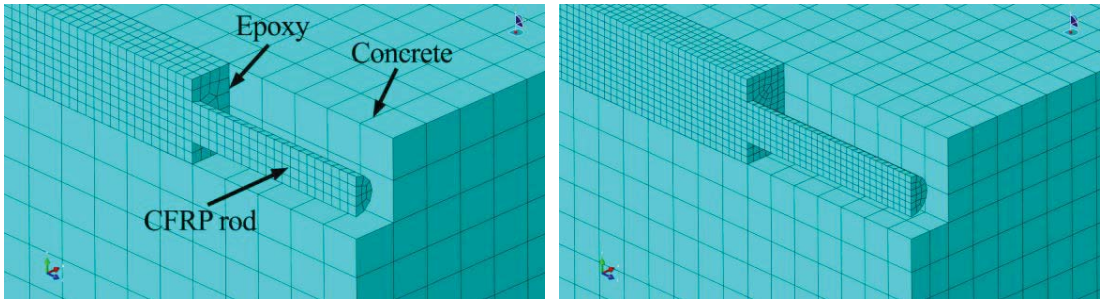

(a) Coarse mesh (b) Medium mesh

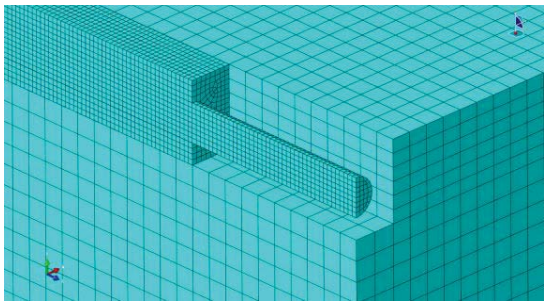

(c) Fine mesh

Fig. 6.15 Three mesh scenarios for the CFRP rod specimen

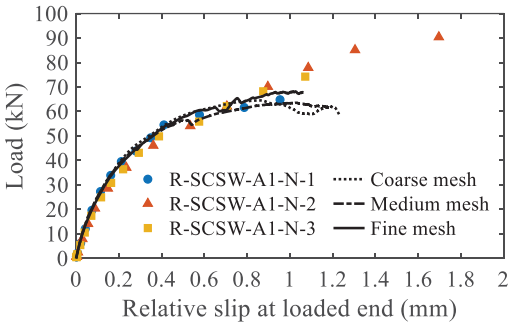

Fig. 6.16 Comparison of different meshes for the load-displacement relationship

6.3.3 Bond stress-slip relationship for the cohesive element

The interfacial (local) bond stress-slip relationship between CFRP reinforcement and epoxy governs the bond behavior of the NSM FRP-to-concrete bonded joints under pull-out force, as discussed comprehensively in the previous chapters. To reproduce the debonding failure mechanism observed in the experiment for the CFRP strip case, two representative bond models for the local bond stress-slip relationship, including both the bilinear model [Fig. 3.2(b)] and trilinear model [Fig. 3.2(d)], were used to determine the damage evolution of the cohesive layer. Thus, the damage variable *D* introduced in Chapter 6.2.4 for both models was derived by means of the calibrating results of Set 4 (Table 5.1) and Eq. 6.21, as illustrated in Fig. 6.17. It should be noted that the damage variable *D* in ABAQUS is specified as a function of the displacement relative to the displacement at damage initiation. The numerical analysis was conducted by following the modeling strategies mentioned above and the FE results are compared to the test results in term of the load-displacement relationship, as presented in Fig. 6.18. It can be seen that both models have the same linear elastic development that matched well with the experimental data before 25 kN. However, the FE result of the bilinear model deviated significantly from the experimental data during the nonlinear stage of the bond development, which was caused by its slower softening rate of the local bond stress-slip relationship. By contrast, the FE result of the trilinear model captured the overall trend of bond development and presented a good consistency with the experimental data. The peak load predicted by both the bilinear and trilinear model was 60.2 kN and 53 kN, being

equivalent to a difference of 10.7% and -2.6% compared to the average pull-out force (54.4 kN) of the CFRP strip specimen, respectively. As a result, the trilinear model was adopted by this research to reproduce the failure procedure of the CFRP strip-to-concrete bonded joints under pull-out force.

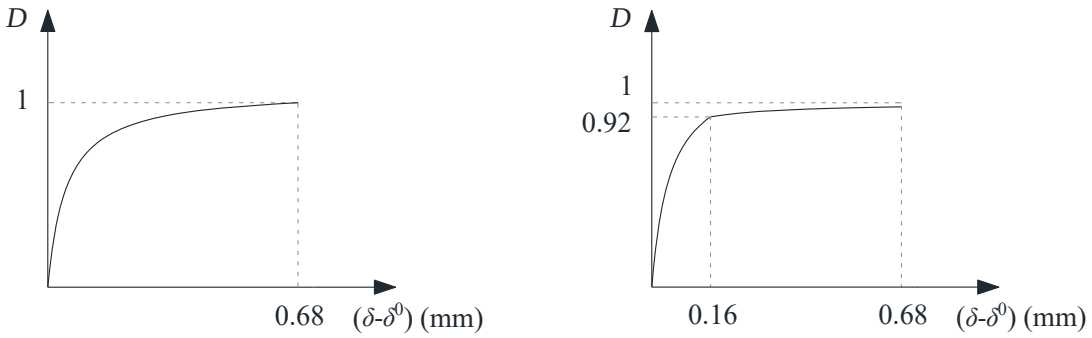

(a) Bilinear model (b) Trilinear model

Fig. 6.17 Damage variable *D* of the cohesive material

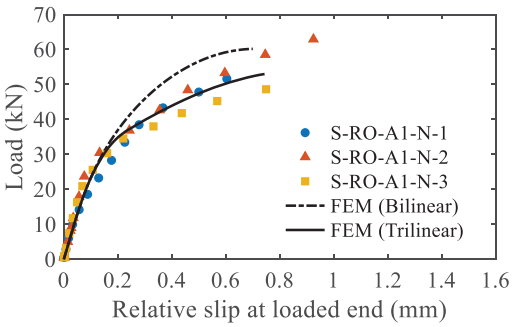

Fig. 6.18 Comparison between FE results and experimental data for the load-slip relationship at loaded for the CFRP strip specimen

6.4 Results and discussion of FE analysis

6.4.1 Bond development and failure mechanism

To illustrate the entire bond development for both CFRP rod and strip specimens, the distribution of the maximum principle stress of concrete was presented at different load levels in Fig. 6.19, where the left column [Fig. 6.19(a)] represents the CFRP rod case and the right column [Fig. 6.19(b)] represents the CFRP strip case. The five subplots of principle stress contour at each column under approximately 20, 40, 60, 80 and 100% of the ultimate pull-out force P_u (kN) are

corresponding to the points labelled on the load-slip curve, i.e., A, B, C, D, and E. At the load level of about 20%P_u (Point A) or less where the bond development was still mostly within the linear elastic stage, the peak principle stress of both CFRP rod and strip case was localized near the loaded end. When the load increased to approximately 40%P_u (Point B), the concrete near loaded end developed into the softening stage with a fast drop in tensile stress. Meanwhile, the peak principle stress migrated toward the free end with a larger region of concrete close to the groove influenced by the load transferred from epoxy adhesive both vertically and transversely. It should be noted that mechanism of the principle stress migration for CFRP rod and strip specimen was not identical, where the rod case was due to the fully development of concrete but the strip case was due to the interfacial debonding between CFRP strip and epoxy. The same pattern of bond development proceeded until the peak principle stress migrated to the region near free end at 80%P_u (Point D) for CFRP rod case or 100%P_u (Point E) for CFRP strip case. It reconfirmed that the concrete was not fully utilized for the CFRP strip specimen because of the premature interfacial debonding. For CFRP rod specimen, from 80%P_u (Point D) to 100%P_u (Point E) more concrete region was developed near the free end transversely within approximately twice the groove width to sustain a further increase of applied load until failure by concrete breakage.

On the other hand, the cracking pattern of concrete block for the CFRP rod specimen could be seen by the contour of plastic strain at failure as shown in Fig. 6.20. The upper limit of the plastic strain illustrated was set as 0.0243, corresponding to 10% of the concrete tensile strength defined in ABAQUS and beyond which the concrete was assumed to be failed completely (colored in grey). The region that enclosed by the perimeter of the plastic strain [Fig. 6.20(a)], representing the cracked concrete in ABAQUS, reached a satisfying agreement with the cracking pattern observed in the experiment [Fig. 6.20(b)].

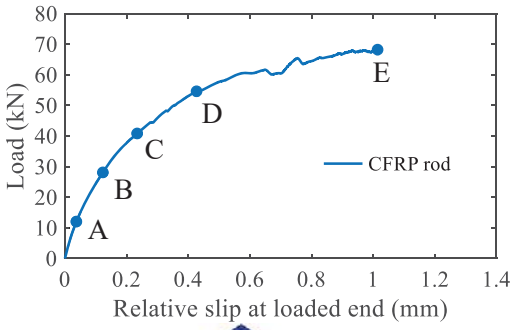

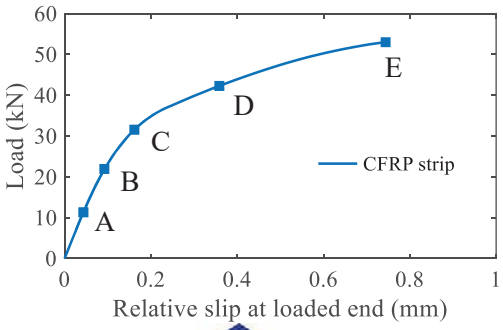

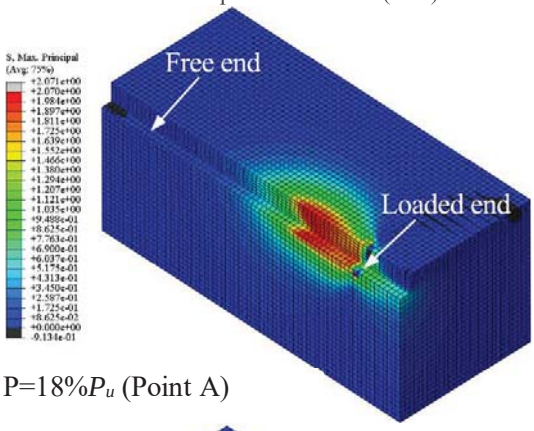

P=18%P_u (Point A)

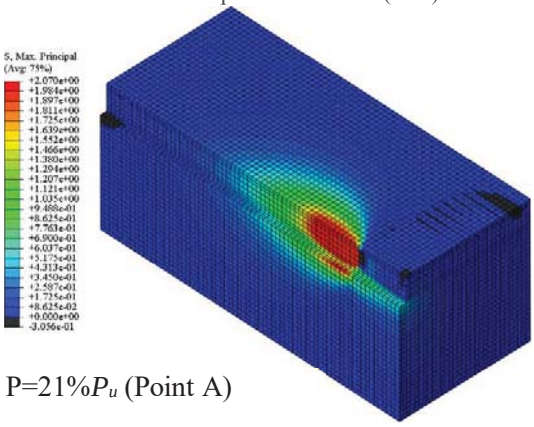

P=21%P_u (Point A)

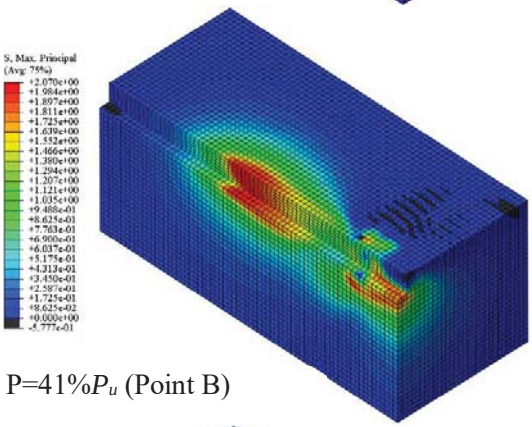

P=41%P_u (Point B)

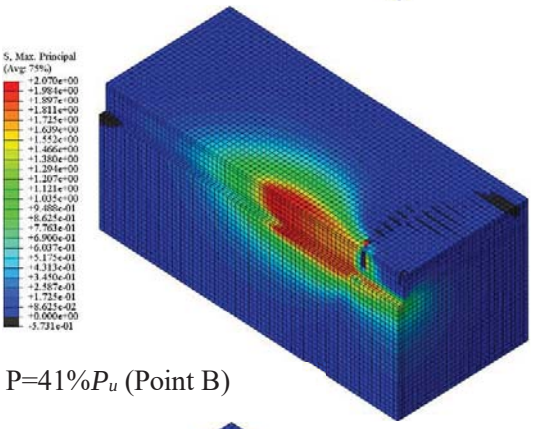

P=41%P_u (Point B)

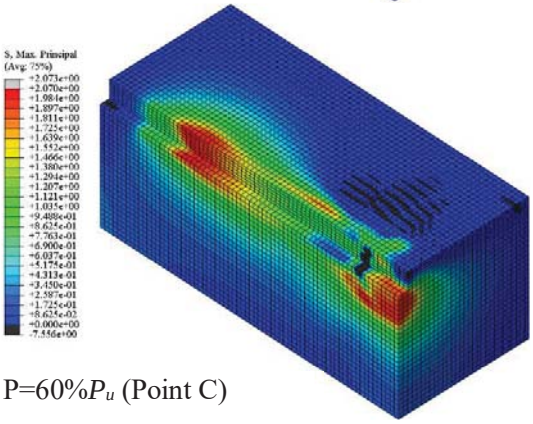

P=60%P_u (Point C)

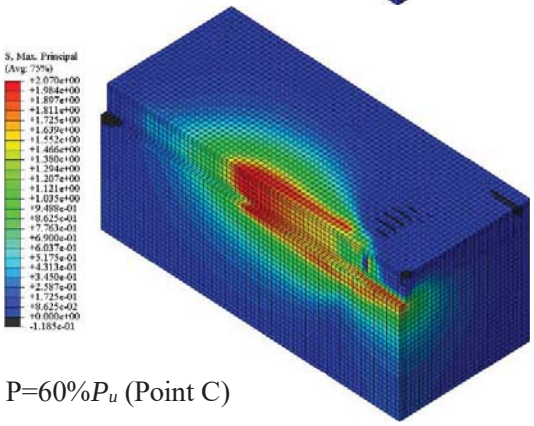

P=60%P_u (Point C)

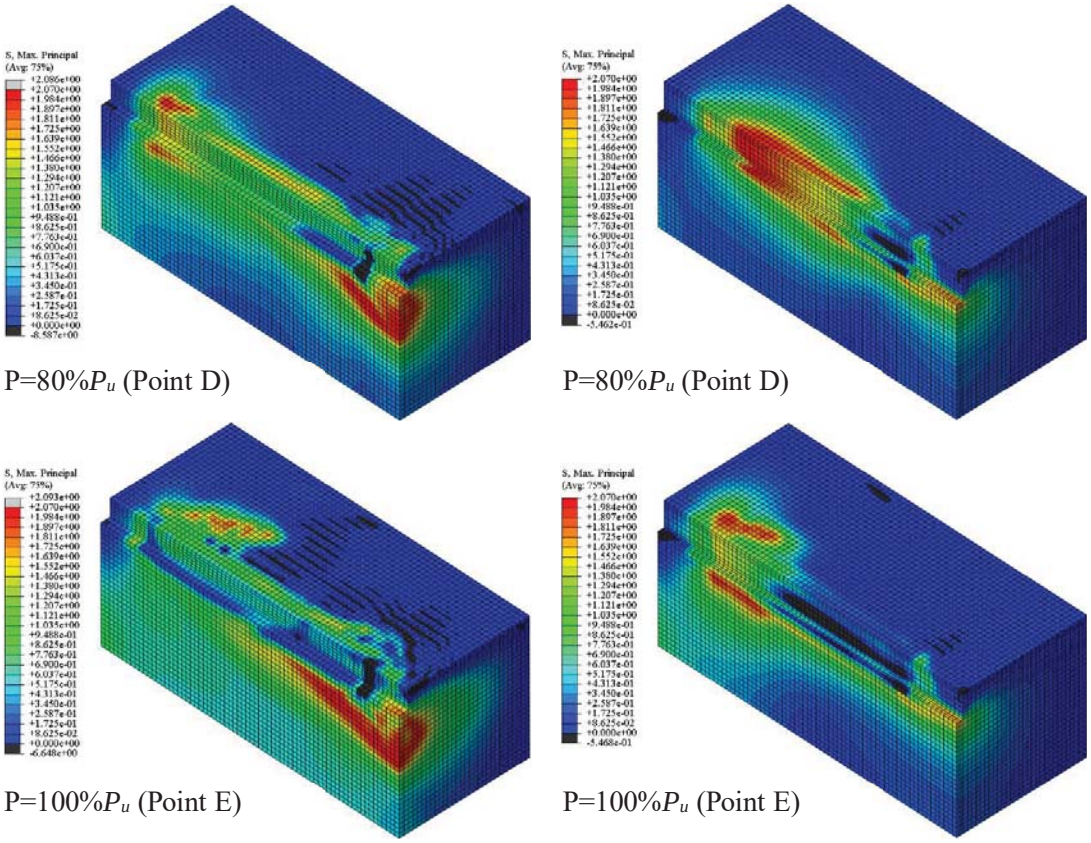

(a) CFRP rod (b) CFRP strip

Fig. 6.19 Bond development for CFRP-to-concrete bonded joints under load

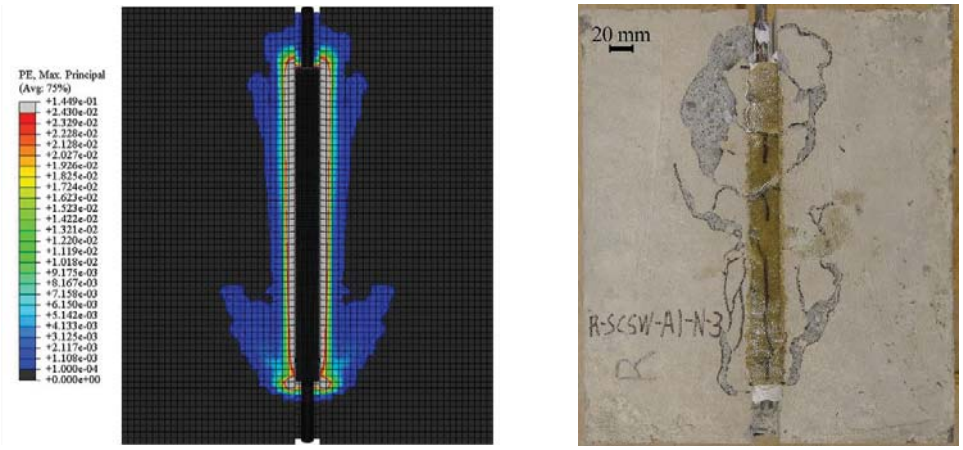

(a) FE result in ABAQUS (b) Failure mode observed in test

Fig. 6.20 Cracking pattern between FE analysis and experiment for CFRP rod specimen

6.4.2 Effect of dilation angle

For granular material such like concrete, its volume will change beyond the elastic limit due to microcracking and frictional sliding along microcracks, as presented Fig. 6.21. This phenomenon of volume change in concrete is called dilation. And the uplift angle φ is defined as the dilation angle which relates the vertical velocity (volumetric plastic deformation) and horizontal velocity (deviatoric plastic deformation) during the inelastic development of the material under shear stress (Vermeer and Borst 1984). The characteristic of concrete dilation significantly affects the passive confinement pressure activated in a reinforced concrete member (Mercan et al. 2010), and an increase in dilation angle will lead to more confinement and accordingly a stiffer axial stress-strain relationship of concrete (Grassl 2004). Though a dilation angle of 13° was already determined to define the plain concrete material used in the experiment, a sensitivity study of the important dilation angle is necessary.

Based on the CFRP rod case where the specimen failed by concrete breakage, dilation angle ranges from 15° to 55° was studied to present its influence on the bond strength in term of the load-slip relationship at the loaded end, as illustrated in Fig. 6.22. The difference in dilation angle did not affect the initial stiffness of the curve within elastic stage below 10 kN, but it drastically changed the bond behavior when the NSM FRP-to-concrete bonded joints developed into the plastic stage. A larger dilation angle led to a stiffer load-slip relationship and a higher load-carrying capacity of the joint as expected, because more passive confinement will be applied to the concrete material near the groove contributed by the boundary conditions as a result of the larger volumetric plastic deformation. The result curve of dilation angle φ = 15° seemed to fit well with the experimental data and was close to the result of FE model used in this study with a dilation angle φ = 13°, this observation also was coincided with the numerical study conducted by Lubliner et al. (1989) and Genikomsou (2016), where a dilation angle between 10° to 20° should be used for low-confined concrete.

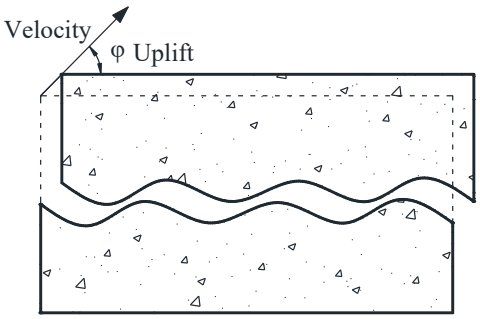

Fig. 6.21 Sliding at microcracks of concrete (Vermeer and Borst 1984)

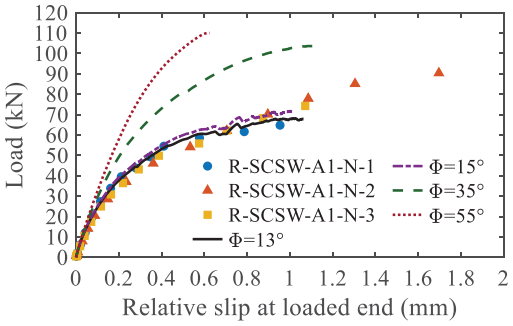

Fig. 6.22 Effect of dilation angle on the load-slip relationship at loaded for the CFRP rod specimen

6.4.3 Effect of concrete strength

Concrete strength always plays important role in the load-carrying capacity of FRP-to-concrete bonded joints, especially under the circumstance that a reliable bond has been constructed to prevent premature debonding failure at interfaces and ends up failing in concrete. In this context, the FE analysis on the same CFRP rod specimen had been further investigated to explore the influence of concrete at different strength levels with 25, 45 and 65 MPa in compression. The tensile strength with respect to the different concrete strength levels were determined from the CEB-FIP (1993) equations as follows:

$$f_t = 1.4\left(\frac{f_c - 8}{10}\right)^{2/3} \tag{6.22}$$

where f_c = cylinder compressive strength of concrete. However, the dilation angle for analysis of this study slightly increased to 20° (Genikomsou 2016) to reach a balance between accuracy of representing the low-confined concrete and computation cost. All the other material properties for this simulation were consistent with the FE model of the CFRP rod specimen mentioned above. The comparison of numerical results among these different concrete strength cases were plotted in Fig. 6.23. The peak pull-out forces were obtained as 61.4, 96.0 and 118.6 kN of the three CFRP rod specimens with different concrete strengths. It can be seen that the peak pull-out force is proportional to the concrete strength, and a larger relative slip needs to be developed as well to reach the load-carrying capacity of the specimen with higher concrete strength. A higher stiffness was observed for the specimen with higher concrete strength as expected because the Young's modulus of concrete defined in the FE model was from on the ACI 318 equation.

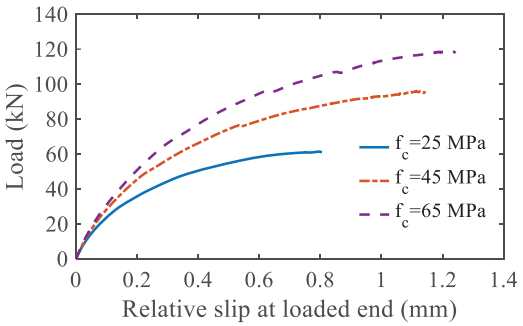

Fig. 6.23 Effect of concrete strength on the load-slip relationship at loaded for the CFRP rod specimen

6.4.4 Effect of groove width

The effect of groove size on the bond performance of NSM FRP-to-concrete joints had been widely studied by former researchers. In the case of concrete breakage failure of the test specimens, a larger groove height-to-width ratio increased the confinement of the joint, allowing stress transfer across the concrete crack via aggregate interlocking and friction (Seracino et al. 2007a, Zhang et al. 2013). Additionally, Oehlers et al. (2008) verified the contribution of extra adhesive cover to the load-carrying capacity when embedding the NSM FRP strips deeper into the groove. To sum

up, an optimum groove dimension of $1.5d_b \times 1.5d_b$ or $2.0d_b \times 2.0d_b$ (width × depth, d_b = diameter of FRP reinforcement) was recommended for most test configurations (Lee and Cheng 2013), which is consistent with the minimum dimensions of groove as specified in ACI 440.2R-08 (2008). And yet, very few studies discussed about the independent effect of groove width on the bond strength with a constant groove depth. Hence, three groove widths w_g of $1.5d_b$, $2.0d_b$ and $2.5d_b$ were selected in this parametric study, in considering both the requirement for FRP installation and minimizing cutting effort, while the groove depth d_g was set as $2.0d_b$. The comparison in terms of the load-slip relationship at loaded for the three groove widths was presented in Fig. 19, based on the same CFRP rod specimen. The peak pull-out forces of the CFRP rod specimen with different groove widths were 74.6, 75.5 and 75.8 kN, respectively, indicating a negligible difference in bond strength when the groove width was within the recommended range. Though a slight difference was also observed in the bond stiffness beyond the initial linear elastic stage, where increasing the groove width benefits the bond stiffness, it yielded a less significant contribution to the bond behavior when compared to other parameters described in previous subsections.

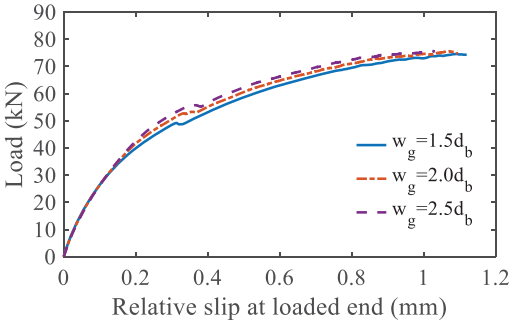

Fig. 6.24 Effect of groove with on the load-slip relationship at loaded for the CFRP rod specimen

6.5 Summary

In this chapter, the NSM FRP-to-concrete bonded joints of direct pull-out test conducted and discussed in Chapter 4 were successfully simulated by using a three-dimensional FE model in ABAQUS, where the nonlinear behavior of plain concrete was described by a concrete damaged plasticity (CDP) model. The CDP model, which includes definitions of concrete uniaxial

compressive and tensile behavior, as well as key parameters for yield surface and plastic flow, e.g., dilation angle $\varphi = 13°$; $\varepsilon = 0.1$; $\sigma_{b0}/\sigma_{c0} = 1.16$; and $K_c = 2/3$, was validated by Barr et al. (2003)'s beam test for plain concrete case. In addition, the interfacial debonding failure mode between CFRP strip and adhesive was accurately reproduced by virtue of the cohesive element and trilinear local bond stress-slip relationship, and the concrete breakage failure of CFRP rod specimen was realized assuming a perfect bond at all interfaces. A good agreement between the numerical predictions and experimental results was verified for both the CFRP rod and strip cases. Thereafter, parametric studies were carried out focusing on the effect due to dilation angle of concrete, concrete strength and groove width for the NSM FRP-to-concrete bonded joints. The following conclusions can be drawn from the numerical analysis:

- The CDP model is reliable of predicting the post-cracking behavior of plain concrete of NSM FRP-to-concrete bonded joints, under the circumstance that an appropriate dilation angle is provided, i.e., 10-20º. The dilation angle has a positive effect on both the bond stiffness within the nonlinear stage and ultimate pull-out force of the bonded joints;
- The bond development of NSM FRP-to-concrete bonded joints under pull-out force is a complex three-dimensional behavior. Concrete close to the groove within a region up to twice the groove width is most exploited and will develop both transversely and vertically with the increase of applied load, from the loaded end to the free end gradually. Interfacial debonding between FRP and adhesive will lower the utilization of concrete material;
- The specimen of NSM FRP rod in concrete, provided a perfect bond at all interfaces, benefits from a higher strength concrete, leading to both a higher load-carrying capacity and bond stiffness as well as a larger relative slip; and
- A larger groove width appears to produce a negligible effect on the load-carrying capacity of the specimen using NSM FRP rod, although the bond stiffness is slightly enhanced.

CHAPTER SEVEN

7 CONCLUSIONS AND FUTURE WORK

7.1 Concluding remarks

In the most recent decade, the retrofitting and strengthening of deficient concrete structures using the fiber reinforced composite (FRP) materials is gradually becoming a common practice. The near-surface mounted (NSM) FRP, as an alternative to the traditional externally bonded (EB) FRP, is highlighted by the advantage of high load-carrying capacity, faster installation, less prone to debonding and better weather-resistant because of the protecting adhesive cover. To ensure the strengthening efficiency of NSM FRP, as well as comprehend the failure mechanism, many experimental efforts have been made to investigate the bond performance of NSM FRP-to-concrete joints through direct pull-out test (DPT) under static loading. But the understanding of bond behavior of NSM FRP in concrete under fatigue loading and its failure mechanism is still lacking.

To investigate the bond characteristics of NSM FRP-to-concrete under fatigue loading, this research includes both experimental and analytical studies focusing on the local bond behavior induced by different factors. Finite element (FE) modeling is also adopted to simulate the joint specimen under the static direct pull-out force and helps understand the failure mechanism of NSM FRP in concrete. Chapter 3 summarizes the theories of FRP-to-concrete joints under the static direct pull-out force in the open literatures and constructs the database of DPTs for NSM FRP specimens. Semi-empirical equations to predict the load-carrying capacity of NSM FRP-to-concrete joints and corresponding failure mode are proposed. It also lays the foundation for the analytical model to describe the local bond behavior of NSM FRP in concrete under fatigue cycles. Chapter 4 describes the entire experimental study on the fatigue bond performance of NSM FRP-to-concrete joints. A total number of 84 specimens are tested under both static and fatigue loading cases, and test results on the local bond characteristics (e.g., local bond stress, FRP strain, relative slip, bond stiffness, etc.), failure mode and bond degradation behavior under fatigue cycles are

thoroughly discussed. Chapter 5 provides the theoretical base to explain and describe the local bond behavior of NSM FRP in concrete under both static and fatigue loading cases. The influence on the bond development under fatigue cycles induced by several key parameters such as the local bond strength, residual bond strength ratio, etc., are examined and compared by using the analytical model. Chapter 6 presents the three-dimensional FE modeling of the NSM FRP-to-concrete bonded joints using the concrete damaged plasticity (CDP) model in ABAQUS, the modeling strategy as well as the definition of materials are introduced. The failure mechanism of both CFRP rod and strip specimens are discussed and compared to the experimental observations. Additionally, parametric study is conducted by virtue of this FE model to supplement the experiment. The main conclusions from this research as summarized above is drawn in this chapter.

7.1.1 Experimental study

The following conclusion were drawn based on the 84 specimens, including 24 static specimens and 60 fatigue specimens. The static load-carrying capacities of the CFRP rod specimens were mostly larger than that of the CFRP strip specimens, indicating a more efficient utilization of the CFRP material of round cross-section in this study. However, the CFRP strip specimens can resist more fatigue cycles than the CFRP rod specimens under the same 10-60%P_f fatigue load range. This is because the fatigue cycles changed the failure mechanism of the CFRP rod specimens from concrete and epoxy breakage (CEB) under static loading to interfacial sliding/debonding between FRP and adhesive (F/A) by different extents, but the strip specimens had the same failure mechanism (F/A) in both loading cases.

All the three typical surface treatments of the CFRP rod specimens tested in this research, including roughened (RO), sand-coated (SC) and sand-coated and spirally wound (SCSW), provided reliable mechanical interlocking to prevent interfacial sliding (F/A) under static loading case. But the SCSW specimens prevailed over others with higher local bond strength, better

utilization of concrete material and slower fatigue bond degradation rate, which led to a longer fatigue life.

For the CFRP strip specimens of which failure was the interfacial sliding, the pull-out force was proportional to the material property of epoxy adhesive under static loading case. And the three-component epoxy adhesive A1 (Pilgrim-Magmaflow Grout-Pak CF) had been verified as the most reliable adhesive with its highest bond strength, good consistency in material property and satisfying fatigue performance in specimens. Concrete strength also had a positive effect on local bond strength and load-carrying capacity of specimens under static loading but it did not noticeably affect the fatigue bond behavior under the same 10-60%P_f fatigue load range. In addition, a higher fatigue load range (i.e., 10-70%P_f) accelerated the local bond degradation significantly and led to a much shorter fatigue life for both CFRP rod and strip specimens.

7.1.2 Analytical study

A trilinear local bond stress-slip model was proposed in this research, including linear elastic stage, softening stage and debonding stage with non-zero residual bond stress, and it was proven to be more representative of the real test results. The analytical model adapted from Yuan et al. (2004) based on the trilinear local bond stress-slip relationship agreed well with the experimental data, including pull-out force, CFRP strain distribution, local bond stress distribution and load-slip relationship at the loaded end. To further extend this model to be applicable under fatigue loading, the finite element (FE) strategy was applied to discretize the bond line of the NSM FRP-to-concrete joints and enabled the independent evolvement of each element by following the governing equations and degradation laws. Exponential degradation laws of local bond strength were calibrated from the experiment for both CFRP rod and strip specimens. The proposed analytical model could describe the overall local bond behavior due to fatigue degradation, e.g., development and distribution of FRP strain, local bond stress and relative slip, and the results reached a good agreement with the experimental data.

Parametric studies by virtue of the proposed analytical model confirms the significant importance of local bond strength which governs the local bond development of NSM FRP-to-concrete joints during fatigue cycles. A higher local bond strength can slow down the bond deterioration and restrict the development of damaged zone under cyclic loading. The residual bond strength ratio, on the other hand, primarily affects the post-softening behavior of the bond. A higher residual bond strength ratio increases the load-carrying capacity within the debonding region and consequently slows down bond development toward the free end. The fatigue bond performance of NSM FRP-to-concrete joints also benefits from a higher Young's modulus of FRP reinforcement.

7.1.3 Finite element modeling

The numerical simulation of NSM FRP in concrete joint specimen under the static direct pull-out force reveals the complexity of NSM FRP-to-concrete bond failure mechanism. Concrete close to the groove within a region up to twice the groove width is most exploited and will develop both transversely and vertically with the increase of applied load, from the loaded end to free end gradually. The CDP model in ABAQUS is reliable of predicting the post-cracking behavior of plain concrete provided that an appropriate dilation angle within 10-20º is defined. It also reconfirms the importance to prevent interfacial debonding failure mode in NSM FRP-to-concrete bonded joints to fully utilize the concrete material.

Parametric study based on the three-dimensional FE model has been conducted and results show that a larger dilation angle increases both the bond stiffness within the nonlinear stage and ultimate pull-out force of the NSM FRP-to-concrete bonded joints. A higher concrete strength yields a higher load-carrying capacity and bond stiffness as well as a larger relative slip of the bonded joints using NSM FRP rod. But a larger groove width seems to produce only negligible effect on the bond performance, though the bond stiffness is slightly enhanced.

7.2 Future work

This study mostly helps comprehend the local bond behavior and failure mechanism of various NSM CFRP-to-concrete joint specimens under fatigue loading case. Analytical models are proposed to explain and describe the bond development due to fatigue degradation for NSM FRP in concrete. The numerical simulation using the CDP model in ABAQUS provides a good reference of 3D FE modeling to study the bond issue of NSM FRP system. However, some other issues still need more efforts in the future research.

- The local bond strength of NSM FRP in concrete plays a pivotal role in the bond performance under both static and fatigue loading case. Yet the most reliable estimation of the local bond strength is through experimental study and obtaining readings from strain gauges. Some models to predict the local bond strength as well as the load-carrying capacity of NSM FRP-to-concrete bonded joints are introduced in Chapter 3 corresponding to different failure modes, but the accuracy of these models is still not satisfactory. Variations in the materials properties used for the NSM FRP technique (i.e., concrete, FRP and adhesive) significantly affect the bond performance and failure mechanism. Thus, further effort is required to improve the construction quality of concrete groove and FRP surface treatment, as well as reduce the variation in adhesive shear (bond) strength;
- The long-term performance of NSM FRP-to-concrete bonded joints is not only limited to the fatigue load. Other factors such like the sustained load and severe environmental conditions (e.g., salty water, freeze-and-thaw cycles, deicing, etc.) also deserve attention to ensure the efficiency of NSM FRP strengthening of structures in long run;
- The analytical model based on the trilinear local bond stress-slip relationship is representative of the test observations and captures the bond development of NSM FRP in concrete under both static and fatigue loading. But the current research only focuses on the bond level of NSM FRP technique, to further extend this analytical model to structural level, e.g., flexural and

shear strengthening of concrete beam, retrofitting of slab and wall, etc., further research is required to corelate the bond and structural level behavior;

- The fatigue bond degradation in this research is primarily quantified by the exponential degradation law of local bond strength calibrated from the experiment and it works fine with the proposed analytical model. Although the direct measurement using strain gauges attached to the surface of FRP reinforcement is common and reliable for experimental study, it is extremely strenuous and time consuming to prepare for the test. A possible alternative to estimate the fatigue bond degradation could be the equivalent bond stiffness of joint specimen, a damage factor could thus be introduced to quantify the reduction in bond stiffness dependent on fatigue cycles. In this sense, further study is necessary to propose a more practical model for the fatigue design of NSM FRP strengthened structures; and
- The FE modeling strategy of NSM FRP-to-concrete bonded joint specimen by using CDP model in ABAQUS is successful in this research. However, the current example models only consider the bond development and failure procedure under static pull-out force. An extension of the current FE model to be adaptable to cyclic loading is possible yet difficult. Some critical issues exist for the bond simulation under fatigue loading, for example, convergency difficulty induced by the inelastic behavior of concrete, quantification of accumulated damage in concrete and adhesive material, possible interfacial debonding between FRP and adhesive, and fatigue failure criteria, etc. A thorough investigation and deep consideration is required to solve the challenges mentioned above, yet the numerical approach is still appealing compared to the strenuous experimental study.

CHAPTER EIGHT

8 REFERENCES

ABAQUS 6.13. "Abaqus analysis users' guide: part vi: elements." Dassault Systèmes, 2013.

ACI Committee 215. "Considerations for design of concrete structures subjected to fatigue loading: ACI 215R-92 (reapproved 1997)." ACI, 1997.

ACI Committee 318. "Building code requirements for structural concrete (ACI 318-19) [and] Commentary on building code requirements for structural concrete (ACI 318R-19)." ACI, 2019.

ACI Committee 440. "Guide for the design and construction of externally bonded FRP systems for strengthening concrete structures: ACI 440.2 R-08." ACI, 2008.

Adimi, M. R., Rahman, A. H., and Benmokrane, B. "New method for testing fiber-reinforced polymer rods under fatigue." *Journal of Composites for Construction* 4.4 (2000): 206-213.

Alfarah, B., López-Almansa, F., and Oller, S. "New methodology for calculating damage variables evolution in plastic damage model for RC structures." *Engineering Structures* 132 (2017): 70-86.

Ali, M. M., Oehlers, D. J., Griffith, M. C., and Seracino, R. "Interfacial stress transfer of near surface-mounted FRP-to-concrete bonded joints." *Engineering Structures* 30.7 (2008): 1861-1868.

Al-Jaberi, Z., Myers, J. J., and ElGawady, M. A. "Pseudo-static cyclic loading comparison of reinforced masonry walls strengthened with FRCM or NSM FRP." *Construction and Building Materials* 167 (2018): 482-495.

Al-Mahmoud, F., Castel, A., François, R., and Tourneur, C. "Anchorage and tension-stiffening effect between near-surface-mounted CFRP rods and concrete." *Cement and Concrete Composites* 33.2 (2011): 346-352.

Al-Mahmoud, F., Castel, A., Minh, T. Q., and François, R. "Reinforced concrete beams strengthened with NSM CFRP Rods in shear." *Advances in Structural Engineering* 18.10 (2015): 1563-1574.

Al-Mahmoud, F., Mechling, J. M., and Shaban, M. "Bond strength of different strengthening systems–Concrete elements under freeze–thaw cycles and salt water immersion exposure." *Construction and Building Materials* 70 (2014): 399-409.

Al-Saadi, N. T. K., Al-Mahaidi, R., and Abdouka, K. "Bond behavior between NSM CFRP strips and concrete substrate using single-lap shear testing with epoxy adhesive." *Composite Structures* 132 (2015): 205-214.

Al-Saadi, N. T. K., and Al-Mahaidi, R. "Fatigue performance of NSM CFRP strips embedded in concrete using epoxy adhesive." *Composite Structures* 154 (2016): 419-432.

Al-Saadi, N. T. K., and Al-Mahaidi, R. "Modelling of NSM CFRP strips embedded in concrete using lap shear tests with epoxy adhesive." *Composite Structures* 153 (2016): 662-672.

Al-Saadi, N. T. K., Mohammed, A., and Al-Mahaidi, R. "Bond performance of NSM CFRP strips embedded in concrete using direct pull-out testing with cementitious adhesive made with graphene oxide." *Construction and Building Materials* 162 (2018): 523-533.

Al-Saadi, N. T. K., Mohammed, A., and Al-Mahaidi, R. "Fatigue performance of NSM CFRP strips embedded in concrete using innovative high-strength self-compacting cementitious adhesive (IHSSC-CA) made with graphene oxide." *Composite Structures* 163 (2017): 44-62.

Baghi, H., and Barros, J. A. "New approach to predict shear capacity of reinforced concrete beams strengthened with near-surface-mounted technique." *ACI Structural Journal* 114.1 (2017): 137.

Barr, B. I. G., Lee, M. K., de Place Hansen, E. J., Dupont, D., Erdem, E., Schaerlaekens, S., Schnütgen, B., Stang, H., and Vandewalle, L. "Round-robin analysis of the RILEM TC 162-TDF beam-bending test: part 1—test method evaluation." *Materials and Structures* 36.9 (2003): 609-620.

Barros, J. A., and Costa, I. "Bond tests on near surface reinforcement strengthening for concrete structures." Report of the Round Robin Tests 2.2 carried out by EN-CORE Project at University of Minho, 2010.

Bažant, Z. P., and Oh, B. H. "Crack band theory for fracture of concrete." *Matériaux et Construction* 16.3 (1983): 155-177.

Bilotta, A., Ceroni, F., Di Ludovico, M., Nigro, E., Pecce, M., and Manfredi, G. "Bond efficiency of EBR and NSM FRP systems for strengthening concrete members." *Journal of Composites for Construction* 15.5 (2011): 757-772.

Biscaia, H. C., Borba, I. S., Silva, C., and Chastre, C. "A nonlinear analytical model to predict the full-range debonding process of FRP-to-parent material interfaces free of any mechanical anchorage devices." *Composite Structures* 138 (2016): 52-63.

Bizindavyi, L., Neale, K. W., and Erki, M. A. "Experimental investigation of bonded fiber reinforced polymer-concrete joints under cyclic loading." *Journal of Composites for Construction* 7.2 (2003): 127-134.

Blaschko, M. "Bond behavior of CFRP strips glued into slits." *Fibre-Reinforced Polymer Reinforcement for Concrete Structures: (In 2 Volumes)*. 2003. 205-214.

Bonacci, J. F., and Maalej, M. "Behavioral trends of RC beams strengthened with externally bonded FRP." *Journal of Composites for Construction* 5.2 (2001): 102-113.

Capozucca, R. "Static and dynamic response of damaged RC beams strengthened with NSM CFRP rods." *Composite Structures* 91.3 (2009): 237-248.

Carloni, C., and Subramaniam, K. V. "Investigation of sub-critical fatigue crack growth in FRP/concrete cohesive interface using digital image analysis." *Composites Part B: Engineering* 51 (2013): 35-43.

Carloni, C., Subramaniam, K. V., Savoia, M., and Mazzotti, C. "Experimental determination of FRP–concrete cohesive interface properties under fatigue loading." *Composite Structures* 94.4 (2012): 1288-1296.

CEB-FIP, MC90. "90, Design of concrete structures. CEB-FIP Model Code 1990." British Standard Institution, London, 1993.

Ceroni, F., Pecce, M., Bilotta, A., and Nigro, E. "Bond behavior of FRP NSM systems in concrete elements." *Composites Part B: Engineering* 43.2 (2012): 99-109.

Chen, C., and Cheng, L. "Fatigue bond characteristics and degradation of near-surface mounted CFRP rods and strips in concrete." *Journal of Composites for Construction* 20.3 (2015): 04015066.

Chen, C., and Cheng, L. "Predicting flexural fatigue performance of RC beams strengthened with externally bonded FRP due to FRP debonding." *Journal of Bridge Engineering* 22.11 (2017): 04017082.

Chen, C., and Cheng, L. "Theoretical solution to fatigue bond stress distribution of NSM FRP reinforcement in concrete." *Composites Part B: Engineering* 99 (2016): 453-464.

Chen, G. M., Teng, J. G., and Chen, J. F. "Finite-element modeling of intermediate crack debonding in FRP-plated RC beams." *Journal of Composites for Construction* 15.3 (2011): 339-353.

Chen, J. F., Yang, Z. J., and Holt, G. D. "FRP or steel plate-to-concrete bonded joints: Effect of test methods on experimental bond strength." *Steel and Composite Structures* 1.2 (2001): 231-244.

Coelho, M. R., Sena-Cruz, J. M., and Neves, L. A. "A review on the bond behavior of FRP NSM systems in concrete." *Construction and Building Materials* 93 (2015): 1157-1169.

Dai, J., Ueda, T., and Sato, Y. "Development of the nonlinear bond stress–slip model of fiber reinforced plastics sheet–concrete interfaces with a simple method." *Journal of Composites for Construction* 9.1 (2005): 52-62.

De Lorenzis, L. "Anchorage length of near-surface mounted fiber-reinforced polymer rods for concrete strengthening—Analytical modeling." *Structural Journal* 101.3 (2004): 375-386.

De Lorenzis, L., and Nanni, A. "Shear strengthening of reinforced concrete beams with near-surface mounted fiber-reinforced polymer rods." *Structural Journal* 98.1 (2001): 60-68.

De Lorenzis, L., and Teng, J. G. "Near-surface mounted FRP reinforcement: An emerging technique for strengthening structures." *Composites Part B: Engineering* 38.2 (2007): 119-143.

De Lorenzis, L., Lundgren, K., and Rizzo, A. "Anchorage length of near-surface mounted fiber-reinforced polymer bars for concrete strengthening-experimental investigation and numerical modeling." *ACI Structural Journal* 101.2 (2004): 269-278.

Diab, H. M., Wu, Z., and Iwashita, K. "Theoretical solution for fatigue debonding growth and fatigue life prediction of FRP-concrete interfaces." *Advances in Structural Engineering* 12.6 (2009): 781-792.

Dias, S. J., and Barros, J. A. "Performance of reinforced concrete T beams strengthened in shear with NSM CFRP laminates." *Engineering Structures* 32.2 (2010): 373-384.

Douadi, A., Merdas, A., and Sadowski, Ł. "The bond of near-surface mounted reinforcement to low-strength concrete." *Journal of Adhesion Science and Technology* 33.12 (2019): 1320-1336.

El-Hacha, R., and Rizkalla, S. H. "Near-surface-mounted fiber-reinforced polymer reinforcements for flexural strengthening of concrete structures." *Structural Journal* 101.5 (2004): 717-726.

El-Hacha, R., Wight, R. G., and Green, M. F. "Prestressed fibre-reinforced polymer laminates for strengthening structures." *Progress in Structural Engineering and Materials* 3.2 (2001): 111-121.

Elwi, A. A., and Murray, D. W. "A 3D hypoelastic concrete constitutive relationship." *Journal of the Engineering Mechanics Division* 105.4 (1979): 623-641.

Fahmy, M. F., and Wu, Z. "Exploratory study of seismic response of deficient lap-splice columns retrofitted with near surface–mounted basalt FRP bars." *Journal of Structural Engineering* 142.6 (2016): 040160.

Fernandes, P. M., Silva, P. M., and Sena-Cruz, J. "Bond and flexural behavior of concrete elements strengthened with NSM CFRP laminate strips under fatigue loading." *Engineering Structures* 84 (2015): 350-361.

Galati, D., and De Lorenzis, L. "Effect of construction details on the bond performance of NSM FRP bars in concrete." *Advances in Structural Engineering* 12.5 (2009): 683-700.

Garzón-Roca, J., Sena-Cruz, J. M., Fernandes, P., and Xavier, J. "Effect of wet-dry cycles on the bond behavior of concrete elements strengthened with NSM CFRP laminate strips." *Composite Structures* 132 (2015): 331-340.

Genikomsou, A. S. "Nonlinear finite element analysis of punching shear of reinforced concrete slab-column connections." UWSpace, 2016.

Genikomsou, A. S., and Polak, M. A. "Finite element analysis of punching shear of concrete slabs using damaged plasticity model in ABAQUS." *Engineering Structures* 98 (2015): 38-48.

Grassl, P. "Modelling of dilation of concrete and its effect in triaxial compression." *Finite Elements in Analysis and Design* 40.9-10 (2004): 1021-1033.

Hassan, T., and Rizkalla, S. "Bond mechanism of NSM FRP bars for flexural strengthening of concrete structures." *ACI Structural Journal* 101.6 (2004): 830-839.

Hillerborg, A., Modéer, M., and Petersson, P. E. "Analysis of crack formation and crack growth in concrete by means of fracture mechanics and finite elements." *Cement and Concrete Research* 6.6 (1976): 773-781.

Hognestad, E. "Study of combined bending and axial load in reinforced concrete members." University of Illinois at Urbana Champaign, College of Engineering. Engineering Experiment Station, 1951.

Hollaway, L. C. "Key issues in the use of fibre reinforced polymer (FRP) composites in the rehabilitation and retrofitting of concrete structures." *Service Life Estimation and Extension of Civil Engineering Structures*. Woodhead Publishing, 2011. 3-74.

Hordijk, D. A. "Local approach to fatigue of concrete (Ph. D. Thesis)." Delft University of Technology, 1991.

Iwashita, K., Wu, Z., Ishikawa, T., Hamaguchi, Y., and Suzuki, T. "Bonding and debonding behavior of FRP sheets under fatigue loading." *Advanced Composite Materials* 16.1 (2007): 31-44.

Jendele, L., and Cervenka, J. "Finite element modelling of reinforcement with bond." *Computers and Structures* 84.28 (2006): 1780-1791.

Kang, T. H. K., Howell, J., Kim, S., and Lee, D. J. "A state-of-the-art review on debonding failures of FRP laminates externally adhered to concrete." *International Journal of Concrete Structures and Materials* 6.2 (2012): 123-134.

Karbhari, V. M., Niu, H., and Sikorsky, C. "Review and comparison of fracture mechanics-based bond strength models for FRP-strengthened structures." *Journal of Reinforced Plastics and Composites* 25.17 (2006): 1757-1794.

Kaya, E., Kütan, C., Sheikh, S., and İlki, A. "Flexural retrofit of support regions of reinforced concrete beams with anchored FRP ropes using NSM and ETS methods under reversed cyclic loading." *Journal of Composites for Construction* (2017): 04016072.

Khalifa, A., Gold, W. J., Nanni, A., and MI, A. A. "Contribution of externally bonded FRP to shear capacity of RC flexural members." *Journal of Composites for Construction* 2.4 (1998): 195-202.

Lee, D., and Cheng, L. "Assessing the strengthening effect of various near-surface-mounted FRP reinforcements on concrete bridge slab overhangs." *Journal of Composites for Construction* 15.4 (2011): 615-624.

Lee, D., and Cheng, L. "Bond of NSM systems in concrete strengthening–Examining design issues of strength, groove detailing and bond-dependent coefficient." *Construction and Building Materials* 47 (2013): 1512-1522.

Lee, D., Cheng, L., and Yan-Gee Hui, J. "Bond characteristics of various NSM FRP reinforcements in concrete." *Journal of Composites for Construction* 17.1 (2012): 117-129.

Lee, J., and Fenves, G. L. "Plastic-damage model for cyclic loading of concrete structures." *Journal of Engineering Mechanics* 124.8 (1998): 892-900.

Lopez-Almansa, F., Alfarah, B., and Oller, S. "Numerical simulation of RC frame testing with damaged plasticity model. Comparison with simplified models." *Second European Conference on Earthquake Engineering and Seismology*, Istanbul, Turkey, 2014.

Lubliner, J., Oliver, J., Oller, S., and Onate, E. "A plastic-damage model for concrete." *International Journal of Solids and Structures* (1989).

Mander, J. B., Priestley, M. J., and Park, R. "Theoretical stress-strain model for confined concrete." *Journal of Structural Engineering* 114.8 (1988): 1804-1826.

Mercan, B., Schultz, A. E., and Stolarski, H. K. "Finite element modeling of prestressed concrete spandrel beams." *Engineering Structures* 32.9 (2010): 2804-2813.

Nakaba, K., Kanakubo, T., Furuta, T., and Yoshizawa, H. "Bond behavior between fiber-reinforced polymer laminates and concrete." *Structural Journal* 98.3 (2001): 359-367.

Novidis, D. G., and Pantazopoulou, S. J. "Bond tests of short NSM-FRP and steel bar anchorages." *Journal of Composites for Construction* 12.3 (2008): 323-333.

Oehlers, D., Seracino, R., and Smith, S. "Design handbook for RC structures retrofitted with FRP and metal plates: Beams and slabs." (2008).

Omran, H. Y., and El-Hacha, R. "Effects of sustained load and freeze-thaw exposure on RC beams strengthened with prestressed NSM-CFRP strips." *Advances in Structural Engineering* 17.12 (2014): 1801-1816.

Oudah, F., and El-Hacha, R. "Research progress on the fatigue performance of RC beams strengthened in flexure using fiber reinforced polymers." *Composites Part B: Engineering* 47 (2013): 82-95.

Palmieri, A., Matthys, S., Barros, J. A., Costa, I., Bilotta, A., Nigro, E., Ceroni, F, Szambo, Z., and Balazs, G. "Bond of NSM FRP strengthened concrete: round robin test initiative." *CICE 2012 6th International Conference on FRP Composites in Civil Engineering*. International Institute for FRP in Construction (IIFC), 2012.

Pellegrino, C., and Sena-Cruz, J. "Design procedures for the use of composites in strengthening of reinforced concrete structures." *STAR* (2015).

Rashid, R., Oehlers, D. J., and Seracino, R. "IC debonding of FRP NSM and EB retrofitted concrete: Plate and cover interaction tests." *Journal of Composites for Construction* 12.2 (2008): 160-167.

Rezazadeh, M., Carvelli, V., and Veljkovic, A. "Modelling bond of GFRP rebar and concrete." *Construction and Building Materials* 153 (2017): 102-116.

SA. "Design handbook for RC structures retrofitted with FRP and metal plates: beams and slabs." HB 305-2008. Standards Australia GPO Box 476, Sydney, NSW 2001, Australia, 2008.

Saenz, L. P. "Discussion of "Equation for the stress-strain curve of concrete" by Desayi and Krishnan." *Journal of the American Concrete Institute* 61 (1964): 1229-1235.

Sasmal, S., Khatri, C. P., Ramanjaneyulu, K., and Srinivas, V. "Numerical evaluation of bond–slip relations for near-surface mounted carbon fiber bars embedded in concrete." *Construction and Building Materials* 40 (2013): 1097-1109.

Sena Cruz, J. M., Barros, J. A., Gettu, R., and Azevedo, A. F. "Bond behavior of near-surface mounted CFRP laminate strips under monotonic and cyclic loading." *Journal of Composites for Construction* 10.4 (2006): 295-303.

Sena-Cruz, J., and Barros, J. A. "Modeling of bond between near-surface mounted CFRP laminate strips and concrete." *Computers and Structures* 82.17-19 (2004): 1513-1521.

Seo, S. Y., Feo, L., and Hui, D. "Bond strength of near surface-mounted FRP plate for retrofit of concrete structures." *Composite Structures* 95 (2013): 719-727.

Seracino, R., Jones, N. M., Ali, M. S., Page, M. W., and Oehlers, D. J. "Bond strength of near-surface mounted FRP strip-to-concrete joints." *Journal of Composites for Construction* 11.4 (2007b): 401-409.

Seracino, R., Raizal Saifulnaz, M. R., and Oehlers, D. J. "Generic debonding resistance of EB and NSM plate-to-concrete joints." *Journal of Composites for Construction* 11.1 (2007a): 62-70.

Sharaky, I. A., Torres, L., Baena, M., and Vilanova, I. "Effect of different material and construction details on the bond behavior of NSM FRP bars in concrete." *Construction and Building Materials* 38 (2013): 890-902.

Silva, P., Fernandes, P. M. G., Sena-Cruz, J., Azenha, M., and Barros, J. A. "Creep behavior and durability of concrete elements strengthened with NSM CFRP strips." *7th International Conference on Fiber Reinforced Polymer (FRP) Composites in Civil Engineering (CICE 2014)*, Vancouver, British Columbia, Canada, 2014.

Soliman, S. M., El-Salakawy, E., and Benmokrane, B. "Bond performance of near-surface-mounted FRP bars." *Journal of Composites for Construction* 15.1 (2011): 103-111.

Standard, A. S. T. M. C39/C39M–17b, "Standard test method for compressive strength of cylindrical concrete specimens," ASTM International, West Conshohocken, PA (2017).

Standard, A. S. T. M. C496/C496M-17, "Standard test method for splitting tensile strength of cylindrical concrete specimens," ASTM International, West Conshohocken, PA (2017).

Standard, A. S. T. M. D7205/D7205M-06, "Standard Test Method for Tensile Properties of Fiber Reinforced Polymer Matrix Composite Bars", ASTM International, West Conshohocken, PA (2016).

Teng, J. G., Zhang, S. S., Dai, J. G., and Chen, J. F. "Three-dimensional meso-scale finite element modeling of bonded joints between a near-surface mounted FRP strip and concrete." *Computers and Structures* 117 (2013): 105-117.

Torres, L., Sharaky, I. A., Barris, C., and Baena, M. "Experimental study of the influence of adhesive properties and bond length on the bond behavior of NSM FRP bars in concrete." *Journal of Civil Engineering and Management* 22.6 (2016): 808-817.

Vandewalle, L., Nemegeer, D., Balazs, L., Barr, B., Barros, J., Bartos, P., Banthia, N., Criswell, M., Denarie, E., Di Prisco, M. and Falkner, H. "RILEM TC 162-TDF: Test and design methods for steel fibre reinforced concrete'-sigma-epsilon-design method-Final Recommendation." *Materials and Structures* 36.262 (2003): 560-567.

Vermeer, P. A., and De Borst, R. "Non-associated plasticity for soils, concrete and rock." *HERON*, 29 (3), 1984 (1984).

Wahab, N., Soudki, K. A., and Topper, T. "Experimental investigation of bond fatigue behavior of concrete beams strengthened with NSM prestressed CFRP rods." *Journal of Composites for Construction* 16.6 (2012): 684-692.

Wang, H. and Belarbi, A. "Static and fatigue bond characteristics of FRP rebars embedded in fiber-reinforced concrete." *Journal of Composite Materials* 44.13 (2010): 1605-1622.

Wu, Y. F., Xu, X. S., Sun, J. B., and Jiang, C. "Analytical solution for the bond strength of externally bonded reinforcement." *Composite Structures* 94.11 (2012): 3232-3239.

WU, Y.F. and Jiang, C. "Analytical identification of bond parameters for EB-FRP joints." Proc., *7th International Conference on FRP Composites in Civil Engineering (CICE2014)*, Vancouver, British Columbia, Canada, 2014.

Yao, J., Teng, J. G., and Chen, J. F. "Experimental study on FRP-to-concrete bonded joints." *Composites Part B: Engineering* 36.2 (2005): 99-113.

Yost, J. R., Gross, S. P., and Deitch, M. J. "Fatigue behavior of concrete beams strengthened in flexure with near surface mounted CFRP." *Proceedings of the 8th International Symposium on Fiber Reinforced Polymer Reinforcement for Reinforced Concrete Structures (FRPRCS8)*, University of Patras, Patras, Greece, 2007.

Yuan, H., Teng, J. G., Seracino, R., Wu, Z. S., and Yao, J. "Full-range behavior of FRP-to-concrete bonded joints." *Engineering Structures* 26.5 (2004): 553-565.

Yuan, H., Wu, Z., and Yoshizawa, H. "Theoretical solutions on interfacial stress transfer of externally bonded steel/composite laminates." *Doboku Gakkai Ronbunshu* 2001.675 (2001): 27-39.

Yun, Y., Wu, Y. F., and Tang, W. C. "Performance of FRP bonding systems under fatigue loading." *Engineering Structures* 30.11 (2008): 3129-3140.

Zhang, S. S. "Bond strength model for near-surface mounted (NSM) FRP bonded joints: Effect of concrete edge distance." *Composite Structures* 201 (2018): 664-675.

Zhang, S. S., and Yu, T. "Effect of groove spacing on bond strength of near-surface mounted (NSM) bonded joints with multiple FRP strips." *Construction and Building Materials* 155 (2017): 103-113.

Zhang, S. S., Teng, J. G., and Yu, T. "Bond strength model for interfaces between near-surface mounted (NSM) CFRP strips and concrete." University of Wollongong, 2014.

Zhang, S. S., Teng, J. G., and Yu, T. "Bond–slip model for CFRP strips near-surface mounted to concrete." *Engineering Structures* 56 (2013): 945-953.

Zhang, Z. Z. "Coefficient of friction between FRP bars and epoxy material.", Internal Master Report, University of California, Davis, 2018.

Zheng, X. H., Huang, P. Y., Han, Q., and Chen, G. M. "Bond behavior of interface between CFL and concrete under static and fatigue load." *Construction and Building Materials* 52 (2014): 33-41.